

# Performance and Technology Readiness of a Freestream Turbine in a Canal Environment

A thesis submitted in partial fulfilment of the requirements for the degree of

Doctor of Philosophy (PhD)

2018

by

Stefan Runge

School of Engineering

Cardiff University, UK







## Acknowledgement

First and foremost, I would like to express the deepest appreciation to Professor Thorsten Stoesser for his excellent supervision, his contagious curiosity and the brilliant experience I gained by participating in this exciting project. Thank you Thorsten!!! I also like to thank the entire Emrgy team and Madeleine in particular who was as happy as I was when we reached TRS 3 (: What a privilege to work with you!!!

Thank you Emily (Emrgy Inc.) and EPSRC for funding this studentship.

I received generous support from many more people. Thanks to the always helpful and inspiring Cardiff University technicians Paul, Harry, Garry, Gareth, Ian, Richard, Steffan, James, Denley, Roger and the magnificent Andrew with his crew. I would be nowhere without you boys!!! Thank you ever so much.

Moreover, I am very grateful for the various collaborations and want to thank Professor Nicholas Jenkins in particular for his support and insights into the electrical domain of kinetic turbines. I also want to thank Dr Ugalde-Loo, Dr Ming and Marios. ευχαριστώ πολύ! I have further greatly benefited from Dr Eton's advice and comments on composite materials and Dr Lacas' and Mr Spenceley's continuous support and help on selective laser sintering. I very much hope we can continue working together in the future.

Further, I had the encouragement and support by our astonishing University administration team who were never tired answering my questions (if I did not forget them...). I also appreciate the University's financial support when I received a research equipment grant.

During my time at Cardiff University, I met so many beautifully minded and inspiring people and am sure some will be friends forever. For your advice, patience, time and friendship, I would like to thank Luis, Pablo, Filipa, Ken, John, Valentine, Claudia, Muaaz, Alex, Neic, Richard, Bruño, Elli, Giovanni, Qianyu and all I forgot. You are awesome guys.

My deepest gratitude goes to Katja, Lukas, Sophie, family and friends. Without your never-ending support and encouragement this project would not have happened and much worse, my life would be meaningless. I love you!



## Abstract

In this thesis, the study of performance and technology readiness of a freestream vertical axis twin turbine in a canal environment is reported. Experimental tests of a 1:10 scale model were carried out in the Hydro-Environmental Research Laboratory at Cardiff University. It is shown that a three-bladed, counter-rotating, vertical axis twin-rotor assembly performs best with a low rotor solidity and that channel blockage ratio influences significantly turbine performance and flow backwater effects.

Blade manufacturing and surface-finishing was investigated and it is shown that a high quality surface finish of the blades is necessary to achieve the best performance. In a twin-turbine setup, the axis to axis distance between the two rotors is also identified as an important parameter. In order to combine the counter rotating motion of the two rotor shafts to one main shaft, a timing belt drive-train was introduced which drives the power take-off device. In the experiments, a mechanical brake and different generators were used in order to quantify the extracted energy and a comparison to the available hydrokinetic energy was performed. The electrical components needed for operating the turbine at different scales are presented and a control strategy for the maximum power point extraction was investigated.

Moreover, the wake recovery downstream of the turbine rotor was investigated in order to predict the interaction between turbines in an array and design parameters such as spacing or direction of rotation accordingly. Three distinct three dimensional wake regions were identified: (i) a near-wake region; (ii) a transition region; and (iii) a far-wake region, where the flow velocity has almost recovered.

In order to justify system functionality and performance in a relevant environment as well as up-scalability, a 1:3 scale model of the twin turbine was successfully implemented and tested in a discharge channel of a water treatment plant. This paved the way for a full-scale application: an array of ten full-scale twin turbine prototypes, including all relevant components such as housing, drive-train, gearbox and generator, are successfully installed, deployed and tested in the South Boulder Canal near Denver, Colorado, USA.

Finally, the development stages of the twin turbine system were benchmarked by performing the Technology Readiness Level (TRL) assessment procedure. It is shown that the described turbine successfully reaches TRL 7 i.e., “full-scale, similar or prototypical system demonstrated in relevant environment”.



# Contents

Declaration .....	I
Acknowledgement .....	III
Abstract .....	V
Contents .....	VII
List of Publications.....	XII
List of Figures .....	XIII
List of Tables .....	IIXX
List of Equations .....	IXX
Nomenclature .....	XX
I. Introduction.....	1
1.1 Motivation.....	1
1.2 Renewable Energy.....	2
1.3 Hydropower.....	4
1.3.1 Kinetic energy.....	7
1.3.2 Horizontal axis turbines (HATs).....	10
1.3.3 Vertical axis turbines (VATs).....	14
1.4 Fields of application for hydrokinetic turbines .....	22
1.4.1 Marine.....	22
1.4.2 Inland.....	24
II. Objectives.....	27
III. Turbine concept and laboratory performance study .....	28
3.1 Introduction .....	28
3.2 Turbine concept .....	29
3.2.1 Housing .....	29
3.2.2 Rotors.....	30
3.2.3 Power take-off.....	30
3.3 Laboratory performance study.....	32
3.3.1 Test facilities .....	33
3.3.2 Rotor testing and results .....	36
3.3.2.1 Blade (air-foil) shape .....	37
3.3.2.2 Pitch angle .....	38
3.3.2.3 Number of blades.....	39
3.3.2.4 Blade twist.....	40
3.3.2.5 Spoke-blade fastening.....	41
3.3.2.6 Blade surface finish .....	42

3.3.2.7 Shaft diameter .....	43
3.3.2.8 Spokes vs discs .....	45
3.3.2.9 Flywheel .....	47
3.3.2.10 Solidity .....	47
3.3.3 Structure testing and results .....	49
3.3.3.1 Blockage .....	49
3.3.3.2 Rotor position .....	51
3.3.4 Twin-rotor testing and results .....	52
3.3.4.1 Single vs twin rotor .....	52
3.3.4.2 Distance between rotors .....	54
3.3.4.3 Inwards vs outwards rotation .....	55
3.3.4.4 Synchronisation of rotors .....	55
3.3.4.5 Rotor offset .....	56
3.3.4.6 Submergence .....	57
3.4 Summary .....	58
IV. Turbulences and wake study .....	61
4.1 Introduction .....	61
4.2 Experimental setup .....	63
4.2.1 Laboratory configuration .....	63
4.2.2 Free-stream flow conditions .....	64
4.2.3 Description of the VAT .....	65
4.3 Wake measurements results .....	66
4.3.1 Horizontal plane at mid-height of the turbine rotor .....	66
4.3.2 Vertical longitudinal plane .....	69
4.3.3 Cross-sectional planes .....	71
4.3.4 Power spectra .....	73
4.3.5 Streamwise momentum recovery .....	74
4.3.6 Skewness of the turbine rotor's wake .....	75
4.3.7 Wake characteristics and recovery .....	77
4.4 Summary .....	79
V. Electrical components .....	81
5.1 Decision making process for electrical components .....	82
5.1.1 Turbine .....	82
5.1.2 Power control .....	83
5.1.3 Direct Current vs Alternating Current .....	84
5.1.3.1 DC (Battery charging) .....	84
5.1.3.2 AC (1 Phase vs 3 Phase) .....	85

5.1.4 Voltage and frequency .....	85
5.1.5 Generator .....	86
5.1.5.1 Synchronous generators (permanent magnet generators).....	87
5.1.5.2 Asynchronous generators (induction motors) .....	88
5.1.6 Remarks .....	89
5.1.6.1 Safety .....	89
5.1.6.2 Durability .....	89
5.1.6.3 Assumptions.....	89
5.2 State of the art.....	89
5.2.1 Laboratory testing (small scale) .....	90
5.2.2 Field testing (demonstrator scale).....	91
5.2.3 Application (full scale).....	94
5.3 Generator testing.....	95
5.3.1 Result LE 300 .....	97
5.3.2 Result LE 450 .....	97
5.3.3 Result DVE 200 .....	98
5.4 Power control .....	98
5.5 Summary.....	99
VI. Field testing in a water treatment plant .....	101
6.1 Introduction .....	101
6.2 Site conditions, deployment concept and test-plan.....	101
6.3 Turbine design .....	103
6.3.1 Flow diverter .....	103
6.3.2 Middle bridge .....	104
6.3.3 Upper Bridge.....	105
6.3.4 Rotors .....	105
6.3.5 Hubs .....	106
6.3.6 Spokes.....	106
6.3.7 Blades.....	107
6.3.8 Shaft and Belt drive.....	109
6.3.9 Power take-off.....	110
6.4 Turbine installation .....	111
6.5 Procedure and Results.....	114
6.5.1 Phase a .....	115
6.5.2 Phase b .....	118
6.5.3 Phase c and hand over .....	119
6.6 Summary.....	121

VII. Application in a fresh water canal .....	124
7.1 Introduction.....	124
7.2 Turbine design and testing environment .....	125
7.3 Procedure and results.....	127
7.4 Scalability .....	131
7.5 Summary .....	132
VIII. Technology readiness.....	133
8.1 Introduction.....	133
8.2 Technology concept (TRL 1-3) .....	134
8.2.1 Overall design .....	134
8.3 Technology development - Laboratory testing (TRL 3-5) .....	135
8.3.1 Experimental rotor optimisation .....	136
8.3.2 Twin turbine testing and optimisation .....	136
8.3.3 Closure .....	137
8.4 Pilot scale testing (TRL 6).....	138
8.4.1 Testing environment and turbine design.....	138
8.4.2 Procedure and results .....	139
8.4.3 Closure .....	140
8.5 System commissioning (TRL 7).....	140
8.5.1 Testing environment and turbine design.....	140
8.5.2 Procedure and results .....	141
8.5.3 Closure .....	142
8.6 Summary.....	142
IX. Conclusions and recommendations .....	143
9.1 Conclusions.....	143
9.2 Recommendations.....	145
List of references .....	149
Appendices .....	163
A. Test result overview.....	163
B. Technical drawings of VAT .....	165
Turbine concept.....	165
Laboratory components .....	166
C. Belt drive sizing and tension .....	170
D. Power diversion assembly.....	171
E. RM Clayton, Atlanta, GA .....	173
Technical drawing of disinfection-channel at RM Clayton, Atlanta, GA.....	173
Discharge data field testing Atlanta .....	174

F.	SBC Denver, CO.....	176
	Water levels up and downstream VAT application testing Denver .....	176
G.	Component manufacturing .....	177
	Sintering/rapid prototyping .....	177
	Composite blade manufacturing .....	178
	Mould .....	179
	Core .....	185
	Mould and Core.....	189
	Summary.....	193
	Autoclave test cycle .....	195
	Torsion test results for laboratory composite blades .....	195
	Blades for potential structural/hydrodynamical assessment .....	196
H.	Data sheets .....	197
	Torque transducer .....	197
	Acoustic Doppler Velocimeter (ADV) .....	199
	Generators .....	199
	Water flow probe .....	202
	SLS polyamide .....	203
	Composite epoxy matrix resin prepregs.....	205
	Permabond.....	209
	Aluminium.....	211
	Nylon .....	212
I.	Data variation.....	213
	Variation of torque .....	213
	Torque ripple and blade twist.....	215
	Torque ripple and rotor offset.....	218

## List of Publications

### Journal paper

- 1) S. Runge, T. Stoesser, E. Morris, M. White. Technology Readiness of a Vertical-Axis Hydro-Kinetic Turbine. *Journal of Power Energy Engineering*, 06 (2018) 63–85.
- 2) P. Ouro, S. Runge, Q. Luo, T. Stoesser. Three-dimensionality of the wake recovery behind a vertical axis turbine. *Journal of Renewable Energy*, 133 (2019) 1066-1077.
- 3) M. Michas, C. E. Ugalde-Loo, W. Ming, N. Jenkins, S. Runge. Maximum Power Extraction from a Hydrokinetic Energy Conversion System. In press, *Journal of IET Renewable Power*, (2019).

### Conference paper

- 1) L. Priegue, T. Stoesser, S. Runge. Effect of blade parameters on the performance of a cross-flow turbine. *E-Proceedings 36th IAHR World Congress*, The Hague, (2015) 11-15.

### Reports to industry sponsor (confidential)

- 1) S. Runge. Composite Blade Manufacturing. Cardiff, 2015
- 2) S. Runge, T. Stoesser. Emrgy's Hydrokinetic Turbine: A Design and Performance Report. Cardiff, 2016
- 3) S. Runge. Emrgy's Hydrokinetic Turbine: A Power Generation Design Report. Cardiff, 2017
- 4) S. Runge, T. Stoesser. Emrgy's Hydrokinetic Turbine: Demonstrator Testing. Cardiff & Atlanta, 2017
- 5) S. Runge, T. Stoesser. Emrgy's Hydrokinetic Turbine: Full-scale Testing. Cardiff & Denver, 2017
- 6) S. Runge, T. Stoesser. Emrgy's Hydrokinetic Turbine: Observations and Recommendations from SBC Capacity Testing. Cardiff & Denver, 2017

## List of Figures

Figure 1. Natural energy flux on the Earth .....	3
Figure 2. Hydrological or natural water cycle .....	4
Figure 3. Typical layout of a conventional hydropower plant .....	5
Figure 4. Hydrokinetic conversion devices .....	6
Figure 5. Channel-flow with changing Froude number .....	8
Figure 6. Evolution in size of commercial wind turbines .....	10
Figure 7. Size comparison between air and water driven HATs .....	10
Figure 8. Hydrokinetic horizontal axis turbine examples.....	11
Figure 9. a) Basic concept of the Bernoulli Effect illustrated on an airfoil-shaped b) Typical pressure distribution over an airfoil-shaped body.....	12
Figure 10. a) Velocity vectors on a HAT b) Change in blade curvature and pitch angle over blade length .....	13
Figure 11. Types of VATs .....	16
Figure 12. Hydrokinetic vertical axis turbine examples.....	17
Figure 13. Velocity vectors and forces on a VAT .....	18
Figure 14. Analytically and numerically derived forces of a straight VAT blade .....	20
Figure 15. a) Typical $\alpha$ vs $\theta$ relation for different TSRs b) Typical torque curve of a four bladed VAT .....	21
Figure 16. a) Global distribution of mean tidal range b) UK distribution of mean spring tide range.....	23
Figure 17. Conceptual CAD drawing of the twin turbine assembly in a channel .....	28
Figure 18. Conceptual CAD drawing of the twin turbine and its components .....	29
Figure 19. Housing subsystem of turbine concept.....	30
Figure 20. Subsystems of turbine concept .....	31
Figure 21. Plan view of two counter rotating VAT rotors in a channel with a typical flow velocity distribution .....	31

Figure 22. Picture of laboratory flume at Cardiff University and main dimensions ..	33
Figure 23. CAD drawings and photographs of PTO used for twin rotor testing .....	34
Figure 24. Photograph of some rotors tested .....	36
Figure 25. Blade shape comparison.....	37
Figure 26. Blade cross-section with nomenclature .....	38
Figure 27. Pitch angle comparison .....	39
Figure 28. Number of blades comparison.....	40
Figure 29. Comparison of straight and twisted blades .....	41
Figure 30. Comparison of countersunk and socket bolts .....	42
Figure 31. Surface roughness comparison.....	43
Figure 32. Different shaft diameter comparison.....	44
Figure 33. CAD drawings of spoke used for laboratory rotor .....	46
Figure 34. Discs vs spokes comparison .....	46
Figure 35. Flywheel comparison .....	47
Figure 36. Rotor with low solidity (green) and high solidity (pink) .....	48
Figure 37. Solidity comparison of very low and low solidity rotor .....	49
Figure 38. Blockage comparison .....	50
Figure 39. Comparison of longitudinal displacement .....	51
Figure 40. Single vs twin comparison.....	53
Figure 41. Twin rotor spacing comparison.....	54
Figure 42. Twin rotor inwards vs outwards rotation comparison .....	55
Figure 43. Twin rotor synchronisation comparison .....	56
Figure 44. Twin rotor offset comparison .....	56
Figure 45. Rotor submergence comparison .....	58
Figure 46. Laboratory PTO and rotor .....	59
Figure 47. Data of the free-stream flow .....	64
Figure 48. a) Turbine rotor and PTO. (b) $C_p - \lambda$ curve.....	65

Figure 49. Location of the cross-sections behind the vertical axis turbine rotor .....	66
Figure 50. Horizontal plane at $z/D = 0$ .....	67
Figure 51. Horizontal profiles at rotor mid-height .....	68
Figure 52. Vertical plane at $y/D = 0$ .....	70
Figure 53. Vertical profiles at flume centre .....	71
Figure 54. Distribution of normalised streamwise velocity ( $U/U_0$ ), turbulence intensity ( $\sigma_u/U_0$ ) and Reynolds shear stresses ( $-u'v'$ and $-u'w'$ ) along four cross-sections downstream of the turbine at $x/D = 1, 2, 3$ and $5$ .....	72
Figure 55. Power spectral density, PSD, of u-velocity .....	73
Figure 56. Cross-sectional average values of the streamwise momentum equation contributors along the locations measured .....	75
Figure 57. Contours of (a-d) $Sk_u$ and (e-h) $Sk_v$ at different cross-sections .....	76
Figure 58. Probability density functions and quadrant analysis .....	77
Figure 59. Distribution along the wake centreline of (a) normalised time-averaged velocity components, (b) turbulence intensities, (c) measured velocity deficit and exponential fit, and (d) Reynolds shear stresses. n-w, m-w and f-w denote near-, mid- and far-wake, respectively .....	78
Figure 60. CAD drawing of 10kW full scale VAT concept .....	81
Figure 61. Decision making process for electrical component design of a VAT .....	82
Figure 62. Exemplary hydropower plant with power control .....	83
Figure 63. Simplified demonstrator (DC) power generation process .....	84
Figure 64. Simplified commercial (AC) power generation process .....	85
Figure 65. Schematic of AC voltage with 0.5Hz and its oscillating behaviour .....	86
Figure 66. Schematic and photograph of 3-phase synchronous generator .....	87
Figure 67. a) Schematic of generator windings and wiring b) Sinusoidal voltage output versus time of a 3Phase generator .....	88
Figure 68. Exploded view of an asynchronous generator .....	88

Figure 69. a) Photograph of low rpm off-the-shelf laboratory generator (DVE200)	
b) Photograph of high rpm custom-made laboratory generator (LE300)	
c) Photograph of PTO where the generator was attached to .....	90
Figure 70. Comparison between electrical and mechanical efficiency .....	91
Figure 71. Schematic and photograph of power diversion assembly .....	92
Figure 72. CAD drawing of 10kW full scale VAT concept .....	94
Figure 73. Generator test rig and components .....	95
Figure 74. Milling machine with LE300 generator and periphery .....	96
Figure 75. Efficiency of LE300 with different resistances.....	97
Figure 76. Efficiency of LE450 with different resistances.....	97
Figure 77. Efficiency of DVE200 with different resistances.....	98
Figure 78. Schematic and photograph of laboratory MPPT .....	99
Figure 79. CAD side view of the UV channel at RM Clayton .....	102
Figure 80. CAD cross-sectional view on twin VAT design for RM Clayton.....	103
Figure 81. CAD side view of constriction design for RM Clayton .....	104
Figure 82. CAD front view of middle bridge with bearings .....	105
Figure 83. a) CAD top view of upper bridge including PTO and rotors	
b) Construction drawing of upper bridge as manufactured.....	105
Figure 84. CAD drawings and photograph of one of the two rotors .....	106
Figure 85. a) CAD top view of the rotor's hub including components	
b) CAD bottom view with spokes .....	106
Figure 86. CAD drawings of one spoke with major dimensions .....	107
Figure 87. a) CAD drawings of one blade with major dimensions	
b) 3D exploded view of the three blade components .....	108
Figure 88. a) CAD design drawings of blade mould with major dimensions.....	108
Figure 89. Exploded view of the drive train design .....	109
Figure 90. CAD design drawing of the PTO with major dimensions.....	110

Figure 91. a) Schematic of a typical waste water treatment process	
b) Aerial picture of RM Clayton water treatment plant .....	111
Figure 92. Pictures of the UV disinfection channels at RM Clayton .....	112
Figure 93. Installation pictures of turbine components and constriction.....	113
Figure 94. Turbine performance curves for tests 160 - 162.....	116
Figure 95. Test results with measured and calculated flow velocities.....	116
Figure 96. Results for Test 162 considering various flow velocities .....	117
Figure 97. Pictures of PTO of Phase b.....	118
Figure 98. Performance curves:	
a) Measured and calculated flow velocities of test 163	
b) Same curve as before with a velocity of 1m/s	
c) Power output from mech. and electr. PTO as a function of $\lambda$ .....	119
Figure 99. Pictures of PTO of Phase c.....	121
Figure 100. Top bridge of VAT system including PTO and PDA/battery case .....	123
Figure 101. Aerial images of the South Boulder Canal at Ralston, Colorado, US.	124
Figure 102. Hydrokinetic twin VAT in full scale, installed in SBC.....	125
Figure 103. Photographs of hydrokinetic twin turbine:	
a) As in operation including gearbox, generator and chain cover	
b) As tested including mechanical PTO .....	126
Figure 104. a) Photographs of mechanical PTO; b) VAT rotor prior to installation	127
Figure 105. Turbine performance curves .....	128
Figure 106. a) Rotors partially submerged and; b) fully submerged .....	129
Figure 107. Turbine's mechanical power vs rotational speed curve .....	130
Figure 108. Performance curves of three selected tests for laboratory, field testing and application scale, operating in different environments and at different sizes .....	131

## List of Tables

Table 1. Advantages and Disadvantages of HATs and VATs.....	9
Table 2. HED impact summary on rivers and engineered canals .....	25
Table 3. Turbine design aspects tested.....	32
Table 4. Flow speeds used in the experiments.....	35
Table 5. Best performing blade shapes.....	37
Table 6. Best performing pitch angle of different blades.....	38
Table 7. List of results from number of blades comparison.....	40
Table 8. List of results for salient fastening comparison .....	41
Table 9. List of results for surface roughness comparison.....	43
Table 10. List of results for shaft diameter comparison .....	44
Table 11. List of results for shaft diameter comparison .....	45
Table 12. List of results for blockage comparison.....	51
Table 13. List of results for rotor position comparison .....	52
Table 14. List of results for single vs twin rotor comparison.....	54
Table 15 Installation, testing and commissioning schedule at RM Clayton .....	102
Table 16. Measured values of electrical and mechanical quantities of Phase c....	120
Table 17. Technology Readiness Levels from DOE guide. ....	134

## List of Equations

1.1	Potential energy.....	6
1.2	Kinetic energy.....	7
1.3	Coefficient of performance.....	7
1.4	Overall efficiency.....	7
1.5	Reynolds number.....	8
1.6	Reynolds number w.r.t. chord length.....	8
1.7	Froude number.....	8
1.8	Bernoulli's principle.....	12
1.9	Lift force (HAT) .....	13
1.10	Drag force (HAT) .....	13
1.11	Overall torque (HAT) .....	14
1.12	Tip speed ratio.....	14
1.12a-e	Geometrical relations of velocity vectors and force coefficients.....	18
1.13	Tangential force (VAT) .....	19
1.14	Normal force (VAT) .....	19
1.14a-d	Geometrical relations between angle of attack and azimuth angle...	19
1.15	Tangential force (VAT) as function of lift and drag coefficient.....	19
1.16	Normal force (VAT) as function of lift and drag coefficient.....	20
1.16a	Simplification term $\phi$ .....	20
1.17	Overall torque (VAT) .....	20
3.1	Solidity.....	47
3.2	Blockage ratio.....	47
3.3	Channel width to rotor diameter ratio.....	47
4.1	Average flow velocity.....	63
4.2	Turbulence intensity.....	63
4.3	Turbulent kinetic energy.....	64
4.4	Reynolds-averaged Navier-Stokes equation.....	74
4.5	Skewness.....	75
4.6	Near-wake to medium-wake transition approximation.....	78
4.7	Dynamic solidity.....	78
4.8	Normalised streamwise velocity deficit distribution.....	79

# Nomenclature

## Abbreviations

AC	Alternating current
ADV	Acoustic Doppler Velocimeter
CAD	Computer aided design
CFD	Computational fluid dynamics
DC	Direct current
FEM	Finite element method
LES	Large eddy simulation
LHS	Left hand side
HAT	Horizontal axis turbine
PDA	Power diversion assembly
PMG	Permanent magnet generator
PSD	Power spectral density
PTO	Power take-off
rms	Root mean square
RANS	Reynolds averaged Navier-Stokes
RHS	Right hand side
SD	Standard deviation
SLS	Selective laser sintering
TKE	Turbulent Kinetic Energy
TRL	Technology readiness levels
TSR	Tip speed ratio
VAT	Vertical axis turbine
WT	Water table
w.r.t	With respect to

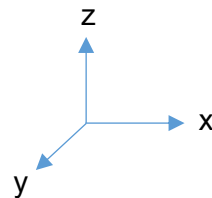
## List of symbols

$\alpha$	[ ° ]	Angle of attack
$\beta$	[ - ]	Blockage ratio
$\beta'$	[ - ]	Horizontal blockage ratio at rotor mid-span

$\gamma$	[ ° ]	Pitch angle
$\eta$	[ - ]	Efficiency
$\theta$	[ ° ]	Azimuth angle
$\lambda$	[ - ]	Tip speed ratio
$\mu$	[ Pa*s ]	Dynamic viscosity
$\nu$	[ m <sup>2</sup> /s ]	Kinematic viscosity
$\pi$	[ - ]	Number Pi
$\rho$	[ kg/m <sup>3</sup> ]	Density
$\sigma$	[ - ]	Solidity
$\sigma_{UI}$	[ - ]	Turbulence intensity
$\tau$	[ Nm ]	Torque
$\varphi$	[ ° ]	Inflow angle (sum of pitch angle and angle of attack)
$\omega$	[ rad/s ]	Rotational speed
$A$	[ m <sup>2</sup> ]	Area
$C_D$	[ - ]	Drag coefficient
$C_L$	[ - ]	Lift coefficient
$C_P$	[ - ]	Coefficient of performance
$CL$	[ m ]	Chord length
$D$	[ m ]	Diameter
$F$	[ N ]	Force
$Fr$	[ - ]	Froude number
$H$	[ m ]	Height
$I$	[ A ]	Current
$L$	[ m ]	Characteristic length
$N$	[ - ]	Number of elements
$P$	[ W ]	Power
$Q$	[ m <sup>3</sup> /s ]	Discharge
$R$	[ m ]	Overall blade length
$Re$	[ - ]	Reynolds number
$Re_D$	[ - ]	Reynolds number w.r.t. rotor diameter
$Re_C$	[ - ]	Reynolds number w.r.t blade chord length
$U$	[ V ]	Electrical potential

$U_i$	[ m/s ]	Mean velocity
$V$	[ m <sup>3</sup> ]	Volume
$W$	[ m/s ]	Relative velocity
$W_c$	[ m ]	Channel width
$g$	[ m/s <sup>2</sup> ]	Gravitational acceleration
$H$	[ m ]	Height or head
$n$	[ - ]	Element
$p$	[ Pa ]	Pressure
$r$	[ m ]	Radius
$t$	[ s ]	Time
$v$	[ m/s ]	Velocity

$x$	[ - ]	Direction vector in x-direction
$y$	[ - ]	Direction vector in y-direction
$z$	[ - ]	Direction vector in z-direction



$U$	[ m/s ]	Average velocity in x-direction
$V$	[ m/s ]	Average velocity in y-direction
$W$	[ m/s ]	Average velocity in z-direction
$u$	[ m/s ]	Spatial velocity in x-direction
$v$	[ m/s ]	Spatial velocity in y-direction
$w$	[ m/s ]	Spatial velocity in z-direction

## I. Introduction

### 1.1 Motivation

All living species strive to secure their survival and humankind is no exception. The difference between humans and most other species is their self-awareness which is seen to be a fundamental issue in psychology, “*from both a developmental and evolutionary perspective*” [1] and may be one of the reasons for the level of development humankind has reached. We are now living in a complex society which has its origins about a million years ago when humans lived in co-existence with nature and eventually developed a way to communicate with each other, learned how to use and control fire and understood to be more successful if collaborating in a team. The ability of communication enabled humans to share knowledge with others and to learn from mistakes [2].

These key features of humans have not changed but the speed of development has. Humans have lived as part of nature for tens of thousands of years. First advanced civilisations date back to the year 2500 B.C. and with the industrial revolution in the 19<sup>th</sup> century, the rate of development changed drastically [3].

Due to progressive engineers and scientists, inventions such as steam engine and electricity has changed the society. Most inventions aim at making existing processes more effective. The steam engine of the first car for example generated an equivalent amount of power as three horses whilst being much smaller, lighter and easier to maintain [4]. With many more inventions and patents, the steam engine became even smaller, more effective, durable, cheaper and powerful. About a hundred years later, only few carriages are being pulled by horses. Modern engines compile the amount of power of hundreds of horses by a fraction of their equivalent weight and costs. However, all modern engines need fuel. Whether it is coal or wood in the earliest steam engine or high performance carbon compounds in modern cars. In order to generate power, the engine converts the fuel’s energy into mechanical work driven by an exothermic chemical reaction. Once initiated, the reaction between oxygen and carbon continues, drives the engine and eventually the wheels. As the retired horse (or the hundreds of retired horses), the engine cannot convert all of the energy stored in the fuel. Some is converted mechanically, the rest dissipates in heat and sound or remains unused and is left with the reaction compounds. The reaction compounds depend very much on the fuel and are either solid or gaseous or a mixture of both. The amount and composition depends on the quality of the chemical reaction and the environment.

Until the late 1960's, most people were not aware of any side effects of this chemical reaction [5]. People were happy to have electricity (produced in very large coal plants) and machines (driven by electrical engines) which helped produce their goods and reduce their workload. However, the amount of reaction compounds emitted to the environment increased proportionally to the invention rate and energy consumption which led to consider another aspect: Human health. Besides energy and machinery related technical evolution, medicine has developed in a similar way and a relation between environmental aspects and health had been observed more than 200 years ago [6].

More recently, a broader impact of an increased fuel burning compound emission has been observed and is known as global warming. In contrast to more obvious, local environmental side effects such as pollution due to the accumulation of solid compounds or the odour of a coal plant exhaust, global warming has an impact on a global scale without any obvious relations to a local coal plant. Global warming is a technical term referring to a global increase in ambient temperatures driven by man-made processes (e.g., burning carbon compounds) which could lead to defrosting the polar caps, increasing the sea water level significantly and changing the entire climate in a potential life-threatening way [7].

Fortunately, humans are aware of the situation and many have the freedom to do something about it. I feel very privileged to have had the opportunity to spend three years on a research project aiming at understanding the behaviour of a turbine which harnesses energy from the movement of water and I very much hope that this project will help to take us one step forward towards a sustainable and non-invasive future.

## 1.2 Renewable Energy

Over the past century, energy consumption has increased significantly and the established fossil resources such as coal, oil and gas are limited. Energy from fossil sources causes emissions which are believed to have an impact on climate change [8]. Moreover, the society has become highly dependent on energy and governments strive for policies which guarantee energy security [9].

Energy from renewable sources has the potential to solve these concerns and beyond. In 1885, Werner von Siemens wrote about the discovery of the photovoltaic effect: *"In conclusion, I would say that however great the scientific importance of this discovery may be, its practical value will be no less obvious when we reflect that the supply of solar energy is both without limit and without cost, and that it will continue*

*to pour down upon us for countless ages after all the coal deposits of the earth have been exhausted and forgotten.”[10].*

Renewable energy is an umbrella term for sources which are infinite on a human timescale and can be divided into three groups: (i) solar energy, which includes wind and hydropower; (ii) geothermal energy, the heat stored in the accessible earth core; and (iii) other/combined sources such as tides which are also influenced by the gravity of moon and sun, Coriolis effect and other factors as depicted in Figure 1. In this thesis, the focus will be on the first group.

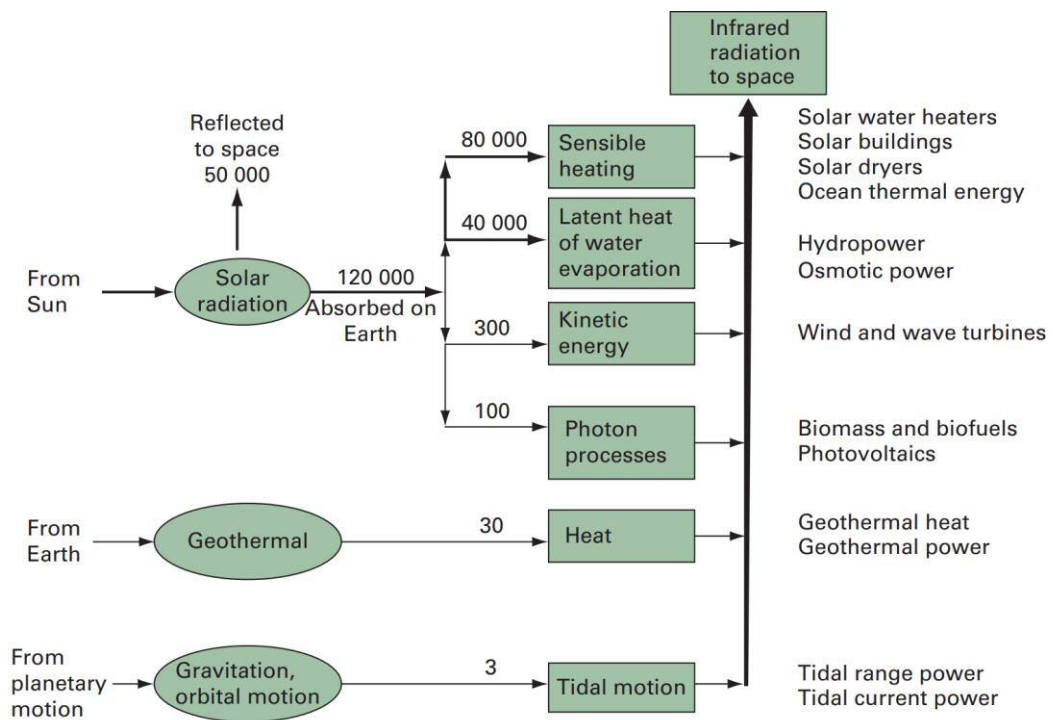


Figure 1. Natural energy flux on Earth in terawatts ( $10^{12}W$ ) [11]

The sun can be seen as an infinite source of energy since it will remain in its state for the next approximately five billion years and provides much more than the energy the world population currently consumes. As a result of the sun's nuclear fusion, light and heat is evenly emitted into space and eventually hits the earth's atmosphere. Most of the radiation is reflected back into space and transferred into heat. Depending on daytime, weather, altitude and latitude, an average of  $165 \text{ W/m}^2$  reaches the ground and can potentially be used for thermo-solar or photovoltaic processes. In an overall estimate,  $500 \text{ W/m}^2$  are accessible if all renewable energy forms are considered compared to approximately  $2000W$  total energy demand per person [11]. Assuming  $7 \times 10^9$  people living on earth and an earth surface area of  $50 \times 10^{12} \text{ m}^2$ , the global energy needs could be covered several times by the sun.

However, the sun is also the main influencer of the earth's complex climate and reason for the seasons, mild temperatures, wind and the hydrological cycle. Sea and other surface water evaporates due to the sun's radiation and accumulates to clouds. Driven by the wind, the clouds travel and eventually condense and precipitate elsewhere as depicted in Figure 2.

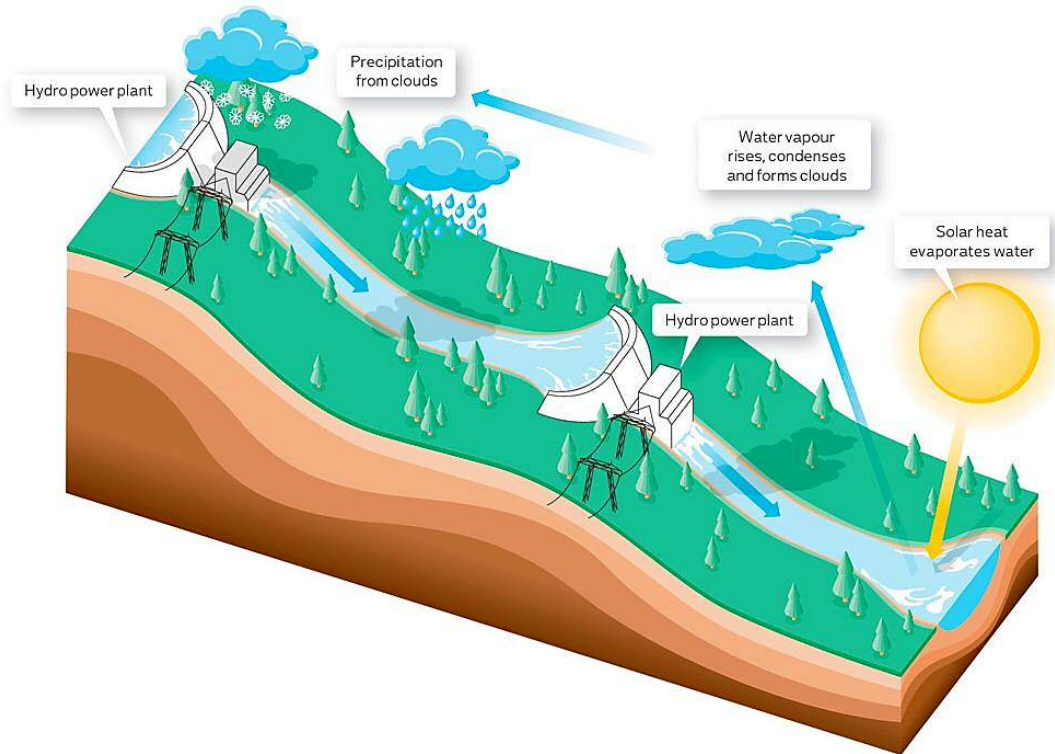


Figure 2. Hydrological or natural water cycle in a hydropower context [12]

This process naturally irrigates the continents and landmasses and allows plants in conjunction with sunlight, warmth and nutrition/soil to grow. The majority of the water, however, accumulates in rivers and flows back into the sea. This process contains a significant amount of energy. The so called hydro-potential energy is given by the fact that water was transported from sea level to a much higher elevation on land and strives, driven by gravity, back to a lower elevation and eventually the sea again.

### 1.3 Hydropower

Hydropower has a long history and is believed to have been used in China, Greece and Mesopotamia more than 5000 years ago. The first applications were designed for water distribution and irrigation of farmland. The first watermills were found in the Middle East more than 2000 years ago. The technology spread across the world and in 1086 AD, 5000 watermills were recorded in the UK alone [4]. With the industrial revolution, Faraday's contribution towards electric generators in the 1830s and a fast developing electrical industry, mostly coal driven power plants became extensively

popular. Thereafter, Benoît Fourneyron invented the first hydro turbine and paved the way towards big scale hydropower schemes and a global application. Nowadays, electricity is produced in several ways using different resources which very much depends on what is locally available and preferred.

Today, the majority of hydropower comes from large-scale hydropower plants which usually consist of a dam, a penstock and a power house containing the turbine and generator. The capacity of the plant depends on the elevation difference between dam and power house and the amount of water discharged. Huge structures such as the Three Gorges Dam built into the Yangtze River in China with its electrical capacity of 22.5 GW, the equivalent of 26 average nuclear plants [13], can provide power to millions of people. However, the environmental impact is equally huge. In case of the Three Gorges Dam, 1.24 million people had to be relocated, 13 cities, 140 towns and 1350 villages were flooded over a stretch of 600km with significant implications on flora and fauna [14].

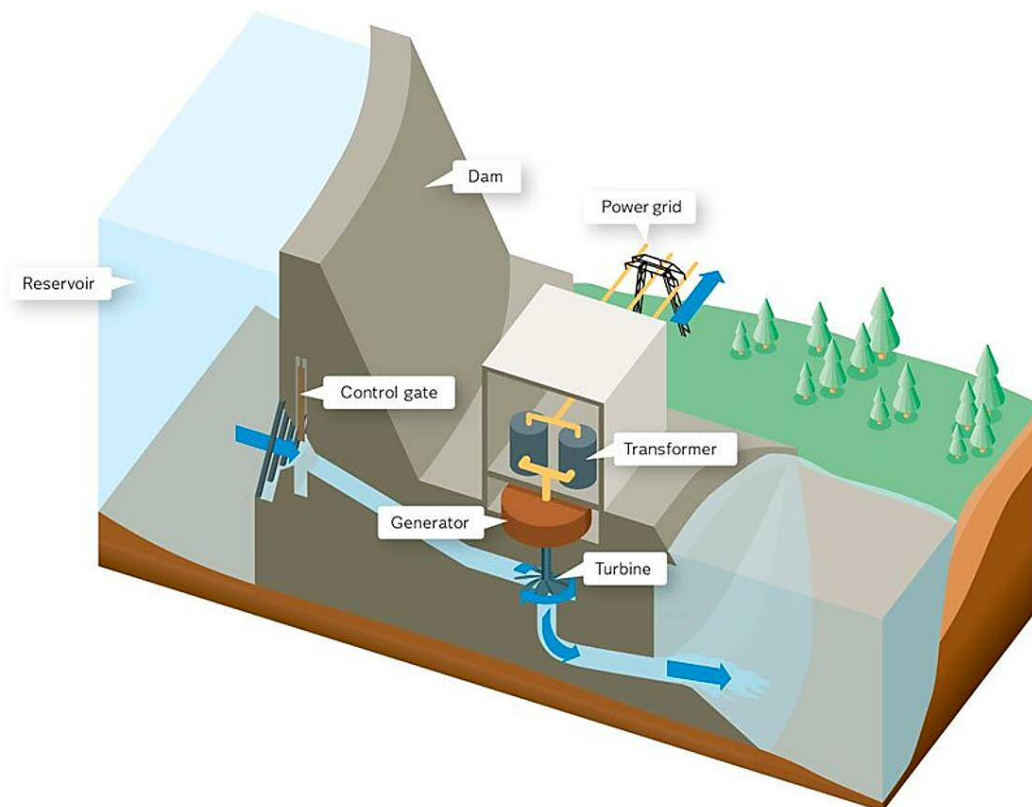


Figure 3. Typical layout of a conventional hydropower plant [15]

As depicted in Figure 3, hydropower is generated by employing an elevation (or head) differential to make use of the gravitational potential energy which can be expressed as presented in Equation 1.1:

$$P_a = \rho * Q * g * h \quad (1.1)$$

where  $P_a$  is the total amount of energy available in Watts,  $\rho$  the density of the object (a body of water in this case) in  $\text{kg/m}^3$ ,  $Q$  is the discharge in  $\text{m}^3/\text{s}$ ,  $g$  stands for the gravitational acceleration in  $\text{m/s}^2$  and  $h$  is the elevation differential in m. From Equation 1.1, it can be seen that besides the discharge, head is the critical variable in a hydropower context and the more difference in elevation is given the more energy is available.

Moreover, hydropower can also be generated by harnessing kinetic energy from flowing water as in ocean currents, tidal streams or inland in rivers or other channels where water is flowing, similar to wind turbines which are harnessing the kinetic energy of wind. Generally, hydrokinetic-turbines can be differentiated by their rotational axis orientation with respect to the flow direction. Best researched and well established in wind industry are horizontal-axis turbines (HATs, also called axial turbines) in contrast to vertical-axis turbines (VATs) which are less researched and rarely commercially applied [16]. Systems which do not fit into these categories are flapping or oscillating energy converters with their non-rotational motion [17–19]. [20] gives an overview of those and further novel hydrokinetic conversion devices. Here, the focus is on the two main conversion schemes: HATs and VATs in particular.

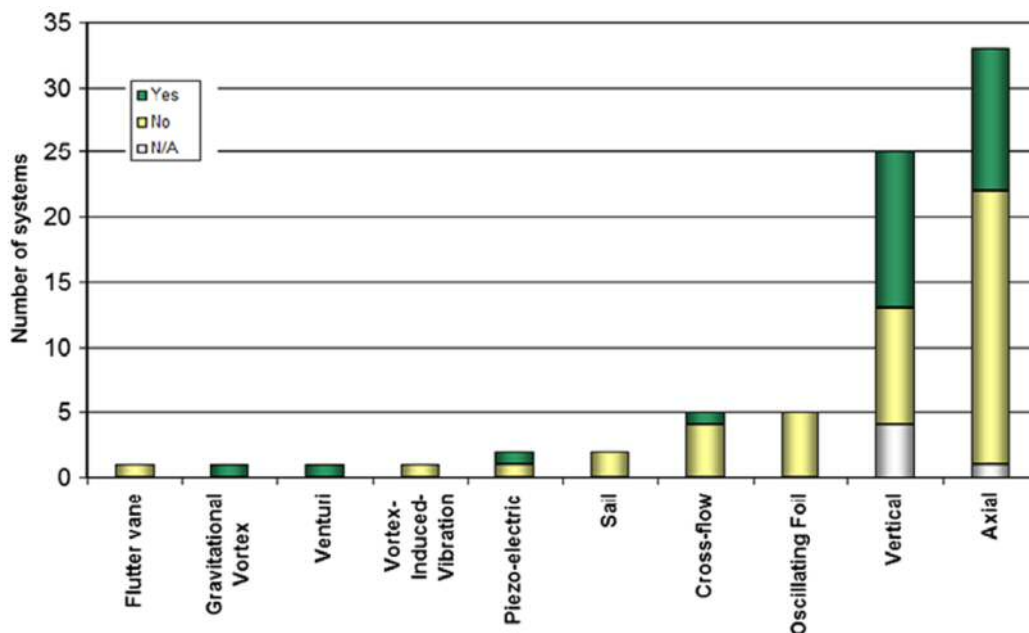


Figure 4. Hydrokinetic conversion devices and the employment of flow augmentation [21]

As shown in Figure 4, the majority of energy converters are VATs and HATs where the employment of a flow augmentations is more common with VATs (about 50%) as compared to HATs (about 30%). In the following, the two hydrokinetic turbine types

will be described in more depth after a description of the kinetic energy source in general.

### 1.3.1 Kinetic energy

In contrast to the potential energy where an elevation differential is needed, kinetic energy is the energy which an object (e.g., a body of water) contains due to its motion. This can be described as shown in Equation 1.2:

$$P_a = 0.5 * \rho * A * U^3 \quad (1.2)$$

where  $A$  is the cross-sectional area in  $m^2$ . In a hydropower context, the amount of extractable energy is therefore a function of the rotor area  $A$  and the flow velocity  $U$  whereas the latter is cubed and becomes more significant the higher it gets [22].

Similar to other machinery and processes, hydrokinetic turbines cannot extract all available energy  $P_a$  due to losses (mostly heat) in the energy conversion or transportation. The rotor shaft for example is held in place and allowed to spin by bearings which, even if well lubricated, apply a certain amount of friction to the shaft and therefore slow it down. The friction or resistance, which is caused by a rotational speed differential between two bodies, is converted into heat and dissipates to the environment or, depending on the amount of heat generated, needs to be cooled down. Therefore, the amount of generated or useable energy is the sum of all the losses subtracted from the available energy. Per definition, the power coefficient  $C_P$  (or coefficient of performance) of a turbine is the amount of energy extracted ( $P_e$ ) divided by the amount of energy available as shown in Equation 1.4:

$$C_P = \frac{P_e}{P_a} = \frac{\omega * \tau}{0.5 * \rho * A * U^3} \quad (1.3)$$

where  $P_e$  is the product of rotational speed  $\omega$  in rad/s and torque  $\tau$  in Nm measured at the rotor. In order to take additional losses such as the previously mentioned bearing friction into account, the term may be extended by applicable factors such as power take-off ( $\eta_{PTO}$ ), generator ( $\eta_{Generator}$ ), power transformation ( $\eta_{Transformation}$ ), power transportation ( $\eta_{Transportation}$ ) and other losses ( $\eta_n$ ) [23] which leads to an overall efficiency  $\eta_{Overall}$  as presented in Equation 1.4:

$$\eta_{Overall} = C_P * \eta_{PTO} * \eta_{Generator} * \eta_{Transformation} * \eta_{Transportation} * \eta_n \quad (1.4)$$

Beside power generation related losses, the entire available kinetic energy  $P_a$  is not harvestable due to the so called Lanchester-Betz limit [24] observed by aeronautic

pioneers Lanchester and Betz in the early 20<sup>th</sup> century in a wind energy context. Their observation stated that just 16/27 of  $P_a$  are extractable with an ideal kinetic extraction machine [25]. No machine has yet been designed which exceeds the Lanchester-Betz limit in an open flow environment. However, the application of VATs in channels (e.g., enclosed, constrained or blocked environments) may not be within the same boundaries as the Lanchester-Betz limit is defined in. Generally, there is a limitation in how much energy can be extracted due to the fact that the flow would stop flowing if all energy is taken out [26]. It will later be shown that a sophisticated flow augmentation and array design enables efficiencies much higher than 16/27 of  $P_a$  [26,27].

Reynolds number (Re) and Froude number (Fr) are dimensionless parameters to characterise a flow. In context of this study, both can be used to compare testing results from differently scaled but geometrically similar experiments. The Reynolds number indicates the ratio between inertial ( $F_i$ ) and viscous force  $F_v$  as shown in Equation 1.5.

$$Re = \frac{F_i}{F_v} = \frac{\rho * U^2 * L^2}{\mu * U / L * L^2} = \frac{\rho * U * L}{\mu} \quad (1.5)$$

where  $\mu$  is the dynamic viscosity and L the characteristic length which is usually the depth of the channel. Further, Re close to the blade surface is of interest and becomes a function of rotational speed ( $\omega$ ) and blade chord length (CL) as shown in Equation 1.6.

$$Re_c = \frac{\rho * \omega * CL}{\mu} \quad (1.6)$$

$$Fr = \frac{U}{\sqrt{L * g}} \quad (1.7)$$

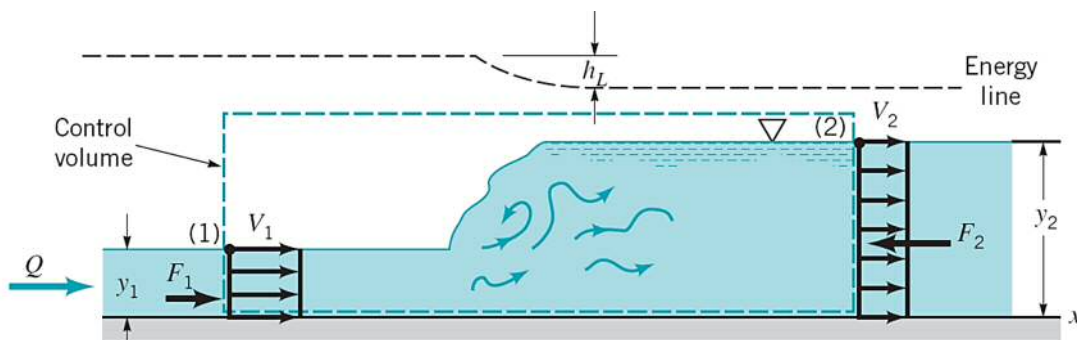


Figure 5. Channel-flow with changing Froude number from supercritical (left hand side (LHS)) to subcritical (right hand side (RHS)) and a hydraulic jump in the middle where  $Fr=1$  [28]

The Froude number as shown in Equation 1.7, is a parameter which is used to characterise the flow as the ratio of inertial and gravitational forces. If  $Fr = 1$ , the flow

is classified as critical. Consequently the flow is classified as subcritical if  $Fr < 1$  and supercritical if  $Fr > 1$  (see Figure 5).

A subcritical flow (such as a flow from a calm section of a river) can be influenced by a hydrokinetic turbine, both up- and downstream the device (e.g., backwater). Re and Fr number, enable to translate observations and findings from small scale laboratory turbine experiments to the desired full-scale design if kept relatively constant.

The two dominant hydrokinetic power extraction devices are HATs and VATs [29]. [30] summarises advantages and disadvantages of both technologies similarly to what is shown in Table 1 and is here added with conclusions from other sources [15, 25–27, 31–33]:

*Table 1. Advantages and Disadvantages of HATs and VATs*

	<b>Advantage</b>	<b>Disadvantage</b>	
<b>Design</b>	Self-starting capability	Sealing of submerged components	<b>HAT</b>
	Gearbox elimination possible	Ducting difficult to design	
<b>Pitch-control</b>	Optimised performance	Costs	
	Over-speed protection		
<b>Operation</b>		Noise	
<b>Design</b>	Simple	Self-starting issue due to low starting torque.	<b>VAT</b>
	Non submerged components		
	Uni-directional	Lower efficiency	
	Rectangular cross-section		
	Ducting (efficiency increase)		
<b>Pitch-control</b>	Not required		
<b>Operation</b>		Torque ripple	

In the following, both turbines will be described with a focus on their similarities, differences, advantages and drawbacks. For further reference, [21] gives an overview of available conversion systems with a focus on river and tidal applications.

### 1.3.2 Horizontal axis turbines (HATs)

HATs are devices which can be used to extract energy from a flowing fluid. The most popular application of HATs are wind turbines whereas the physical concept is independent from the fluid it is operating in. Horizontal-axis wind turbines (HAWTs) have been operated commercially for decades and have been further developed as presented in Figure 6. Soon, HAWTs with capacities up to 12 MW, a total height of 260m and a blade length more than 100m will be available [34].

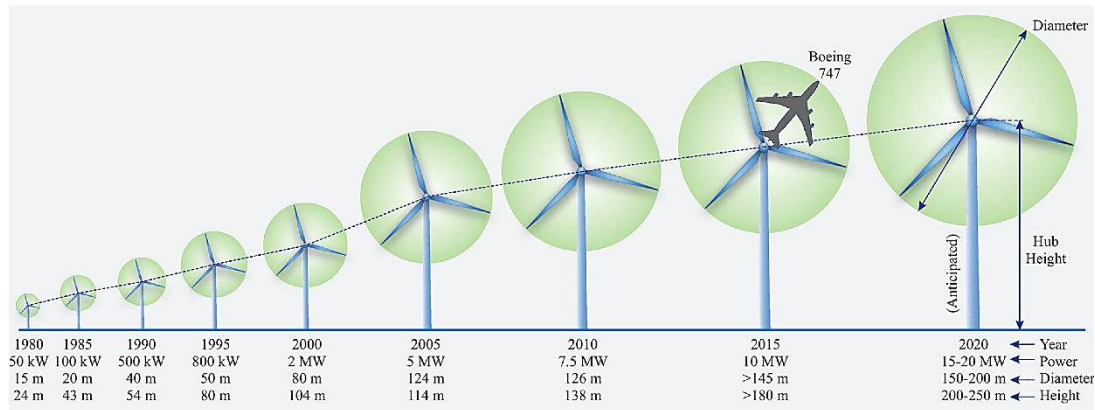


Figure 6. Evolution in size of commercial wind turbines [35]

Due to the significant difference in fluid density, hydrokinetic HATs are much smaller than their wind turbine counterparts with a similar power output as exemplified in Figure 7. However, the development of HATs for application in water is progressing but is certainly not as advanced as in the wind energy sector. [36] gives a detailed

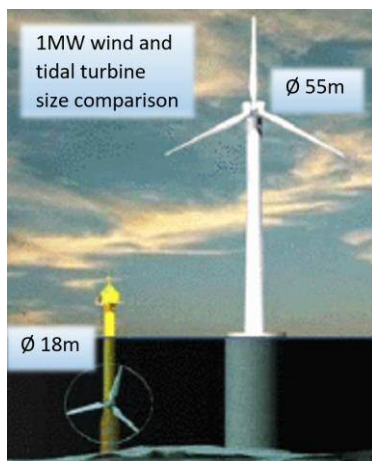


Figure 7. Size comparison between air and water driven HATs [187]

overview of large marine current turbine technologies and their development status. Figure 8 depicts some of the large scale hydrokinetic turbines which are currently under development and a CAD model with their main components. This type of turbine usually consists of a rotor, a nacelle and a foundation. The mooring can vary depending on the overall design and the site conditions. In the example shown, the foundation is a tripod which rests on the seabed. Alternatives are pile foundations, floating foundations or the attachment of the turbine to an existing structure. The rotor consists of several blades and a pitching mechanism which aligns the blade according to the flow velocity and the rotor's rotational speed. The nacelle is the interface between foundation and rotor. It allows

rotational movement in order to align the rotor with the direction of flow and it hosts the power take-off (PTO) which usually contains gearbox, generator, sensors and controllers.

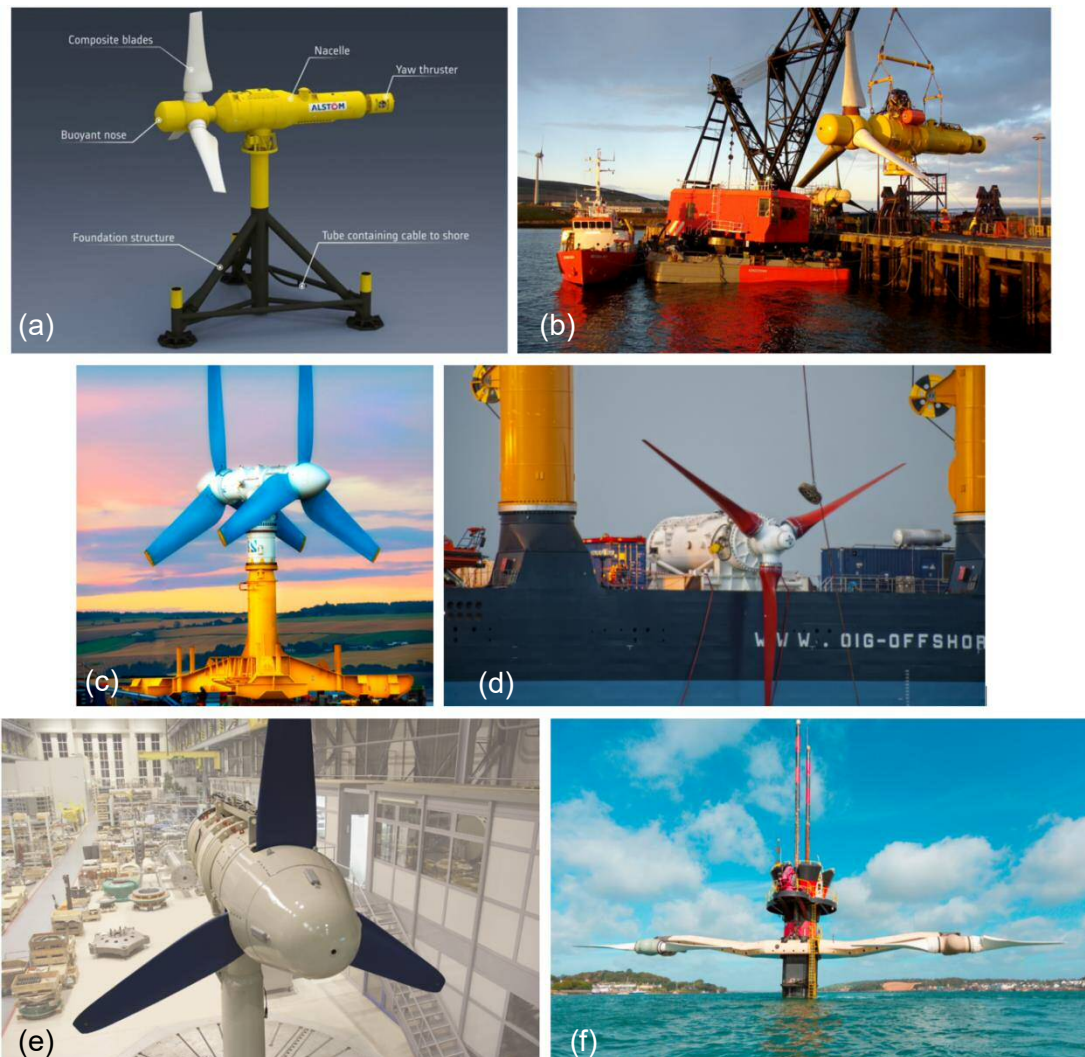


Figure 8. Hydrokinetic horizontal axis turbine examples: a) Alstom component CAD-drawing [37], b) Alstom Oceade [38], c) Atlantis AR1000 [39], d) Andritz Hammerfest [40], e) Voith HyTide [41] and f) Atlantis SeaGen [42]

In 2013, Alstom's Oceade with a capacity of 1.4 MW was successfully tested in Orkney Scotland [43]. However, GE bought Alstom's power and grid businesses in 2015 [44] and suspended the Oceade project in 2017 [45]. Atlantis (1.5 MW), Voith (1MW) and Andritz (1 MW) are developing similar turbines. Atlantis has further developed SeaGen, a HAT device which consists of two two-bladed 1 MW rotors. The rotors are attached to a horizontal beam which in turn is attached to a tubular tower which allows vertical movement of the cross-beam. SeaGen was the first grid-connected megawatt-level marine current power extraction device in 2008 [46].

Whether the flow of water or the flow of air is used as kinetic source does not impact on the physical principles of HATs which are described in the following.

HATs are lift driven machines which are generating forces due to the Bernoulli Effect. In the 18<sup>th</sup> century, the Swiss scientist Daniel Bernoulli discovered and mathematically described the hydrodynamic phenomenon of two opposed, curved bodies which are pulled together when air streams in-between [47]. This was rather counterintuitive as one would expect the bodies to be pushed apart. Bernoulli postulated an equation which links the critical variables of incompressible, steady flowing fluids in the following form:

$$\frac{U_1}{2} + \frac{p_1}{\rho} + g * h_1 = \frac{U_2}{2} + \frac{p_2}{\rho} + g * h_2 = \text{const.} \quad (1.8)$$

Velocity  
Energy

Pressure  
Energy

Elevation  
Energy

where  $p_1$ ,  $p_2$  is the absolute pressure and  $h_1$ ,  $h_2$  the elevation at a given point. Equation 1.8 shows that the sum of the three energy components (velocity, pressure and elevation) must be equal which implies that an increase in velocity (airflow between bodies) causes a decrease in pressure (bodies are pulled together) if the elevation is constant. This fundamental observation led to further innovations such as the Venturi tube, lift-turbine blades and airplane wings. The air approaching a wing of an airplane has to travel faster over its curved top surface since the travel path is longer than that of the bottom surface which generates a pressure differential *lifting* the wing and hence the plane upwards (see Figure 9).

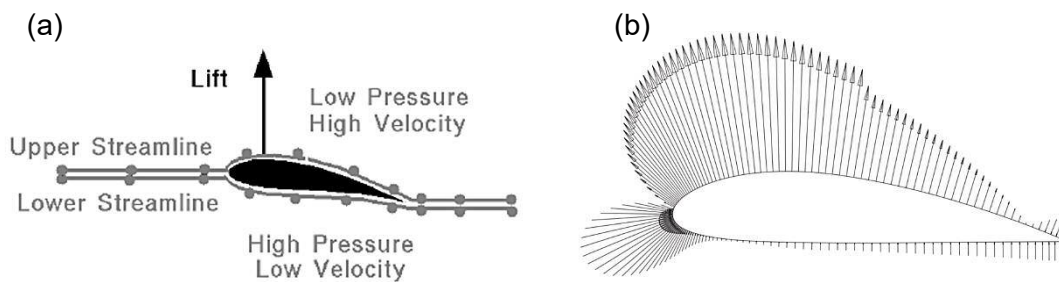


Figure 9. a) Basic concept of the Bernoulli Effect illustrated on an airfoil-shaped body [48]; b) typical pressure distribution over an airfoil-shaped body [16]

In contrast to an airplane wing which is facing the approaching airflow in a relatively constant position in order to generate sufficient lift to carry the weight of the plane, a turbine blade of a HAT is supposed to rotate around its centre in order to drive a mechanism, or more specifically, a generator. Here, the airfoil-shaped rotor blades face the approaching fluid in such a way that the generated lift force points towards the desired direction of rotation and the rotor starts to spin [49]. Due to the rotational

movement of the blades and the higher rotational speed towards the tip of the blade, the pitch angle  $\gamma$  of the blade has to change relative to the distance from its centre in order to archive an optimum lift force. Figure 10 depicts a typical cross-section of a HAT rotor blade. The approach flow  $U_\infty$  combined with the rotational speed  $\omega$  equates to the relative velocity  $W$ . A sophisticated blade design therefore has to change the curvature, chord length and pitch angle over its length (or rotor radius)  $r$  since  $\omega$  is a function of  $r$  and increases the further away from the centre of rotation.

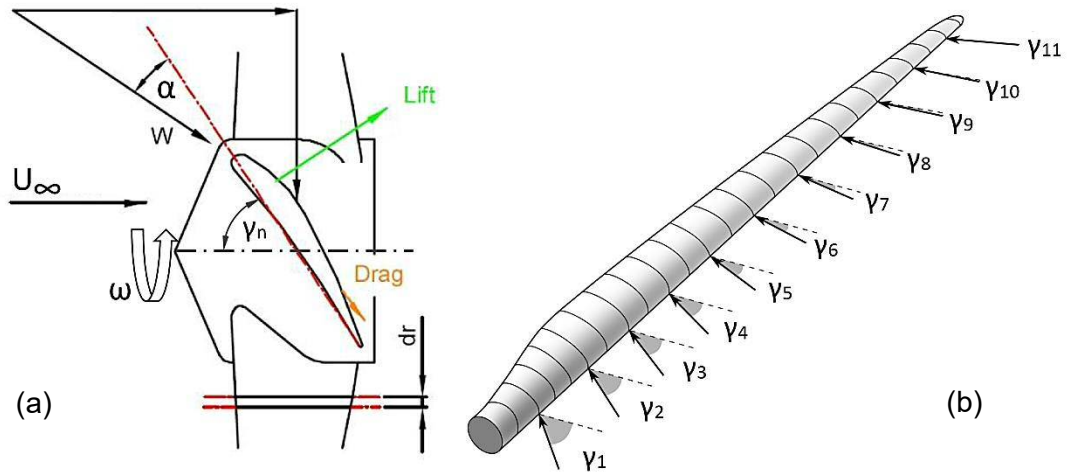


Figure 10. a) Velocity vectors on a HAT [50]; b) change in blade curvature and pitch angle over blade length [51]

In order to increase the self-starting ability, optimise the efficiency with varying flow velocities and avoid over-speeding, a blade pitching mechanism is usually included at the interface between blade and rotor hub. In order to operate the turbine at its optimum rotational speed, the pitch angle  $\gamma$  (angle between chord line (red dotted line in Figure 10a) and rotor axis) is constantly adjusted by a controller which measures parameters such as flow speed, rotational speed and power extraction. However, some HAT designs (small scale in particular) have no pitching mechanism and have to compromise on the previously mentioned aspects [52].

Shown as orange and green arrows in Figure 10a, the forces acting on the turbine blade are lift ( $F_L$ ) and drag ( $F_D$ ) and can be expressed by Equation 1.9 and 1.10 as:

$$F_L = \frac{1}{2} * \rho * v^2 * C_L * A_i \quad (1.9)$$

$$F_D = \frac{1}{2} * \rho * v^2 * C_D * A_i \quad (1.10)$$

where  $A_i$  is the area of the cross-section at a certain radius,  $C_L$  the lift coefficient and  $C_D$  the drag coefficient. Both empirical coefficients are blade-curvature specific and vary depending on the angle of attack  $\alpha$ . In order to calculate the overall forces and ultimately the overall torque  $\tau$ , the forces must be integrated over the entire length of the blade. However, as the curvature changes constantly along the length and thus all depending variables, a computer aided summation of  $N$  elements is usually performed and can be expressed as shown in Equation 1.11:

$$\tau = \sum_{n=1}^{n=N} \frac{1}{2} * \rho * v_{r,n}^2 * CL_n * (C_L \sin \phi_n - C_D \cos \phi_n) * r_n * \frac{R - r_{hub}}{N} \quad (1.11)$$

where  $N$  is the number of equally long elements,  $CL$  the blade chord length,  $R$  the overall blade length and  $\Phi$  the inflow angle which is the sum of pitch angle  $\gamma$  and angle of attack  $\alpha$ .

Further, a convenient way to express the rotational speed of the blade independently from the position along the blade is shown in Equation 1.12.

$$\lambda = \frac{r * \omega}{U_\infty} \quad (1.12)$$

The so called tip-speed ratio  $\lambda$  or TSR is a dimensionless parameter and an important measure in a kinetic turbine context which is used to compare differently scaled turbines and their efficiencies for both HAT and VAT.

In the following section, the similarities and differences to vertical axis turbines are shown.

### 1.3.3 Vertical axis turbines (VATs)

Similar to HATs, VATs or cross-flow turbines are lift-driven devices (except Savonius, see Figure 11) and take advantage of the same hydrodynamic phenomenon described before. However, the rotor axis of VATs is perpendicular to the flow which causes significant differences to HATs, both in design and operation.

The main advantages in comparison to HATs are: i) simple design; ii) non submerged components; iii) uni-directional; iv) rectangular cross-section and v) simple ducting (efficiency increase) [30].

- i) The design of VATs is simple [53] since the only moving part is the rotor itself. The blades are rigidly attached to the shaft, no pitch control is necessary.

- ii) In case of an application in water, all water sensitive components such as generator and power control can be installed above the water surface.
- iii) The rotation does not depend on the flow direction, hence, no mechanism for flow alignment is necessary.
- iv) The cross-section of the rotor is rectangular which is beneficial in shallow waters since a bigger area is occupied compared to a circular cross-section of a HAT rotor.
- v) Rectangular cross-section of the flow augmentation simplifies the design [21] in contrast to the conical shape of a HAT which imposes a structural weakness.

The drawbacks of VATs are mainly due to the oscillating lift force generation. Since the blades of HATs in operation are aligned uniformly towards the approaching flow and can be designed to generate even lift forces along the blade, the following aspects are disadvantageous in comparison: i) self-starting behaviour; ii) lower efficiency; iii) torque ripple:

- i) Due to a very low starting torque, self-starting is a concern and may require a starting mechanism.
- ii) Lower efficiencies since the rotor peak performance is at lower tip speed ratios.
- iii) Torque ripple caused by the constant changing angle of attack. Even negative torque values are possible.

Figure 11 depicts the main types of VATs. Squirrel cage Darrieus turbines (a) have straight airfoil-shaped blades which are caged between two endplates or discs whereas the H-Darrieus type (b) has arms or spokes holding the blades in place. The Darrieus rotor (c) in its initial form has curved blades with their tips attached to the shaft. The French engineer Georges Jean Marie Darrieus invented this turbine in the 1920s and a patent was filed in 1931 [54]. Alexander Gorlov has advanced Darrieus's design by introducing helical blades and patented the so called Gorlov type turbine (d) for the application in water in 1995 [55]. In contrast to the previous VATs, the Savonius turbine (e) is a predominantly drag driven device and considered to be reliable but less effective [56]. It was invented by Sigurd Johannes Savonius and patented in 1925 [57].

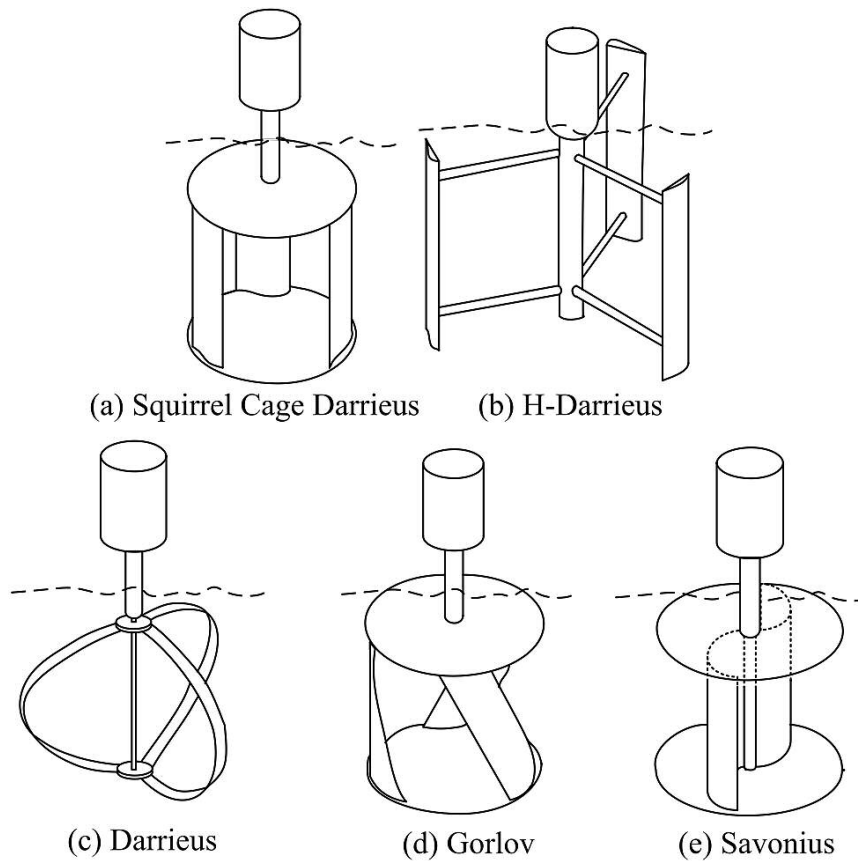


Figure 11. Types of VATs [21]

The VAT rotor consists mainly of three parts; i) rotor; ii) shaft; and iii) PTO. Similar to HATs, forces on the blade parallel (drag force) and perpendicular (lift force) to the flow are generated. When a fluid flows across the rotor these forces are transmitted to the shaft either via endplates or spokes and apply a turning moment. Since the shaft is free to rotate, the applied torque results in a rotational movement of the rotor if it is big enough to overcome stagnation. As soon as the rotor rotates, the angle of attack changes continuously and consequently the generated forces and torque.

In contrast to HATs, only few VATs are commercially available. According to [16], Ocean Renewable Power Company (ORPC) is the only company capable to make a significant impact on the renewable energy market. ORPC designed their cross-flow turbine rotor similar to the Gorlov rotor but with its axis orientated horizontally. Their design is adjusted for the application in rivers (RivGen®) and marine currents (TidGen®) [58]. Figure 12 depicts the ORPC turbine alongside systems from New Energy and Instream Energy systems. New Energy's EnviroGen is designed for the application in rivers and available from 5 to 50 kW. The company is currently developing the larger EnCurrent 125 VAT with an output capacity of up to 250 kW [59]. Instream Energy Systems developed and successfully implemented a 25 kW

VAT unit which is attached to a beam. The beam traverses the channel and several units can be attached next to each other [60].

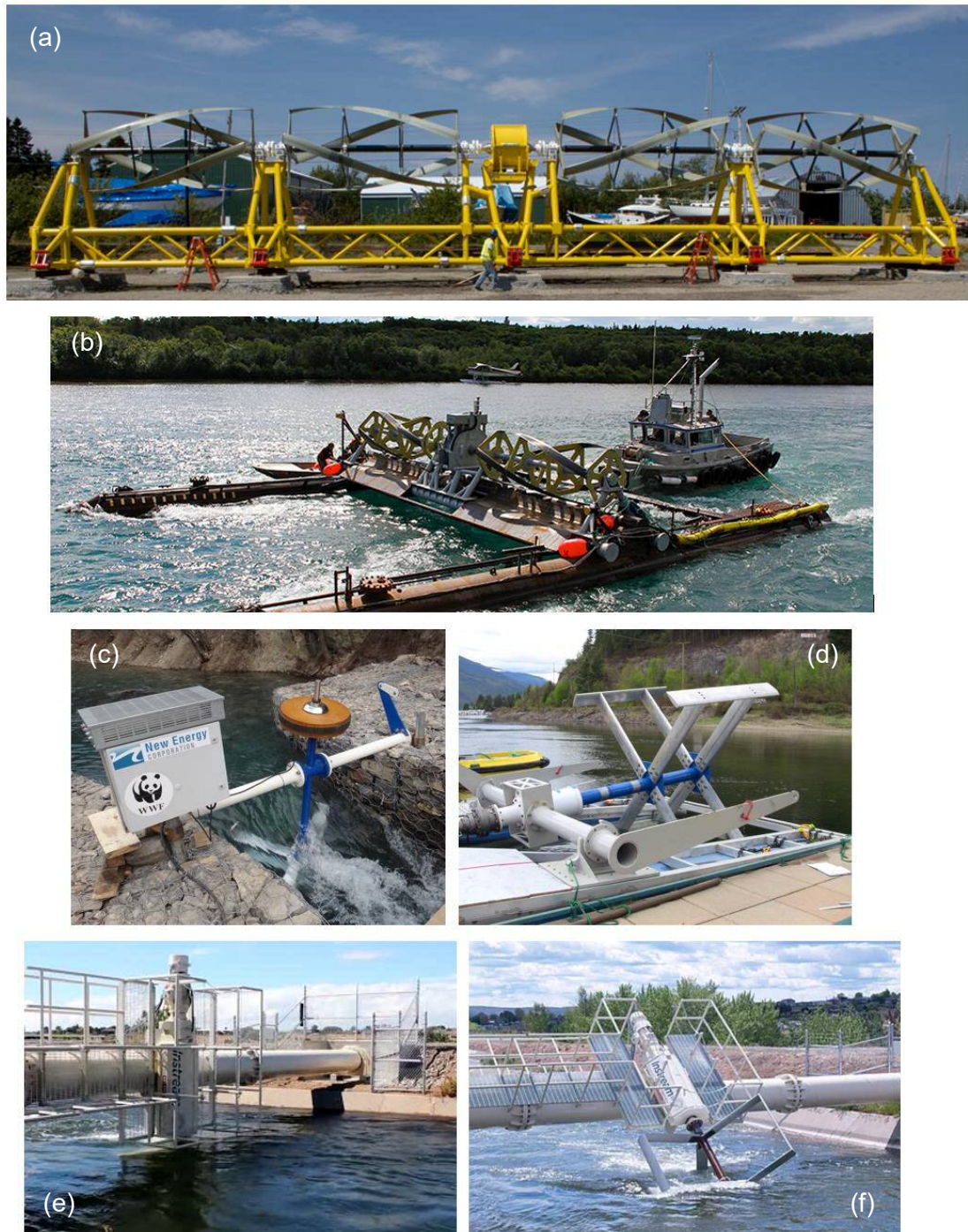


Figure 12. Hydrokinetic vertical axis turbine examples: a) ORPC's TidGen [61] and b) RivGen [62], c) New Energy's EnviroGen 05 [63] and d) EnCurrent 025 [64], e) Instream Energy Systems 25kW Hydrokinetic Turbine submerged [65] and f) partly submerged [60]

In the following, an analytical procedure will be described to estimate the forces generated by VATs (type a, b, d in Figure 11) and it will be shown that the analysis of the forces is more involved as with their HAT counterparts. This procedure was used

to design the rotor components structurally. In operation, the blade changes its position on the circumference with radius  $R$  constantly. For simplicity, two dimensions are considered ( $v_a \neq f(H)$ ) and a uniform, steady flow throughout the system ( $v_a = \text{constant}$ ) [66–68].

The notation is similar as before with the angle of attack  $\alpha$  between the chord of the blade and the relative flow velocity vector  $W$  and the azimuth angle  $\theta$  between the chord and the actual flow direction as depicted in Figure 13.

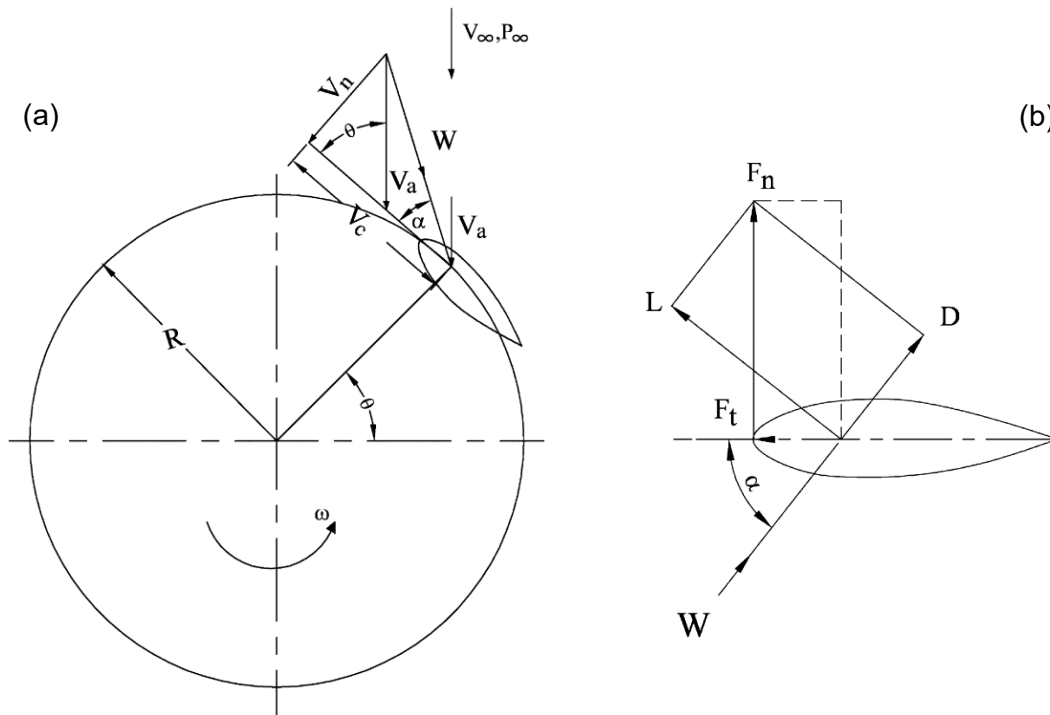


Figure 13. a) Velocity vectors and b) forces on a VAT [66]

The relation between angular velocity of the blade ( $\omega$ ) and the flow velocity component can be expressed by their geometrical relation as presented in Equation 1.12a and 1.12b respectively:

$$v_c = R\omega + v_a \cos \theta \quad (1.12a)$$

$$v_n = v_a \sin \theta \quad (1.12b)$$

where  $v_c$  is the chordal velocity component and  $v_n$  the velocity component normal to  $v_c$ . Hence, the relative flow velocity  $W$  can be expressed as shown in Equation 1.12c:

$$W = \sqrt{v_c^2 + v_n^2} \quad (1.12c)$$

The tangential force coefficient  $C_t$  and normal force coefficient  $C_n$  are introduced as shown in Equation 1.12d and 1.12e respectively:

$$C_t = C_l \sin \alpha - C_d \cos \alpha \quad (1.12d)$$

$$C_n = C_l \cos \alpha - C_d \sin \alpha \quad (1.12e)$$

The generated forces, both, in tangential and normal direction can then be estimated as presented in Equation 1.13 and 1.14 respectively:

$$F_t = C_t \frac{1}{2} \rho * CL * H * W^2 \quad (1.13)$$

$$F_n = C_n \frac{1}{2} \rho * CL * H * W^2 \quad (1.14)$$

where CL is the blade's chord length and H the blade's height. For the structural design of VATs it is important to consider both forces even if the force normal to the blade does not contribute to the power output. However,  $F_n$  is usually much higher in magnitude than  $F_t$  which needs to be appreciated for the structural component design. Further, lift and drag coefficients  $C_l$  and  $C_d$  are derived empirically or by numerical simulations [69]. In order to appreciate the changing position of the blade on its path along the circumference, the relation between angle of attack  $\alpha$  and azimuth angle  $\theta$  can be expressed as shown in Equation 1.14a:

$$\alpha = \tan^{-1} \left( \frac{v_n}{v_c} \right) = \tan^{-1} \left( \frac{v_a \sin \theta}{R\omega + v_a \cos \theta} \right) \quad (1.14a)$$

Substituting Equation 1.12 gives

$$\alpha = \tan^{-1} \left( \frac{\sin \theta}{\lambda + \cos \theta} \right) - \gamma \quad (1.14b)$$

where  $\gamma$  is the blades pitch angle. Considering the geometrical relations presented in 1.14c and 1.14d,

$$\sin(\tan^{-1}(x)) = \frac{x}{\sqrt{1+x^2}} \quad (1.14c) \quad \text{and} \quad \cos(\tan^{-1}(x)) = \frac{1}{\sqrt{1+x^2}} \quad (1.14d)$$

Equation 1.13 becomes 1.15,

$$F_t = \left( C_l \left( \frac{\sin \theta}{\sqrt{1+(\sin \theta)^2}} \right) - C_d \left( \frac{1}{\sqrt{1+(\sin \theta)^2}} \right) \right) \frac{1}{2} \rho * CL * H * W^2 \quad (1.15)$$

and Equation 1.14 becomes 1.16,

$$F_n = \left( C_l \left( \frac{1}{\sqrt{1+(\varphi)^2}} \right) + C_d \left( \frac{\varphi}{\sqrt{1+(\varphi)^2}} \right) \right) \frac{1}{2} \rho * CL * H * W^2 \quad (1.16)$$

where  $\varphi$  (Equation 1.16a) is used to simplify the expression.

$$\varphi = \left( \frac{\sin \theta}{\lambda + \cos \theta} \right) \quad (1.16a)$$

The average torque  $\tau$  generated by one blade can be obtained by:

$$\tau_a = \frac{1}{2\pi} \int_0^{2\pi} F_t R d\theta \quad (1.17)$$

This analytical procedure was used to estimate the forces acting on the blade and the structural components of the later presented laboratory turbine in order to design connections and select materials. Figure 14 depicts results for a typical straight VAT blade in terms of tangential and normal force versus azimuth angle derived by applying the previous procedure in comparison to results from [53].

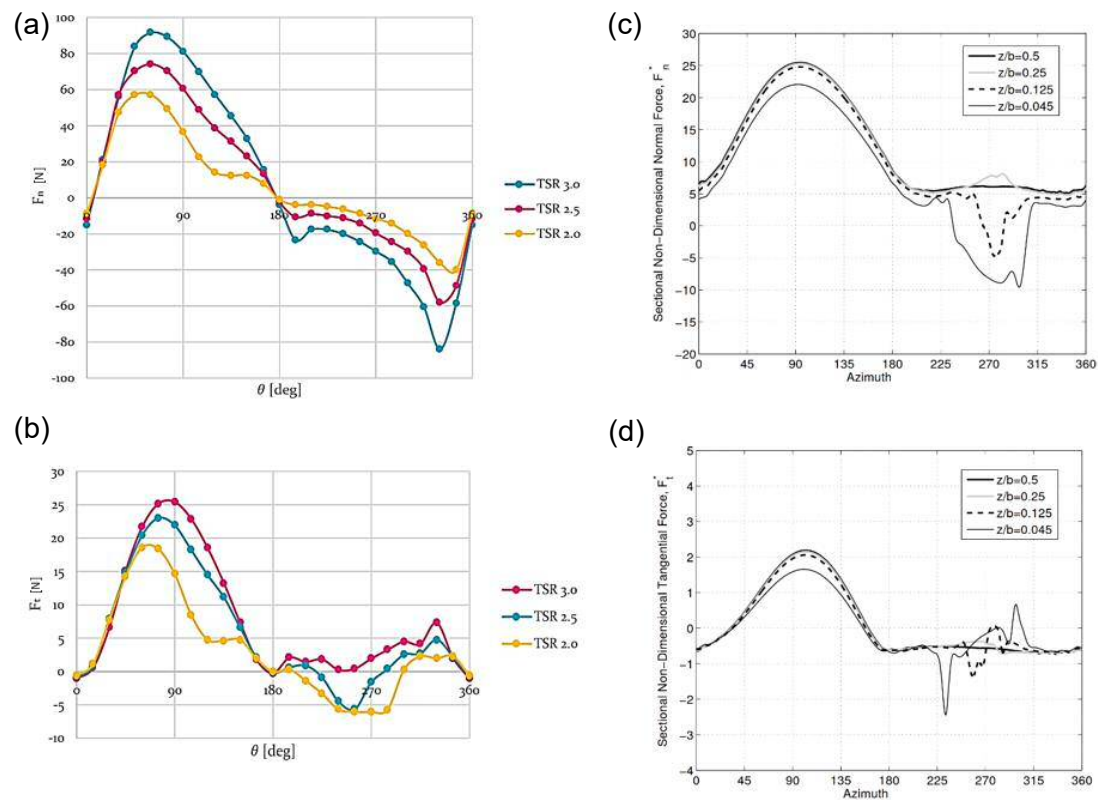


Figure 14. Analytically derived normal (a) and tangential (b) forces of a straight VAT blade; numerical derived normal (c) and tangential (d) forces of a straight VAT blade [53]

Considering the tangential forces, it can be seen that the difference in change of force generation is worse the slower the turbine spins. At  $TSR=2.0$  and  $TSR=2.5$ , the tangential force reaches negative values whereas at  $TSR=3.0$  the tangential force remains positive. Figure 15 depicts the relation of angle of attack and azimuth angle as a function of rotational speed relative to the approach flow ( $TSR$ ). It shows that the curve flattens the faster the turbine spins which consequently flattens the torque fluctuations [69] since a negative angle of attack can cause negative tangential forces. Further, a typical torque versus azimuth angle curve is shown for a four-bladed VAT indicating the characteristic torque ripple.

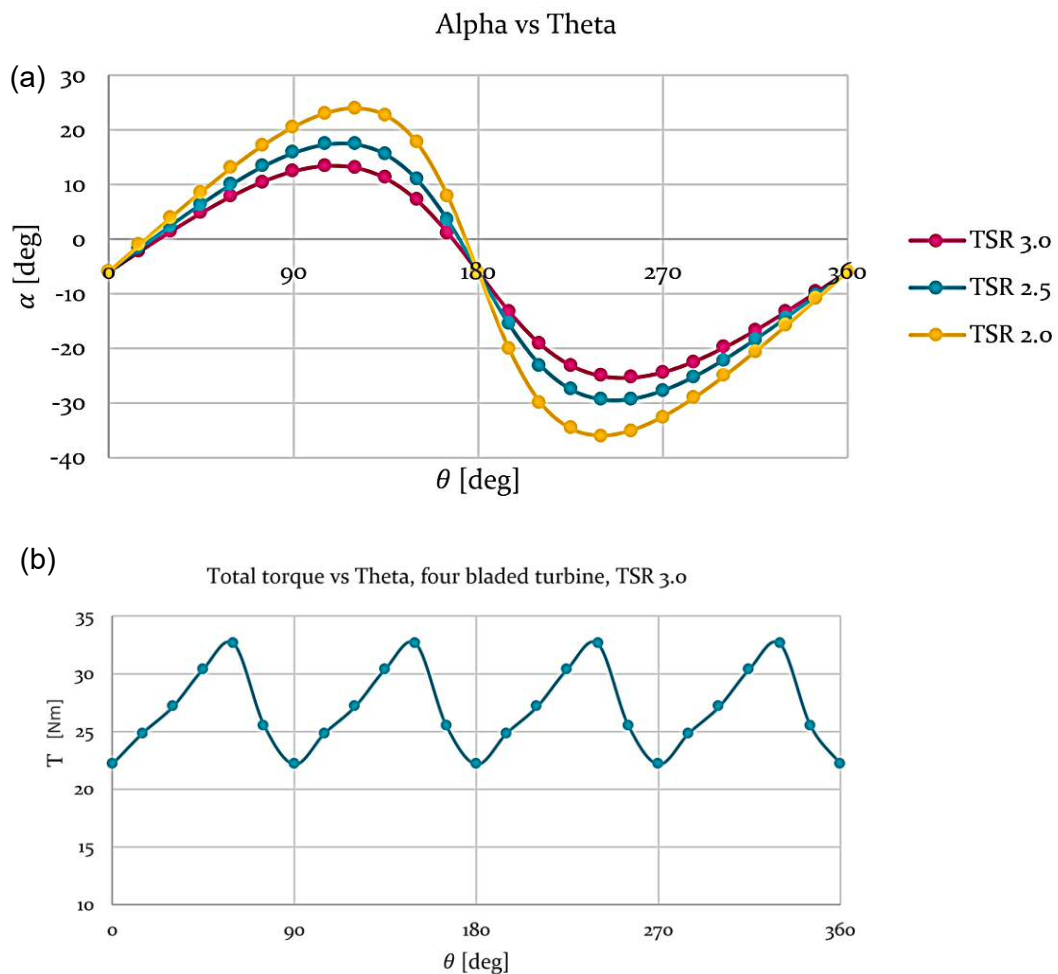


Figure 15. a) Typical  $\alpha$  vs  $\theta$  relation for different  $TSR$ s; b) typical torque curve of a four bladed VAT

The procedure remains an estimation tool for initial turbine component design. In reality, the hydrodynamics of a VAT are three-dimensional and the approach flow velocity not constant (neither in magnitude nor in direction) [70]. In order to appreciate the complexity of wakes and turbulences within the domain of the turbine, numerical models are employed to shed light on the interaction between rotor and fluid flow [71–

74]. In Chapter IV, the investigation of the wake downstream of the turbine's rotor is described and the three-dimensional nature of it appreciated.

Besides the critical hydrodynamic behaviour of the device, the environment of deployment is of importance and will be described next.

## 1.4 Fields of application for hydrokinetic turbines

Generally, hydrokinetic energy can be harnessed anywhere water flows. However, critical parameters are flow velocity, topography, accessibility, environmental aspects, water quality and distance to the grid feeding point [75]. In the following, the fields of application are differentiated between marine and inland.

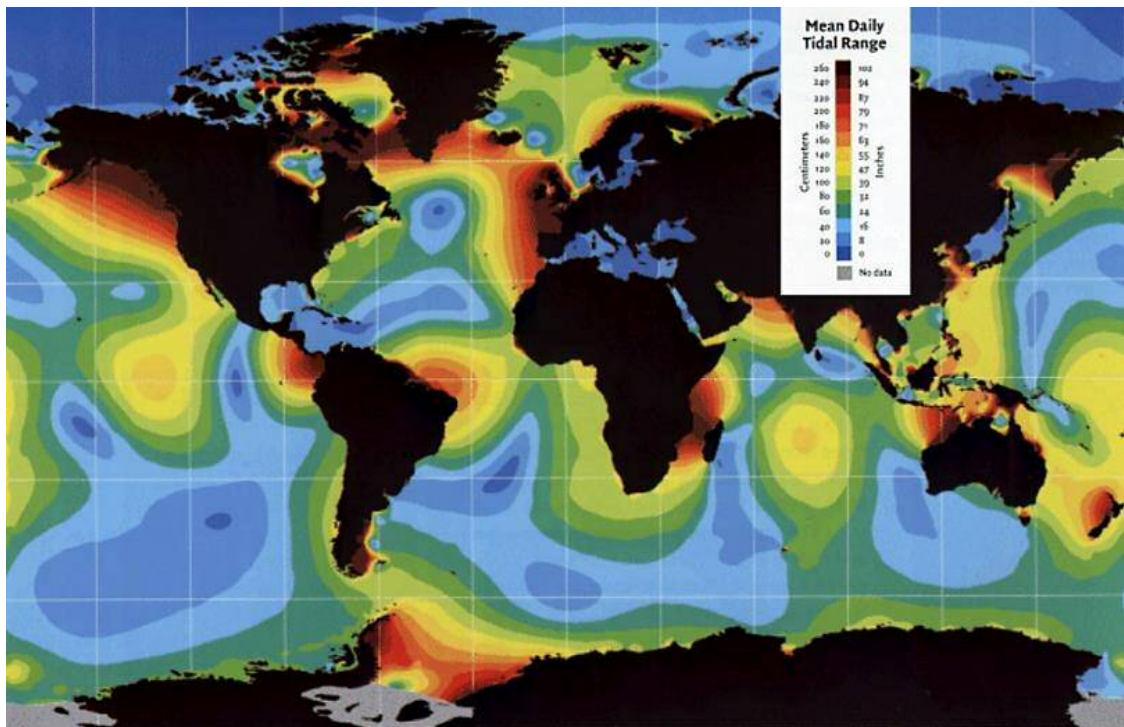
### 1.4.1 Marine

Marine hydrokinetic energy is the kinetic energy in oceanic currents which are driven by different parameters such as temperature and salinity gradients, wind, rotation of the earth, gravitational forces of moon and sun and are effected by landmasses and bathymetry [76]. While in deep sea regions the tidal range may be less than 1m, larger tidal ranges are observed close to landmasses such as in the Bay of Fundy, Canada or around the British coastline with mean ranges of more than 10m [77] [78].

The Bristol Channel (or Severn Estuary, black circle in Figure 16b) was identified as one of the biggest single sources for marine hydrokinetic energy in the UK with an estimated extractable amount of approximately 17 TWh/y (or ~4.7% of UK electricity consumption in 2020) [79,80] which is due to the unique combination of a very high tidal range and beneficial bathymetry where a huge amount of seawater is moved back and forth through the narrow estuary and therefore causes very high flow velocities. Several marine power schemes are discussed including a barrage spanning from Cardiff to Weston-Super-Mare [81].

According to [82], it is estimated that around 7% of the world's electricity demand could be covered by ocean energy based devices by 2050. However, the VAT researched in this study is designed for an application onshore and the focus is therefore on potential inland sources.

(a)



(b)

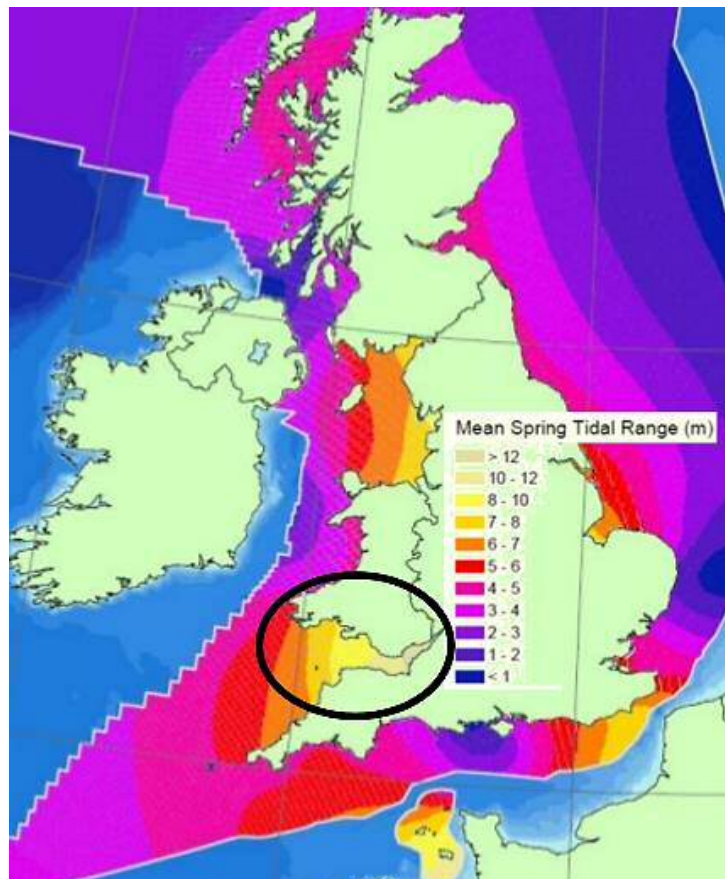


Figure 16. a) Global distribution of mean tidal range [83]; b) UK distribution of mean spring tide range [84]

### 1.4.2 Inland

The US Federal Energy Regulatory Commission stated in 2007: *“Estimates suggest that new hydrokinetic technologies, if fully developed, could double the amount of hydropower production in the United States, bringing it from just under 10 percent to close to 20 percent of the national electric energy supply. Given the potential benefits of this new, clean power source, the Commission has taken steps to lower regulatory barriers to its development.”* [85].

Nonetheless, an estimation of the global potential of hydrokinetic energy from rivers or engineered waterways appears to be difficult since it is usually not included in resource assessments due to the predominant application of potential energy in a hydropower context [86]. In a United Nations report from 2000, the global annual amount of runoff water from precipitation on land which is neither evaporated nor absorbed by vegetation is estimated to be 47 000 km<sup>3</sup> [87]. Besides being vague, this number does not include any process-driven water flows such as water treatment plant effluents, irrigation channels or cooling water discharges (engineered or man-made canals in general). Further, it is unknown how often this amount of water and its hydrokinetic energy can be used. For example with regards to the river Thames which is 346 km long has an average discharge of 65.8 m<sup>3</sup>/s and an elevation difference from spring to sea level of 110m [88], there is no straightforward procedure to estimate how the local flow conditions are and how many hydrokinetic energy extraction devices could be implemented profitably [89]. By reviewing literature on flow data for two large rivers, a water supply canal and laboratory flumes, Oak Ridge National Laboratory developed a reference model for assessing the viability of hydrokinetic technologies in rivers and engineered canals [90]. It was concluded that the maximum flow speed ( $u_{\max}$ ) experienced by a device installed near the surface can be estimated as  $7/6 U_0$ . The flow velocity closer to the bed is more difficult to predict due to bigger variations in turbulences. Therefore, a sophisticated assessment tool needs individual flow and bathymetry data which also appreciates the general variation of water depth and flow over the life-span of the device [91].

Generally, there is no difference in terms of power extraction whether the hydrokinetic extraction device (HED) is deployed in a river or an engineered canal as long as the geometry and flow characteristics suit the device. However, there can be a significant difference in operational and environmental impact. In the following, rivers and engineered canals will be compared as potential energy sources and field of application of a HED.

Based on [92–95] and the previously listed literature, the following criteria were identified as critical for HED implementation. An attempt was made to point at the impact on rivers and engineered canals (see Table 2) and to identify the main advantages of the application of HEDs in engineered canals.

*Table 2. HED impact summary on rivers and engineered canals with key advantages highlighted*

	<b>River</b>	<b>Engineered canal</b>
<b>Availability</b>	Widely available and often close to residential areas with energy demand.	Widely available and often close to residential areas with energy demand.
<b>Flow data</b>	Well monitored, often over a very long period of time.	Well monitored, often over a very long period of time.
<b>Aquatic life</b>	Yes.	No.
<b>Flooding</b>	Yes.	No, but overflow.
<b>Sediment transport</b>	Yes.	Potentially.
<b>Debris</b>	Yes.	Potentially.
<b>Bathymetry/Bed</b>	Varies significantly (if not canalised) in all dimensions.	Generally regular in cross section with engineered embankment and bed.
<b>Climate</b>	Depends on location, could freeze in winter or be dry in summer.	Depends on location, could be closed off seasonally.
<b>Reliability</b>	Depends on location, generally very reliable discharge.	Depends on location, generally very reliable discharge.
<b>Accessibility</b>	Depends on location, varies.	Depends on location, generally good.
<b>Water quality</b>	High quality, potentially drinking water.	Varies from drinking water to waste water.
<b>Permitting procedure</b>	Depends on location, rather difficult.	Depends on location, rather simple.
<b>Operational impact</b>	Water traffic or water sports could be disturbed.	Operational processes could be disturbed.
<b>Cultural/Social impact</b>	Yes.	No.

A vast aquatic life and an integral role in the hydrological cycle and the surrounding ecosystem makes rivers important components of the environment and the implementation of HEDs may have a significant impact [96]. For that reason, environmental agencies have permitting procedures in place which evaluate the proposed HED scheme in detail. Natural Resources Wales for example splits their assessment in terms of rights of access, flow standards, designated sites, conservation and heritage, fish passing, geomorphology and photo-survey, approvals and licences, weir pools, water framework directive, cumulative and in combination effects, competing schemes, fish screening, monitoring and weirs [97]. The applications process is complex and costly, both in terms of time and investment for data gathering but can be justified by the intended avoidance of negative impact on the river.

Whether or not a HED has an impact on a river is beyond the scope of this study. Engineered or man-made channels are designed to fulfil a certain purpose such as discharging waste water effluent to a river or diverting fresh water from between reservoirs. They are usually not a habitat for aquatic life and are not used for transportation or any other reasons besides its design purpose. However, implementing HEDs in engineered canals without any risks for the environment, and therefore, without any permitting procedures, is a non-invasive way to gather data and gain experience in order to simplify the permitting process for rivers on a later stage. Engineered canals are of regular cross-section with a regular slope which makes the HED (array) design straight forward. They are accessible since the operator has to maintain the canal regularly.

Fundamentally, the HED presented later in this work can be operated in any environment, however, the engineered channels have been chosen due to the much simpler implementation at this early stage of development.

## II. Objectives

The aim of this research is to observe the performance of a hydrokinetic VAT at laboratory scale (1:10) and improve it by iteratively adjusting certain components according to experimental findings in order to up-scale the best performing design to field (1:3) and application scale (1:1) and confirm its performance at various scales. Therefore, the following aspects will be tested and researched in depth:

- Optimise rotor shape and twin rotor assembly
  - o Increase performance
  - o Eliminate self-starting issue & flatten torque fluctuations
- Investigate housing structure and flow augmentation
  - o Ameliorate synergy of merging housing, foundation and augmentation
  - o Increase rotor performance
- Examine blockage and solidity
  - o Increase performance
  - o Increase rotational speed

A VAT is an assembly of several parts. Rotor components such as blades and spokes with non-regular surfaces are difficult and costly to machine. Beside the energy harnessing rotor and the supporting structure, a mechanical power take-off device is needed to translate the rotors' motion to an electrical generator. Further, the electrical components need to be determined. Therefore, the following aspects will be researched:

- Acquire knowledge of component manufacturing
  - o Milled plastic & aluminium
  - o Laser-sintered plastic
  - o Carbon-fiber composite
- Investigate the power take-off
  - o Individual vs combined power take-off (twin application)
  - o Belt drive
- Understand the generation of electricity
  - o Identifying design aspects by differentiating between laboratory, demonstrator and full scale application
  - o Power control

The objective list does not reflect the order of content. The thesis chapters are listed in a design and progress order.

## III. Turbine concept and laboratory performance study

### 3.1 Introduction

Growing energy demand and climate change are the main drivers for the fast evolution of novel energy conversion systems. While energy production during the second half of the past century was focused on large-scale fossil or nuclear power plants, the 21st century could be the era of eco-sensitivity, sustainability and decentralisation of power generation. In other words, many small “green” units could replace few large environmentally questionable plants with the benefit of low capital costs and zero carbon emission [22].

This study focuses on the development of a twin VAT for harvesting energy from flowing water in man-made channels. The idea is to provide a channel operator (e.g., water utilities) with a device that generates electricity without impacting their main operations and without modification of existing structures or processes. The hydrokinetic turbine is designed as a “ready-to-use” unit to be placed in a channel without further construction works as depicted in Figure 17.

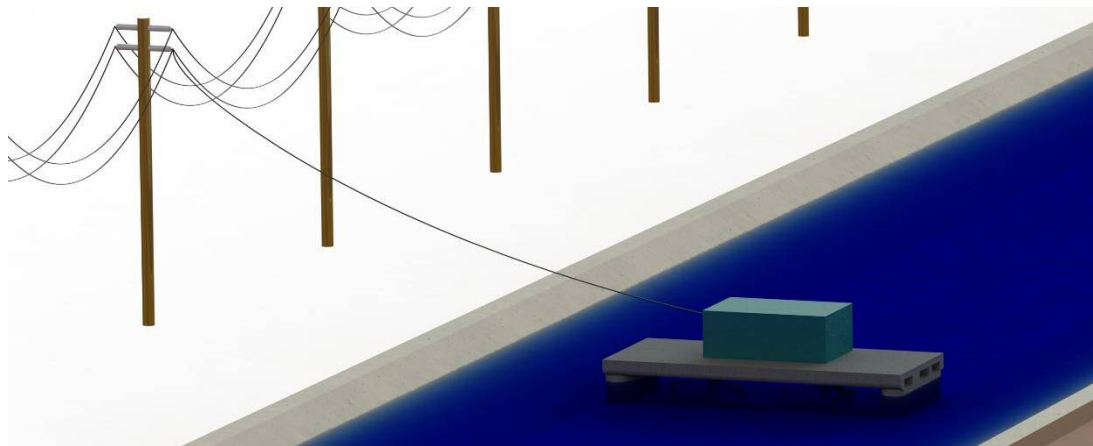


*Figure 17. Conceptual CAD drawing of the twin turbine assembly in a channel*

This chapter summarises the design concept of the hydrokinetic turbine, its components and the data of extensive laboratory tests. The turbine design will be laid out in the next section followed by a description of the test facilities and how the laboratory tests were undertaken. The main outcomes are consolidated, linked together and their specific impact on the design is explained. Solidworks® was used as CAD software for most drawings and MS Excel® for data analysis and plotting of results.

### 3.2 Turbine concept

The aim of the turbine is to convert the movement of flowing water in a channel into mechanical torque and consequently, into electricity in the most efficient and sustainable way. The initial concept was derived from collaborations prior to this project [98]. Each component of the turbine system has been designed to integrate as a unit and can be split into three subsystems:

- Housing (1-4)
- Rotors (5-6)
- PTO (7-9)

Figure 18 depicts a conceptual CAD drawing of the twin turbine with its individual components. Further drawings are attached to Appendix A.

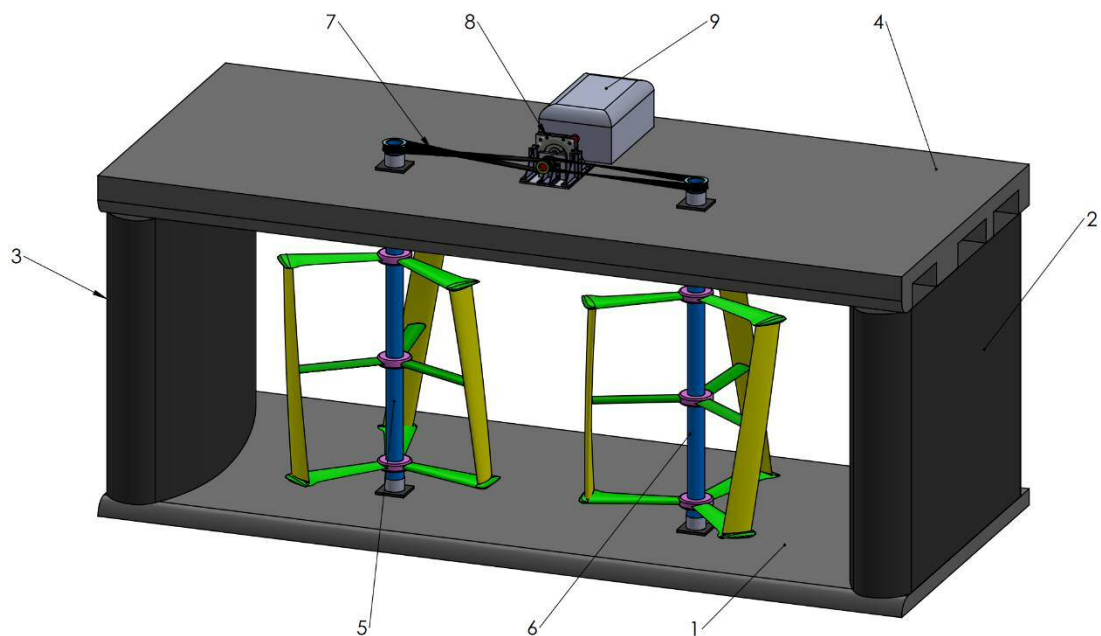


Figure 18. Conceptual CAD drawing of the twin turbine and its components  
(1. bottom plate; 2&3. column; 4. bridge; 5&6. rotor; 7. belt drive; 8. gear box; 9. generator)

#### 3.2.1 Housing

The cementitious-material based structure comprises four individual parts: a bottom plate (1); two columns (2&3); a bridge (4) and serves several purposes:

- As the structural member to hold the turbine components in place safely.
- As a gravity base (stays in place due to its mass) which makes additional foundation unnecessary.
- As flow augmentation.

In operation, the bridge is not submerged and hosts belt drive system, gear box and electrical generator. The bridge is walkable which simplifies operation and maintenance of the turbine. The components of the housing structure are presented in Figure 19. Note that the columns are hydrodynamically optimised (airfoil shaped cross-section) in order to be less obstructive and funnel the flow of water towards the rotors. The bottom slab hosts the two columns as well as the bottom bearings of the two rotors. The bridge is attached to the top of the two columns and features two holes for the rotor shafts. The surface of the bridge allows space and support for the installation of the periphery.

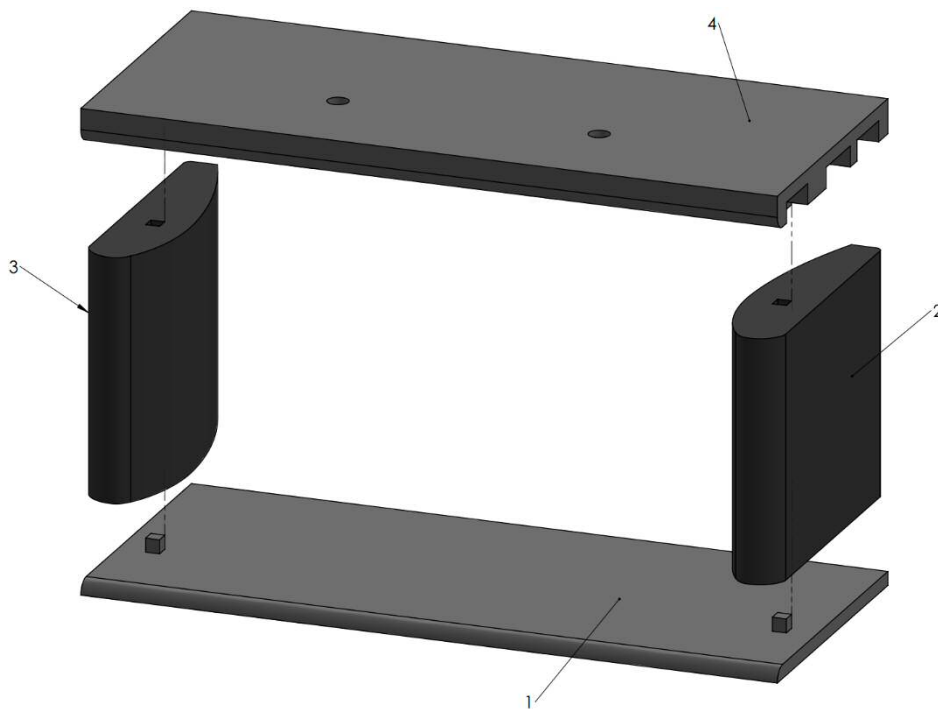


Figure 19. Housing subsystem of turbine concept (1. bottom plate; 2&3. column; 4. bridge)

### 3.2.2 Rotors

The structure hosts a co-rotating vertical axis twin rotor system which is placed between bridge and bottom plate as depicted in Figure 20. The rotors are held in place by four bearings (18). Each rotor consists of a stainless-steel shaft (17), three hubs (10), six spokes (12-16) and three blades (11). As soon as water flows across the rotors at a certain minimum speed, the airfoil-shaped blades generate enough lift to start rotating. Both rotors rotate in opposite directions towards the flow at centre position in order to benefit from the highest velocities in the middle of the channel.

### 3.2.3 Power take-off

The rotational movement of the rotor is transferred via the two rotor shafts (17&19) to a belt drive which consists of two 90° twisted timing belts (22&23), two large pulleys

(20&21), two small pulleys (24&25) and a horizontally oriented main shaft (26). The belt drive enables transferring the torque from the two rotor shafts onto a main drive train shaft and allows a speed or torque adjustment to appreciate gearbox or generator specification by choosing the desired gear ratio (e.g., number of teeth of small and large pulley). Attached to the main drive train shaft is a gearbox and subsequently an electrical generator [98].

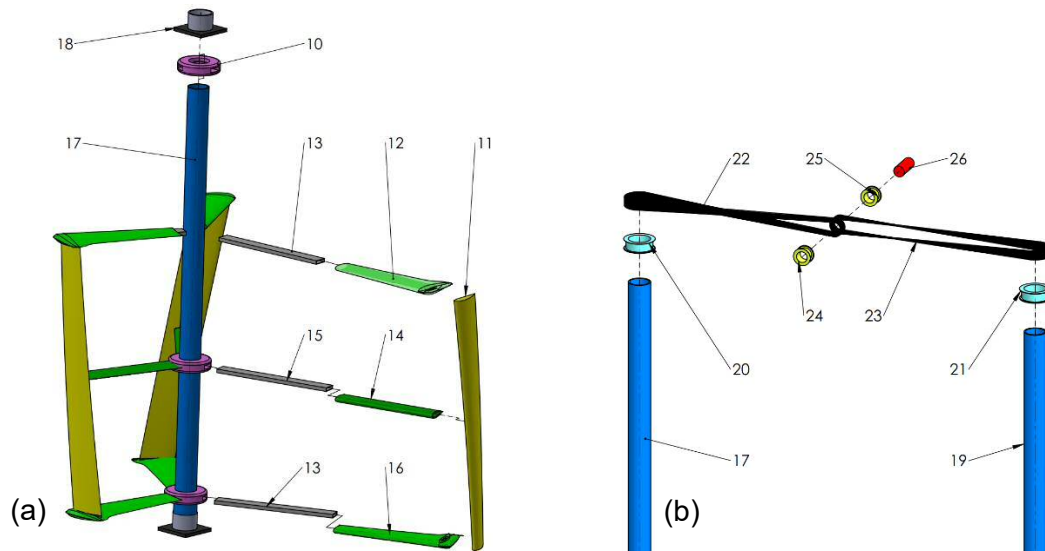


Figure 20. Subsystems of turbine concept: a) Rotor (10. hub; 11. blade; 12-16 spoke; 17. shaft; 18, bearing); b) PTO (excluding gearbox and generator; 17&19. rotor shaft; 20&21. rotor pulley; 22&23. belt; 24&25. main shaft pulley; 26. main shaft)

The previously described full scale concept encompasses components such as gearbox, generator and other electrical components which are not further specified since the focus is on the rotor and its hydrodynamic performance. However, in Chapter V and VI some of these peripheral aspects are further described and researched.

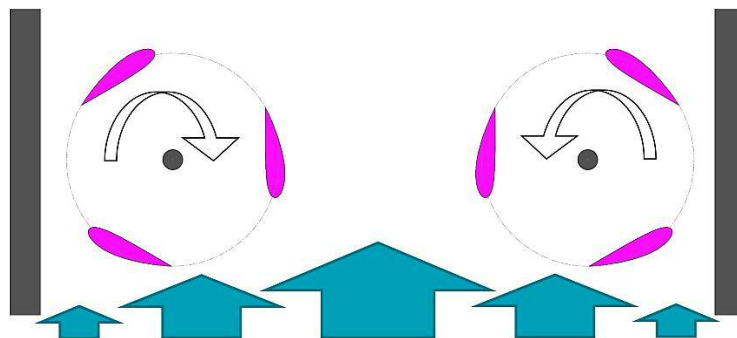


Figure 21. Plan view of two counter rotating VAT rotors in a channel with a typical flow velocity distribution (blue arrows, big arrow = fast velocity; small arrow = slow velocity)

The combination of the previously mentioned VAT-advantages stimulated towards a system of two counter rotating rotors in an augmented environment with a non-

submerged PTO and a gravity based-structure. The hypothesis is that two counter-rotating rotors will benefit from the high flow velocities in the centre of a stream as the rotor generates the highest torque in this particular area [69] if positioned as shown in Figure 21 and experiences less resistance closer to the side-walls where the flow velocities are low (in Chapter IV the velocity distribution in a channel with and without a turbine is explained in more detail). From a hydrodynamic point of view, the structure serves the purpose of reducing the channel width in order to increase the flow velocity and adjust the blockage ratio.

### 3.3 Laboratory performance study

The rotors and parts of the housing were built in a 10<sup>th</sup> scale model and tested at the Hydro Laboratories at Cardiff University. In total, more than 200 individual tests were conducted (for a full list please see Appendix A) with the aim to study and optimise the rotor, the housing structure and, eventually, the twin-rotor assembly. The design was iteratively adjusted and the performance improved with the ultimate goal to up-scale the twin turbine assembly. In various studies, it was shown that VAT parameters cannot be designed in isolation and a transition from wind VAT research outcomes is not straightforward [71, 99, 100]. Symmetric NACA aerofoils achieved, for example, high performance in wind experiments whereas chambered or asymmetrical aerofoils have outperformed their symmetrical counterparts in the application in water [101]. Therefore, the laboratory experiments were planned to systematically investigate the impact of design changes. Parameters listed in Table 3 were researched.

Table 3. Turbine design aspects tested

Design aspect	
<b>Rotor</b>	
Blade (air-foil) shape	Pitch angle
Number of blades	Blade twist
Spoke-blade fastening	Blade surface finish
Shaft diameter	Spokes vs discs
Flywheel	Solidity
Submergence	
<b>Structure</b>	
Blockage	Rotor position
<b>Twin assembly</b>	
Single vs twin rotor	Distance between rotors
Inwards vs outwards rotation	Synchronisation of rotors
Rotor offset	

### 3.3.1 Test facilities

The testing took place at Cardiff University's Hydro Laboratories in a 17m long and 1.2m wide flume. The water flow is driven by an impeller which sits in a 0.6m diameter recirculation pipe underneath the flume's glass body which allows flow speeds of up to 2 m/s at the given water depth. For most experiments, the water level is set to 0.5m (submergence and wake measurements were also taken at different water depths). The discharge is manipulated by changing the electrical power applied to the pump (as a percentage value). Velocity profiles were conducted in previous studies [102,103] and the average spatial velocity was used for further reference. The turbine's bottom bearing is placed on a 25mm thick plastic sheet which is attached to the bed of the flume. The top bearing is attached to a bridge which sits above the water surface and can be slit in and perpendicular to the flow direction. The channel side walls are made out of glass which allows visual observations during testing as depicted in Figure 22.

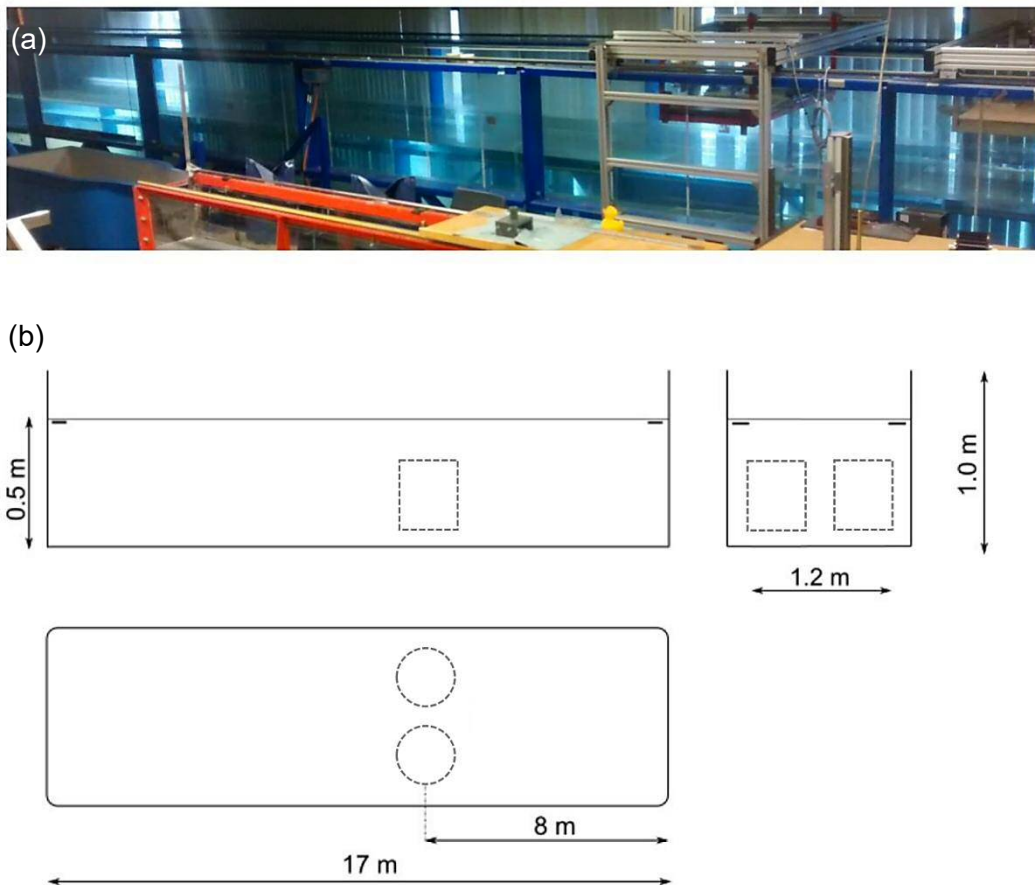


Figure 22. a) Picture of laboratory flume at Cardiff University and b) main dimensions

For some experiments, different structures, similar to the columns of the turbine's structure were employed. The channel-width-to-water-depth ratio was then reduced to 8:5 (as opposed to a 12:5 channel-width-to-water-depth ratio without the structure)

which provided further vertical blockage. The turbine rotors were mounted to the bottom of the flume via lubricated stainless steel bearings which were screwed onto a PVC board that was glued to the flume bed. The PVC board had various threaded holes which allowed for different rotor positions within the flume.

The top of the rotor was held by a pillow block bearing which was attached to a movable bridge across the top of the flume allowing a rotor displacement in any direction. Further, the bridge accommodated the main shaft, generator and measurement equipment. When the twin rotors were tested, the rotational movement of the individual rotor was transferred to the main shaft by timing belts. On top of each rotor shaft, a pulley with forty teeth was attached. Two pulleys with twenty teeth each were attached to the end of the main shaft which resulted in a gear ratio of two to one. Two belts were mounted with a 90° twist between rotor- and main shaft pulleys (see Figure 23). The mechanical power take-off including belt drive is further described in Chapter VI.

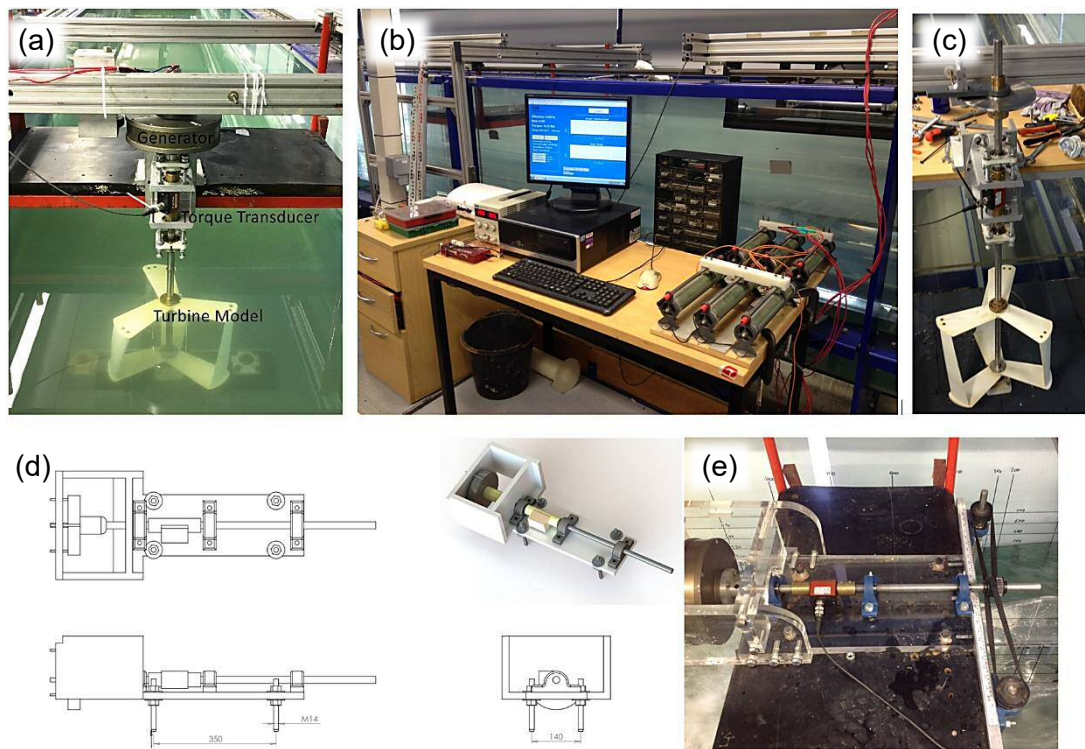


Figure 23. CAD drawings and photographs of PTO used for twin rotor testing: a) Single rotor testing with torque transducer and generator; b) resistor bank, computer, LabJack U6 and DC power source; c) single rotor testing with torque transducer and disc brake; d) CAD drawing of twin rotor PTO; e) twin rotor PTO with belt-drive, shaft, bearings, torque transducer and generator

In the experiments, rotational speed and torque applied to the turbine is recorded with a combined encoder and torque sensor (Futek TH605, see specifications sheet in Appendix H). For data acquisition, a LabJack U6 was used which converted the analogue sensor output into digital signals which were then compiled by a self-written

code within a DAQ software (DAQexpress). Measures are taken for one minute at a frequency of 100Hz from free-wheeling (first test, no torque applied to the turbine) until stall (last test, just before rotor stops spinning under load) and several steps in between. The test equipment has measurement tolerances  $< 0.5\%$ . Misalignment, manufacturing inaccuracies, surface and bearing friction, ambient temperature and other aspects add an element of uncertainty towards the results [101–103].

However, the resistance torque to the rotor was applied in two ways. Either mechanically, with a braking mechanism (e.g., disc brake) or electrically, with a generator in combination with an adjustable resistor bank. In the latter case, voltage and current were recorded by using two standard multi-meters. The tested design parameters are described in the following and the results are presented in form of so called performance or  $C_P$ - $\lambda$ -curves alongside a CAD drawing or picture of the item concerned. The performance curve shows the coefficient of performance ( $C_p$ , ratio of power input to output) on the y-axis and TSR on the x-axis. Data variation is not shown but discussed in Appendices I. In addition to the data points, a dotted trend line is included in the graphs. The individual outcome is stated at the end of each item.

In general, the tests were conducted at several flow speeds ranging from 0.59 m/s up to 1.6 m/s. The velocity was set by manipulating the electrical power applied to the flume's impeller. Table 4 shows the velocities used depending on pump power, channel width and water depth. In some experiments (test 001-049 and 076-097), a structure was used in order to reduce the width of the flume and increase the velocity. In that case, the water level dropped slightly when the discharge was increased. Please see Appendix B for more details.

*Table 4. Flow speeds used in the experiments with channel width at turbine position (1200mm = bare unblocked flume; 800mm = flume blocked with structure)*

<b>Pump power</b>	<b>Water depth</b>	<b>Channel width</b>	<b>Discharge [Q]</b>	<b>Velocity [v]</b>
%	mm	mm	m <sup>3</sup> /s	m/s
20	500	1200	0.351	0.59
25	500	1200	0.431	0.72
30	500	1200	0.510	0.85
35	500	1200	0.588	0.98
40	500	1200	0.653	1.09
45	500	1200	0.689	1.15
20	475	800	0.351	0.92
25	465	800	0.431	1.16
30	450	800	0.510	1.42

The flow velocities were measured in previous studies with an uncertainty of up to 1.6% [102,103].

### 3.3.2 Rotor testing and results

As far as the individual rotor design and testing was concerned, the focus was on:

- Quantifying the rotor efficiency in comparison to design variations with a target efficiency of  $C_P > 30\%$  (see also Appendices I).
- Justifying benefits of very low solidity such as an increased TSR, less torque ripple and better self-starting behaviour.
- Optimising the blade-shaft connection (e.g., spokes).

Overall, the rotor was built in a 1:10 scale from the original design for testing in the laboratory flume and results from other studies [101, 104] were considered. The blade height was set to 300mm, the rotor diameter varied between 200, 360, 400 and 600mm (see Figure 24).

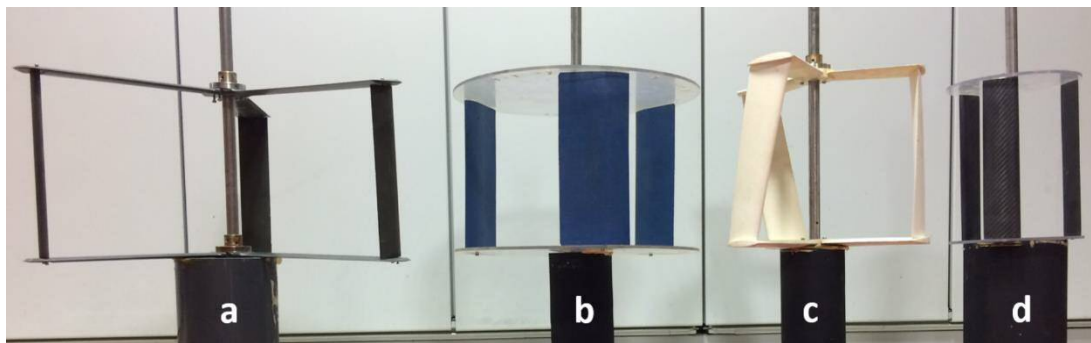


Figure 24. Photograph of some rotors tested, a) 600mm, b) 400mm, c) 360mm, d) 200mm diameter

However, the comparison to other wind or hydrokinetic VAT and HAT research studies is difficult since so many parameters impact on the overall performance. Some studies show promising results from symmetrical NACA airfoils [105, 106] whereas others observed better performance with chambered blades [107, 108]. Ultimately, the lift-to-drag ratio defines the performance of a blade. In operation, the blade is constantly changing its position relative to the approach flow and the blade with the highest average lift-to-drag ratio is performing the best [109]. It should further be mentioned that structural and machining aspects influence the shape of the blade and may restrict a design to a certain minimum thickness [110].

In the following, the parameter testing results (see Table 3) are listed and described. A direct result comparison with other studies is avoided for the individual parameter testing due to the previously mentioned complexity of the matter. For some tests, one rotor was employed where the torque transducer as well as the disc-brake/generator was attached directly to the rotor shaft (see Figure 23a and c).

3.3.2.1 Blade (air-foil) shape

The shape of the blade has a major impact on performance, self-starting behaviour and mechanical strength. It is a complex parameter which is strongly influenced by other parameters such as flow speed, pitch angle, rotor solidity and surface roughness. Therefore, a holistic perspective is needed to improve the overall turbine rotor design. For example, the same NACA4421 blade which achieved a  $C_P$  of 60% would perform much worse with a different pitch angle or a much higher or lower solidity (i.e., rotor diameter). The order of how the test results and design features are presented is therefore not chronological but ordered by subject. For all different blades, the optimum pitch angle was observed in the first place (see next subject).

Several different blade shapes were investigated during this study and are listed in Table 5 where the best performing individual test is shown.

Table 5. Best performing blade shapes

Blade shape	Flow velocity [v]	Rotor Ø [D]	Chord length [CL]	$C_P$ max
---	m/s	mm	mm	%
NACA0018	1.16	400	100	49
Eppler 715	1.16	400	100	39
NACA4421	1.15	600	59	56
NACA4421	1.09	360	80	60

Exemplarily, Figure 25 depicts two blades used for the test series, NACA0018 and Eppler 715 with a chord length of 100mm and a rotor diameter ( $\varnothing$ ) of 400mm. Here, the symmetrical NACA blade outperformed the Eppler blade by approximately 10 %.

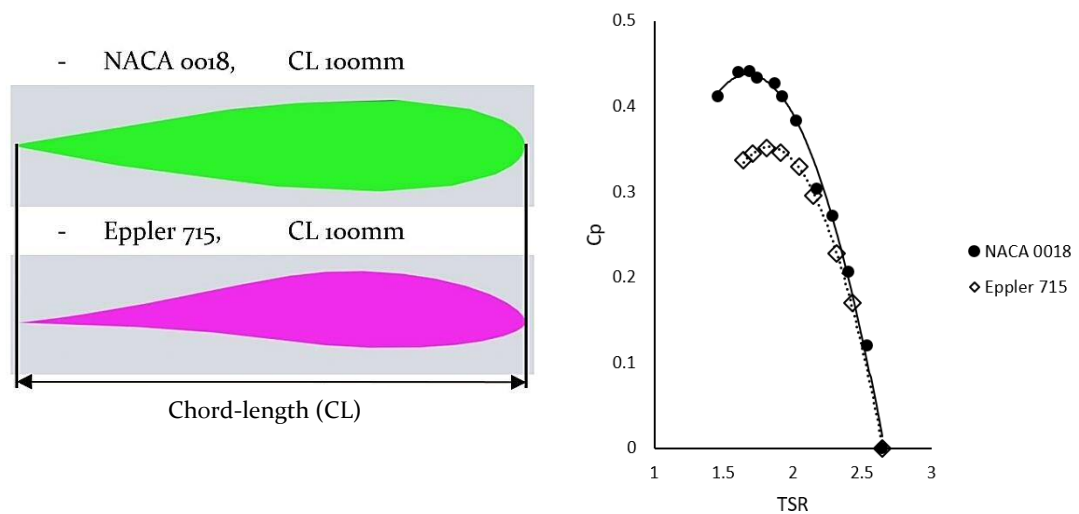


Figure 25. Blade shape comparison @  $v \approx 0.9m/s$  (tests 001 and 048)

Differentiation criterion is the curvature, not general dimensions (i.e., chord length or relative thickness). From table 4, it can be seen that a chambered NACA4421 airfoil performed best with up to 60%. The number coding defines the NACA (National Advisory Committee for Aeronautics, later NASA) airfoil shape. For a four digit NACA as given here, the first number represents the maximum chamber divided by 100, the second number is the position of the maximum chamber along the chord line divided by 10 and the last two digits specify the thickness of the airfoil as percentage of the chord length (i.e., length of chord line, see Figure 26). [111] was used to generate the geometry of the airfoils.

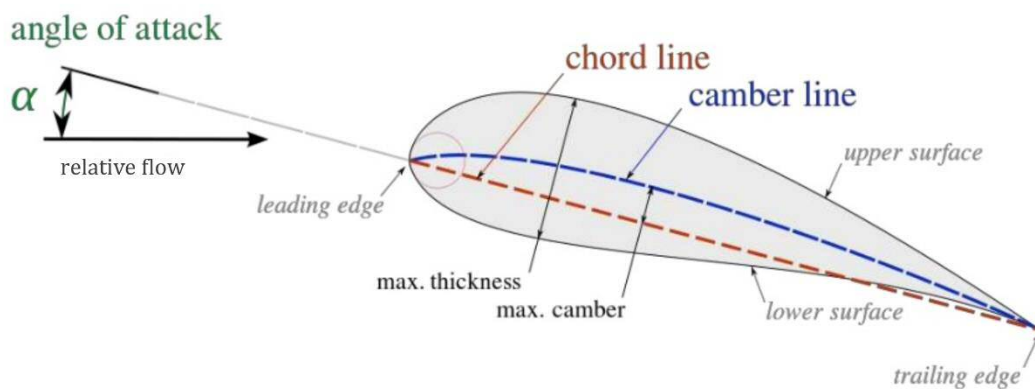


Figure 26. Blade cross-section with nomenclature [112]

### 3.3.2.2 Pitch angle

The pitch angle (angle between the centre line of the blade and the tangent of the rotor circumference, see Figure 27) is closely linked to the shape of the blade and any blade has an optimum pitch angle. In contrast to HATs, the position of the VAT blade is constantly changing during rotation relative to the flow and a translation from HAT to VAT design is not possible. Here, it was tested at what pitch angle the individual blade performed best. The results are listed in Table 6.

Table 6. Best performing pitch angle of different blades

Blade shape	Flow velocity [v]	Rotor Ø [D]	Chord length [CL]	Pitch angle [γ]
---	m/s	mm	mm	deg
NACA0018	0.92	400	100	5
Eppler 715	0.92	400	100	5
NACA4421	0.92	600	59	5.5
NACA4421	0.92	360	80	5.5

Figure 27 depicts a plan view of a CAD drawing of a blade (green) on the rotor circumference with pitch angle, centre and tangent line indicated alongside a result graph of the Eppler 715 blade for different pitch angles.

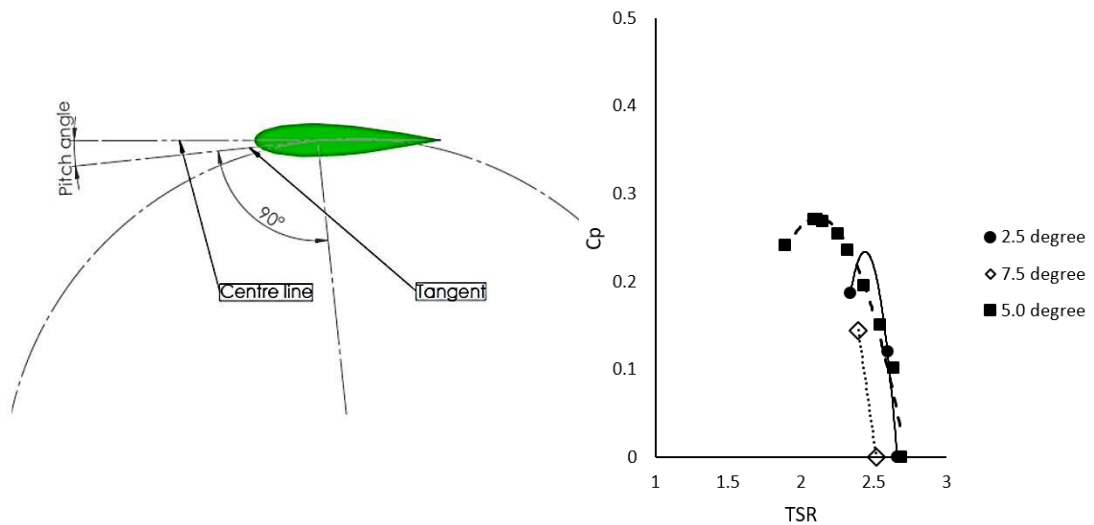


Figure 27. Blade on the rotor circumference including nomenclature and pitch angle comparison @  $v \approx 0.9 \text{ m/s}$  (tests 003, 004 and 005) with Eppler 715

It can be seen that the blade performs the best at 5° pitch angle. A variation of +/- 2.5° leads to a drop in performance of approximately 50%. Similar results were found elsewhere [104,113–115].

### 3.3.2.3 Number of blades

The amount of blades used for a rotor of a VAT has several major implications. The more blades

- the more expensive the rotor,
- the more torque/power is generated,
- the better the self-starting behaviour,
- the less vibrations [116],
- the lower the TSR [68].

Here, the effect of the number of blades on the overall performance of the rotor was evaluated. Rotor solidity, which is the ratio of total blade chord length and rotor circumference (Equation 3.1), plays an important role in this context as well and will be covered separately. Table 7 gives an overview of the number of blades comparison for NACA and Eppler blades, all with a chord length of 100mm and at a flow velocity of 1.16 m/s.

Table 7. List of results from number of blades comparison

Blade shape	No of blades	Solidity [ $\sigma$ ]	$C_{P \max}$	TSR [ $\lambda$ ]
---	---	%	%	---
Eppler 715	2	16	35	2.3
Eppler 715	3	24	39	1.9
Eppler 715	4	32	36	1.6
NACA0018	2	16	44	2.1
NACA0018	3	24	49	1.8

From Table 7 and Figure 28, it can be seen that the rotational speed of the rotor is decreasing the more blades are employed and that performance with three blades is best.

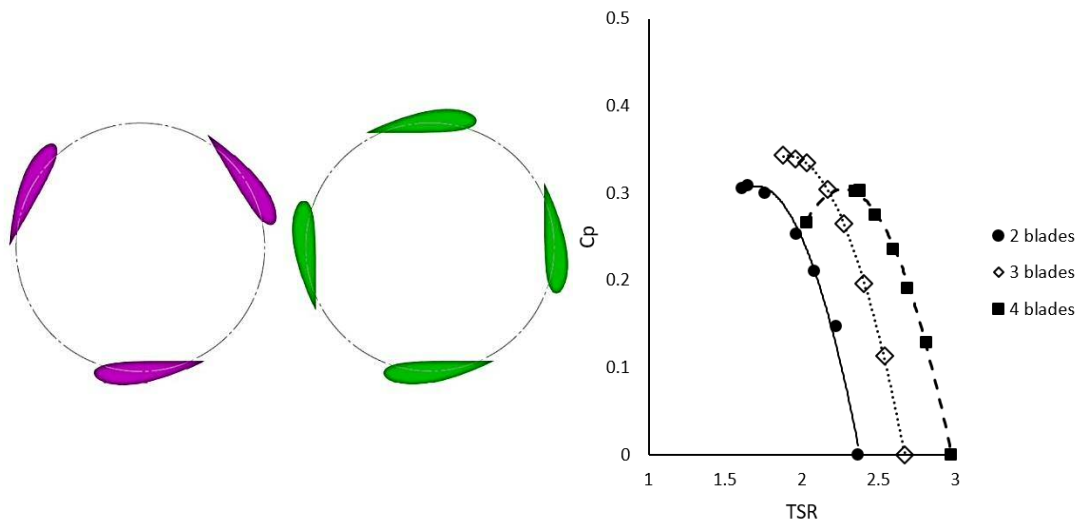


Figure 28. Pink: rotor with three blades, green: rotor with four blades, and number of blades comparison @  $v \approx 0.9 \text{ m/s}$  with Eppler 715 (tests 042, 044, 046)

### 3.3.2.4 Blade twist

A major drawback of VATs is their poor self-starting behaviour and its torque ripple due to the constant change in angle of attack. Several studies [69,100,117] suggested that it is beneficial to twist the blade along an imaginary cylinder, coinciding with the rotor radius. It was further observed that a twisted blade lacks in efficiency when compared to a straight blade, mainly due to increased drag losses of the bigger blade surface area and the reduced magnitude of the generated forces. Figure 29 depicts a CAD representation of a straight (green) and a 20° twisted blade (pink) and their achieved efficiency in a comparison of two different velocities (0.92m/s and 1.16m/s).

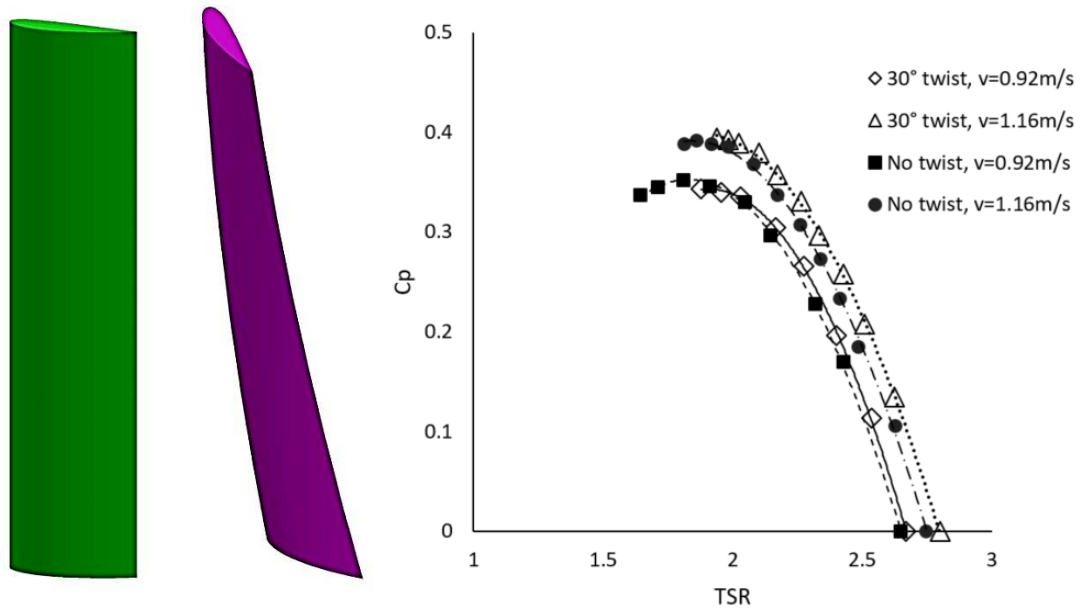


Figure 29. Green: straight blade, pink: twisted blade and comparison of straight and twisted Eppler 715 (tests 044, 045, 048, 049)

In contrast to the previously mentioned studies, there was no significant difference in terms of performance and rotational speed. The  $C_P$  for both blades peaked at a TSR of about 1.9 at approximately 35% and 39% respectively. Further, both rotors self-started under all conditions and the deviation from average torque was  $< 0.5$  Nm for both blades which gave no indication of a significant improvement in terms of torque ripple. In Appendices I, the variation of torque relative to TSR is further discussed.

### 3.3.2.5 Spoke-blade fastening

Blades, spokes and shaft need to be attached to each other. Bolts are used to connect the individual components. Using the same set-up of blades, spokes and shaft, two different kind of bolts were used in order to observe the impact of friction between bolt head and water on the performance of the entire turbine. Figure 30 depicts the countersunk and socket bolts used for the comparison and shows how significant the impact of protrude bolt heads is on the performance.

Table 8. List of results for salient fastening comparison using three NACA4421 blades with a chord length of 59mm and a rotor diameter of 600mm

Bolt type	Flow velocity [v]	Solidity [ $\sigma$ ]	$C_P$ max	TSR [ $\lambda$ ]
---	m/s	%	%	---
Socket	0.85	9	25	3.1
Socket	0.98	9	29	3.0
Socket	1.09	9	31	3
Countersunk	0.85	9	41	3.4
Countersunk	0.98	9	44	3.2
Countersunk	1.09	9	45	3.3

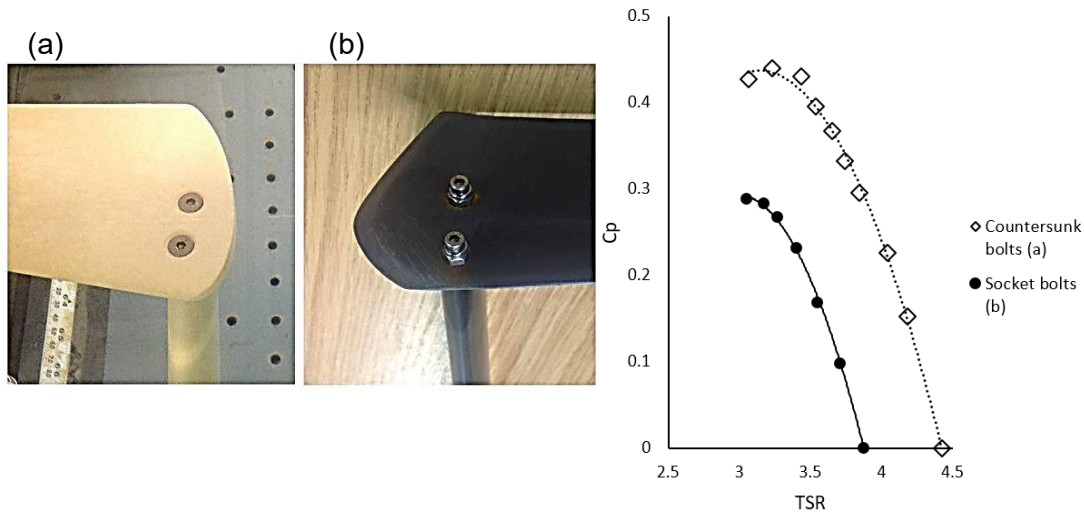


Figure 30. White blade with countersunk bolts (a), black blade with socket bolts (b) and comparison results of countersunk and socket bolts (both used on black spoke) @  $v \approx 0.98$  m/s (tests 066, 069)

Table 8 shows the testing results for different flow velocities. It can be seen that the increased drag of the bolt heads is causing a performance drop of approximately 14% alongside a reduction in rotational speed of approximately 10%.

Further, it was observed that the rotor always self-started with the countersunk bolts but never with the M5 socket bolts which stuck out 5mm. Two bolts are needed for each point of contact which sums up to 12 bolts for the tested three-bladed rotor. It is assumed that the severe performance drop is enhanced by the low solidity of the rotor and the relatively high rotational speed. However, a smooth and non-salient fastening is crucial in designing the rotor component connections, particularly between spokes and blades where the rotational speed and hence the impact of drag is the highest.

### 3.3.2.6 Blade surface finish

In operation, the turbine rotor is constantly moving through the water and it is assumed that drag due to friction is reduced the smoother the surface of the rotor components is [99]. Since the blades are the fastest moving members of the system, the impact of surface roughness must be the highest here.

For this experiment, two different blades were used on the same three bladed rotor ( $\varnothing$  600mm): Blade A is made of carbon fibre composite material with a rough and untreated surface; blade B is milling machined from a solid plastic sheet (glass filled nylon 66) and features a smooth and sanded surface (see Figure 31). Both NACA4421 blades are straight and have a chord length of 59mm. Details about materials and manufacturing can be found in Appendix G. Table 9 lists the results of the tests at different flow velocities.

Table 9. List of results for surface roughness comparison using three NACA4421 blades with a chord length of 59mm and a rotor diameter of 600mm. Blade A was made out of composite material, Blade B milling machined out of Nylon.

Blade	Flow velocity [v]	Solidity [ $\sigma$ ]	$C_{P \max}$	TSR [ $\lambda$ ]
---	m/s	%	%	---
A	0.85	9	25	3.1
A	0.98	9	29	3.1
A	1.09	9	31	3.0
B	0.85	9	50	3.2
B	0.98	9	52	3.1
B	1.09	9	56	3.2

Figure 31 depicts sections of the two blades tested and the irregularities on the surface of the composite blade A can be seen which has a dramatic impact on performance with a difference of more than 20% compared to the smooth milled and sanded blade B.

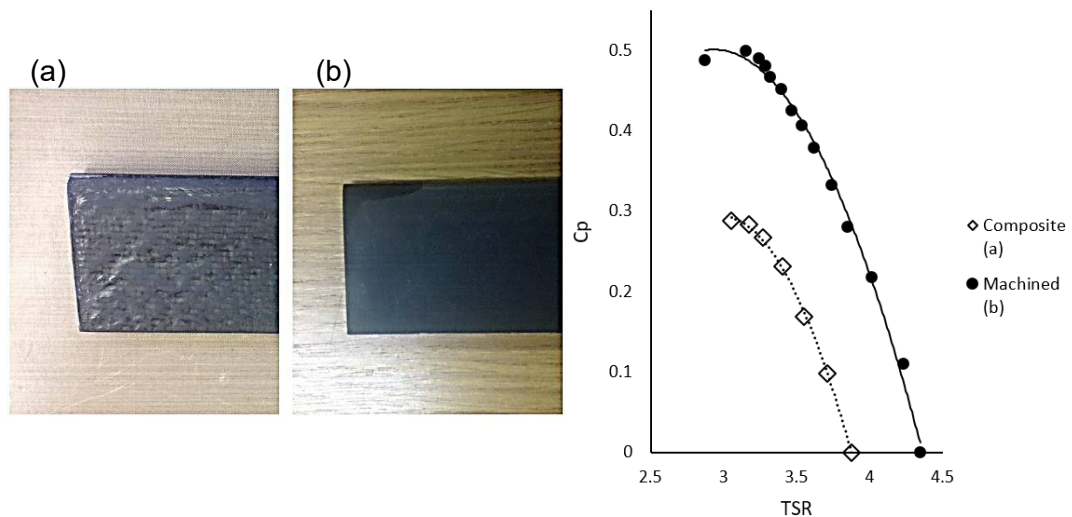


Figure 31. Composite blade (a) with rough surface, milling machined blade (b) with smooth surface and results of roughness comparison @  $v \approx 0.98$  m/s (tests 052, 066)

There is a certain amount of uncertainty whether or not geometrical integrity is given for the composite blade. It was planned to compare the initial design CAD file to the actual geometry of the two manufactured blades but a lack of resources prevented this step (see Chapter IX and Appendix G for further notes on manufacturing).

### 3.3.2.7 Shaft diameter

The axis is a necessary structural member of the rotor which does not contribute towards energy harnessing but transfers the torque to the PTO and holds the rotor in place via spokes. However, the axis also causes vortices which interfere negatively with the blades downstream [118]. Since the shaft cannot be eliminated without compromising on the overall rotor design (e.g., reinforce spokes and blades), it was

studied whether the shaft diameter has an impact on the performance of the rotor. Figure 32 depicts the different shaft diameters tested and the impact on the rotor performance. Up to a shaft diameter of 1/4 turbine diameters D, no significant drop in performance was observed. Shaft diameters of 140mm and more caused a reduction in efficiency.

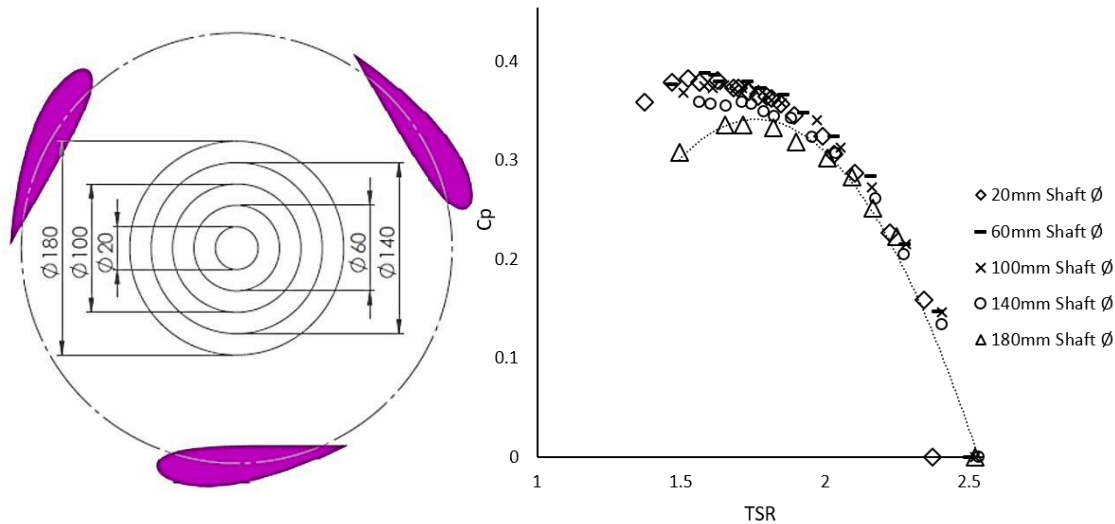


Figure 32. Different shaft diameters tested and results comparison @  $v=0.92$  m/s (tests 007, 009, 011,013, 015), trend-line for 180mm shaft shown only.

The tests were conducted at two different velocities as shown in Table 10 using a three bladed rotor with a diameter of 400mm featuring the Eppler 715 blade with a chord length of 120mm.

Table 10. List of results for shaft diameter comparison using three Eppler 715 blades with a chord length of 120mm and a rotor diameter of 400mm

Shaft $\phi$	Flow velocity [v]	Solidity [ $\sigma$ ]	$C_{P \max}$	TSR [ $\lambda$ ]
mm	m/s	%	%	---
20	0.92	29	38	1.5
20	1.16	29	42	1.6
60	0.92	29	39	1.6
60	1.16	29	42	1.6
100	0.92	29	38	1.6
100	1.16	29	42	1.7
140	0.92	29	36	1.6
140	1.16	29	40	1.7
180	0.92	29	34	1.7
180	1.16	29	37	1.7

Similar tests were conducted with smaller blades (Eppler 715, Chord length 80mm) and, hence, with a lower solidity. The results are listed in Table 11.

Table 11. List of results for shaft diameter comparison using three Eppler 715 blades with a chord length of 80mm and a rotor diameter of 400mm

Shaft Ø	Flow velocity [v]	Solidity [ $\sigma$ ]	$C_{P \max}$	TSR [ $\lambda$ ]
mm	m/s	%	%	---
20	0.92	19	27	2.1
20	1.16	19	31	2.2
60	0.92	19	27	2.1
60	1.16	19	31	2.1
100	0.92	19	24	2.1
100	1.16	19	27	2.2
140	0.92	19	22	2.1
140	1.16	19	26	2.3
180	0.92	19	17	2.0
180	1.16	19	20	2.0

Ignoring the fact that the smaller 80mm blades perform worse ( $C_P$  17 - 31%, see Table 11) than their 120mm counterparts ( $C_P$  34 - 42%) while spinning faster, increasing the shaft diameter has a similar impact. Up to a shaft diameter of 100mm (1/4 rotor diameter), the performance is not significantly affected which implies that the shaft design is purely driven by structural and economical aspects.

### 3.3.2.8 Spokes vs discs

In contrast to HATs, where the blades' root coincides with the centre of rotation, the blade of a VAT is at a certain distance to the centre of rotation (e.g., the distance equals the rotor radius). Therefore, a structural member is necessary to overcome the distance from rotor shaft to blade and further, to transfer the generated forces to the shaft (torque). For simplicity, acrylic discs were used for the first experiments since it allowed one to test many different blade configurations easily and cost-effectively. The two discs, however, are hydrodynamically disadvantageous due to the large surface area. They were replaced by six spokes as depicted in Figure 33 and were attached to the blade-ends.

The spokes' cross-section has a symmetrical airfoil shape (NACA0024, CL 60mm at the root and is constantly changing towards NACA0012, CL 100mm at the tip) in order to provide minimum drag without compromising on structural integrity [119,120]. At the tip, the spoke features a recess for attaching the blade and is further overlapping slightly in order to prevent tip vortices disrupt the flow over the blade near the ends, thereby maintaining maximum lift and minimum drag near the blades' tips [121]. More detailed design drawings of the laboratory rotors are provided in the Appendix B.

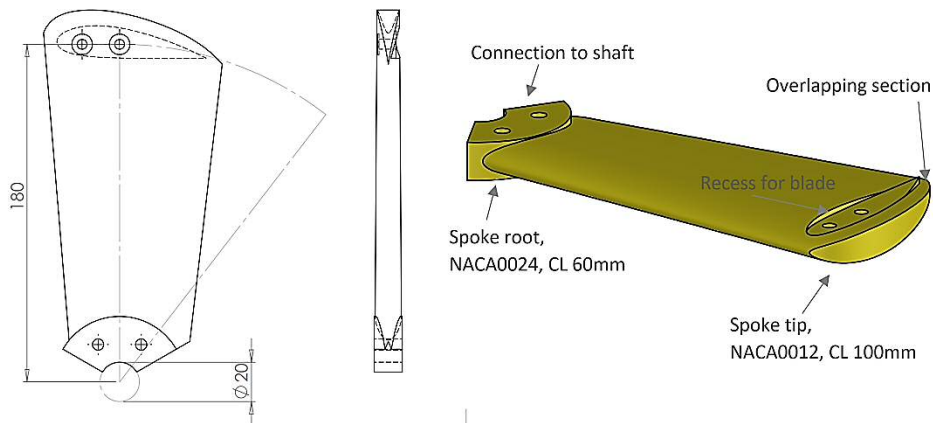


Figure 33. CAD drawings (top, side and perspective view) of spoke used for laboratory rotor

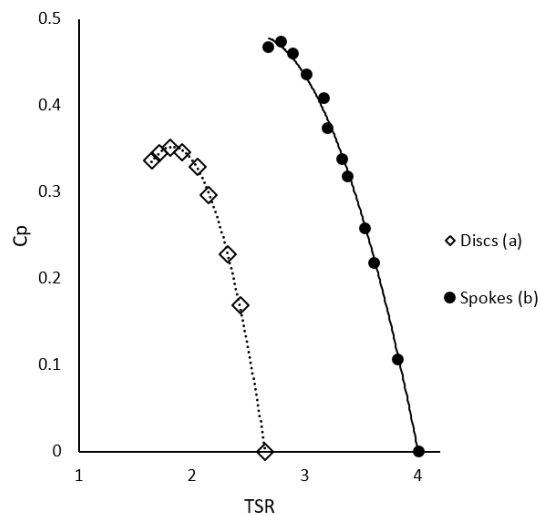
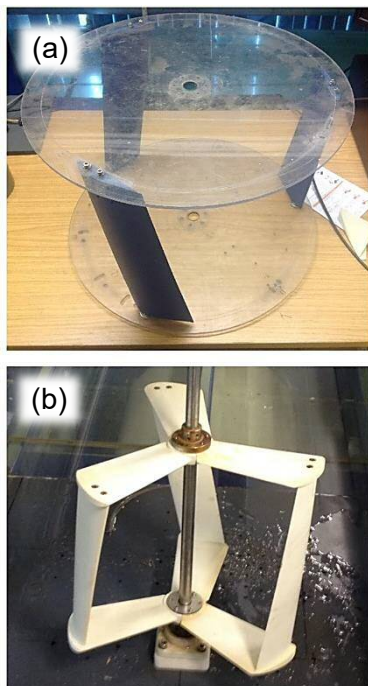


Figure 34. Blades attached to shaft via discs (a) and spokes (b). Result comparison @  $v \approx 0.9$  m/s (tests 048, 071)

Figure 34 depicts the two rotors tested alongside the performance comparison where a significant increase in rotational speed and performance can be seen if the discs are replaced by spokes. At peak performance, the rotor with disc spun at a  $\lambda = 1.8$  with  $C_P = 35\%$  whereas the rotor with spokes achieved  $\lambda = 2.8$  and  $C_P = 47\%$ . Nonetheless, a significant improvement in performance was expected since the discs were chosen as a device which can be easily adopted for parameter testing and not for optimised performance. The spokes as shown in Figure 33 were finalised after the parameter tests were analysed. It was further planned to analyse the forces acting on the spokes, confirm the structural and geometrical integrity and potentially optimise

the geometry which was abandoned due to a lack of resources. See Appendix G for further manufacturing and structural analysis details as well as Chapter IX.

### 3.3.2.9 Flywheel

Due to the nature of VATs, forces acting on the blade during a revolution are highly fluctuating. Therefore, the entire system experiences a change of stress and strain from one moment to another (i.e., vibrations). It was therefore studied how an increase of inertia (increased weight of the rotating system) would impact on both vibrations and performance. Ideally, the weight of the blades would be increased [122] by using aluminium or stainless steel instead of plastic for example. This would imply to redesign all structural components due to the higher weight and forces. Instead, two different weights, similar to weight lifting discs (6 and 12 kg) were used as flywheel (see Figure 35).

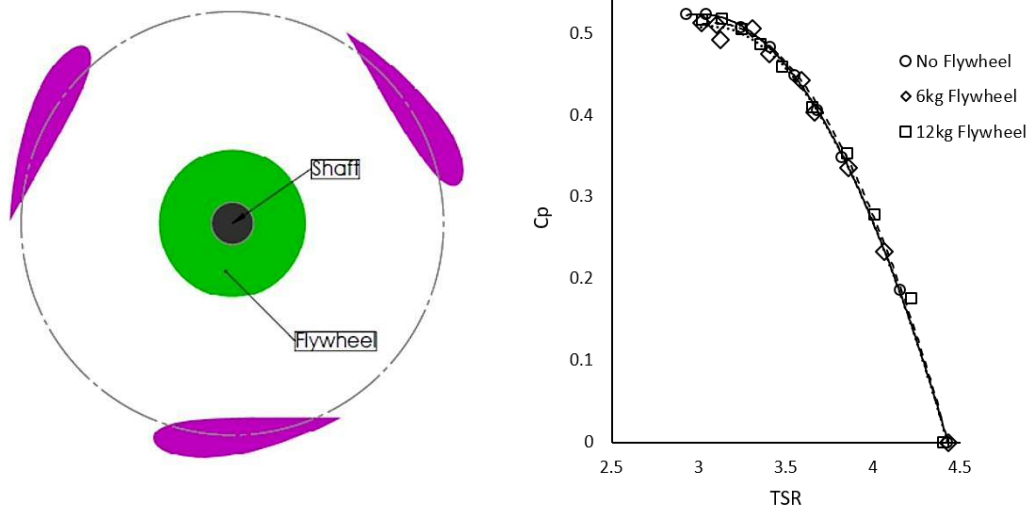


Figure 35. Top-view of rotor with flywheel in green. Flywheel comparison @  $v \approx 1.0 \text{ m/s}$  with NACA4421 (test 053, 056, 059)

Neither an impact on performance nor on vibrations (visual observation during testing) was observed. Instead, the self-starting ability of the rotor became worse at lower flow speeds due to the increased inertia.

### 3.3.2.10 Solidity

The solidity ( $\sigma$ ) of a VAT describes the ratio between the sum of blade chord lengths (CL) and rotor circumference as shown in Equation 3.1.

$$\sigma = \frac{\sum CL}{\pi * D} \quad (3.1)$$

$$\beta = \frac{A_R}{A_F} \quad (3.2)$$

$$\beta' = \frac{D_R}{W_C} \quad (3.3)$$

Hence, the bigger the total blade chord length for a given rotor diameter, the bigger the solidity. Solidity is a key feature of the rotor with several implications. High solidity

rotors ( $\sigma > 25\%$ ) benefit from high torque output and improved self-starting behaviour whereas low solidity rotors ( $\sigma < 15\%$ ) persuade by low costs/weight and high TSR which again impacts on generator costs and vibration reduction [68] [106].

Several studies suggest that blade shape, number of blades, blockage and solidity are strongly interlinked and it is concluded that a holistic design approach should be considered [123–125]. For example, in the previously described result section for number of blade testing, the same blades were used with a constant rotor diameter. Therefore, the solidity increased with an increased number of blades. Alternatively, the rotor diameter could be adjusted in order to keep  $\sigma$  constant. Consequently, the blockage ratio  $\beta$  would change and needed adjustment.  $\beta$  is defined as the ratio between cross-sectional area of rotor ( $A_R$ ) and waterbody ( $A_F$ ) (see Equation 3.2). The higher the blockage ratio of a rotor, the less water can bypass the rotor and vice versa. Blockage is one of the tested parameters and is described in more detail later. It can be seen that one aspect is interlinked to another and a clear differentiation is difficult.

Here, the impact on performance, TSR and self-starting behaviour was observed by testing three different Eppler 715 blades with chord lengths of 80, 100 and 120mm which computes to rotor solidities of 19, 24 and 29% respectively at a rotor diameter of 400mm. Figure 36 depicts the rotor with two different blades alongside the results.

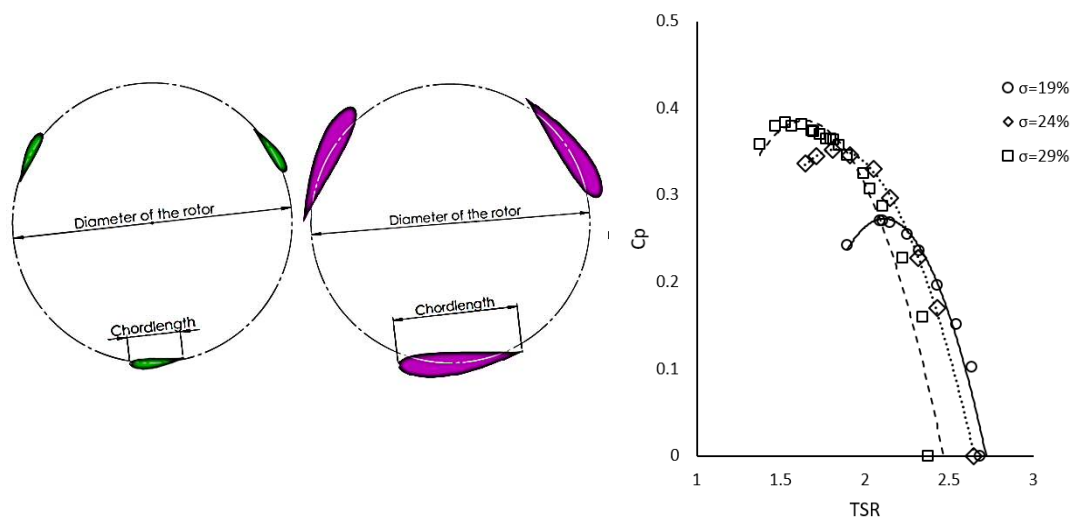


Figure 36. Rotor with low solidity (green) and high solidity (pink). Solidity comparison @  $v \approx 0.9\text{m/s}$  with Eppler 715 (test 005, 007, 048)

It can be seen that the performance improves with higher the solidity, which is in agreement with the prediction. Further, the rotor was self-starting for all tests. However, the desired design of this study features a low solidity rotor and existing literature suggests that a very low solidity rotor ( $\sigma \leq 10\%$ ) can perform well, mainly

due to the much higher rotational speed [126]. Figure 37 depicts another solidity test with a very low solidity rotor using a NACA4421 blade with a chord length of 59mm, both, on a 600 and 400mm rotor (e.g.,  $\sigma = 9$  and 14% respectively).

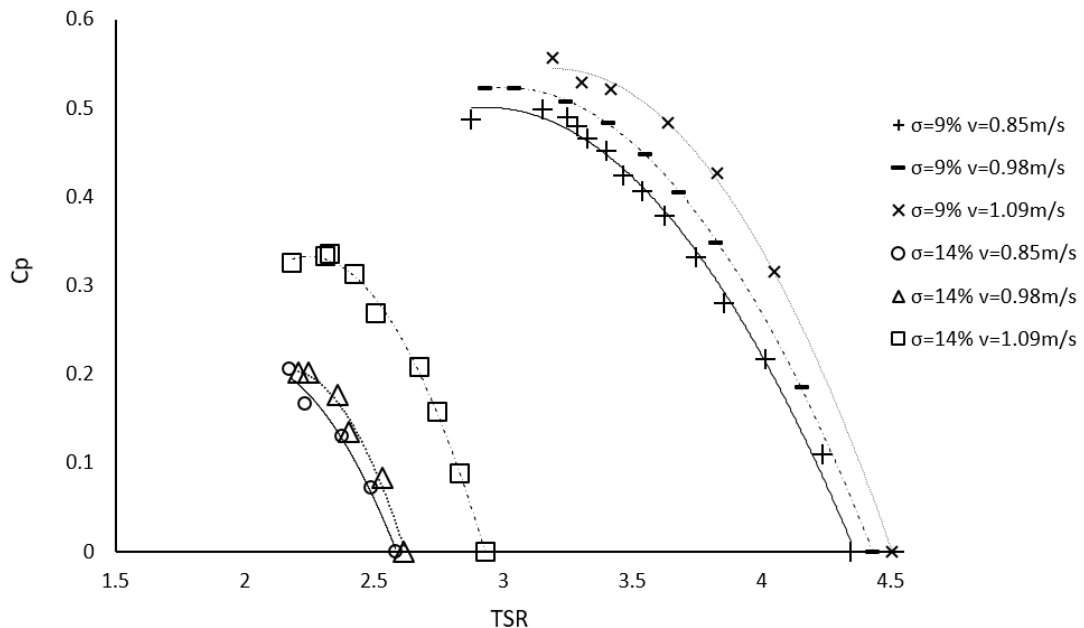


Figure 37. Solidity comparison of very low and low solidity rotor (test 052 - 054, 061 - 063)

The straight comparison between different rotor configurations is difficult. Here, two different rotor radii were used in contrast to different blade chord length in the test results shown before. However, it is shown that the 600mm rotor with NACA4421 blades and  $\sigma = 9$  achieved a power coefficient of 50% and above. The rotational speed at peak performance was much higher than in any other configurations ( $\lambda > 3$ ). Self-starting ability, however, was not given.

### 3.3.3 Structure testing and results

The concept of the twin turbine presented at the beginning of this chapter features a cementitious housing which acts as the structural member, a gravity base and a flow augmentation. The first two structural aspects are not further discussed since their design is straightforward and mainly driven by turbine/channel size and flow regime. Here, it was tested at what blockage ratio and what longitudinal position within the housing the rotor performed best.

#### 3.3.3.1 Blockage

Flowing water is considered to be blocked if the flow is constrained in one or more dimensions. For example, flowing water in the sea or wide, deep river can be seen as unblocked, flowing water in a narrow channel or flume (as used in these experiments) as blocked. The blockage ratio ( $\beta$ ), ratio between rotor and channel

cross-section (Equation 3.2), is a measure to quantify the amount of blockage and represents another important parameter in hydrokinetic turbine design. The reason for blocking or constraining the flow is to reduce its cross-section and therefore increase its velocity at a given discharge (Equation 1.2). Here, the velocity is cubed and has a significant impact on the power available.

In this experiment, the optimum blockage ratio was observed by constraining the flume width with a streamlined structure (see Figure 38) and changing the rotor diameter. Initially, without structure,  $\beta = 18\%$  if the water level is at 0.5m and a rotor with  $\varnothing = 360\text{mm}$  is employed. Since the distance between flume-bed and rotor, the height of the rotor and the water table has not changed, the blockage ratio from now onwards will be expressed as ratio between rotor diameter ( $D_R$ ) and channel width ( $W_C$ ) and denoted as  $\beta'$  (Equation 3.3). Therefore,  $\beta = 18\%$  becomes  $\beta' = 30\%$ .

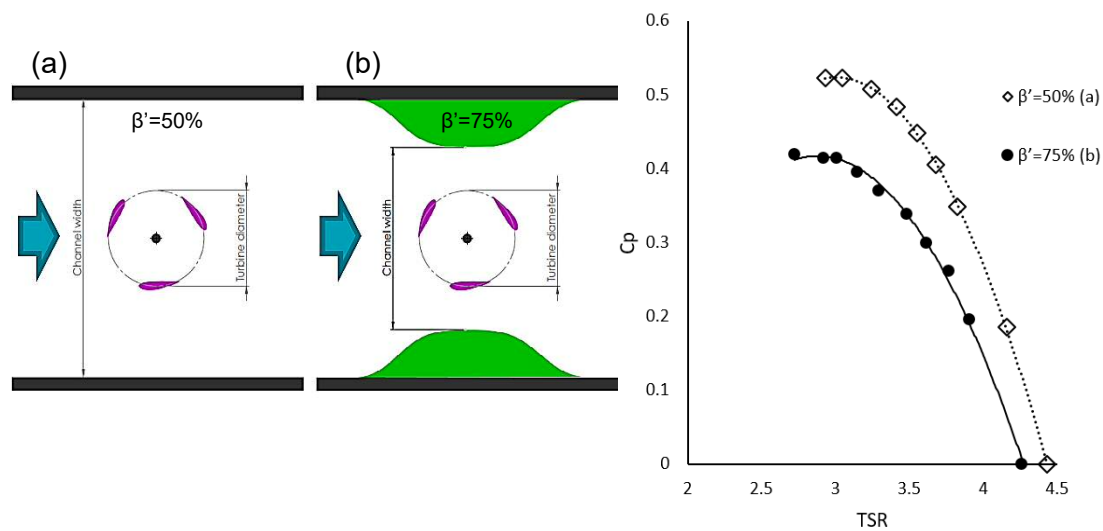


Figure 38. Unconstrained (a) and constrained (b) flume with rotor at its centre. Blockage comparison @  $v \approx 0.9\text{m/s}$  with NACA4421, chord length 59mm,  $\varnothing 600\text{mm}$  rotor (test 053, 076)

Several rotors with and without constriction (green structure as depicted in Figure 38) were tested and the maximum power extraction with a single rotor employed was found to be  $C_P = 69\%$  with  $\beta' = 50\%$  (test 074, see Appendix A for all test results). However, a significant increase in backwater was observed, proportional to the increase in blockage and discharge. At  $\beta' = 75\%$ , the efficiency dropped drastically as shown in Figure 38. Table 12 shows all blockage test results with the NACA4421 blade.

It shall be noted that in a wind or ocean current context usually a blockage correction is applied where the performance enhancement due to blockage is subtracted. Here, the enhancement is desired and an integral part of the design and is therefore not subtracted. Further, the Lanchester-Betz limit sets the upper limit for kinetic energy

extraction devices in an unconstrained flow. However, in a constrained flow, the Lanchester-Betz limit ( $C_{Pmax} < 60\%$ ) does not apply [127] since the flow is unable to bypass the channel's cross-section and efficiencies of up to 90% are predicted elsewhere [128].

Table 12. List of results for blockage comparison using three NACA4421 blades with a chord length of 59mm

Blockage [ $\beta'$ ]	Flow velocity [ $v$ ]	Solidity [ $\sigma$ ]	$C_{Pmax}$	TSR [ $\lambda$ ]
%	m/s	%	%	---
25	0.92	19	27	1.3
25	1.16	19	31	1.5
25	1.42	19	27	1.5
33	0.85	14	21	2.2
33	0.98	14	20	2.2
33	1.09	14	33	2.3
33	1.15	14	29	2.2
50	0.85	9	50	3.2
50	0.98	9	52	3.1
50	1.09	9	56	3.2
75	0.92	9	41	3.0
75	1.16	9	45	3.1

### 3.3.3.2 Rotor position

If a stream is constrained by a structure such as a turbine housing, the velocity of the flow changes while passing through it. It was assumed that the longitudinal position of the turbine may have an impact on the performance (see Figure 39).

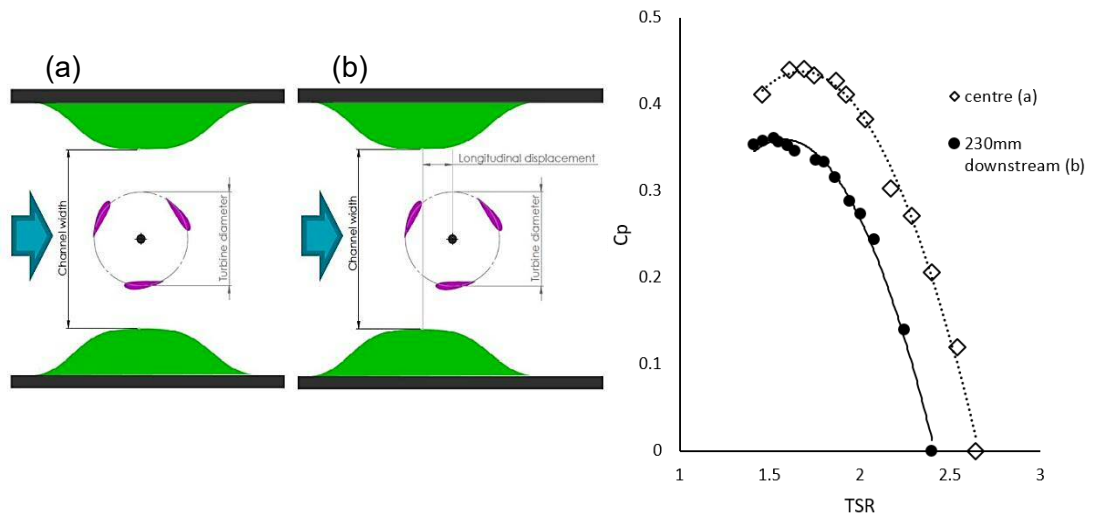


Figure 39. Rotor in a constrained channel at centre position of the structure (a) and further downstream (b). Comparison of longitudinal displacement @  $v \approx 0.9\text{m/s}$  with NACA0018 (test 001, 025)

It was observed, that the rotor performed best at centre position of the structure. Table 13 shows the peak values for  $C_P$  and TSR for two different velocities. A deficit of up to 9% was found if the rotor is shifted downstream.

Table 13. List of results for rotor position comparison using three NACA0018 blades with a chord length of 100mm and a rotor diameter of 400mm at centre of constriction and 230mm downstream (d.s.)

Position	Flow velocity [v]	Solidity [ $\sigma$ ]	$C_{P \max}$	TSR [ $\lambda$ ]
---	m/s	%	%	---
Centre	0.92	24	44	1.8
Centre	1.16	24	49	1.7
230mm d.s.	0.92	24	36	1.5
230mm d.s.	1.16	24	40	1.5

Due to time constrains, just two positions were tested. For a more sophisticated result, further positions should be tested, also upstream (see Chapter IX for further conclusions and recommendations).

### 3.3.4 Twin-rotor testing and results

The main aim of this study was to investigate the interaction of two rotors in a twin assembly and to justify the prediction of a beneficial overall performance. Two similar rotors were installed and the overall performance data captured in the same fashion as previously described. In addition, a PTO was employed consisting of two timing belts and four pulleys in order to combine the rotor's motion to one shaft (see Figure 23).

The PTO also contained a generator or a mechanical brake at the very end, shoulder bearings to support the shaft and a device to measure torque and rotational speed. The PTO was firmly attached to the bridge and the rotational speed and generated torque measured at the common shaft as explained earlier.

#### 3.3.4.1 Single vs twin rotor

The hypothesis of the twin rotor application is that two identical rotors sitting next to each other improve the overall performance of two individual rotors by increasing the flow velocity at the centre of the channel. Figure 40 depicts a comparison between single and twin assembly.

It might appear obvious that two rotors perform better than one but further considerations should be made.

- The twin turbine extracted at peak performance approximately 50 Watts at  $v = 0.85$  m/s whereas one rotor extracted 14 Watts. The product of two

single rotors is consequently 28 Watts and significantly lower than the power extraction of twin system (shown in Figure 40c,d)

- The coefficient of performance from the single rotor ( $C_{P_{\text{single}}} = 42\%$ ) is significantly lower than the equivalent of the twin ( $C_{P_{\text{twin}}} = 77\%$ ).
- The twin system has higher friction losses due to the PTO (mainly belt-drive and bearings) which are estimated to sum up to a 5% efficiency deficit (see synchronisation of rotors).

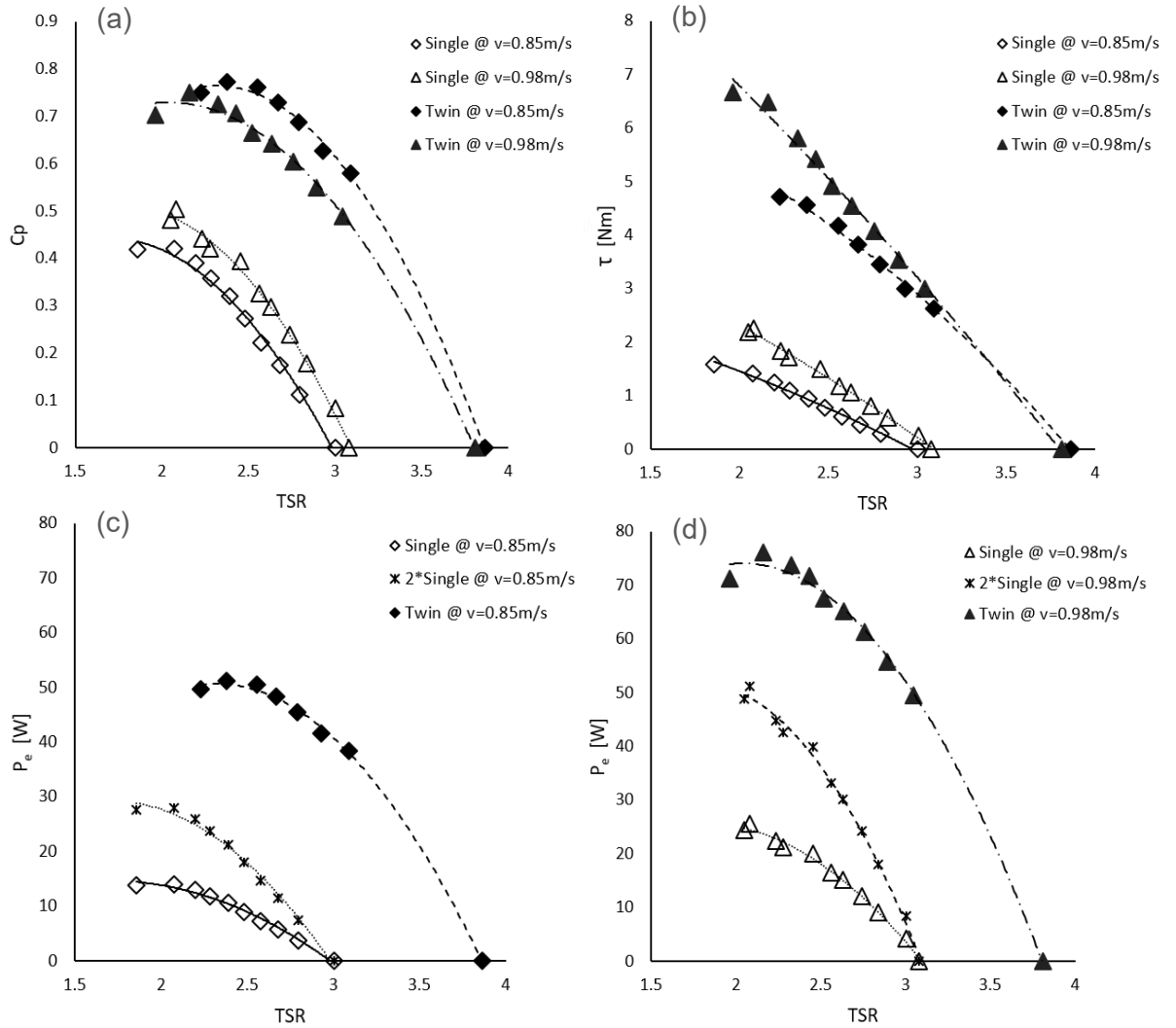


Figure 40. Single vs twin comparison showing results for two velocities: a)  $C_P - \lambda$  curve; b)  $\tau - \lambda$  curve; c-d)  $P_e - \lambda$  curve including the sum of two single rotors (test 128, 129, 156, 157)

Even if the previously mentioned blockage correction ( $C_{P_{\text{corrected}}} = C_P \cdot (1-\beta)^2$ ) is applied, the twin system ( $C_{P_{\text{twin corr}}} = 32\%$ ) outperforms the single rotor ( $C_{P_{\text{single corr}}} = 28\%$ ), particularly for lower flow velocities. It was further observed that the twin rotor has the better self-starting ability which is due to the higher velocities at the centre of the rotors. Table 14 shows all results from the single vs twin comparison.

Table 14. List of results for single vs twin rotor comparison using three NACA4421, CL80mm and a rotor diameter of 360mm

	Flow velocity	Blockage	Power extracted	$C_{P \max}$	TSR
	[v]				
	m/s	%	W	%	---
Single	0.72	30	7	32	2.2
	0.85	30	14	42	2.1
	0.98	30	26	50	2.1
	1.09	30	42	60	1.9
	1.15	30	43	52	2.1
Twin	0.72	60	30	75	2.4
	0.85	60	51	77	2.4
	0.98	60	76	75	2.2
	1.09	60	96	69	2.4
	1.15	60	116	70	2.6

3.3.4.2 Distance between rotors

If the hypothesis of a beneficial effect on turbine efficiency by an increased velocity in the centre of the two rotors is correct, then there must be an optimum spacing between them. First and foremost, it is assumed that due to a symmetrical rotor design and channel cross-section, the rotors should be installed symmetrically. Hence, the distance from the centre of the channel to the centre of the rotor axis is the same for both rotors and they both sit on the same longitudinal plane as shown in Figure 41. The distance between both rotor axis is presented as a function of the rotor diameter D and four different values were tested: 1.4, 1.5, 1.6 and 1.75 D.

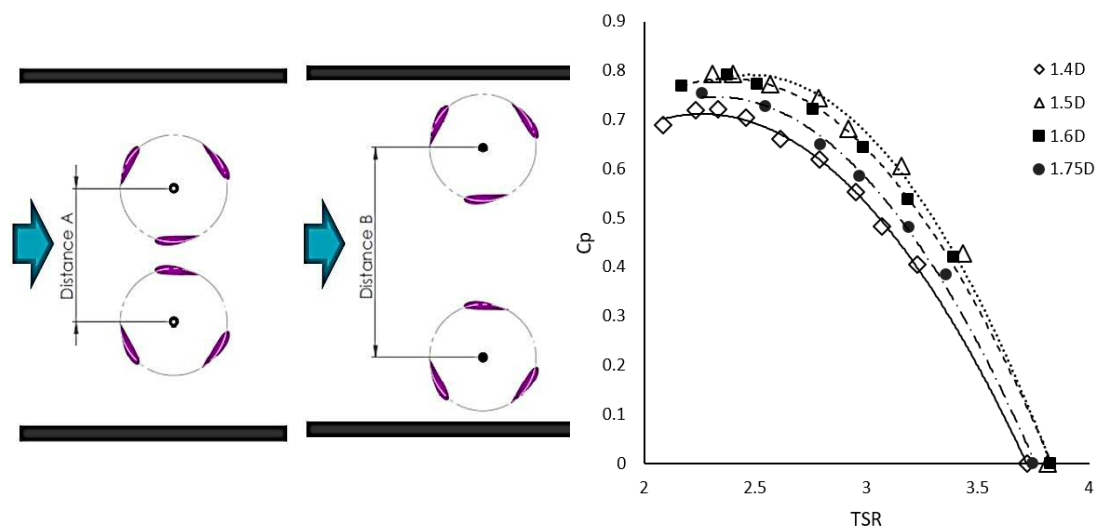


Figure 41. Twin rotor with different spacing. Spacing comparison @  $v \approx 0.9 \text{ m/s}$  with NACA4421, chord length 80mm,  $\varnothing 360 \text{ mm}$  rotor (test 110, 112, 116, 119)

It was observed that the rotors performed best at a spacing of 1.5 – 1.6 D with a peak efficiency of  $C_P = 79\%$ . If the distance was further increased or reduced, the efficiency dropped by 5 and 9% respectively. At higher flow speeds, a spacing of 1.5 D led to better performance as compared to 1.6 D (see Appendix A for result table, Test 108-122). All further twin-turbine tests were conducted by placing the rotors 1.5 D apart.

### 3.3.4.3 Inwards vs outwards rotation

From the turbine concept, the rotors spin inwards as shown in Figure 42 A. This design feature was justified by comparing performance data to data from the same rotors but spinning in the opposite direction as shown in B.

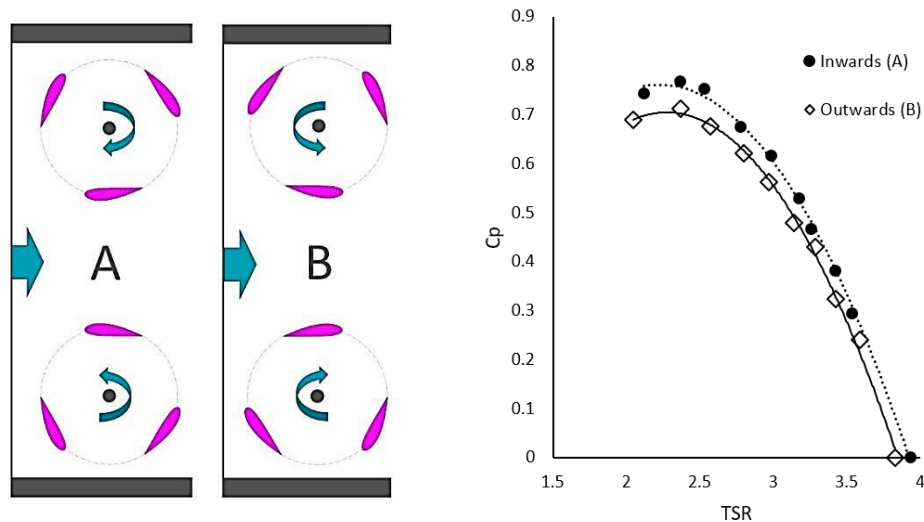


Figure 42. Twin rotor rotating inwards (A) and outwards (B). Inwards vs outwards comparison @  $v \approx 0.9 \text{ m/s}$  with NACA4421, chord length 80mm,  $\varnothing 360 \text{ mm}$  rotor (test 171, 172)

The difference was not as significant as expected which may be due to small scale of the laboratory set up or the overall symmetry of the system since at 1.5 D, the distance between centre of the flume and rotor axis as well as sidewall of the flume and rotor axis are similar.

### 3.3.4.4 Synchronisation of rotors

Due to the PTO, the twin rotors are naturally synchronised, i.e., spin at the same speed at any time. Both rotor shafts are connected to the main (generator) shaft via timing belts which synchronise the rotational motion due to the gearing of the belts' and pulleys' teeth (similar to a chain drive). Here, it was tested if the synchronisation has an impact on performance.

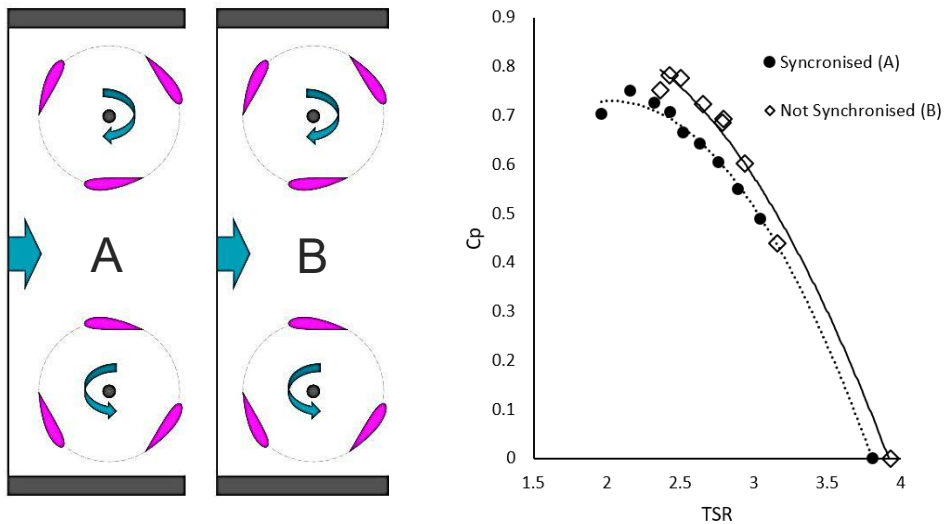


Figure 43. Twin rotor rotating synchronised (A) and not synchronised (B). Synchronisation comparison @  $v \approx 0.9\text{m/s}$  with NACA4421, chord length 80mm,  $\text{Ø}360\text{mm}$  rotor (test 141-149, 157)

Figure 43 depicts both scenarios, not synchronised (A, individual PTO for each rotor) and synchronised (C, combined, belt-drive PTO) with the same overall set-up. It can be seen that the not synchronised rotors spin slightly faster and perform approximately 5% better which is mainly due to the belt-drive friction losses. From visual observation, no difference was observed.

### 3.3.4.5 Rotor offset

Torque ripple and self-starting difficulties are major concerns of VATs. Both issues are linked to the fact that the blade is changing its position relative to the flow. It was investigated whether a  $60^\circ$  offset of one of the rotors has a beneficial impact (see Figure 44).

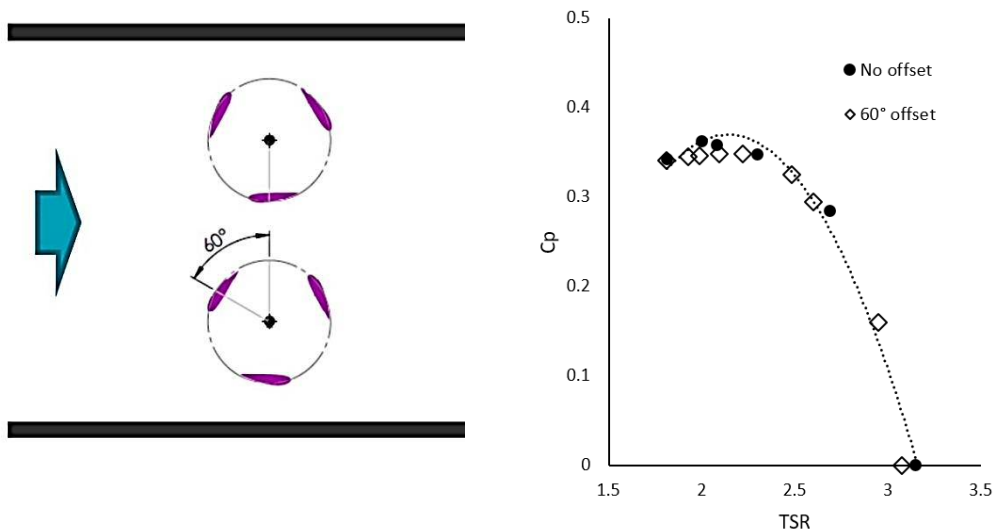


Figure 44. Twin rotor rotating with a  $60^\circ$  offset. Offset comparison @  $v \approx 0.9\text{m/s}$  with NACA4421, chord length 59mm,  $\text{Ø}200\text{mm}$  rotor (test 078, 080), trend-line for no offset shown only.

Performance-wise, no significant difference was observed whether or not the rotors are offset. As mentioned earlier, the lift and drag forces of each blade change constantly while the rotor spins which causes regular variations of torque in form of vibrations. If the rotors are offset, it is assumed that the torque ripple of both rotors will not occur at the same time and it was suggested that an offset of the rotors may reduce the torque ripple. However, with the rotors tested, the vibrations became much worse if offset by  $60^\circ$  which was visually observed during the experiment (the related data is attached to Appendices I). Moreover, the self-starting ability did not change compared to the rotor without offset.

#### *3.3.4.6 Submergence*

Whether or not the rotor is submerged has a great effect on the turbine's performance. Obviously, if the rotor is fully submerged then the entire blade surface area is in contact with the water and, therefore, more energy can be extracted in comparison to a rotor that is not fully submerged. In addition, the blade hydrodynamics are disturbed if the blades are not fully submerged by air-entrainment which reduces the density of the fluid that is in contact with the blade, and hence, results in a reduction of lift forces generated in this area. Further, the upper spokes could slice through the water surface during their rotational movement which results in significant splashing and an additional drag torque on the rotor shaft, which ultimately reduces the turbine's efficiency.

It was tested how an increased or decreased water depth would impact on the performance if a constant flow velocity is maintained. Five scenarios were tested (see Figure 45):

- Water table well above the rotor, WT = 0.65m
- Water table at usual level, WT = 0.50m
- Water table at level with top of rotor, WT = 0.45m
- Water table below top of rotor, WT = 0.40m
- Water table well below top of rotor, WT = 0.35m

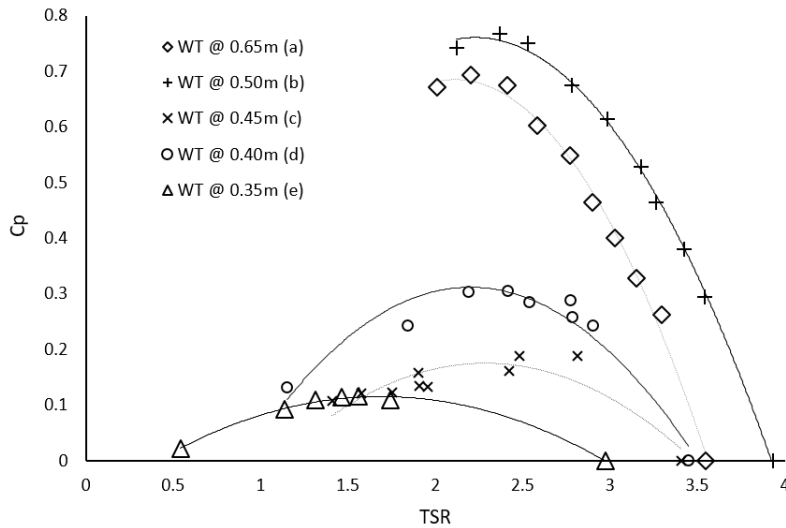
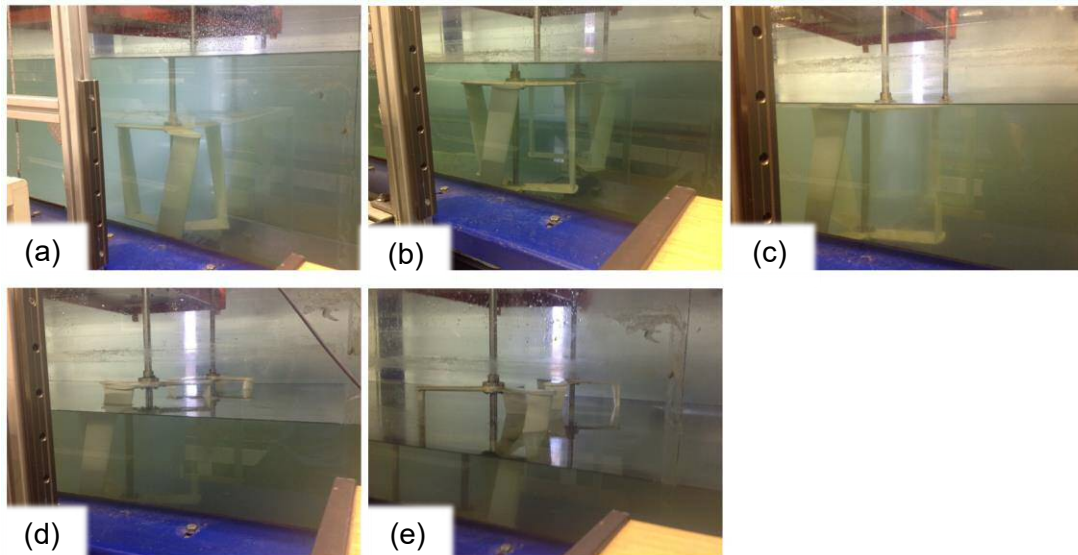


Figure 45. Rotor submergence tests at a water depth of: a) 0.65m; b) 0.50m; c) 0.45m; d) 0.40m; e) 0.35m; and submergence comparison @  $v=0.85\text{m/s}$  using NACA4421 blades,  $\varnothing=360\text{mm}$  (test 172, 174, 176, 178, 179)

The rotors perform best at a water depth of 0.5m, when they are covered by approximately 100mm of water (usual testing set-up). When the water table was increased by 150mm, performance dropped by 6% which is mainly due to the reduced blockage ratio  $\beta$  since more water can flow undisturbed above the turbine. When the water table was reduced by 50mm, the performance dropped dramatically by 50%. The spokes sliced through the water surface which caused a high level of noise, splashing water and air entrainment. A further reduction in water depth made the performance even worse.

### 3.4 Summary

The twin turbine design (10<sup>th</sup> scale) was extensively tested in the laboratory and is ready for upscale testing in a real channel environment. The latest laboratory tests

concluded to turbine efficiencies of more than 75% and conclusions and recommendations are summarized as follows:

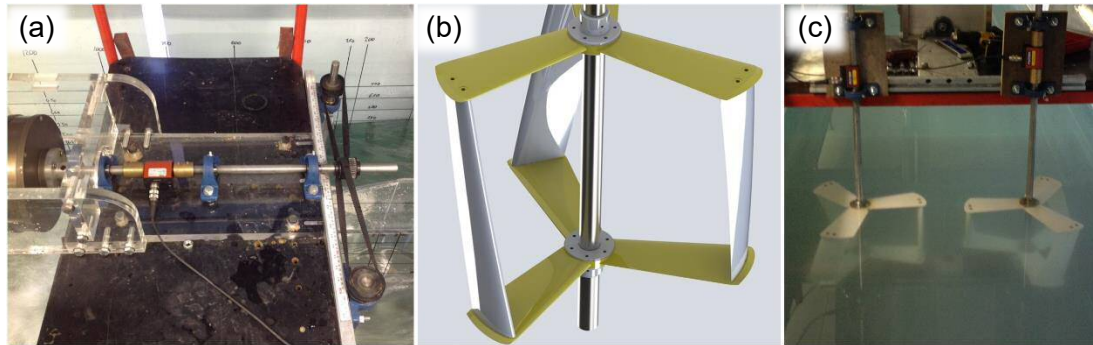


Figure 46. a) Combined laboratory PTO including generator, torque transducer and belt-drive; b) CAD drawing of the best performing rotor tested; c) individual laboratory PTOs including two torque transducer and disc brakes (not shown)

**Rotor:** The hydrodynamic behaviour of the rotor and its components is well understood and, as far as performance is concerned, the rotor operates very well above a  $C_P$  of 50% which is more than anticipated ( $C_P > 30\%$ ). The current design, however, needs confirmation by upscaling and field tests (see Chapter VI, VII and VIII). Several different rotor designs were tested in the laboratory with the focus on quantifying the rotor efficiency of different design variations. Very low solidity such as an increased TSR, less torque ripple and better self-starting behaviour were found to be beneficial. Furthermore, the blade-shaft connection (i.e., spokes) was optimised.

The latest design features a three bladed rotor with NACA4421 airfoil-shaped blades, a chord length of 80mm, a pitch angle of  $6^\circ$  and a twist of  $20^\circ$  in combination with hydrodynamically optimised NACA0012/24 airfoil shaped spokes. It performed best and self-started in many cases (see Figure 46). Due to the small scale, the laboratory rotor solidity was chosen to be 21% (i.e., 80 mm chord length) but will be reduced for upscaling and field-testing in order to achieve a higher rotational speed and a reduced torque ripple.

**Structure:** Similar to the rotor, the hydrodynamics of the structure is well understood and the design can be applied for testing in real conditions. Besides improving the overall performance of the turbine, the key feature of the structure focusses on the assembly of the entire system in an efficient and safe way. The ideal channel-width-to-rotor-diameter ratio  $\beta'$  was found to be approximately 60%. The position of the rotor should be at the centre of the constriction.

**Twin turbine assembly:** The twin turbine operates with high efficiencies in the laboratory. The hypothesis that the twin turbine setup can provide additional efficiency

in comparison to a single rotor was confirmed. The ideal distance between the rotors was found to be  $1.5D$  with both rotors rotating inwards. Neither the synchronisation nor an offset of the two rotors had a positive effect on performance. However, submergence was found to be a critical parameter with a dramatic drop in performance if the water table is level with the upper spoke or below. If the water table is much higher than anticipated, the performance drop is less significant (~6%).

Power take-off: In several laboratory experiments, the belt-drive has shown its potential for solving mechanical difficulties such as changing direction and orientation of an applied torque while ensuring a safe and continuous operation (see Figure 46). Alternatively, two individual PTOs could be used which improved the overall performance by ~5% due to less frictional losses. Further, a manually controlled low-speed three-phase AC generator was successfully employed. However, a functional power control and system for grid-feeding is needed (see Chapter V).

In conclusion, the twin turbine showed very promising performance and was found to be ready for field testing (see Chapter VI). In terms of further research, structural analysis, condition monitoring, durability and fatigue as well as operation and maintenance were identified as crucial issues that should be addressed (see Chapter IX).

In the following chapter, the hydrodynamic impact of the latest turbine design on the downstream channel flow (e.g., wake) is investigated via detailed velocity measurements using an Acoustic Doppler Velocimeter. The measurements were analysed and the wake recovery characterised in order to understand the flow regime downstream the rotor and, ultimately, be able to design an array of turbines in a channel (e.g., spacing between VATs) without compromising on available power due to turbulent/disadvantageous flow conditions.

## IV. Turbulences and wake study

This chapter is published in a similar form as a journal paper to the Journal of Renewable Energy with the title “Three-dimensionality of the wake recovery behind a vertical axis turbine”, co-authored with Dr. Pablo Ouro, Ms. Qianyu Luo and Prof. Thorsten Stoesser [129]. Some aspects of this chapter were already covered in previous chapters but it was decided to keep it close to its submitted form with the intention to present it as a self-contained chapter.

### 4.1 Introduction

The flow regime experienced by VATs depends on the operating Reynolds number attained by the rotating blades, which will determine the relevance of dynamic stall of the blades or the mixing of the turbine rotor’s wake with the ambient flow. [130] tested a high-solidity VAT in a towing tank for different operational Reynolds numbers and found that drag forces and power coefficients approximate a constant value asymptotically, i.e., independent of the Reynolds number, for  $Re_D = UD/v > 1 \cdot 10^6$  or  $Re_C > 2 \cdot 10^5$  where  $Re_D$  represents the Reynolds number based on the rotor’s diameter and  $Re_C$  based on the blade’s chord length (see Equation 1.6). The acting forces on the blades are a consequence of the flow separation on their suction side which is fully turbulent once the former flow condition threshold is achieved. Using 2D-Partial Image Velocimetry (PIV), [131] observed how flow separation on the blades varies depending on its rotational speed. Similarly, [70] used high-fidelity numerical simulations to evidence the different nature of dynamic stall vortices whose effect becomes more prominent at low TSRs.

The performance of different turbine designs is also influenced by the generation of dynamic stall vortices and their convection within the rotor’s swept perimeter which eventually interact back with the blades during the downstream half of the rotation. [132] identified from water tank experiments how such a blade-vortex interaction is characterised by leading- and trailing-edge vortices whose shedding pattern varies with the rotor’s rotational speed. [133] observed a varying wake recovery pattern at different tip speed ratios as a consequence of the vortex dynamics happening within the swept rotor area. With similar scope, [70] visualised in their large-eddy simulations that at low rotational speeds the blades undergo deep dynamic stall causing a drop in performance, whilst at high rotational speed, above peak performance, the blades lack of lift-generation capabilities to be sufficiently efficient. Therefore, an adequate balance in the interaction of the generated dynamic stall vortices with the moving blades is a key aspect in the development of efficient vertical axis turbines.

Another study investigated the three-dimensional nature of the wake behind vertical axis turbines [134] by using PIV to measure different planes throughout the turbine's wake. Their phase-averaged results indicated the mechanism responsible for the generation of tip vortices as a result of the flow moving over the blade's tip and the low-pressure area on the blade suction side. These large-scale flow structures kept coherent until a distance of two turbine rotor diameters ( $2D$ ) downstream. Further, a vertical expansion was observed due to the action of tip vortices moving towards the outside of the rotor's swept area. Thereafter, these rotor-induced energetic structures merge with the low-momentum wake which then starts to develop a vertical contraction.

Further, [135] discussed the significance of vertical momentum advection in the near-wake recovery which is reinforced by [136]'s field measurements of different vertical axis wind turbine array arrangements. In this study, it was further observed that rotor-induced turbulence aids in recovering wake momentum with wake velocity values close to the free-stream velocity at  $6D$  downstream, which suggests a closer cluster capability of VATs compared to HATs. Moreover, [134] identified a circulation-induced phenomenon known as Magnus effect in the near-to-far wake transition which was also observed in the LES of [137] being this more noticeable at higher tip speed ratios.

In another study, Large-scale coherent motion of VATs' wakes were analysed for different turbine rotors equipped with two to five blades by using spectral analysis and proper orthogonal decomposition. Three regions in a wake were observed: (i) near-wake, dominated by periodic blade vortex shedding; (ii) transitional region, where the shear-layer formed in between the rotor's low-velocity wake and ambient flow became unstable; and (iii) far-wake, dominated by bluff body-like wake oscillations. The wake characteristics appeared to vary depending on the dynamic solidity, a parameter that correlates with the rotor's geometric solidity to the tip speed ratio. Low dynamic solidity values indicated a strong ability of the free-stream flow to penetrate through the rotor while high values of this parameter caused a larger obstruction of the turbine rotor to the flow and thus enhancing bypass flows. Consequently, the larger amount of fluid flowing through the rotor the faster its wake recovers and vice versa [138].

Apart from dynamic stall as a key characteristic in the wake of vertical axis turbines, other key features in the wake of VATs were found by [134] who identified a skewed nature of the wake based on the time-averaged velocity distribution far downstream the device. [139] employed a stereo-PIV technique and observed two pairs of asymmetrical-counter-rotating vortices at the horizontal edges of the wake as a result

of a variation in cross-flow momentum. Analogously, [140] observed that the strength of this pair of vortices is directly related to the turbine rotor's rotational speed.

This chapter provides a detailed insight into the three-dimensional dynamics of the wake developed behind a three-bladed vertical axis turbine rotor. Results include first, second and third-order flow statistics throughout the wake based on velocity measurements captured by using an Acoustic Doppler Velocimeter (ADV) and obtained from 0.75D to 14D downstream of the turbine's rotor in addition to quantification of dynamic stall vortices decay in the near-wake, and velocity deficit recovery in the streamwise direction.

## 4.2 Experimental setup

### 4.2.1 Laboratory configuration

The experiments were conducted in the same recirculating hydraulic flume at Cardiff University as presented in Chapter III. The flow rate was controlled by an axial flow impeller set to a constant value of  $Q = 0.75\text{m}^3/\text{s}$  providing a flow depth of  $H = 0.65\text{m}$ . A honeycomb flow straightener was installed at the inlet of the flume in order to smooth the approaching flow.

Velocity measurements of the flow in the flume without turbine (hereinafter free-stream flow conditions) were obtained at the proposed turbine position prior to its deployment. An ADV (Nortek Vectrino, see Appendix H for details) was used to measure velocities in x, y and z directions at 336 points over the selected cross-section. The measurements had an accuracy of  $\pm 0.5\%$  and were taken at a frequency of 200Hz over a sampling period ( $t_n$ ) of 120s. Results were post-processed and filtered by removing those samples whose correlation coefficient values were inferior to 70% [141], and a signal-to-noise ratio (SNR) of  $> 15$  dB was considered. The time-averaged velocity  $U_i = (U, V, W)$  is calculated from the measured velocity field  $u_i = (u, v, w)$  as,

$$U_i = \frac{1}{t_n - t_0} \int_{t_0}^{t_n} u_i(t_n) dt \quad (4.1)$$

Reynolds decomposition was applied to calculate the root-mean-square (rms) of the velocity fluctuation  $u_i' = (u', v', w')$  resulting from subtracting to the mean velocity  $U_i$  the instantaneous velocity values  $u_i$ , i.e.,  $u_i' = U_i - u_i$ . The turbulence intensities  $\sigma_{ui} = (\sigma_u, \sigma_v, \sigma_w)$  are the root-mean-square (rms) of the velocity fluctuation  $u_i'$ , and read,

$$\sigma_{ui} = (u_i' u_i')^{0.5} \quad (4.2)$$

The turbulent kinetic energy ( $k$ ) was calculated from the normal Reynolds stresses as,

$$k = 0.5 * (u'u' + v'v' + w'w') \quad (4.3)$$

Note that from hereinafter  $u_i'$  refers to its time-average value, and all flow variables are normalised with the free-stream velocity  $U_0$  and the rotor diameter  $D$ .

#### 4.2.2 Free-stream flow conditions

The approaching flow is depicted in Figure 47 which presents vertical profiles of the mean streamwise velocity ( $U/U_0$ ) and turbulence intensities ( $\sigma_{ui}/U_0$ ) in the centreline of the flume ( $y/D = 0.0$ ) and contours of the streamwise velocity in a cross-section of the flume without turbine. The mean cross-sectional  $U$ -velocity was found to be 0.97m/s which is considered to be the free-stream or bulk velocity  $U_0$ . The bulk Reynolds ( $Re_H = U_0H/\nu$ ) and Froude ( $Fr = U_0/(gH)^{0.5}$ ) numbers under these flow conditions were  $Re_H = 6.3 \cdot 10^5$  and  $Fr = 0.38$ , respectively. Note that due to ADV measurement limitations close to the channel bed, side-walls and water surface, flow velocities were measured between  $-0.60 < z/D < 0.65$  in the vertical direction and  $-1.55 < y/D < 1.55$  in the spanwise direction.

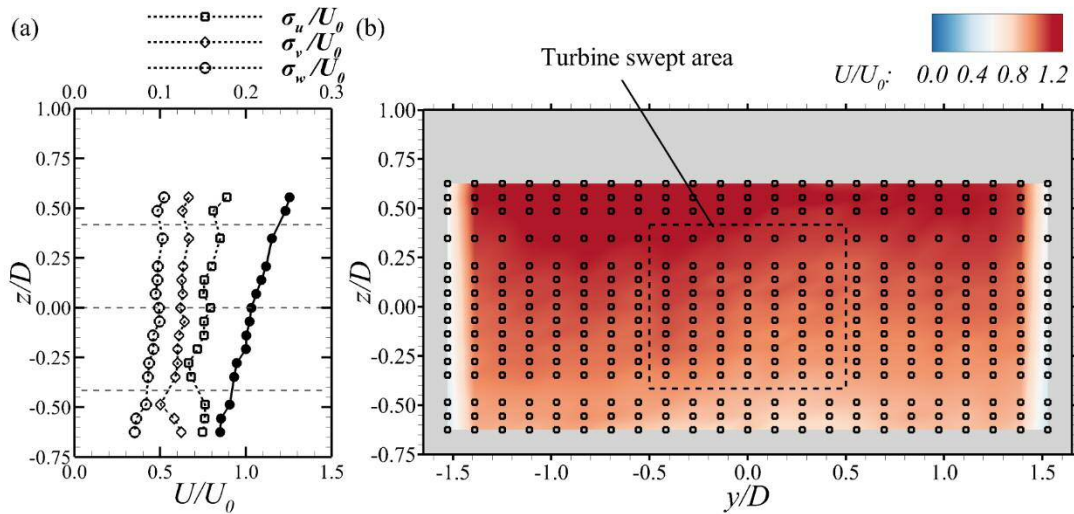


Figure 47. Data of the free-stream flow: (a) vertical profiles of mean streamwise velocity (solid line and filled symbols) and root-mean-square of velocity fluctuations (dashed lines and blank symbols); and (b) cross-section with contours of normalised time-averaged streamwise velocity

According to Figure 47a, the mean streamwise velocity fluctuation ( $\sigma_u/U_0$ ) was approximately equal to 15% at the centre of the channel whilst transversal ( $\sigma_v/U_0$ ) and vertical ( $\sigma_w/U_0$ ) turbulence intensities were 12.3% and 9.2%, respectively. The resulting anisotropic ratio  $\sigma_u : \sigma_v : \sigma_w$  is 1.0 : 0.8 : 0.6 being slightly higher than those found in other channel flows, e.g., 1.0 : 0.71 : 0.55 [142], which is most likely caused

by the high Reynolds number of the flow, the relatively narrow section of the channel and the flow asymmetry induced by the flume's impeller. Turbulence intensity values along the whole cross-section (not shown here) were fairly consistent with those found for the centreline shown in Figure 47a.

#### 4.2.3 Description of the VAT

The best performing laboratory VAT rotor (e.g., a three bladed rotor with NACA4421 airfoil shaped blades, a pitch angle of  $6^\circ$  and a twist of  $20^\circ$  in combination with hydrodynamically optimised, NACA0012/24 airfoil shaped spokes) was placed in the previously described flume at 10 m downstream of the inlet. Blades and arms were made of laser-sintered PA 2200 material. Hub, shaft and submerged bearings were made of stainless steel. The rotor diameter ( $D$ ) was 0.36 m with a height ( $H_t$ ) of 0.30 m which gave a rotor aspect ratio ( $D/H_t$ ) equal to 0.85. The blades featured a chord length ( $c$ ) of 0.08 m which resulted in a rotor solidity of  $\sigma = 21\%$ . The Reynolds number based on the diameter,  $Re_D$ , was approximately  $3.5 \cdot 10^5$  and that based on the chord length was  $Re_c = 7.8 \cdot 10^4$ . The rotor swept cross-sectional area extended between  $-0.5D < y < 0.5D$  and  $-0.4D < z < 0.45D$  occupying 14 % of the channel's cross-section.

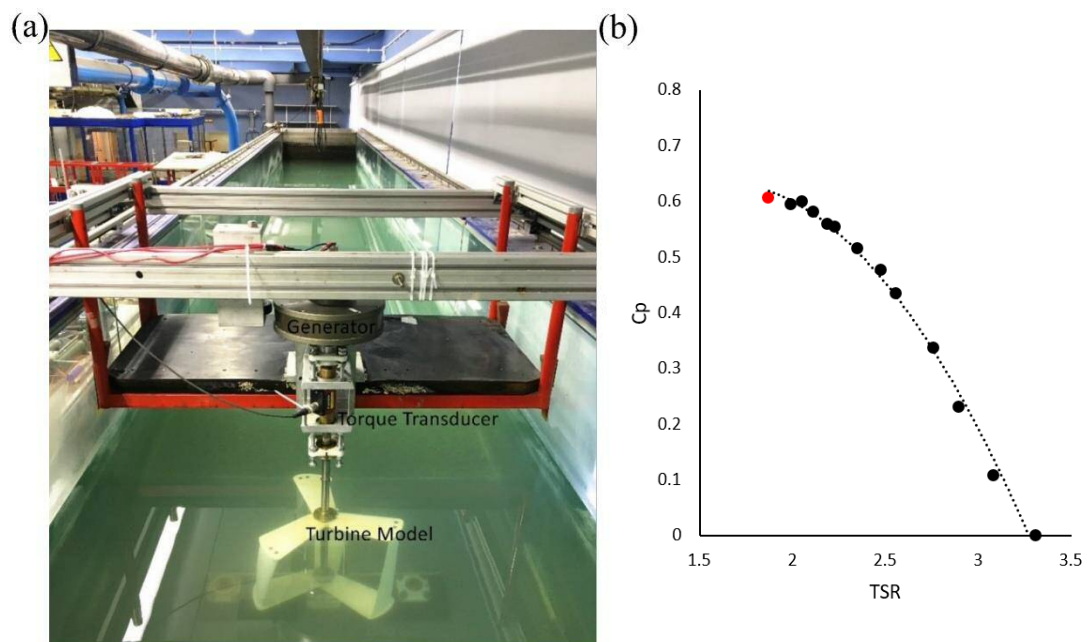


Figure 48. (a) Turbine rotor, generator and torque transducer assembled in the hydraulic flume at Cardiff University. (b)  $C_p - \lambda$  curve @  $v \approx 1.09 \text{ m/s}$  using NACA4421 blades,  $\varnothing = 360 \text{ mm}$  (test 130) with the point of maximum efficiency indicated by a red dot

The rotor was attached to a 0.02 m diameter shaft which drove a permanent magnet generator that converts the shaft's rotational motion into electrical energy as depicted in Figure 48. Adjustable resistors were used to apply a resistance to the electrical

circuit and dissipate energy in order to operate the rotor at the desired rotational speed. A combined encoder and torque sensor (Futek TRS605) was placed between the generator and rotor in order to measure rotational speed and torque. The rotor was held in place by a bearing adhered to the flume's bed and another bearing that was attached to a bridge which rested on the side-walls of the flume well above the water surface as shown in Figure 48a.

The performance of the turbine was calculated in the same fashion as described in the previous chapter and is presented in Figure 48b. The highest efficiency was attained at  $\lambda = 1.9$  with a peak  $C_p$  value of 0.56. During the wake measurements, the turbine always operated at such peak efficiency conditions, i.e., the rotational speed of the device was kept constant by monitoring and controlling the torque applied to the rotor.

### 4.3 Wake measurements results

The wake behind the operating turbine was measured at several cross-sections located downstream of the device at distances of  $0.75D$ ,  $1.0D$ ,  $1.5D$ ,  $2.0D$ ,  $2.5D$ ,  $3.0D$ ,  $4.0D$ ,  $5.0D$ ,  $7.0D$ ,  $10.0D$  until  $14.0D$ . Figure 49 shows the position of the chosen planes along the flume. Each cross-section consists of 11 vertical profiles with 10 points per profile, i.e., 110 locations, yielding a total of 1,100 measurements. Based on the data, two planes of interest are reconstructed: a horizontal plane at  $z/D = 0$ , i.e., at the rotors mid-height; and a longitudinal plane at  $y/D = 0$ .

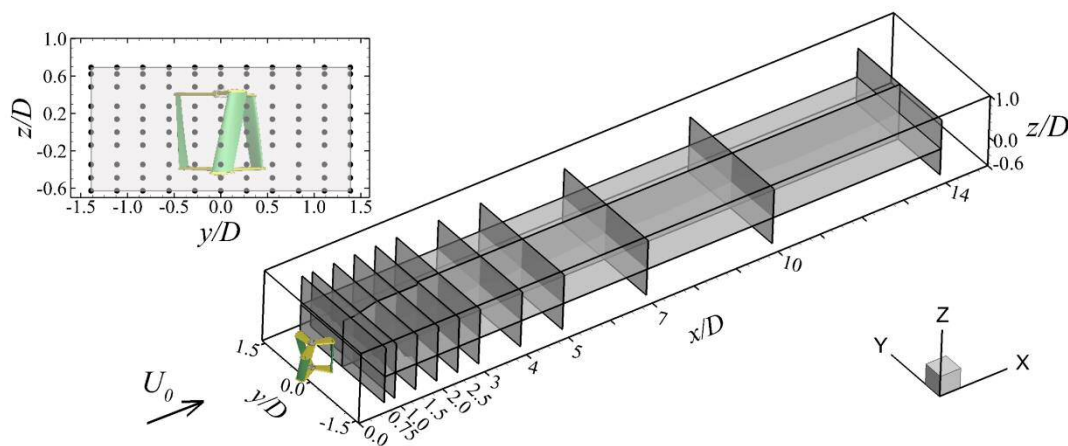


Figure 49. Location of the cross-sections behind the vertical axis turbine rotor along the hydraulic flume and including velocity measurement points in the cross-section (top left insert)

#### 4.3.1 Horizontal plane at mid-height of the turbine rotor

Figure 50 presents an overview of the downstream evolution of the wake behind the turbine with the distribution of mean streamwise velocity ( $U/U_0$ ), u-velocity fluctuation ( $\sigma_u/U_0$ ), turbulent kinetic energy ( $k/U_0^2$ ) and primary Reynolds shear stress ( $-u'v'/U_0^2$ )

along a horizontal plane at mid-height of the rotor. The wake exhibits a notable asymmetry in the horizontal plane with a low-momentum region immediately downstream of the rotor featuring velocities below  $0.25U_0$  which are generally found on the  $y/D < 0.0$  side. Considering the rotor spins counter-clockwise, this side corresponds to the half of the rotor's swept circumference in which the blades travel in the same direction as the flow, i.e., the downstroke half of one revolution [70]. During the blade's downstroke motion the flow separates at the blade's inner side and dynamic stall vortices are shed and consequently convected downstream [70,132,143]. These flow structures are responsible for the isolation of the low-momentum wake area from the unperturbed high-velocity flow.

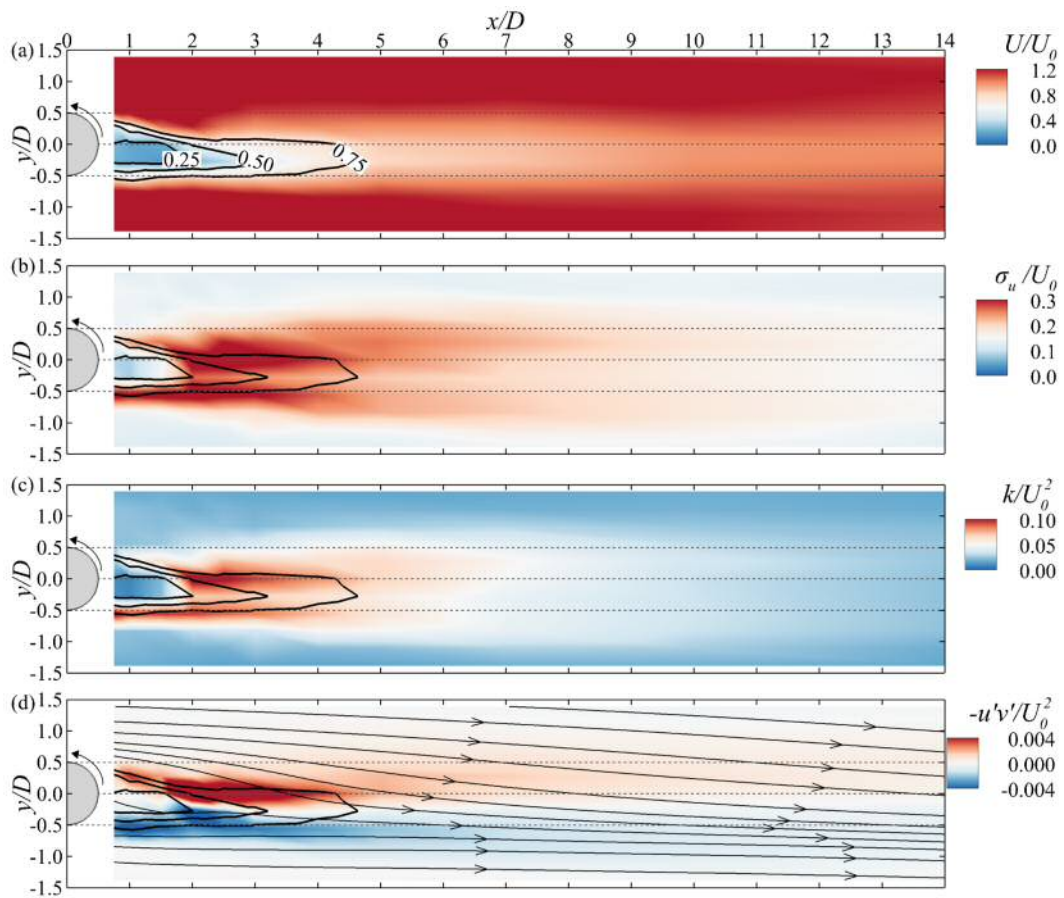


Figure 50. Horizontal plane at  $z/D = 0$  with distribution of mean (a) streamwise velocity, (b) streamwise velocity fluctuation, (c) turbulent kinetic energy, and (d) Reynolds shear stress  $-u'v'$ . Solid line indicates  $U = 0.25U_0$

In the vicinity of the rotor, contours of high  $\sigma_u$  and  $k$  (Figure 50b and c) are found along the iso-lines of  $U/U_0 = 0.50$  and  $0.75$  from behind the turbine's rotor until  $x/D = 4 - 5$  when the turbulence levels in the wake start to decay. The energetic dynamic stall vortices shed from the rotor's blades move downstream following a path that overlaps those iso-lines [70,138] and therefore they contribute significantly to such

highly-turbulent areas in the outskirts of the turbine's wake. This phenomenon generates a shear layer between the ambient flow and the low velocity area as reflected in the large values of  $-u'v'$  shown in Figure 50d.

Flow streamlines drawn in Figure 50d indicate that in the centreline of the wake the approaching flow diverts due to its interaction with the rotor and starts to converge again at  $x/D = 2$ , which eventually triggers turbulent fluctuations and enhances wake deficit recovery. However, the latter bypass flow at  $y/D > 0.5$  is stronger than on the other side of the wake, i.e., at  $y/D < 0.5$ , as on either side the relative velocity between the ambient flow and the counter-rotating blades is different. Note that at  $x/D = 0.0$ ,  $y/D = 0.5$  the blades are moving into the flow experiencing the maximum relative velocity, whereas at  $x/D = 0.0$ ,  $y/D = -0.5$  the blades move with the flow, i.e., attaining the minimum relative velocity. The rotor's rotation is responsible for the wake asymmetry in the horizontal plane.

Figure 51 presents horizontal profiles of streamwise mean velocity (a) and velocity fluctuation (b), Reynolds shear stress  $-u'v'$  (c) and streamwise velocity gradient (d) at mid rotor height and at selected locations downstream of the turbine rotor. These plots allow to quantify the asymmetry of the flow and its turbulence features. Minimum values of  $U$  are found predominantly over the  $y/D < 0$  side and the asymmetry is more visible closer to the turbine rotor. Note that the bypass flow, i.e., at  $|y/D| > 0.5$ , features streamwise velocities of approximately  $U/U_0 = 1.5$  as a consequence of the turbine rotor's flow blockage.

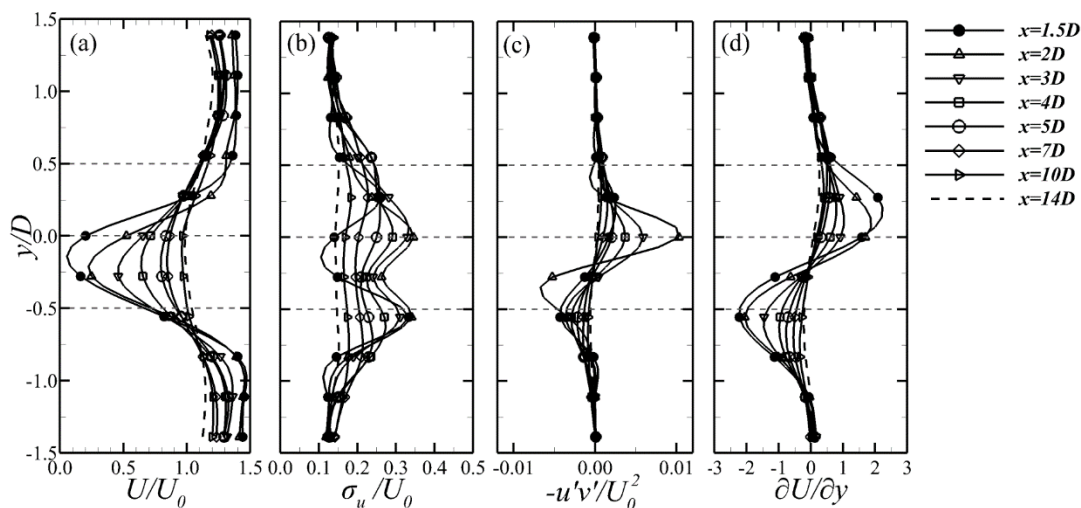


Figure 51. Horizontal profiles at rotor mid-height of (a) streamwise velocity, (b) streamwise velocity fluctuations, (c) shear stress  $-u'v'$ , and (d) horizontal gradient of mean velocity  $\partial U/\partial y$

In accordance with the distribution of  $U$  in Figure 50a, the velocity asymmetry reduces after  $x/D = 7 - 10$  with minima of  $U$  above  $0.8U_0$ .

The profiles of  $\sigma_u$  in Figure 50b exhibit two distinct distributions. In the near wake (at  $x/D = 1.5$ ) a distinct low-turbulence region is identified immediately downstream of the rotor, it coincides with low-momentum and is the result of the blades blocking the flow. The two peaks in the  $x/D = 1.5$   $\sigma_u$  profile signify the dynamic stall and/or trailing vortices, respectively, which are being flushed out of the inner turbine area. In the mid-wake, two distinct peaks located at  $y/D = 0.0$  and  $-0.5$  coinciding with regions of significant turbulence as seen in Figure 50 which are the signatures of aforementioned vortices being advected downstream. The peaks diminish further away from the turbine rotor suggesting that the vortices weaken as the wake is being filled with ambient fluid. Between  $x/D = 2$  and  $5$ , previously elevated levels of streamwise turbulence in the bypass flow reduce to those found in free-stream conditions. From  $x/D = 7$  onwards, the profiles of  $\sigma_u$  smooth-out across the channel width until a uniform value of  $\sigma_u/U_0 = 0.12$  is attained at  $x/D = 14$ .

The location of the largest momentum exchange between the turbine wake and the free-stream flow is identified by maxima and minima in the  $-u'v'$  profiles presented in Figure 51c. Positive peaks of the transversal shear stress are found at approximately  $y/D = 0$  while negative peaks are found at  $y/D = -0.5$  at most locations except for  $x/D = 2$ . Momentum exchange is a result of the streamwise velocity gradients,  $\partial U/\partial y$ , and Figure 51d presents spanwise profiles of  $\partial U/\partial y$ . As can be seen their distribution is similar to  $-u'v'$ , except in the near-wake which is dominated by flow overtopping and undergoing the turbine rotor and hence at the location of the peak of the velocity gradient at  $x/D = 1.5$  there is relatively low spanwise shear.

#### 4.3.2 Vertical longitudinal plane

The longitudinal plane along the vertical direction through the centre of the channel is presented in Figure 52 showing contours of  $U/U_0$ ,  $\sigma_u/U_0$ ,  $k/U_0^2$  and  $-u'w'/U_0^2$ . The low-momentum area extends over the entire projected rotor swept area, i.e.,  $-0.4 < z/D < 0.45$  and vanishes after  $x/D \approx 1.8$ . A certain asymmetry of the wake is observed in the vertical direction, evident from the iso-line of  $U/U_0 = 0.25$  which is skewed towards the bottom half of the channel and extending until  $x/D \approx 2$ . This is caused by the downwash of fluid due to the flow overtopping the rotor depicted from the flow streamlines in Figure 52b, which aids in recovering wake momentum mainly above  $z/D = 0$ . An upwards motion arises from the gap between the rotor's bottom tips and the channel bed which enhances the wake recovery for  $z/D < 0$  but this is less intense than the overtopping flow. The difference in wake recovery rate above and beneath the turbine rotor is similar to the behaviour of the wake behind vertical axis wind turbines operating in a boundary layer flow [139].

In the transitional-wake region, i.e.,  $2 < x/D < 5$ , the interaction between the fast-moving water above the rotor and the low-momentum wake area triggers high levels of turbulence as depicted in Figure 52b and c. Contours of the Reynolds shear stresses  $-u'w'/U_0^2$  are plotted in Figure 52d showing an axisymmetric distribution with respect to  $z/D = 0$ . It can further be seen that this shear stress converges to a fairly uniform distribution over the water depth once the far-wake region is reached, i.e.,  $x/D > 5$ .

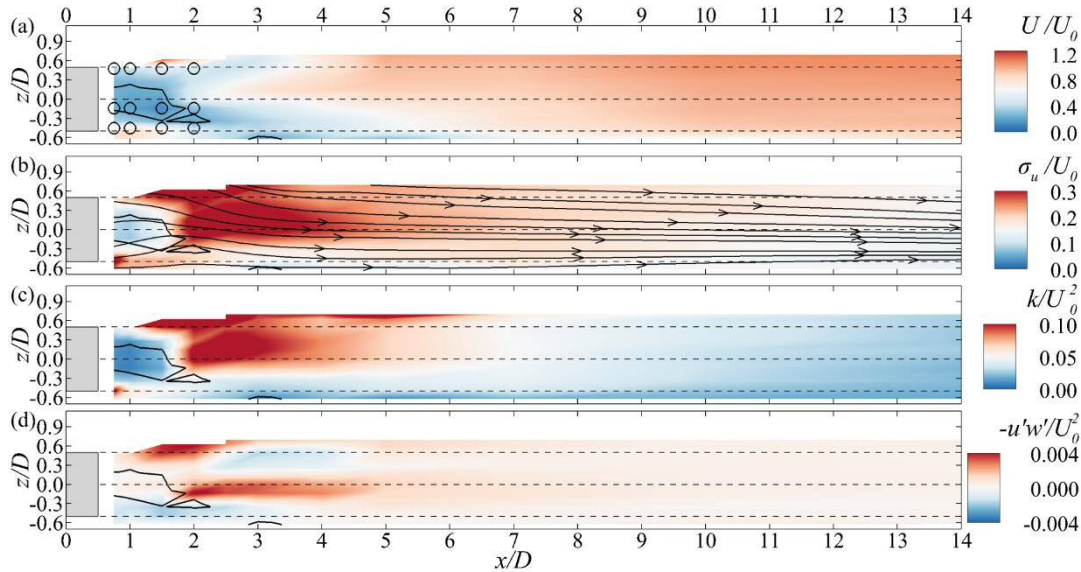


Figure 52. Vertical plane at  $y/D = 0$  with distribution of (a) streamwise velocity, (b) streamwise velocity fluctuation, (c) turbulent kinetic energy and (d) Reynolds shear stress  $-u'w'$ . Solid line indicates  $U = 0.25U_0$

Figure 53 presents profiles of  $U$ ,  $\sigma_u$ ,  $-u'w'$  and  $\partial U/\partial z$  at different cross-sections downstream of the rotor. The vertical profiles of  $U$  exhibit a clear non-uniformity in the wake recovery behind the turbine, especially in the locations closest to the turbine at  $x/D > 3$ . The different velocity magnitude between the flow overtopping the rotor and that coming from the bottom part of the channel induce an uneven vertical distribution of the streamwise velocity in the profiles along the mid-wake. Analogously to the horizontal profiles in Figure 51, the streamwise momentum is almost recovered at  $x/D = 10$  as its distribution matches that at  $x/D = 14$  being both very close to the free-stream profile from Figure 47a.

The profile at  $x/D = 1.5$  intersects the low-momentum region and the vertical profile of  $\sigma_u$  exhibits values in the range of 0.12 - 0.15, i.e., close to the free-stream turbulence intensity and hence suggests that the low-momentum area features very low turbulence intensities as well. Downstream of the near wake the mixing between the rotor's wake and the ambient flow increases and the streamwise turbulence

intensity reaches a peak of approximately 0.35 at  $x/D = 2$  and 3 in between  $-0.45 < z/D < 0.4$ . Note that near the free-surface at 1.5 and 2D downstream the turbine rotor,  $\sigma_u$  is triggered as a result of the turbulent downwash, i.e., flow coming from the top of the rotor. After  $x/D =$  there is a progressive decay of  $\sigma_u$  that features the highest values in the region  $-0.2 < z/D < 0.4$ . In the far-wake region,  $\sigma_u$  exhibits a similar value to those found in free-stream flow conditions.

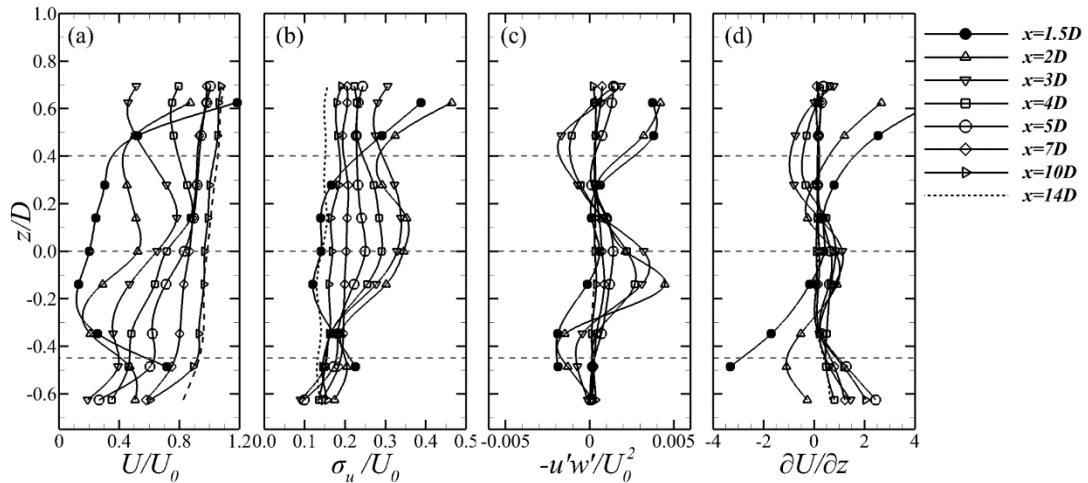


Figure 53. Vertical profiles at flume centre of (a) streamwise velocity, (b) streamwise velocity fluctuations (c) Reynolds shear stress  $-u'w'$ , and (d) vertical gradient of streamwise velocity,  $\partial U/\partial z$

The mid-wake exhibits a notably irregular distribution of  $-u'w'$  along the water depth as a result of the complex interaction between the rotor's wake with the ambient flow whilst in the far-wake the distribution of this shear stress is found to be more uniform with negligible values beyond  $x/D = 10$ . In Figure 53d the vertical gradient of mean streamwise velocity is plotted and its distribution is similar to  $-u'w'$ .

The Boussinesq approximation for isotropic turbulent flow states that Reynolds shear stresses are proportional to the velocity gradients, i.e.,  $-u'v' = (\nu_t) \partial U/\partial y$  and  $-u'w' = (\nu_t) \partial U/\partial z$  where  $\nu_t$  denotes the eddy viscosity. In the present flow such an approximation would not be valid in the near- and mid-wake regions as the profiles of shear stress and velocity gradients do not show peaks at the same location suggesting that the eddy viscosity varies significantly over the depth.

### 4.3.3 Cross-sectional planes

The three-dimensional nature of the turbine wake is further investigated in Figure 54 showing the distribution of streamwise velocity, streamwise velocity fluctuation and shear stresses in four cross-sectional planes (i.e., at  $x/D = 1, 2, 3$  and 5) normal to the flow direction.

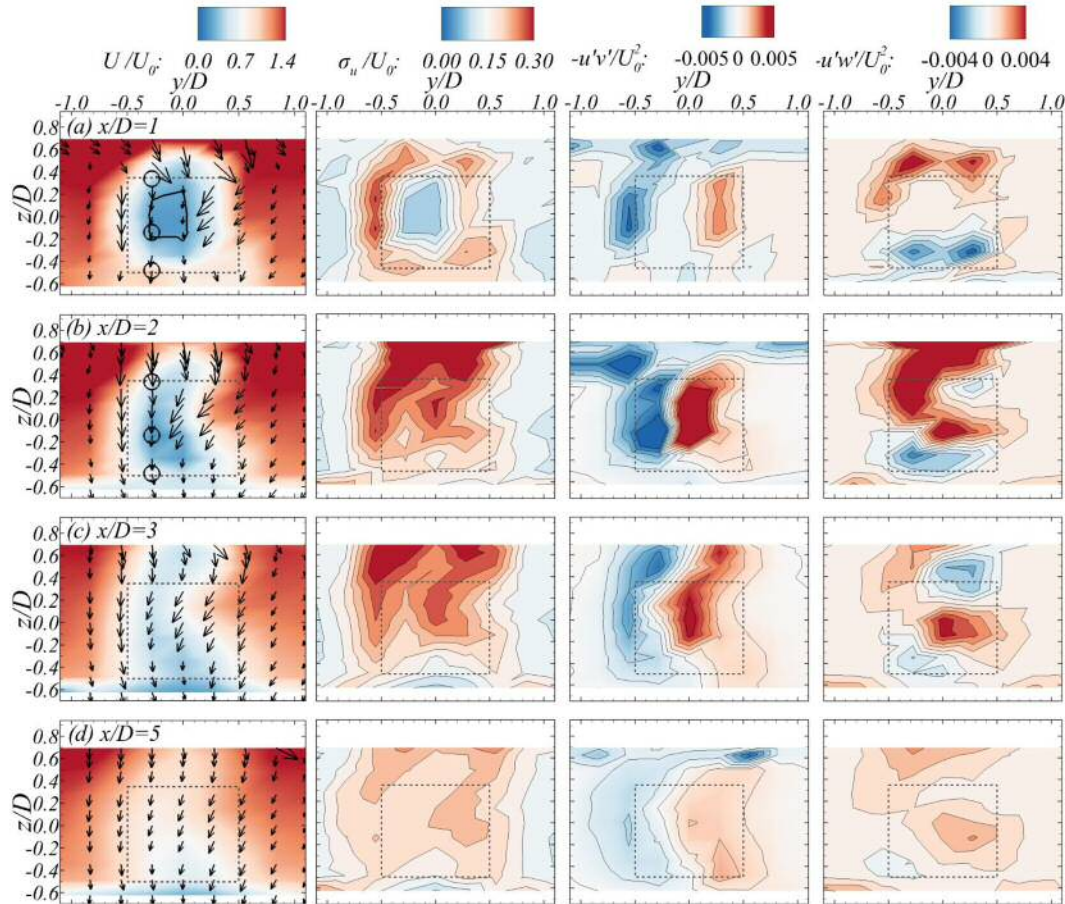


Figure 54. Distribution of normalised streamwise velocity ( $U/U_0$ ), turbulence intensity ( $\sigma_u/U_0$ ) and Reynolds shear stresses ( $-u'v'$  and  $-u'w'$ ) along four cross-sections downstream of the turbine at  $x/D = 1, 2, 3$  and  $5$ . Solid line indicates  $U = 0.25U_0$

At the section closest to the turbine ( $x/D = 1$ ), the region of  $U < 0.25U_0$  (solid lines) is predominantly found for  $y/D < 0$ . Velocity vectors illustrate that in all considered sections the ambient flow entrains into the wake region more pronouncedly for  $y/D > 0$  with large negative vertical velocities as a result of the downwash. At  $x/D = 1$ , the regions of high turbulence levels coincide with the projected rotor's swept perimeter which is in agreement with the path described by the dynamic stall vortices shown in Figure 50. The largest values of shear stresses are found along  $y/D = -0.6$  and  $0.4$  for  $-u'v'$  and  $z/D = -0.35$  and  $0.55$  for  $-u'w'$ . The peaks of  $-u'w'$  almost coincide with the projected location of the blades' tips as they are slightly shifted upwards.

At 2D downstream of the turbine, the low-momentum region expands over a larger vertical area and the velocity minima surpass values above  $0.25U_0$ . Velocity vectors evidence the inwards interaction of the bypass flow into the low-velocity area generating a C-shaped distribution of the wake. The largest values of  $\sigma_u$  are observed between the free-surface and top of the rotor as a result of the overtopping flow, and also at  $y/D \approx -0.5$  and  $0.0$  where the change from low to high streamwise velocities

is relatively fast, as depicted in Figure 51d. The highest  $-u'v'$  and  $-u'w'$  values are located within the rotor swept area as a result of the larger entrainment of high-momentum flow from the ambient flow into the low-momentum wake. At  $x/D = 3$  and 4 (the latter not shown here), a similar distribution of  $U$ ,  $\sigma_u$  and  $-u'v'$  to that at  $x/D = 2$  is found as all of these belong to the transitional-wake region in which the wake maintains a similar pattern. Further downstream at  $x/D > 5$ , the dynamics of the wake changes as the momentum is recovered and the C-shaped low-velocity region is no longer observed. The magnitudes of the Reynolds stresses are also reduced whilst their overall distribution remains similar to that found in the cross-sections at  $x/D = 2$  and 3.

#### 4.3.4 Power spectra

The transition from near-wake to transitional-wake is marked by the role of the dynamic stall vortices in the momentum recovery. The presence of these large-scale turbulent structures  $3f_b$  are identified via Power Spectral Density (PSD) of  $u$ -velocity time-series and presented in Figure 55. In the calculation of the PSDs, each signal was decomposed into 10 overlapping segments spanning 60s each and a Hann window was applied in order to obtain each of their transformations. The resulting spectra are the average of these segments.

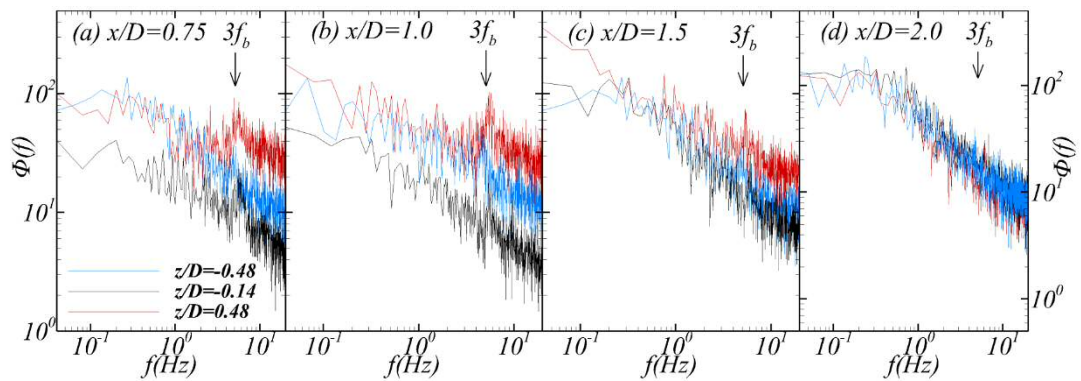


Figure 55. Power spectral density, PSD, of  $u$ -velocity obtained at three vertical locations at four locations downstream of the turbine

A total of 12 PSDs are computed from points vertically aligned with the top, centre and bottom of the wake at different locations within the near-wake as indicated in Figure 55a. At distances of  $x/D = 0.75$  and 1.0 the spectra show a clear energetic peak at a frequency of  $3f_b$ , with  $f_b$  standing for the blade passing frequency, revealing the presence of dynamic stall vortices shed by the rotor's blades. At  $x/D = 1.5$ , the energy peaks become more diffused as a result of the energetic vortices losing coherence during their convection downstream whilst interacting with the turbulent

ambient flow. In the onset of the mid-wake region at  $x/D = 2.0$ , no significant energy peaks at a frequency of  $3fb$  are discerned indicating that dynamic stall vortices are no longer coherent at this stage of the wake, which allows a larger entrainment of the bypass flow into the low-velocity area of the wake.

#### 4.3.5 Streamwise momentum recovery

The contributors to the replenishment of the momentum deficit behind the turbine as a result of its interaction with the main flow are accounted via the Reynolds-averaged Navier-Stokes (RANS) Equation 4.4 in the x-direction, which reads,

$$\frac{\partial U}{\partial x} = \frac{1}{U} \left( \underbrace{-V \frac{\partial U}{\partial y}}_I - \underbrace{W \frac{\partial U}{\partial z}}_{II} - \underbrace{\frac{\partial u'u'}{\partial x}}_{III} - \underbrace{\frac{\partial u'v'}{\partial y}}_{IV} - \underbrace{\frac{\partial u'w'}{\partial z}}_V - \underbrace{\frac{1}{\rho} \frac{\partial P}{\partial x}}_{VI} - \underbrace{\frac{\partial^2 U}{\partial x_i^2}}_{VII} \right) \quad (4.4)$$

In the present analysis, the flow is deemed stationary in its time-averaged characteristic, the streamwise derivative of the Reynolds stress  $u'u'$  (term III) is discarded due to the relatively large spacing between cross-sections, the pressure term VI is omitted as this variable was not measured using ADV, and the last term VII (representing the viscous diffusion) is also omitted due to the high turbulent nature of the flow and thus viscous effects are deemed negligible [135].

In Equation 4.4, the momentum transport terms I, II, IV and V denote y-advection, z-advection, y-turbulent transport and z-turbulent transport, respectively, and these are integrated over every measured cross-section and normalised by  $D/U_0$  as presented in Figure 56. In most of the cross-sections, y- and z- advection representing secondary flow action and are the dominant terms in replenishing momentum into the wake whilst the turbulent transport terms IV and V attain values between one to two orders of magnitudes lower for most locations.

Comparing the relative contribution between the advection terms at  $x/D = 1$ , vertical advection has a greater value over the transversal advection suggesting that, in the near wake, overtopping and underflow of the turbine rotor are mainly responsible for filling the turbine wake. This is in line with the findings of [135]. At  $x/D = 2$ , the lateral flow entrainment (i.e., y-advection) reaches a peak and is approximately three times greater than the z-advection term. In the region between  $x/D = 3 - 5$ , the momentum deficit recovers which is evidenced by a decrease in the magnitudes of spanwise advection reaching similar values to vertical advection. In the far-wake, the values of the advection terms diminish whilst the turbulent transport terms seem to increase at  $x/D = 7$  and  $x/D = 10$ .

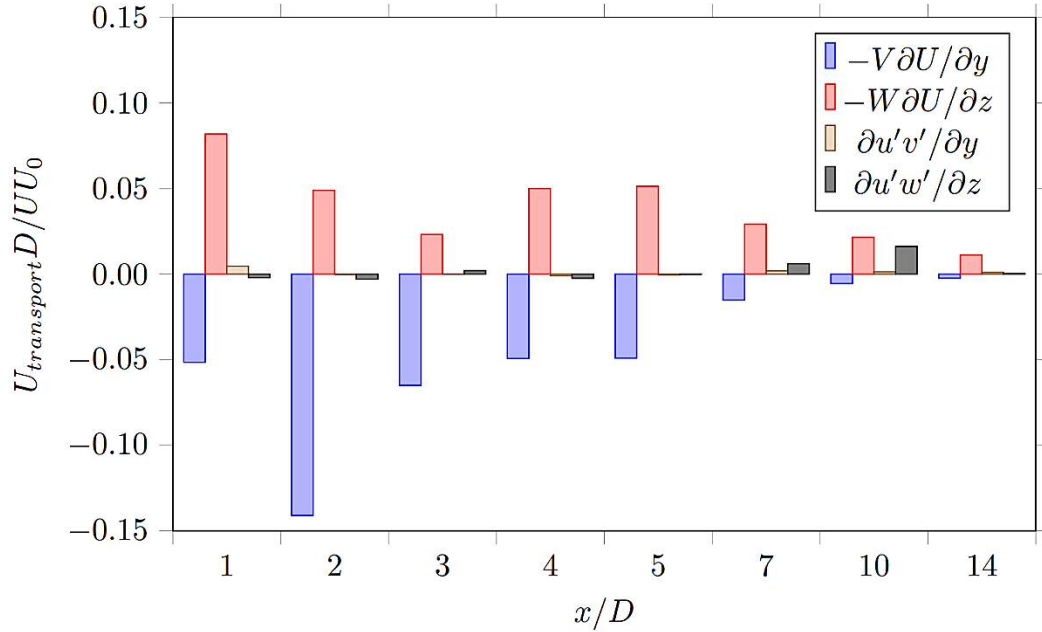


Figure 56. Cross-sectional average values of the streamwise momentum equation contributors along the locations measured

These results indicate that, close to the rotor, vertical advection is the key ingredient to recover momentum in the wake, while in the transition from near to mid-wake, spanwise advection dominates. Along the mid-wake and over the far-wake, both advection terms have a similar net contribution which results from the large mixing of the rotor-induced wake with the ambient flow.

#### 4.3.6 Skewness of the turbine rotor's wake

Skewness, or third-order-moment, indicates the asymmetry of the probability density function of velocities. [144,145] outlined the importance of flow skewness together with mean velocity and turbulence intensity to determine the available power that can be harnessed by wind turbines. Therefore, it is of particular interest to quantify the skewness in the wake downstream of the vertical axis turbine as it can provide further insights into high-order wake effects towards designing arrays of turbines. The skewness of the  $i$ -component of velocity fluctuations  $Sk_{u_i}$  is defined as:

$$Sk_{u_i} = \frac{\sum_{n=1}^N u_i'(t_n)^3}{N\sigma_{u_i}^3} \quad (4.5)$$

Figure 57 presents contours of the streamwise ( $Sk_u$ ) and spanwise ( $Sk_v$ ) skewness together with iso-lines of the streamwise velocity at four different locations in the transitional- and far-wake region, i.e.,  $x/D = 3, 4, 7$  and  $10$ . At  $x/D = 3$ , areas of large positive  $Sk_u$  correlate with low streamwise velocities and vice versa, whilst areas of

approximately zero skewness are found where the spanwise shear stress,  $-u'v'$  is at its maximum. Velocity arrows in Figure 54c indicate the inward motion of the free-stream flow into the low-momentum region at  $y/D > 0$  resulting in negative values of  $Sk_v$ . The distribution of the skewness of  $u$ - and  $v$ -velocities at  $x/D = 4$  is similar to those observed at  $x/D = 3$  although  $Sk_v$  features larger values at the latter location due to a more pronounced interaction between the rotor's wake and the free-stream flow. The pattern of  $Sk_u$  and  $Sk_v$  at  $x/D = 7$  and  $10$  is comparable, albeit with smaller values to those found at  $x/D = 3$  or  $x/D = 4$ , showing that rotor-induced effects in the flow field remain present until  $10D$  downstream of the device. Skewness contours at  $14D$  (not presented) show a similar distribution to those found in free-stream conditions.

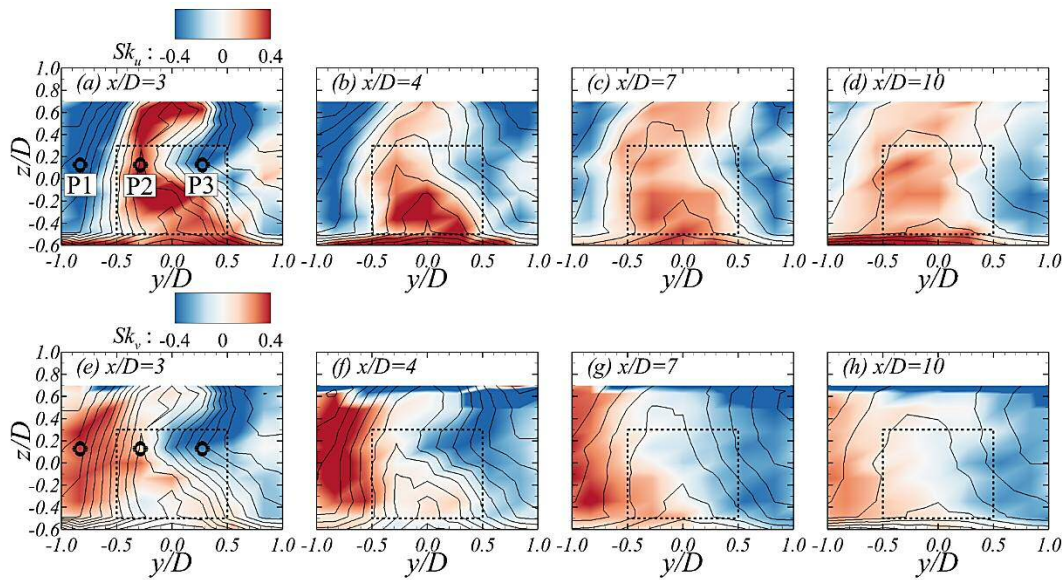


Figure 57. Contours of (a-d)  $Sk_u$  and (e-h)  $Sk_v$  at different cross-sections behind the turbine

The velocity fluctuations at  $x/D = 3$  are further analysed at three selected locations P1, P2 and P3 (indicated in Figure 57a and e) which belong to regions with distinct velocity skewness. Probability Density Functions (PDFs) of  $u'$  and  $v'$  at these locations are shown in Figure 58a to c. The PDFs at P1 indicate a reversed skewed distribution of  $u'$  compared to  $v'$  being the median of  $u'$  positive while that of  $v'$  negative, albeit both of similar magnitude. The PDF of  $u'$  features a longer tail along the negative values until  $u'/\sigma_u < -4$  whilst, in the positive region of  $Sk_u$ , it reaches almost zero values for  $u'/\sigma_u > 2$ . Such a distribution indicates that, on the negative side, there are fewer turbulent events but these have a larger turbulence intensity than events triggering positive  $u'$  which happen more frequently and with lower intensity. At the centre of the wake, i.e., at P2, both PDFs exhibit an almost Gaussian distribution. On the other side of the wake, at P3, the PDFs of  $u'$  and  $v'$  are biased to the positive side

with a similar positive median which is again in good agreement with the contours of skewness (Figure 57a and e) as these are both of negative and similar magnitude at this point.

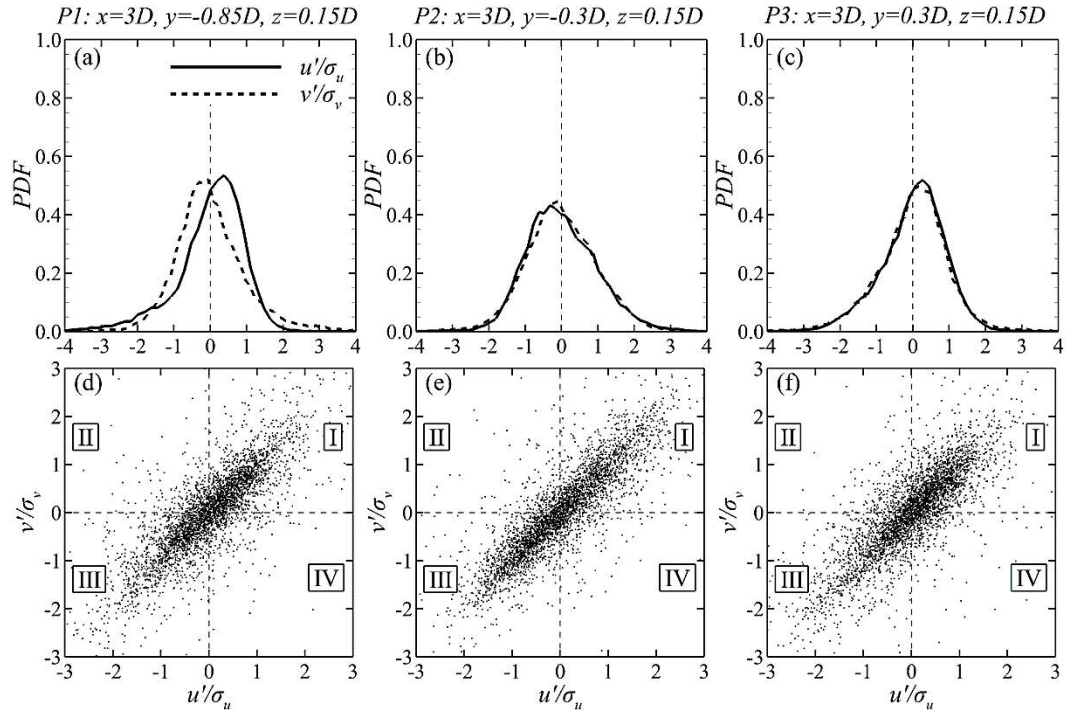


Figure 58. Probability density functions (top row) and quadrant analysis (bottom row) of velocity fluctuations at P1, P2 and P3

These observations on the asymmetric distribution of velocity fluctuations are complemented with Figure 58d to f which plot normalised values of velocity fluctuations in streamwise and spanwise directions. The quadrant analysis at the three reference points show that the majority of the velocity fluctuation values reside within the quadrants I, i.e.,  $u' > 0, v' > 0$ , and III, i.e.,  $u' < 0, v' < 0$ . In the centre of the wake (P2) the symmetry in both PDFs agree with the quadrant analysis the centre of mass of which is located at the origin of coordinates. The predominant distribution of velocity fluctuations over quadrants I and III suggests a predominance of outward and inward interactions and reflects the anisotropic nature of turbulence in the VAT's wake.

#### 4.3.7 Wake characteristics and recovery

The recovery of the flow along the channel centreline is presented in Figure 59, including three components of time-averaged velocity ( $U_i$ ) and velocity fluctuation ( $\sigma_{ui}$ ), the velocity deficit in the streamwise direction ( $\Delta U = (U - U_0)$ ) and the three Reynolds shear stresses  $-u'v'$ ,  $-u'w'$  and  $-v'w'$ .

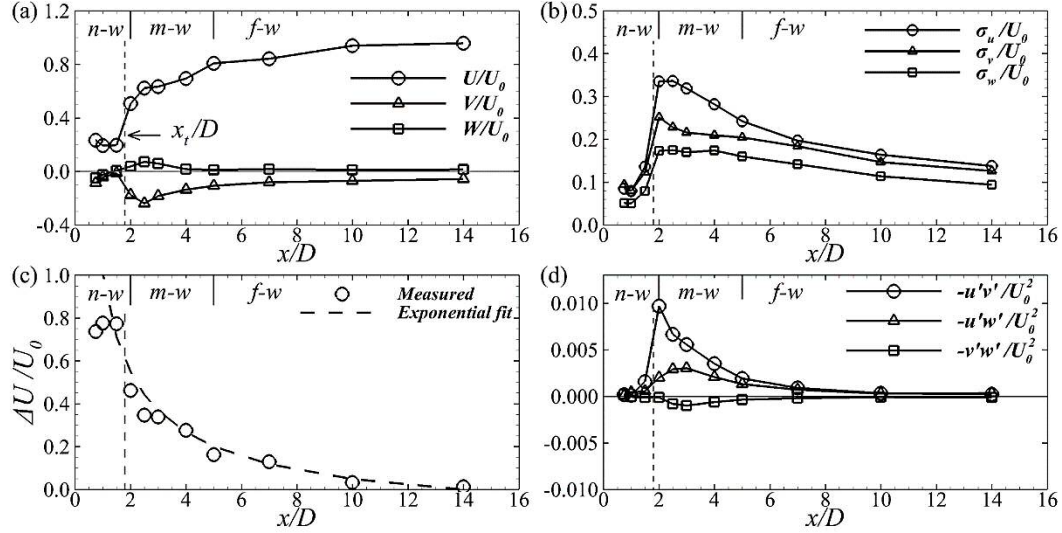


Figure 59. Distribution along the wake centreline of (a) normalised time-averaged velocity components, (b) turbulence intensities, (c) measured velocity deficit and exponential fit, and (d) Reynolds shear stresses. *n-w*, *m-w* and *f-w* denote near-, mid- and far-wake, respectively

Figure 59 depicts that the lowest streamwise velocities are found in the near-wake (*n-w*) with the minimum velocity  $U_{\min}$  which approximately equals  $0.2U_0$  (which equates to a velocity deficit of  $\Delta U/U_0 = 0.8$ ) located in the transition from near- to mid-wake (*m-w*) at about  $2D$  downstream of the rotor's axis. Based on measurements of the wake behind multiple VATs, [138] proposed that the location of the near-wake to mid-wake transition ( $x_t$ ) can be approximated by

$$x_t/D = 4.78 - 4.93\sigma_D \quad (4.6)$$

where  $\sigma_D$  is the dynamic solidity, a parameter that links the design solidity of the turbine rotor with its actual TSR  $\lambda$ , and is calculated as,

$$\sigma_D = 1 - \frac{1}{2\pi\sigma\lambda} \quad (4.7)$$

For the current study,  $\sigma_D$  equals 0.60 and, applying Equation 4.6, the value of  $x_t$  is equal to  $1.82D$  which matches with the present observations. Considering that the Reynolds number of this flow is almost one order of magnitude above that of [138]'s experiments, Equation 4.6 is considered a fair estimation tool for the transition from near- to mid-wake for VATs over a range of Reynolds numbers.

Similarly, second order statistics reach their minima in the near-wake region as shown in Figure 59b and d. In the onset of the mid-wake, the entrainment of external turbulent flow into the wake increases momentum and triggers turbulence. Thus, velocity fluctuations attain their maxima. In other words, a fast transition from a quasi-steady region close to the rotor (*n-w*) to a stage of fast-rate momentum recovery and

high-turbulence levels (m-w) was observed. Transversal and vertical velocities feature their largest values in the mid-wake reaching a maximum of  $V \approx -0.25U_0$  and  $W \approx 0.10U_0$ .

A more subtle transition of flow quantities is observed from mid- to far-wake. Here, the streamwise velocity features a value of  $U = 0.8U_0$  and achieves a magnitude close to the free-stream velocity at  $x/D = 10$ . Vertical and transversal velocities as well as Reynolds stresses exhibit a progressive decay along the far-wake, reaching their minima at  $x/D = 14$  and at  $x/D = 10$  for the shear stresses.

In spite of the complexity of the wake recovery pattern, the normalised streamwise velocity deficit ( $\Delta U/U_0$ ) along the wake centreline is in agreement with the following distribution:

$$\Delta U/U_0 = a \left( \frac{x}{D} \right)^{-b} - U_{\min} \quad (4.8)$$

According to [138] who proposed such exponential decay of the velocity deficit for VATs,  $a$  and  $b$  are 1.168 and 0.684, respectively. Hence, Equation 4.8 allows to estimate the wake deficit recovery by measuring  $U_{\min}$  which was found in the near-wake. The velocity deficit attains its maximum value before the transition point  $x_t$  (see Figure 59c). Beyond this location a good match between the measured velocity deficit and the exponential fit was observed.

#### 4.4 Summary

The wake generated behind a VAT rotor operating at its peak efficiency has been characterised based on experiments carried out in Cardiff University's hydraulics laboratory. The three-dimensional nature of the wake was captured by using an ADV, analysed and characterised. The wake can be divided into three distinct regions:

- (i) a near-wake region featuring a low-momentum area just downstream of the turbine rotor in which dynamic stall vortices play a key role and limit the entrainment of ambient flow into the low-velocity region;
- (ii) a transitional-wake (or mid-wake) region, extending 2 to 5 rotor diameters ( $D$ ) downstream of the turbine rotor that is characterised by a fast rate of momentum recovery, high intensity of turbulence and, in addition, a C-shaped distribution of the low velocities due to the inward motion of the ambient flow entraining into the wake generating an asymmetric distribution of the velocity field;

(iii) and a far-wake region that begins at approximately 5D downstream of the rotor with an almost full recovery of the momentum deficit as streamwise velocities reach values above 0.8 times the bulk velocity, whilst high-order effects, such as elevated levels of flow skewness in comparison to those in free-stream conditions, persist until a distance of 14D downstream of the turbine location.

The contours of flow skewness and the probability distribution function at selected locations evidenced the effect of the rotating rotor in producing an asymmetric wake in terms of flow velocities and turbulence. The quadrant analysis of the streamwise and spanwise velocity fluctuations suggested strong inward and outward interactions, again the result of flow asymmetry. The integration of the streamwise Reynolds-averaged momentum Equation quantified that transversal and vertical advection terms are main contributors to momentum replenishment. In the near-wake, vertical advection is the most relevant due to significant flow overtopping and undergoing the rotor while spanwise advection is the main contributor to momentum replenishment in the transitional wake. Despite the complex mechanisms involved in the wake recovery, the velocity deficit recovery can be approximated with reasonable accuracy with an empirical exponential distribution.

In conclusion, the study of the wake of the latest VAT design showed that the flow disturbance caused by the rotational motion of the rotor can be traced until 14D downstream which implies that an array of VATs should be designed accordingly. The flow in near- and mid-wake was found to be highly turbulent and may not be suitable for placing the next VAT due to fluctuations of momentum which would increase the stresses in the turbine components and ultimately reduce its lifetime as well as its performance. The far-wake region appears more suitable for operating the VAT. However, this aspect was not part of this study and should be researched in more depth. Furthermore, the wake of the twin rotors should be investigated in order to learn whether it recovers in a similar fashion (see Chapter IX).

The turbine is designed to generate electricity and after investigating the hydrodynamic behaviour of the VAT and confirming its capability of harnessing mechanical energy from the flow of water this energy somehow needs to be converted into electrical power. In the following chapter, the typical electrical components of a VAT are presented and put into context of this study.

## V. Electrical components

This chapter summarises the research undertaken on electrical components of the VAT. Several PTO tests with three different generators (LE300, LE450 and DVE200, specifications see Appendix H) were undertaken, achieving generator efficiencies of up to 70, 75 and 85% respectively and a DC battery charging device was designed and manufactured. Further, in a collaboration with the electrical engineering department of the School of Engineering at Cardiff University, a MPPT controller was designed, built, tested and a journal paper published by the Journal of IET Renewable Power Generation with the title “Maximum Power Extraction from a Hydrokinetic Energy Conversion System”, co-authored with Dr Marios Michas, Dr Carlos Ernesto Ugalde-Loo, Dr Wenlong Ming and Prof Nick Jenkins [146].

The aim of this chapter is to highlight the importance of an appropriate electrical design and to describe the important design parameters of a stand-alone power take-off system. Firstly, a decision making process introduces the technical challenges followed by a description of the state of the art of the tested turbine at laboratory stage and gives an outlook on further project steps such as field testing and application stage as depicted in Figure 60.

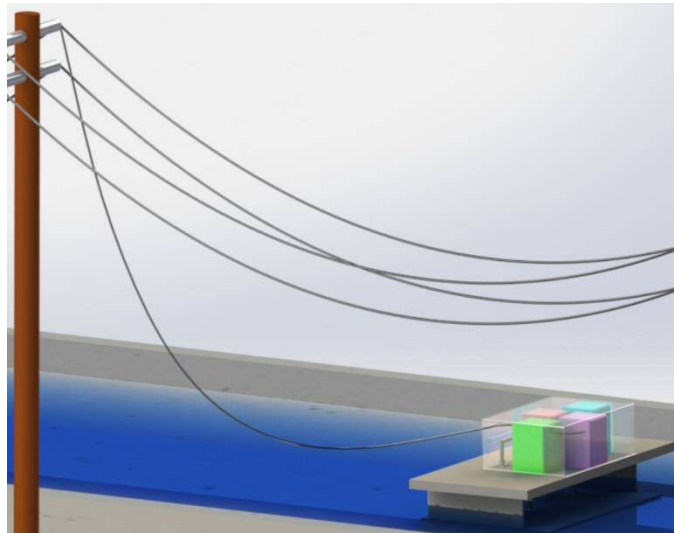


Figure 60. CAD drawing of 10kW full scale VAT concept

Although well understood and established since many decades, the generation, control, storage and distribution of electricity is a complex topic. Several textbooks and guidelines were used to tailor possible solutions and benefit from studies and experience gained elsewhere. [23] gives insight into the implementation of hydropower in developing countries with very limited financial and equipment sources. [25,147–150] were used as further reference about specifications such as

voltage and frequency, different generator types, power control and power electronics as well as safety and durability.

### 5.1 Decision making process for electrical components

The flow chart in Figure 61 shows a possible decision making process adopted for designing the electrical components for the VAT described in Chapter IV.

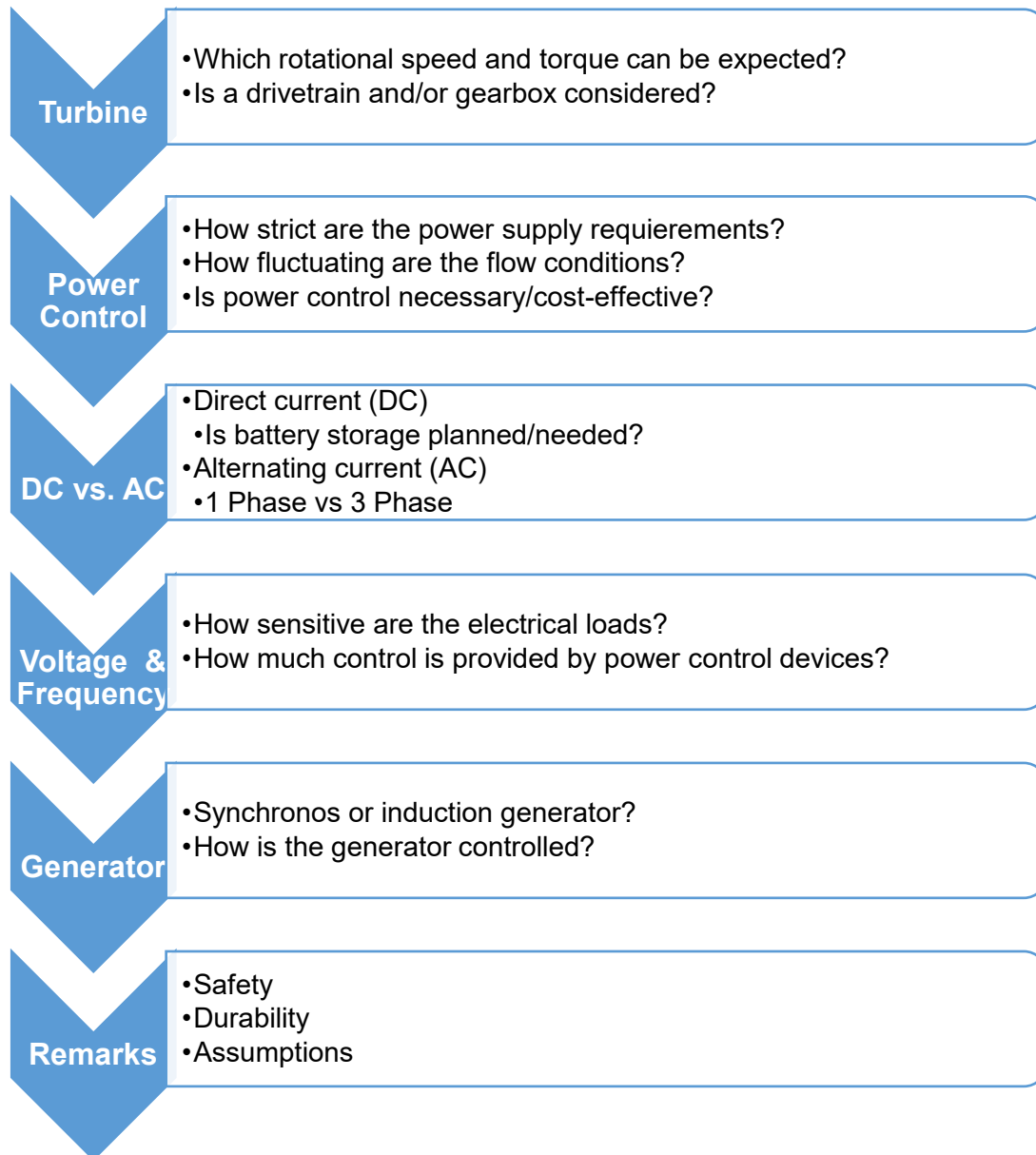


Figure 61. Decision making process for designing the electrical components of a VAT

#### 5.1.1 Turbine

As a first step, a suitable turbine for a given hydrodynamic situation must be selected. In this case, a low head environment in the form of man-made channels is considered and a freestream VAT as described in Chapter III was selected.

Due to the given circumstances in man-made channels such as fresh water supply channels or waste water treatment plant effluents, discharges may vary and flow velocities are relatively low since these flows are usually gravitationally driven and depend on demand. It is further assumed that existing structures and processes should remain unaffected. The described twin-rotor turbine system is designed to harness the kinetic energy in the flow without any significant changes to the channel and its operation by translating the kinetic energy of the fluid into mechanical torque at the rotor shaft. It includes a PTO system that converts the mechanical torque into power. The generated power can either be used or stored on site or fed into the grid. However, all factors and features listed have an impact on the electrical design of the PTO system which will be described in the following subsections.

### 5.1.2 Power control

All turbines, regardless of type, shape or size, are designed by considering certain parameters such as flow-velocity, discharge, electrical demand, etc. In order to ensure an efficient turbine operation, a power control may be required. This may be necessary if the loads (mechanical or electrical demand) change or if the flow conditions vary.

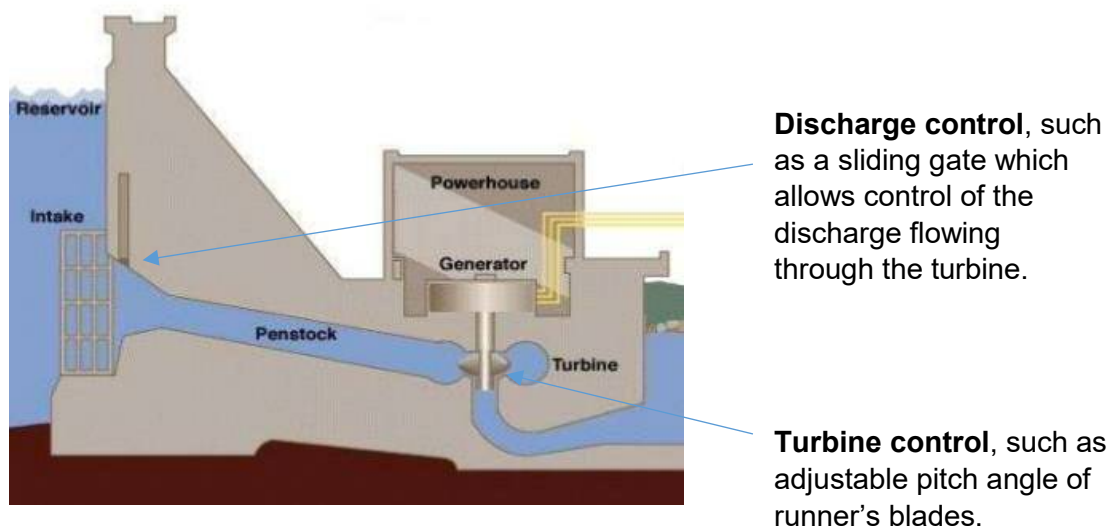


Figure 62. Exemplary hydropower plant with power control [151]

As depicted in Figure 62, a power control device changes the behaviour of the turbine and/or the flow (such as a pitch control mechanism of the blades or a discharge control of the inflow) with respect to the mechanical or electrical demand and peak performance of the turbine. These devices are costly and cause additional maintenance.

(Hydro) power control is not considered for the given design since the investment costs are not seen to be proportional to possible performance benefits. Therefore, fluctuating (electrical) power output has to be controlled with little drawbacks in terms of performance but significant cost savings on investment and operation.

### 5.1.3 Direct Current vs Alternating Current

Electricity or the flow of electrical charge can be differentiated between AC (alternating current) which changes direction periodically and DC (direct current) which flows constantly in one direction. Due to advantages in generation and transmission, AC is worldwide the predominant approach. Therefore, electrical AC appliances are globally available and cost-effective. Off-grid and small-scale solutions, however, are potentially in favour of a DC system because cost-effective energy storage is based on batteries which operate only on DC and matching electrical appliances are available (such as automotive electronical components).

#### 5.1.3.1 DC (Battery charging)

In technical terms, there is no particular reason which would make either DC or AC preferable. The decision is predominantly economically driven and depends on several aspects. DC is preferable if no grid integration is planned (e.g., at field testing stage) and batteries are charged. The electrical grid operates in AC and an inversion from DC to AC is costly, both, in terms of investment and energy losses.

In conclusion, a DC power generation scheme is preferable for research and demonstrator purposes due to its simplicity, autarky and the fact that electricity is not mainly produced for sale (see Figure 63). If knowledge gain about AC generators on demonstrator stage is crucial, the electricity could still be produced by using an AC generator and converted into DC by using a rectifier. Converting from AC to DC is much simpler and cheaper as the other way around.



Figure 63. Simplified demonstrator (DC) power generation process

### 5.1.3.2 AC (1 Phase vs 3 Phase)

Due to advantages in production, transmission and distribution, AC electricity networks are most common in any part of the world. It is therefore sensible to generate AC power in the first place if a grid connection is anticipated (see Figure 64).

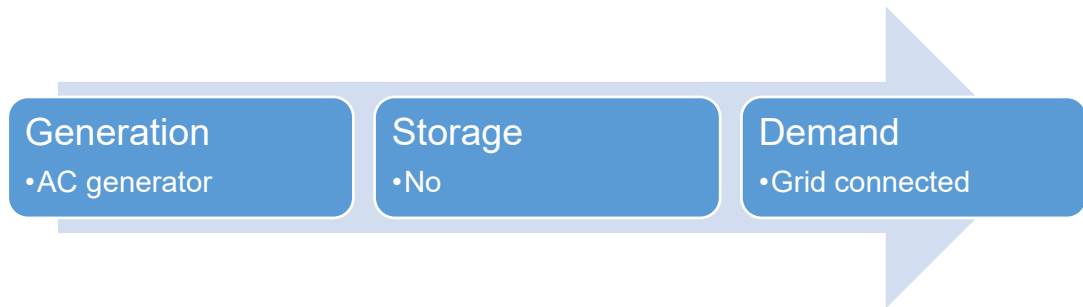


Figure 64. Simplified commercial (AC) power generation process

1 Phase AC generators have a single coil, a power and a neutral line, similar to DC generators whereas 3 Phase AC generators have three coils, three power lines and a common neutral line (see following Generator section for further details). The main difference is that the voltage is distributed evenly between the three lines (or phases) which reduces the load on the individual phase and, consequentially, reduces the wires diameter. For example, in a 5kW 1Phase generator, all components need to sustain 5kW whereas, in a 5kW 3Phase generator, the individual coils and wires need to sustain approximately a third of 5kW. Costs might be again the decision criterion since both techniques are commonly used. [23] suggests that for smaller units up to 10 kW, a 1 Phase generator is likely to be more cost effective than a 3 Phase generator. However, an AC power generation should be considered if grid connection is planned. Standalone systems are in favour of DC schemes. Nonetheless, power generated in AC can be easily converted into DC by using a rectifier.

### 5.1.4 Voltage and frequency

The electrical power output of a turbine is usually quantified in Watts. Further important design parameters of the PTO are voltage (i.e., Volts, difference in electrical potential) and frequency (or utility frequency in Hertz (Hz), oscillations of current flow direction per second, see Figure 65) which depend on the electrical circuit the generator is connected to.

For DC generators and circuits, frequency is not a criterion since the current travels in only one direction. For AC systems, the electrical load has a specific frequency, for example 60Hz in the US, which means the current oscillates 60 times per second. Loads which are supplied with a frequency other than specified may be disturbed in

operation or even damaged such as overheating. It is therefore important to ensure that the generator runs synchrony with the system's frequency.

The generator's frequency is driven by the amount of poles and the rotational speed. A two pole generator, for example, has one cycle (oscillation or changes in directions) per revolution. In order to produce power with 60Hz, a rotational speed of 60 revolutions per second (rps) or 3600 revolutions per minute (rpm) is needed. For a four pole generator with two cycles per revolution, it would be 1800 rpm, six poles and three cycles rotates at 1200 rpm, eight poles and four cycles rotates at 900 rpm and so forth. Additional poles have an impact on weight and price of the generator which often is the reason for implementing a gearbox in the PTO if the turbine cannot provide a rotational speed according to the generator specifications.

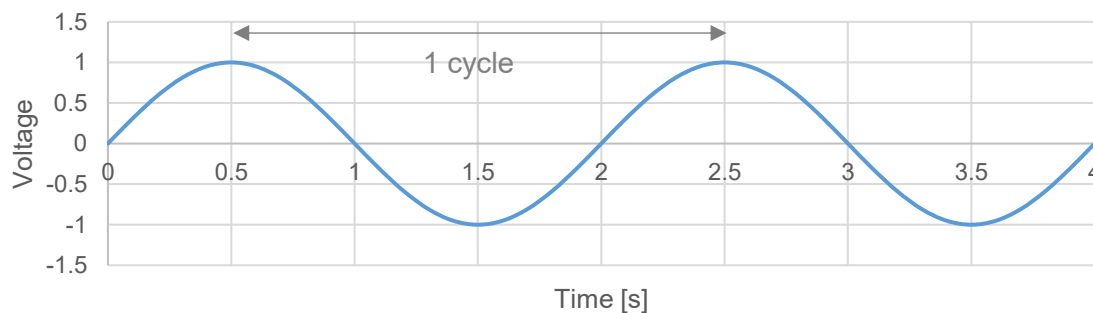


Figure 65. Schematic of AC voltage with 0.5Hz and its oscillating behaviour over time

Another important design parameter is the electrical voltage which is mainly driven by rotational speed, torque and generator size (i.e., size/amount of windings, temperature, etc.). Loads which are supplied with a voltage other than specified may be disturbed or damaged such as overheating. The synchronisation of the potentially fluctuating generator output and the specific load can be controlled in several ways. Automatic voltage regulators, electronic load and induction generator controllers are just some of them.

### 5.1.5 Generator

The conversion of mechanical power into electricity is accomplished by an electrical generator. Careful generator design/choice is therefore as critical as the design of the other components of a hydro turbine. Even though generators are well understood and easily available with different specifications, the right product must be chosen in order to match both the customer needs and the turbine characteristics.

Important design parameters are:

- Flow characteristics (power input)
- Stand alone or grid connected (power output)
- Costs and durability

Several different types of generators are available. For the purpose of this chapter, the most common types, AC synchronous and asynchronous (induction) generators, were chosen in order to highlight the main differences and explain the functionality exemplarily.

#### 5.1.5.1 Synchronous generators (permanent magnet generators)

Synchronous generators (SG) are either excited by current carrying windings (not considered here) or permanently excited by magnets (see Figure 66) which make an electrical excitation redundant and the generator design and operation simple. Due to high costs of magnetic materials and the correlation between magnet size and generator power, SG are not cost effective at a bigger scale.

SGs provide AC current either as 1Phase if equipped with one set of magnets and coils (circuits) or as 3Phases with three circuits. In the context of micro-hydropower, the 3Phase SG are commonly used. Here, three coils are assembled in a so called star-arrangement as shown in Figures 66 and 67.

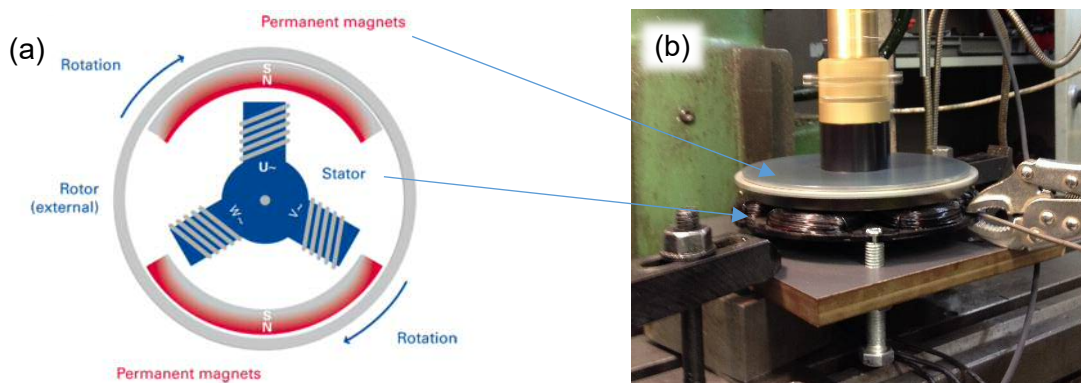


Figure 66. a) Schematic of 3-phase synchronous generator [152]; b) photograph of 3-phase synchronous generator LE 450 with fixed windings

The coils (or windings) have a common neutral and individual power lines or phases. If the windings are fixed in position as depicted in Figure 66, just the magnets, which are connected to the turbine shaft, have to rotate. This makes brushes or slip rings redundant and the generator's design fairly simple. As the windings in the star-arrangement have an offset of 120 degrees, so does the voltage output of the 3Phases (see Figure 67).

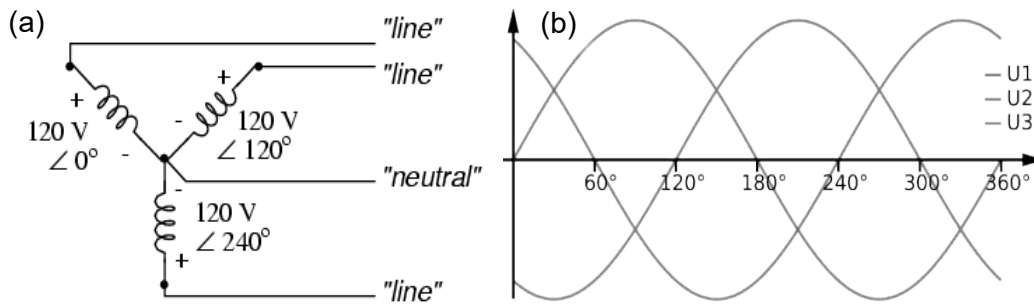


Figure 67. a) Schematic of generator windings and wiring; b) Sinusoidal voltage output versus time of a 3-Phase generator [153]

#### 5.1.5.2 Asynchronous generators (induction motors)

Induction motors are the most common type of electrical machinery and can be used as generators without any modification, they are easily available and cost-effective. Induction or asynchronous generators (AG) stand out due to their reliability and straightforward grid integration.

In contrast to SGs, an AG needs a power supply in order to excite a magnetic field. This criterion is given in case of grid integration but more difficult in an autarkic system. Assuming the AG is connected to a power supply, the rotor shaft will rotate. The movement is caused by a rotating magnetic field of the stator at synchronous speed which drags the ferromagnetic rotor at a slightly lower speed (see Figure 68). The difference between synchronous and rotor speed is called slip. If the rotor shaft's rotational speed is larger than the synchronous speed of the stator's magnetic field, electricity is produced and fed into the grid.

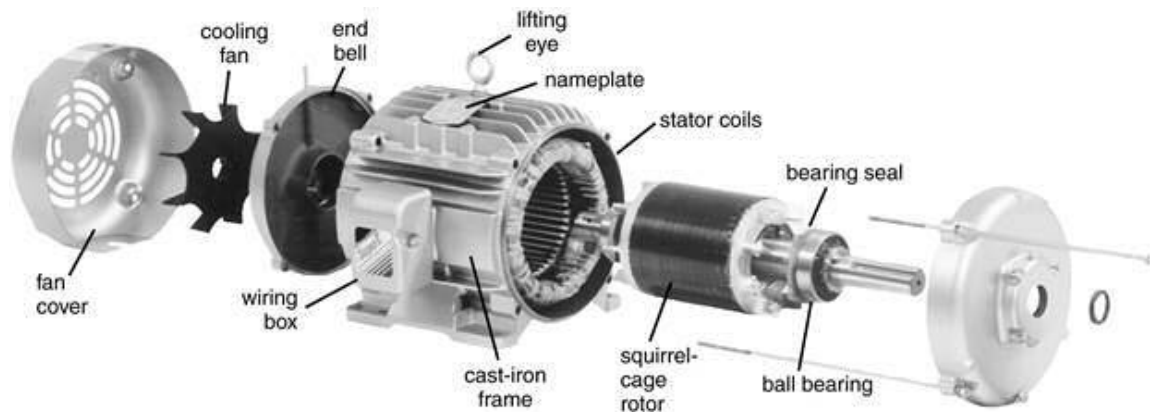


Figure 68. Exploded view of an asynchronous generator [153]

Noteworthy, if self-starting of the hydro turbine is of concern, an induction generator can be used to overcome the initial torque and kick-start the rotors. A permanent magnet SG on laboratory and field testing scale is to be preferred due to simple operation, design and autarkic operation. Induction generators can be considered in the long run due to their advantages in grid connectivity, reliability, cost-effectiveness

and the possibility to use it as a starter-motor if needed. In any case, power electronics are crucial and a conversion or adaptation from the produced power to the load specifications is necessary.

### 5.1.6 Remarks

Further, important aspects in relation to generators concern their safety and durability. Both are not directly linked to the technical specifications but need to be considered in the design process and the life cycle analysis.

#### 5.1.6.1 Safety

Electricity, even with small voltages, is dangerous and can be harmful if exposed to living creatures. A safe and state-of-the-art design is therefore crucial and must be addressed by an expert in the field. Some important aspects are:

- Insulation and water protection
- Thermal control
- Impact of turbine over-speed

#### 5.1.6.2 Durability

The aim of the twin turbine is a continuous production of electricity for many years. This has an impact on the generator design since some machinery is not designed for permanent use, wear and tear as well as overheating may become an issue. Further, the power take-off is thought to be underneath a weather cover which may heat up and needs cooling.

#### 5.1.6.3 Assumptions

This chapter summarises the key aspects of power generation with a choice of suitable products and solutions chosen to the best of my knowledge. Several assumptions were made in order to predict efficiency and cost-effectiveness. For any potential site, an individual electrical design must be developed which includes power control components such as voltage regulators and (decoupled) source converters. In the following, the electrical components for laboratory, field testing and application are suggested.

## 5.2 State of the art

The main aim of this study is to test and analyse the hydrodynamic behaviour of the rotors. However, an electrical circuit for laboratory purposes was needed in order to apply a realistic load to the rotors and to gain knowledge about the electrical components in general. Further, electrical designs for field testing and application stage are suggested.

### 5.2.1 Laboratory testing (small scale)

Three 3Phase AC permanent magnet generators were used. These were a low rpm, off-the-shelf generator (DVE200) and two custom made high rpm generators (LE 300 & LE 450) with 300 and 450 Watts, respectively.

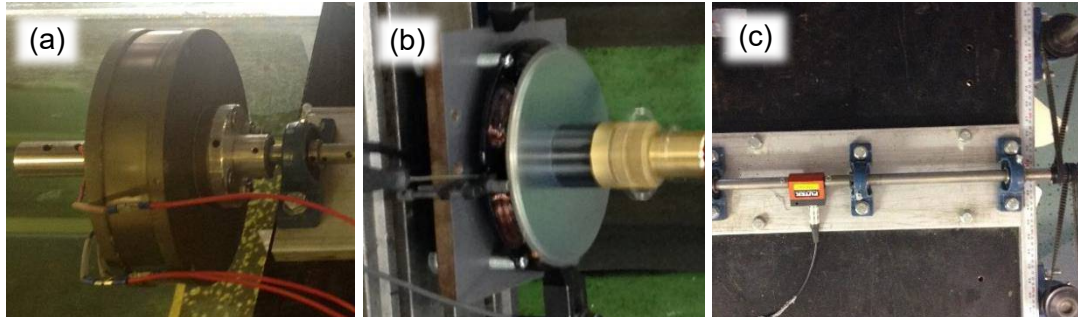


Figure 69. a) Photograph of low rpm off-the-shelf laboratory generator (DVE200); b) photograph of high rpm custom-made laboratory generator (LE300); c) photograph of PTO where the generator was attached to

The generators' rotors were attached to the main shaft which was driven by the two rotors via belts. The main shaft was supported by three pillow block bearings, the generators' stators were held by aluminium profiles which were attached to the supporting structure. Additionally, a torque transducer/encoder was attached to monitor the mechanical input (i.e.,  $\omega$  and  $\tau$ , see Figure 69).

Most of the times, the DVE200 generator was used since both LE generators performed less efficiently due to the given rotational speed of the driving shaft which matched the specifications of the DVE200 (about 250 rpm). The LE generators perform better at rotational speeds  $> 1000$  rpm. Generator performance tests were conducted separately and are presented in the generator testing section of this chapter.

However, the generators' three phases were connected to a rectifier which converted AC into DC. The DC circuit consisted of wires from and to the rectifier and a bank of adjustable resistors (potentiometer, 0-60  $\Omega$ ). Current (Amperes) and voltage (Volts) was recorded with two multimeters simultaneously and different resistances ( $\approx 0, 2.5, 5, 7.5, 10, 15, 20, 30, 40, 60 \Omega$ ) were applied at a certain flow-speed. The mechanical input was further compared to the electrical output which allowed a statement about generator efficiency and system compatibility as depicted in Figure 70.

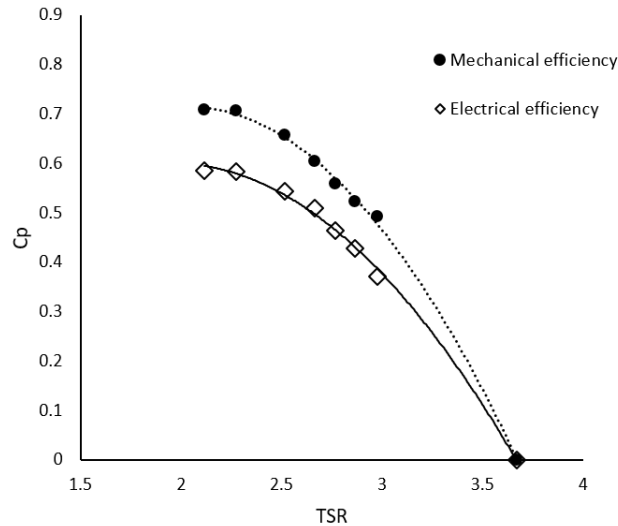


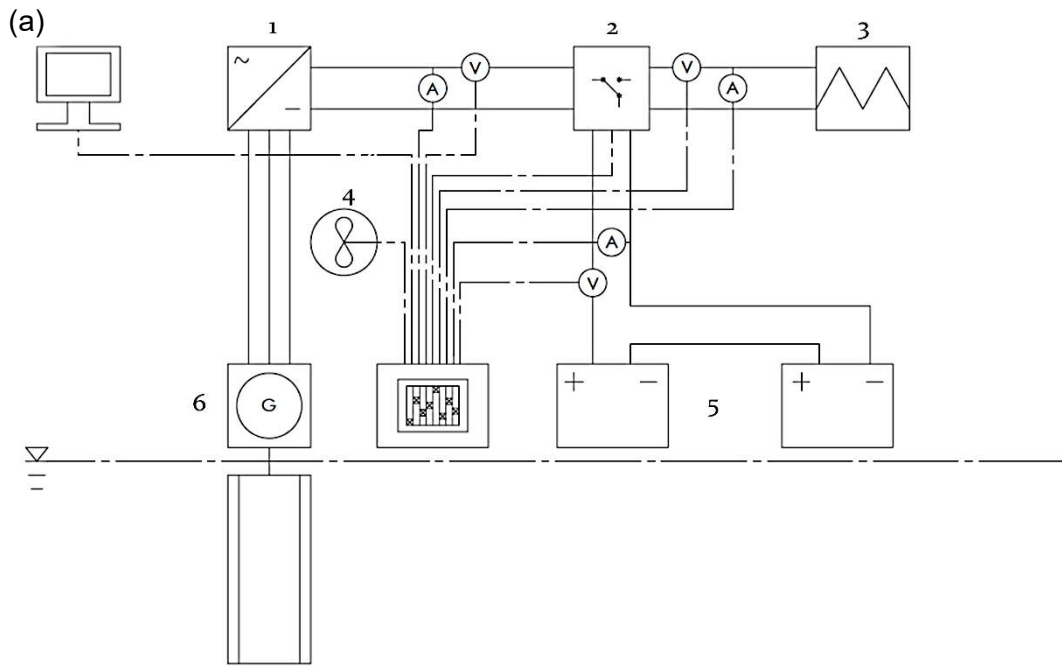
Figure 70. Comparison between electrical and mechanical efficiency (test 125)

At peak performance, a drop in efficiency of 12% was observed between mechanical generator input and measured electrical output. It shall be noted that the resistors and the rectifier warmed up during testing which increased the losses. Nonetheless, [23] suggests generator losses between 3 and 7% are to be expected.

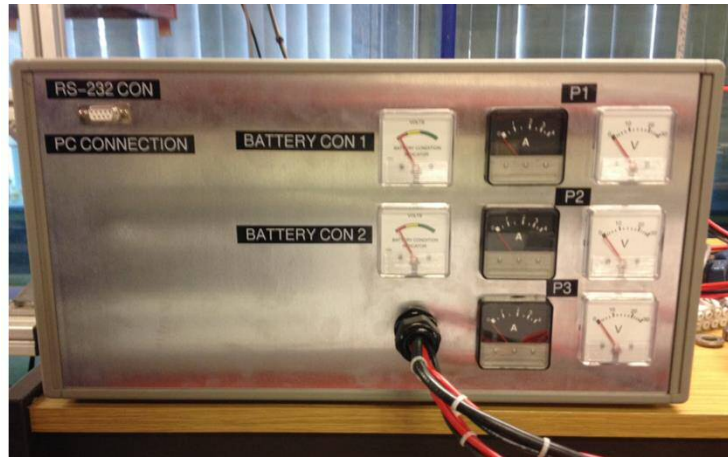
### 5.2.2 Field testing (demonstrator scale)

The tenth scale laboratory rotor presented in Chapter III was up-scaled to third scale and tested in a water treatment plant (see Chapter VI). Here, an electrical circuit was designed with the focus on battery charging and power supply for monitoring purposes such as charging a laptop and operational purposes such as a cooling fan (see Figure 71). Generator performance is not of significant importance, neither on laboratory nor on field testing stage. The tests aim at understanding the mechanics and learning about the implementation and liaison of the individual components of the turbine.

For that purpose, a power diversion assembly (PDA) was designed and built at Cardiff University which consists of housing, rectifier (1), load control (2), dump load (3), cooling fan (4), batteries (5) and wires in order to have a portable, off-grid device to connect to the turbine's generator (6) (see Figure 71). Further details about the PDA components are presented in Appendix D.



(b)



(c)

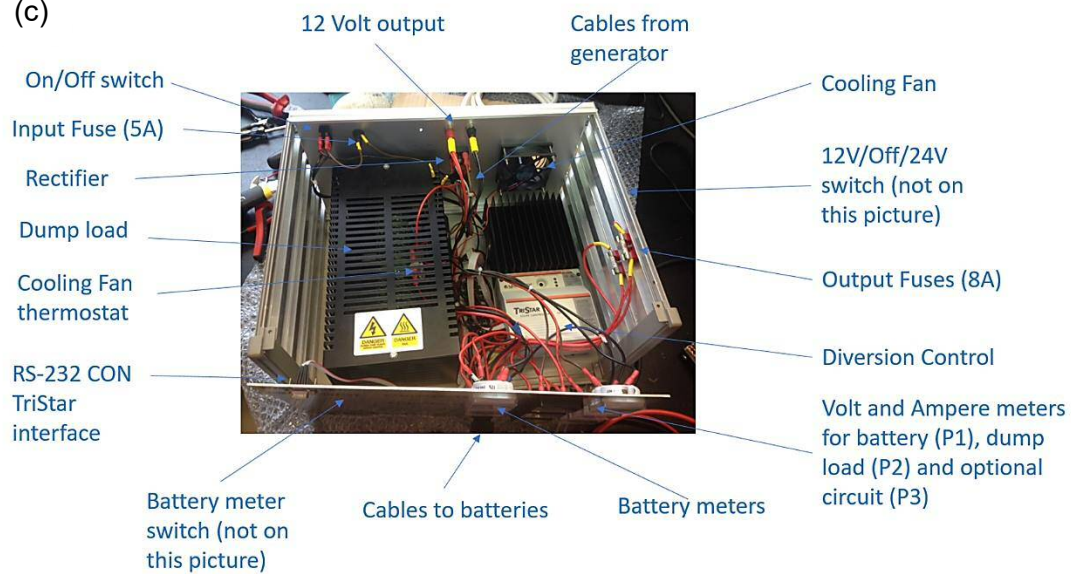


Figure 71.a) Schematic of power diversion assembly (PDA); b) photograph of PDA; c) PDA components

The PDA features a TriStar 45A diversion controller which is commonly used in an off-grid photovoltaics context such as solar panels attached to a caravan. The controller diverts the generated power either to the battery or a dump load in case the battery is fully charged. However, the device is not able to control the turbine in any way. In order to operate the turbine at peak performance a power control system is needed which will be covered later in the Power control section of this chapter.

The PDA is designed to be operated at 12 (one battery) and 24 Volts (two batteries connected in series) and further consists of:

- 500 Watt dump load to dissipate power in case the battery is fully charged
- Rectifier for converting AC from the generator into DC for the battery circuit
- Battery voltage meters
- Connection cables to generator and batteries
- Volt and Ampere meters for dump load and battery circuit
- Fuses and a main on/off switch
- Cooling fan which is controlled by a thermostat attached to the dump-load
- 12 Volt power supply
- RS-232 Con TriStar interface to connect the diversion controller to a computer and gather real-time data or change settings

The PDA was successfully tested in the laboratory using one battery (12V) and two batteries in series (24V). The device was connected to the DVE200 generator and the battery circuit. The batteries were connected to the generator until they were fully charged. The PDA then switched automatically to the dump-load. At a temperature of  $>35^{\circ}\text{C}$ , controlled by the thermostat which is attached to the dump load, the fan was automatically switched on and ventilated the housing until the temperature decreased to  $<25^{\circ}\text{C}$ . The battery charging level could be read from the meters as well as the voltage and current values diverted either to the battery or the dump load. The 12 Volt power supply was used to supply an inverter and a laptop was charged exemplarily. The RS-232 Con TriStar interface was connected to a computer and real-time data (i.e., diversion mode, time, voltage and current) were read. From this test, it was concluded that the device fulfils its purpose and is ready for the application in the field.

### 5.2.3 Application (full scale)

The 10kW concept of the twin turbine as presented in Chapter III is the ultimate development goal. The electrical design depends on many factors and needs to be targeted to a specific site. Nonetheless, a general layout will be attempted at this section.

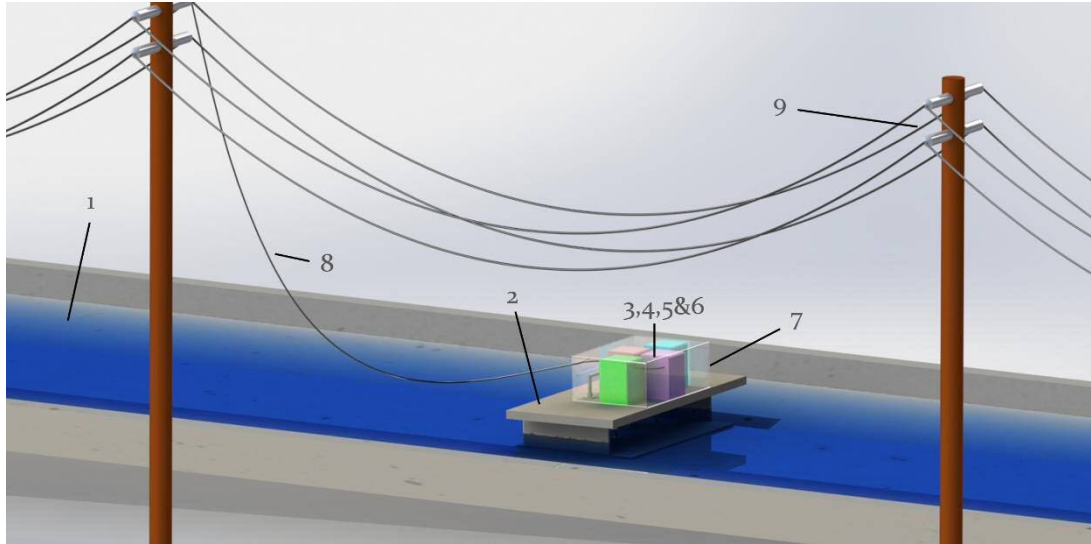


Figure 72. CAD drawing of 10kW full scale VAT concept

The entire system can be divided into the following subsystems as depicted in Figure 72. In this Figure, the VAT is placed into in a channel (1), e.g., a fresh-water supply for a reservoir. The twin-turbine-structure (2) consists of a concrete frame featuring two VATs. Both components need to be designed according to the channel geometry and discharges. On top of the structure, underneath a weather cover (7), a power take-off assembly is installed which is composed of a gearbox (3), generator (4), monitoring (5) and control devices (6). The gearbox (red box) is attached to the rotor shafts and accelerates with a rotational speed by a desired ratio in order to accommodate generator specifications. The generator (purple box) is placed in line with the gearbox and converts the rotational movement into power. The purpose of the monitoring and control device (green and blue boxes) is to ensure an efficient and safe power production, grid connection and real-time tracking of performance data. A powerline (8) is connected from the generator to the grid (9) and feeds the generated electricity to the utilities. In terms of electrical design, the control device is of highest importance. Its purpose is to maintain the turbine's operation at peak performance at all times independent of flow variations (so called maximum power point tracking (MPPT), see Power control section).

### 5.3 Generator testing

For laboratory and field-testing, three different PMGs (LE300, LE450 and DVE200) were used and tested prior to that in order to quantify the losses and to identify the optimal rotational speed for best generator performance. The results from the initial generator tests are presented on the following pages. Figure 73 depicts the test rig and its components.

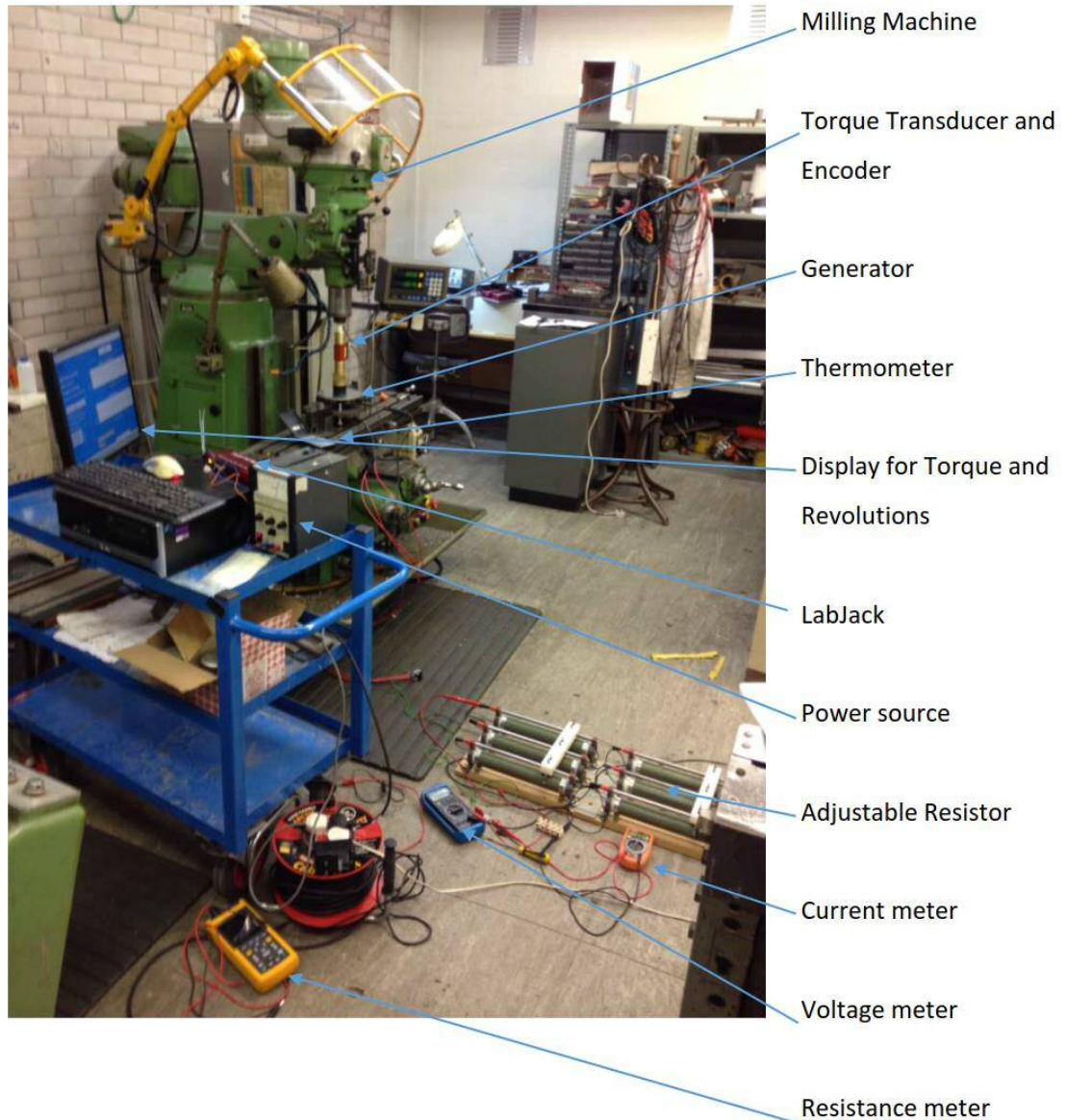


Figure 73. Generator test rig and components

The generator was attached to a milling machine with a variable speed control. Torque transducer and encoder were used to measure the rotational speed and torque. The mechanical input power was calculated by multiplying these two averaged values which were based on raw data that were captured for one minute at a frequency of 100Hz (similar to data capture procedure from turbine testing). The generator temperature was further monitored in order to avoid overheating. The

temperature was kept below 45°C at all times. Electrically, the generator was connected to a rectifier which converted the 3Phase AC to DC. The DC circuit consisted of the rectifier, a voltage, current and resistance meter and an adjustable resistor (see Figure 74). Each test was run at a certain resistance (5, 7.5, 10, 15, 20, 30, 40, 50  $\Omega$ ) and at a certain speed (100 – 1500 rpm in 100 rpm steps, for LE300 and LE450 and 60, 75, 100, 125, 150 -450 in 50 rpm steps for DVE200) for one minute. The readings from current and voltage meter were recorded, averaged and the electrical output power was calculated by multiplying current and voltage.

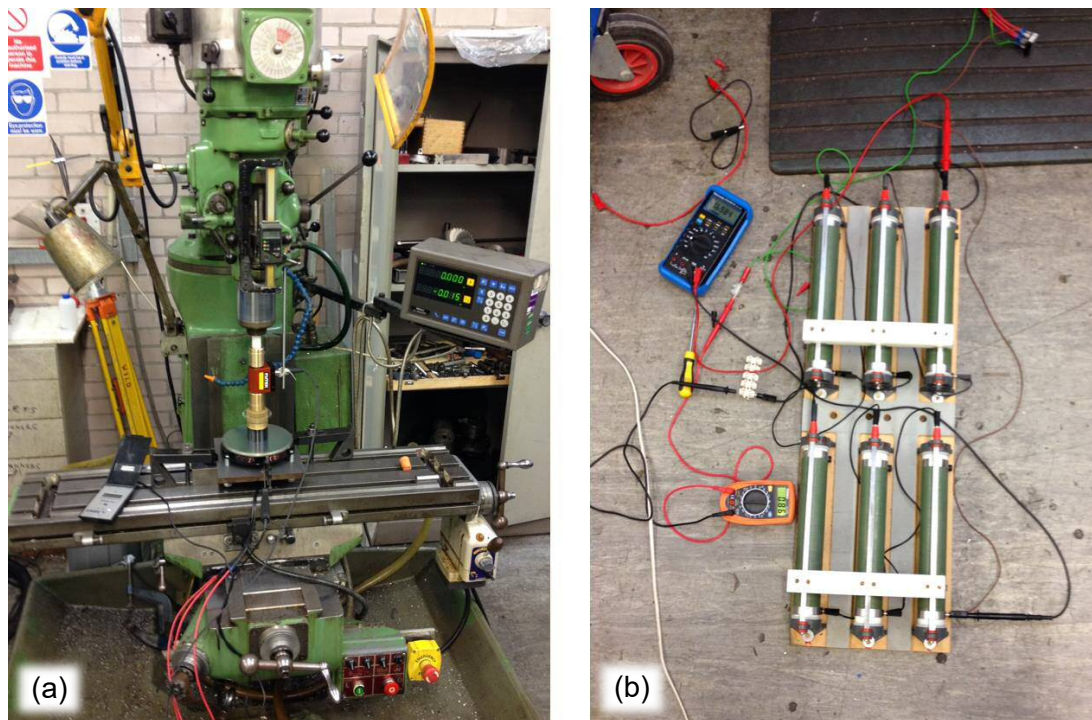


Figure 74. a) Milling machine with LE300 generator and thermometer; b) adjustable resistor with current and voltage meter

The generator efficiency ( $\eta$ ) was then calculated by dividing the electrical output power by the mechanical input power. In comparison, the LE300 generator appeared to perform the worst with efficiencies around 70% at relatively low loads (50 – 30  $\Omega$ ) and rotational speeds beyond 800 rpm. Analogously, the LE450 generator reached similar efficiencies but over a wider load range (50 – 15  $\Omega$ ). The DVE200 generator performed better with efficiencies of up to 85%, even at low rotational speeds. The results are presented on the following pages in form of efficiency vs. rotational speed graphs with a curve for each individual resistance (see Figure 75-77). It is concluded that both LE generators are not suitable for the hydrokinetic turbine since the turbines' rotational speed is far below the speed range (< 400 rpm) where the generators become efficient.

### 5.3.1 Result LE 300

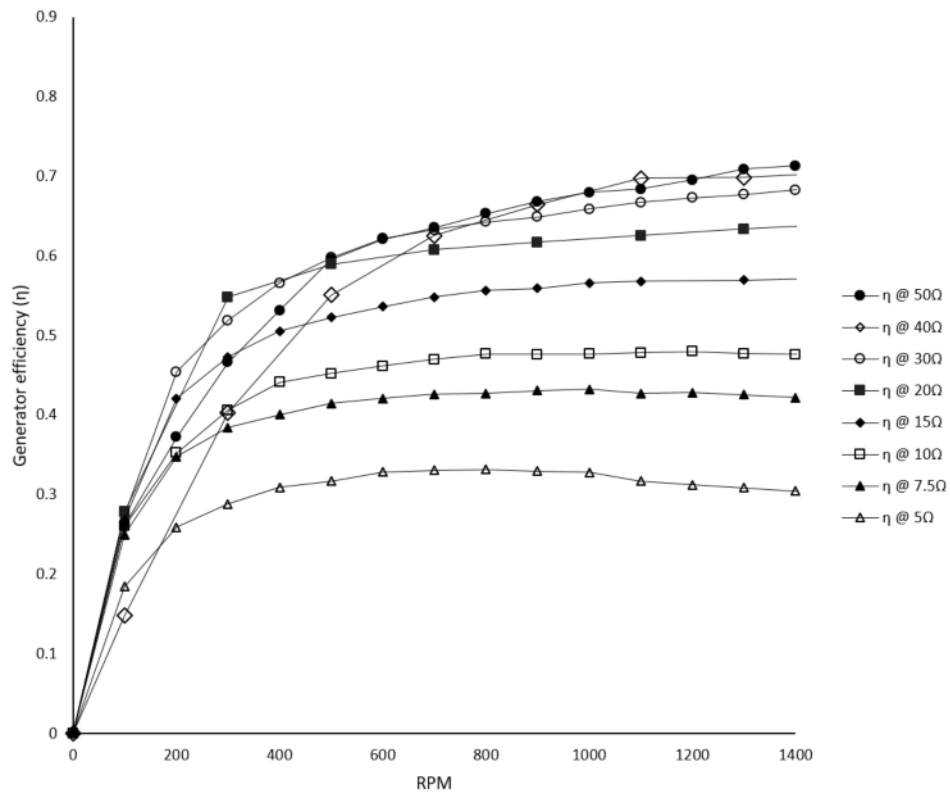


Figure 75. Efficiency of LE300 with different resistances (electrical output vs. mechanical input)

### 5.3.2 Result LE 450

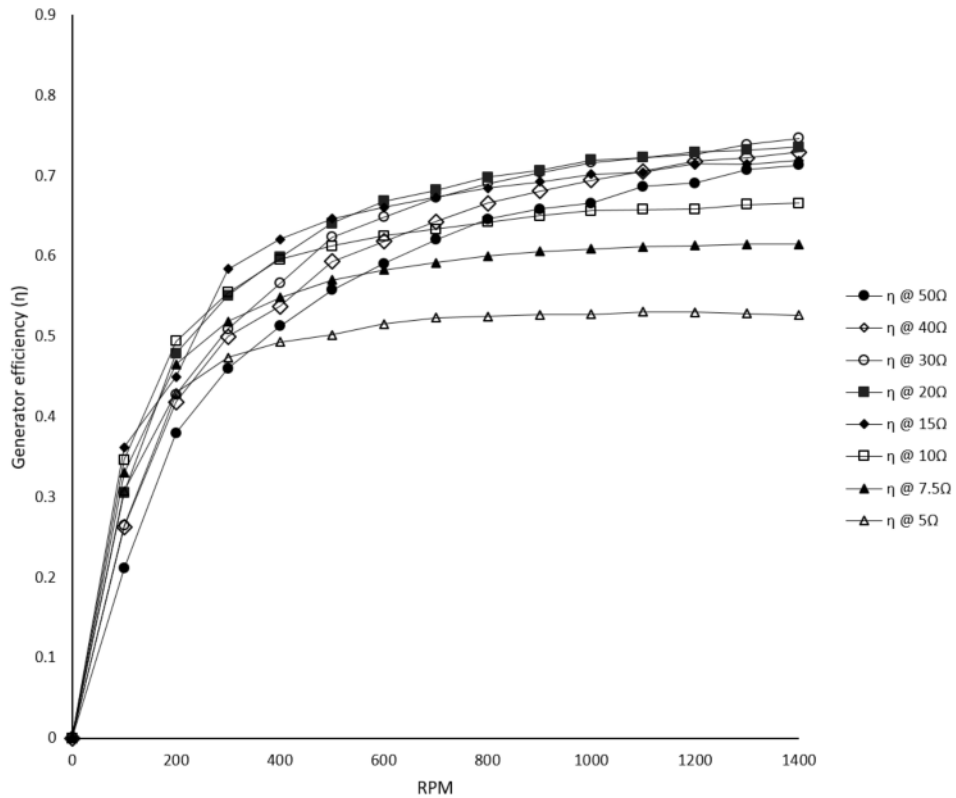


Figure 76. Efficiency of LE450 with different resistances, efficiency (electrical output vs. mechanical input)

### 5.3.3 Result DVE 200

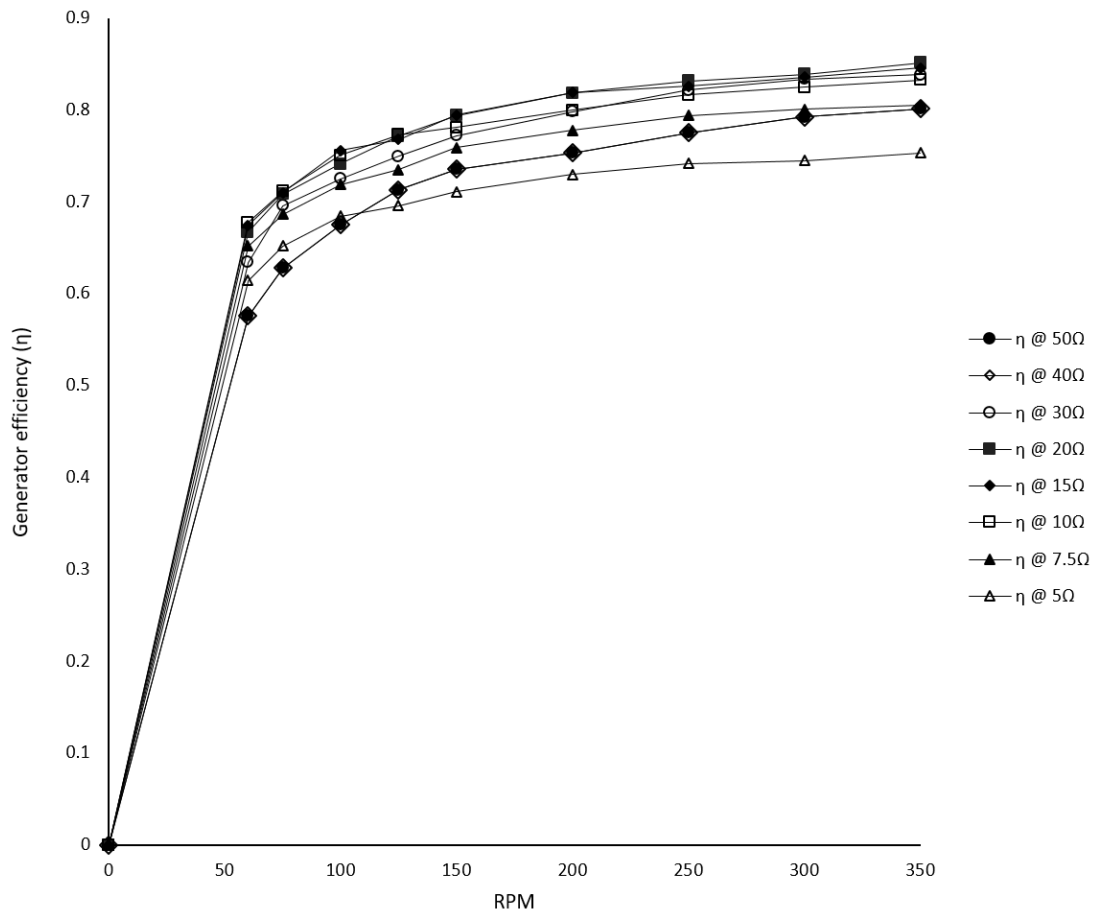


Figure 77. Efficiency of DVE200 with different resistances, efficiency (electrical output vs. mechanical input)

### 5.4 Power control

In a collaboration with the electrical engineering department of the School of Engineering at Cardiff University, a MPPT (maximum power point tracking) controller was designed, built, tested and a journal paper submitted (see list of publications).

An electrical subsystem was designed for the power take-off and the MPPT of the laboratory prototype of the hydrokinetic VAT. The electrical subsystem consists of a rectifier, a DC-DC converter and two 12 V batteries connected in series, as shown in Figure 78. The rectifier is used to rectify the generator voltage. The voltage  $V$  at point B is fixed by the batteries. The DC-DC converter is used so that for a fixed voltage  $V$ , the rectifier voltage  $V_r$  is varied. There is a linear relationship between the voltage  $V_r$  and the amplitude of the AC voltage at the generator terminals. Therefore, with the variation of  $V_r$ , the voltage at the generator terminals changes linearly. As the terminal voltage of the generator becomes higher the mechanical resistance of the generator

decreases linearly and the rotor accelerates. When the terminal voltage of the generator becomes lower, the rotor decelerates.

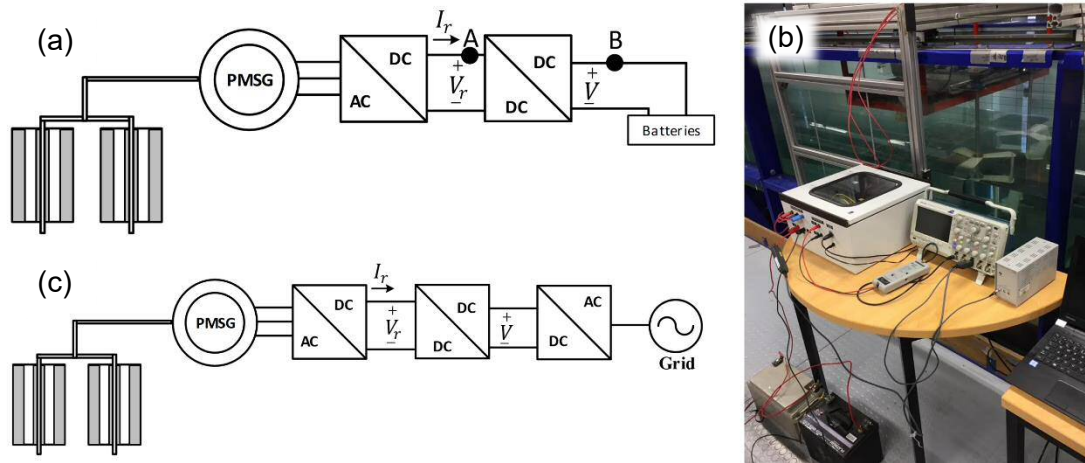


Figure 78. a) Schematic and b) photograph of laboratory MPPT; c) full scale MPPT schematic concept

The DC-DC converter is controlled in order to extract the maximum power from the hydrokinetic energy conversion system. The rectifier voltage  $V_r$  and current  $I_r$  is measured and changes in  $V_r$  are applied accordingly. For a specific perturbation of  $V_r$ , such as an increase in electrical power, a step change in  $V_r$  of the same direction takes place and vice versa if the electrical power decreases.

For the full-scale system, a three-phase inverter is used instead of the batteries for connecting the VAT system to the grid, as shown in Figure 78. The inverter is controlled in order to keep the voltage  $V$  fixed, so that the same control strategy as with the experimental system is followed.

## 5.5 Summary

In a first step, a decision making process was derived by considering relevant literature in order to identify the most important aspects of an electrical design. Turbine and generator specifications, power control, current, voltage and frequency were identified, described and put into context of the hydrokinetic VAT described in Chapter III.

The VAT undergoes three testing stages: laboratory testing (scale 1:10); field testing (scale 1:3) and application testing (scale 1:1). For each stage, an electrical design is presented:

- For laboratory testing, three different PMGs were used to apply a resistance to the rotors instead a mechanical mechanism (e.g., disc brake) in order to assess the turbine's performance. The circuit consists of a 3Phase AC PMG (LE300, LE450 or DVE200), an AC-DC rectifier and an adjustable resistor.

- For field testing, an electrical circuit was designed with the focus on battery charging and power supply for monitoring and operation. Therefore, a PDA was designed and built in order to have a portable battery charger to connect to the turbine's generator. The circuit consists of a 3Phase AC PMG, an AC-DC rectifier, the PDA and two 12 V batteries.
- For the application of the VAT, a site-specific electrical design is needed. Nonetheless, the main components of the design are identified as generator and gearbox, grid connection, monitoring and control devices in addition to site-specific information such as turbine specifications and flow rates.

Further, the PMG's were tested in order to quantify the losses and identify the rotational speed for best generator performance. The DVE200 was found to perform best ( $\eta_{\max} = 85\%$ ) at rotational speeds that can be implemented in the laboratory and in field testing of the turbine ( $100 < \text{rpm} < 450$ ). The other generators (LE300 and LE450) need much higher rotational speeds ( $\text{rpm} > 400$ ) to perform reasonably well. It shall be noted that in a full scale application, a gearbox is included for that reason. Cost-effective generators generally need higher rotational speeds than the VAT can provide.

Moreover, a MPPT controller was successfully designed, built and tested. The controller is an integral part of the full scale electrical design which operates the turbine automatically at peak performance according to changes in rotational speed (i.e., flow speed) and adjusts the produced electricity to the load (i.e., battery voltage).

In conclusion, the study of the electrical components of the VAT showed that a sophisticated electrical design is needed in order to minimise conversion losses from mechanical to electrical power and benefit from synergy effects such as implementing an induction generator which could also act as a starter motor. For the full-scale application of the VAT, an automated power control device (such as a MPPT controller) is suggested in order to operate the VAT at peak performance at all times (see Chapter IX). However, for laboratory testing, a manual power control strategy was applied and a similar approach suggested for field testing which is presented in the following chapter.

## VI. Field testing in a water treatment plant

### 6.1 Introduction

The hydrokinetic VAT underwent intensive laboratory testing in Cardiff University's Hydro Laboratories. In Chapter III, the principal design of the turbine, the laboratory setup and flow conditions are described and the test results are provided. From these tests it was concluded that the laboratory scale turbine is capable of achieving coefficients of power of approximately 70%. The next development step is to up-scale the turbine from 1:10 scale to 1:3 scale and confirm its performance and workability in a relevant environment.

After finalising the turbine design, the city of Atlanta (Georgia, USA) provided the opportunity to deploy the twin-rotor VAT system into an ultraviolet (UV) radiation channel which is the last stage of water treatment at RM Clayton water treatment plant. The deployed turbine consists of two low solidity, three bladed, counter rotating rotors, a belt drive to combine the rotational motion and torque to one shaft and a PTO system. In order to achieve maximum performance, a flow diversion structure was installed in the channel in order to reduce its cross sectional area and increase the flow velocity. In the following, the steps from design to deployment and testing are outlined and the test results in form of power curves are reported.

### 6.2 Site conditions, deployment concept and test-plan

Figure 79 sketches the UV channel into which the turbine was installed, including the clearance of the UV lamp (yellow circle), the flow diverter (orange) and the turbine consisting of a submerged twin rotor system and a PTO that is located above the channel. The channel is approximately 1.9m wide and 4m deep, and the inflowing water is controlled via a rectangular weir and a gate (see Appendix E for further details). The water flows at a depth of approximately 2m through the UV radiation device upstream of the turbine rotors. The flow diverter's function is to force the water to flow through a smaller cross-sectional area thereby increasing its velocity so that reasonable amounts of hydrokinetic energy is available for extraction. The water then drives the two counter-rotating rotors and, consequently, the main drive shaft which is positioned on a PTO bridge above the channel. Downstream of the rotors, the water discharges over a weir into a channel which eventually releases the treated water into the Chattahoochee River.

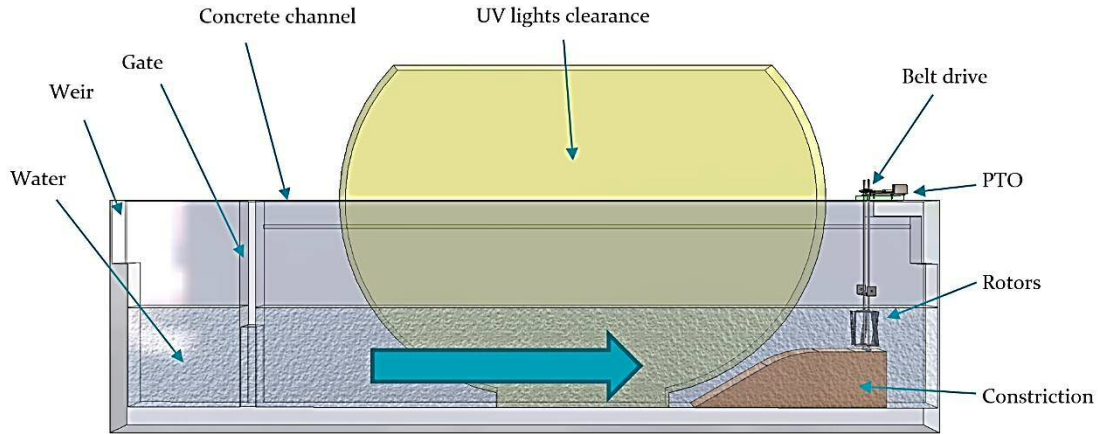
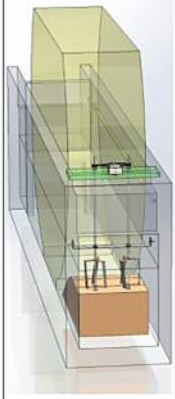


Figure 79. CAD side view of the UV channel at RM Clayton including various turbine components

Table 15 provides an overview of the anticipated turbine testing plan for the first four days after deployment. First of all, the turbine was to be tested for its capability of producing mechanical power by using a mechanical disk brake to apply torque and a torque transducer and an encoder to measure mechanical torque ( $\tau$ ) and rotational speed ( $\omega$ ) from which mechanical power ( $P_M$ ) can be calculated using  $P_M = \tau\omega$ .

Table 15 Installation, testing and commissioning schedule undertaken in May 2017 at RM Clayton

Day	Monday, 15 <sup>th</sup> May	Tuesday, 16 <sup>th</sup> May	Wednesday, 17 <sup>th</sup> May	Thursday, 18 <sup>th</sup> May	Friday, 19 <sup>th</sup> May	Saturday	
Phase	Installation	a	b	c	Handover		
Components	Structure & Turbine	Torque transducer Disc break	Torque transducer Low RPM Generator	Torque transducer High RPM Generator	Box & Batteries High RPM Generator		
Schematic		<div style="text-align: center;"> <div style="border: 1px solid black; padding: 5px; width: 60px; margin: 5px auto;">Disc break</div> <div style="text-align: center;">↓</div> <div style="border: 1px solid black; padding: 5px; width: 60px; margin: 5px auto;">Torque transd.</div> <div style="text-align: center;">↓</div> <div style="border: 1px solid black; padding: 5px; width: 60px; margin: 5px auto;">PC</div> <div style="text-align: center;">↓</div> <div style="border: 1px solid black; padding: 5px; width: 60px; margin: 5px auto;">C<sub>p</sub> vs λ &amp; P<sub>mech</sub></div> </div>	<div style="display: flex; justify-content: space-around;"> <div style="text-align: center;"> <div style="border: 1px solid black; padding: 5px; width: 60px; margin: 5px auto;">Low RPM Generator</div> <div style="text-align: center;">↓</div> <div style="display: flex; justify-content: space-between; width: 100%;"> <div style="border: 1px solid black; padding: 5px; width: 45%;">Resistor</div> <div style="border: 1px solid black; padding: 5px; width: 45%;">Torque transd.</div> </div> <div style="text-align: center;">↓</div> <div style="border: 1px solid black; padding: 5px; width: 60px; margin: 5px auto;">Multi meter</div> <div style="text-align: center;">↓</div> <div style="border: 1px solid black; padding: 5px; width: 60px; margin: 5px auto;">Amp, V &amp; P<sub>el</sub></div> </div> <div style="text-align: center;"> <div style="border: 1px solid black; padding: 5px; width: 60px; margin: 5px auto;">Low RPM Generator</div> <div style="text-align: center;">↓</div> <div style="border: 1px solid black; padding: 5px; width: 60px; margin: 5px auto;">PC</div> <div style="text-align: center;">↓</div> <div style="border: 1px solid black; padding: 5px; width: 60px; margin: 5px auto;">C<sub>p</sub> vs λ &amp; P<sub>mech</sub></div> </div> </div>	<div style="display: flex; justify-content: space-around;"> <div style="text-align: center;"> <div style="border: 1px solid black; padding: 5px; width: 60px; margin: 5px auto;">High RPM Generator</div> <div style="text-align: center;">↓</div> <div style="display: flex; justify-content: space-between; width: 100%;"> <div style="border: 1px solid black; padding: 5px; width: 45%;">Resistor</div> <div style="border: 1px solid black; padding: 5px; width: 45%;">Torque transd.</div> </div> <div style="text-align: center;">↓</div> <div style="border: 1px solid black; padding: 5px; width: 60px; margin: 5px auto;">Multi meter</div> <div style="text-align: center;">↓</div> <div style="border: 1px solid black; padding: 5px; width: 60px; margin: 5px auto;">Amp, V &amp; P<sub>el</sub></div> </div> <div style="text-align: center;"> <div style="border: 1px solid black; padding: 5px; width: 60px; margin: 5px auto;">High RPM Generator</div> <div style="text-align: center;">↓</div> <div style="border: 1px solid black; padding: 5px; width: 60px; margin: 5px auto;">PC</div> <div style="text-align: center;">↓</div> <div style="border: 1px solid black; padding: 5px; width: 60px; margin: 5px auto;">C<sub>p</sub> vs λ &amp; P<sub>mech</sub></div> </div> </div>	<div style="text-align: center;"> <div style="border: 1px solid black; padding: 5px; width: 60px; margin: 5px auto;">High RPM Generator</div> <div style="text-align: center;">↓</div> <div style="border: 1px solid black; padding: 5px; width: 60px; margin: 5px auto;">Box</div> <div style="text-align: center;">↓</div> <div style="border: 1px solid black; padding: 5px; width: 60px; margin: 5px auto;">Battery</div> <div style="text-align: center;">↓</div> <div style="border: 1px solid black; padding: 5px; width: 60px; margin: 5px auto;">LED</div> </div>		<b>Buffer</b>

After that, two different generators (high rpm LE450 and low rpm DVE200) were to be used in conjunction with a resistor bank which allows to apply an electrical load and voltage (V) and current (A) are measured via multimeters. Electrical power ( $P_E$ ) in Watts can be obtained via  $P_E = VA$ . Finally, the turbine was to be equipped with an

off-grid power take off system, consisting of the high-rpm generator, PDA and a 12V battery. The generated electricity is used to power an electronic display board.

In the following sections, the design of each component of the turbine is described in more detail, followed by a description of the test procedure, the report and discussion of the results.

### 6.3 Turbine design

Figure 80 presents a 3D view of the turbine from downstream (LHS) and a cross-section of the system with detailed measurements in mm (RHS). The ~1.1m tall constriction is attached to the bottom and side walls of the channel. The turbine housing/structure is designed to overcome the distance between channel top and water surface. The rotors are approximately 0.1m away from constriction and water table, the width occupies approximately 60% of the channel width. The three-bladed rotors are designed based on the findings from the laboratory tests.

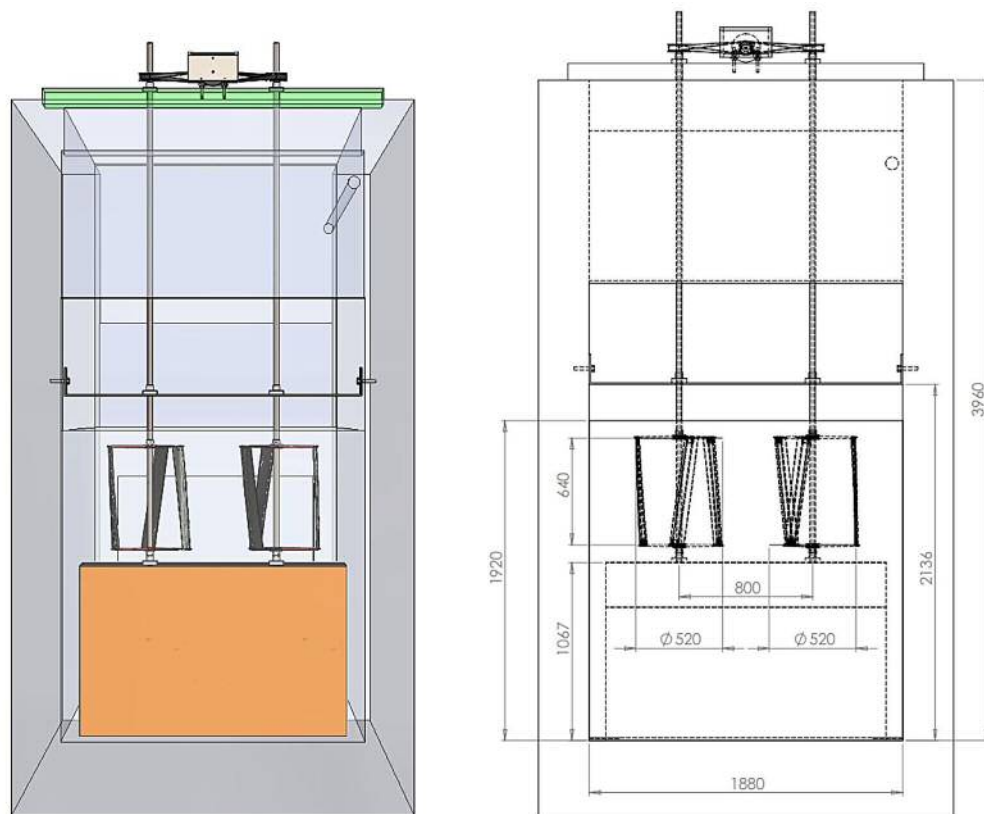


Figure 80. CAD cross-sectional view on twin VAT design for RM Clayton as seen from downstream

#### 6.3.1 Flow diverter

The main aim of the flow diverter is to reduce the cross sectional area of the channel with the aim to increase the flow velocity in the remaining cross-section. With a given discharge ( $Q$ ), which varies throughout the day, the spatially-averaged flow velocity

(v) in the channel is only a function of the cross-sectional area ( $A$ ) and is obtained from  $v = Q / A$ . Therefore, the flow velocity in the channel increases linearly with the reduction of the cross sectional area. Here, the area of the constriction ( $\sim 2\text{m}^2$ ) is slightly more than half of the area of the wetted channel cross sectional area ( $3.6\text{m}^2$ ) and therefore, reasonable flow velocities are expected in an otherwise relatively low velocity channel.

The constriction, which is depicted in Figure 81, is shaped to minimize hydrodynamic losses in the form of dead zones or recirculation zones and to smoothly accelerate the water before approaching the rotors by maintaining its slope just below  $30^\circ$ . The upstream extent of the constriction is limited by the UV lights clearance radius. The bottom shaft bearings are attached to the constriction.

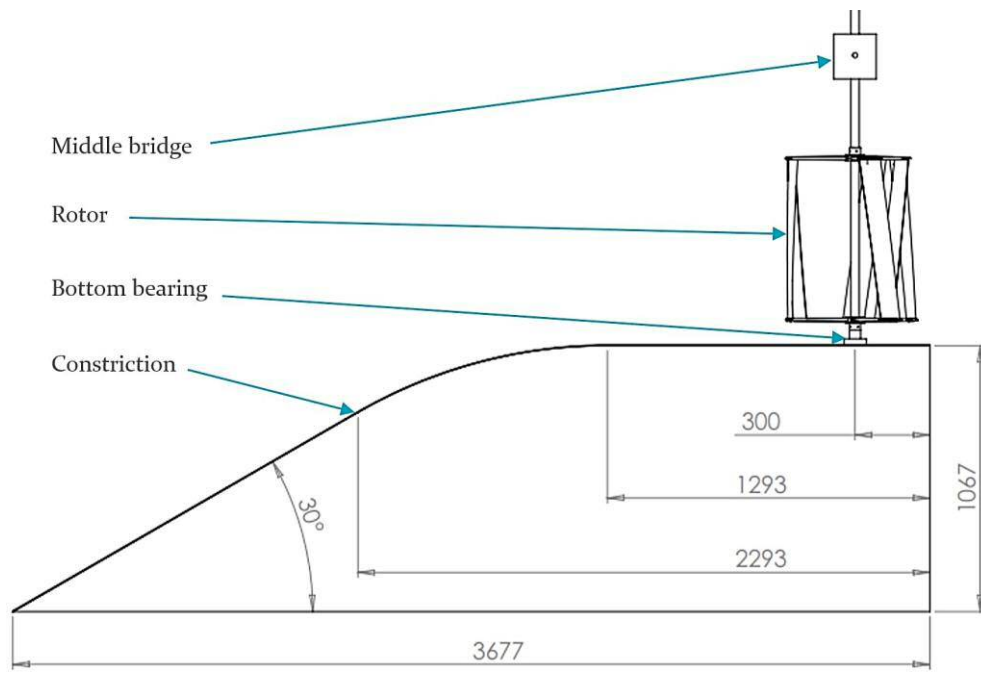


Figure 81. CAD side view of constriction design for RM Clayton including rotor and middle bridge

### 6.3.2 Middle bridge

The water depth in the UV channel is approximately 1.8m, however, the entire depth of the UV channel is approximately 4m. The PTO is located on a bridge above the UV channel, hence very long rotor shafts are required. In order to avoid extensive bending of the rotors' shafts, a middle bridge is introduced with two additional bearings attached to it as depicted in Figure 82. The bridge is installed close to the water surface to minimise bending of the shaft close to the rotors.

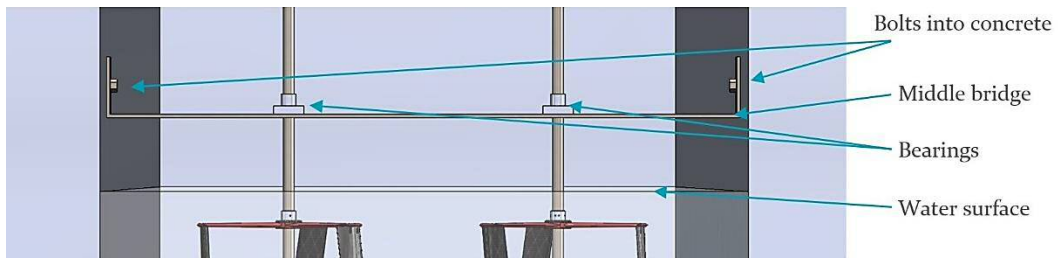


Figure 82. CAD front view of middle bridge with bearings and attachment to the concrete channel

### 6.3.3 Upper Bridge

The upper bridge is depicted in Figure 83 and serves multiple purposes including supporting the top bearings of the rotor shafts, accommodating the PTO and covering the UV channel. It is manufactured of mild steel with a coating which is applied to prevent corrosion and is attached via bolts to the concrete channel.

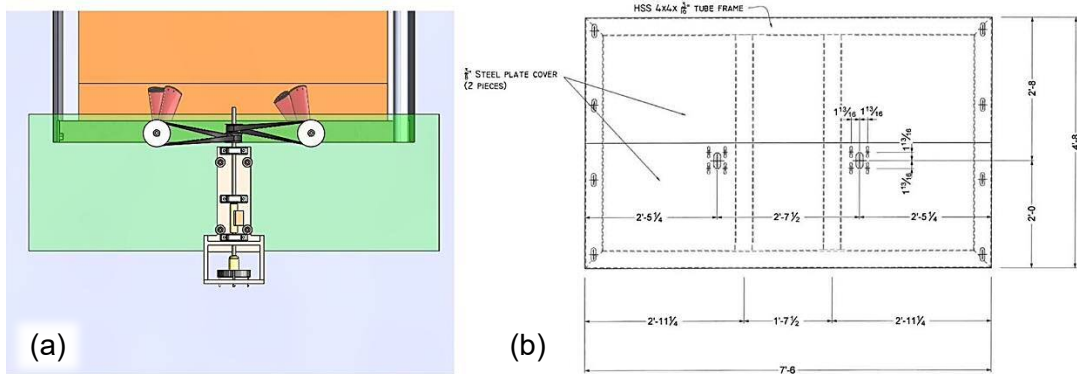


Figure 83. a) CAD top view of upper bridge (green) including PTO and rotors; b) Construction drawing of upper bridge (as manufactured by Abuck Ltd., Atlanta, measures in inch)

### 6.3.4 Rotors

Figure 84 shows one of the two twin-rotors in various views, in the form of CAD construction drawings on the left hand side and as a 3D drawing on the right hand side. The rotor is comprised of three main components: three blades; six spokes; and two hubs. The parameters of the rotor design and rotor testing results from the laboratory were covered in Chapter III, the general dimensions of the rotors utilised here are driven by the geometry of the channel and the constriction dimensions.

The three individual components are described on the following pages.

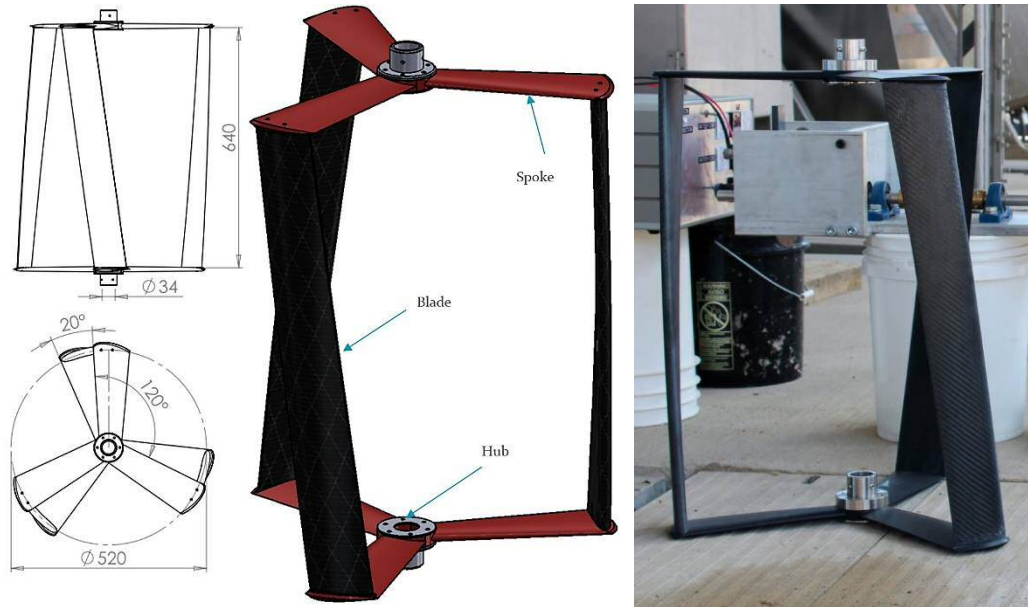


Figure 84. CAD design drawings and photograph of one of the two rotors with components and major dimensions

### 6.3.5 Hubs

Figure 85 details the hubs consisting of a shaft sleeve and washer. The spokes are sandwiched between the sleeve and the washer and are held by six stainless M6 button head socket bolts and nuts. The sleeve has four M5 tapered holes which are used for set-screws to rigidly connect the hub to the shaft so that the torque is transferred. Sleeves and washers are machined and are made out of stainless steel, grade 303.

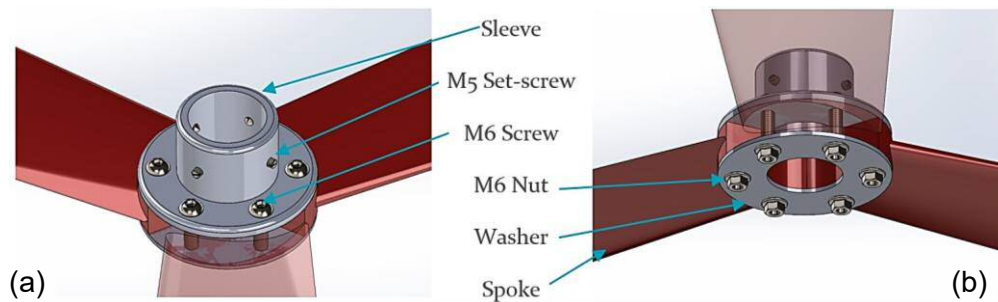


Figure 85. a) CAD top view of the rotor's hub including components; b) CAD bottom view with spokes in red and partially transparent

### 6.3.6 Spokes

Figure 86 presents detailed design drawings, including the main dimensions and a 3D visualisation of one of the spokes. The airfoil-shaped spokes are structural members connecting the blade to the shaft and transferring the forces generated by the blades to the shaft. The shape is optimised in order to provide minimum drag without compromising on structural integrity. Further, the tip of the spoke overlaps

slightly with the blade in order to prevent tip vortices to disrupt the flow over the blade near the ends, thereby maintaining maximum lift and minimum drag near the blades' tips. The spokes were machined by Nylacast Ltd., Leicester, UK and are made of glass-reinforced nylon.

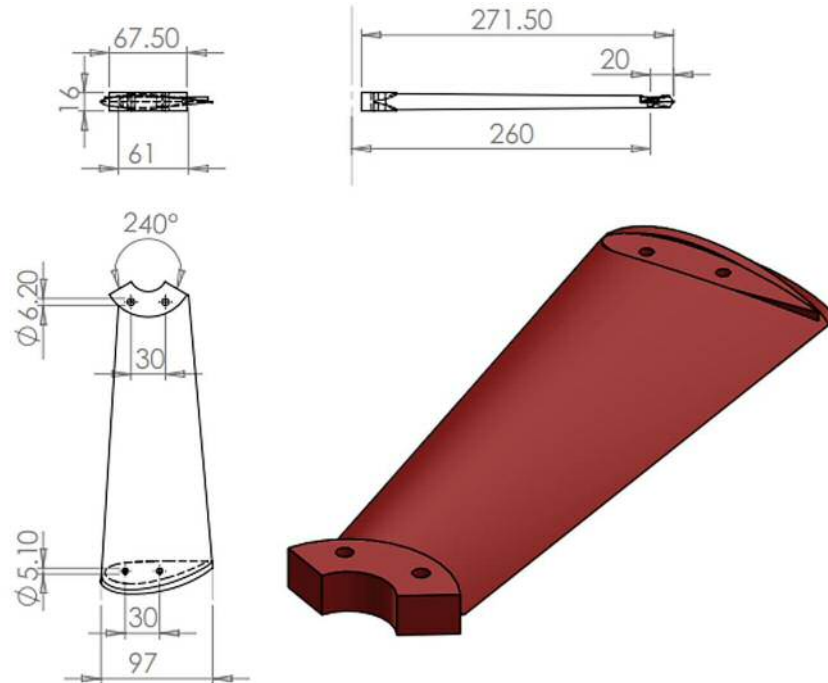


Figure 86. CAD drawings of one spoke with major dimensions

The spoke's root has a circular segment so that it assembles with the two other spokes to form a ring around the shaft and all three spokes are sandwiched between the two washers of the hub as shown in Figure 85. From the ring segment, the spoke is air foil shaped using a symmetric NACA0024 profile which increases in width until the tip of the spoke where a NACA0010 profile is used while the spoke thickness stays approximately constant. Near the tip, the spokes feature a rotor blade-shaped recess into which the blade is seated.

### 6.3.7 Blades

Figure 87 presents design drawings (left) including the main dimensions and a 3D visualisation of one of the blades. The helical airfoil shaped composite blades ( $20^\circ$  twist, NACA4421, chord length 90mm) were manufactured at Cardiff University and consist of a sintered core (selective laser sintering, SLS, EOS PA2200), two stainless steel inserts (grade 303) and a multi-layer carbon fiber shell (Cyttec MTM 28).

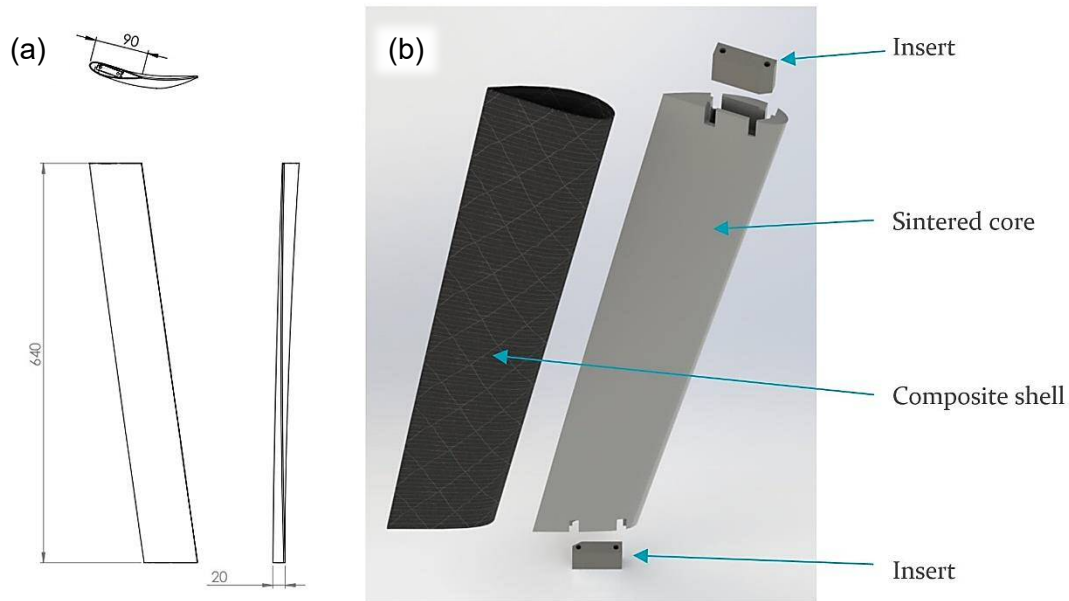


Figure 87. a) CAD drawings of one blade with major dimensions; b) 3D exploded view of the three blade components i.e., shell, core and inserts

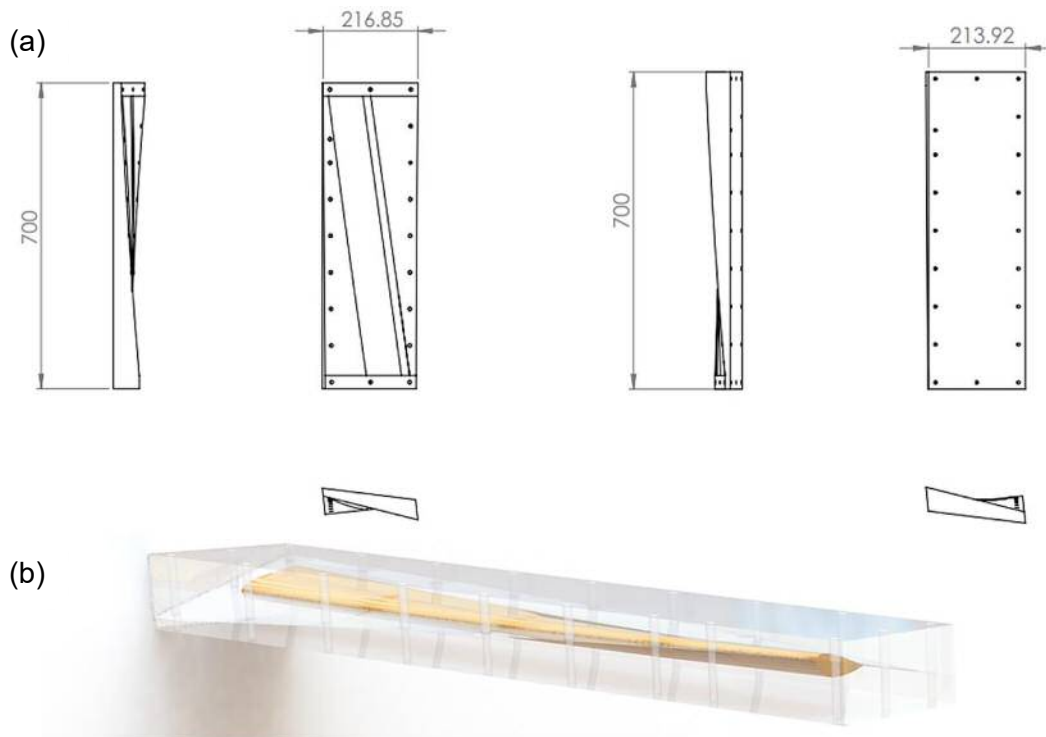


Figure 88. a) CAD design drawings of blade mould with major dimensions; b) 3D visualisation of the blade (orange) inside the mould (transparent)

The composite design was chosen to replace aluminium or stainless steel in order to reduce manufacturing costs without compromising on strength and durability of the blades. The core of the blade provides the shape, fills and stiffens the composite shell and accommodates the stainless steel inserts. The selective laser sintering (SLS) material is suitable as a filling material for the carbon fiber shell but, based on previous

laboratory experience, it was concluded that it is not strong enough to be threaded and to accommodate bolts. Therefore, the inserts were made of grade 303 stainless steel. Each insert has two threaded holes which accommodate the bolts in order to attach the blade to the spoke. The inserts are slotted into the openings of the SLS core and are bonded to core and shell using carbon fiber high-performance epoxy resin during the autoclave curing process. The blade shell consists of four layers of carbon fiber plies which are evenly applied to the SLS core; with a 90° fiber offset in order to improve torsional resistance. The raw composite was then placed in a SLS mould, which is depicted in Figure 88, vacuum bagged, heat and pressure treated and cured in an autoclave [154]. To the best of my knowledge, the combination of SLS core and mould with pre-impregnated composite fibers (prepregs) is unique and was established together with the mechanical engineering department at Cardiff University. The procedure and components are further described in the manufacturing summary in the Appendix G.

### 6.3.8 Shaft and Belt drive

Figure 89 depicts a part of the drive train of the PTO. The rotational movement of the rotors is transferred via the two rotor shafts (17&19) to a belt drive which consists of two 90° twisted timing belts (22&23), two large pulleys with 44 teeth (20&21), two small pulleys with 28 teeth (24&25) and a horizontally orientated main shaft (26). The belt drive enables the transfer of torque and rotational speed from the two rotor shafts onto the. PTO shaft.

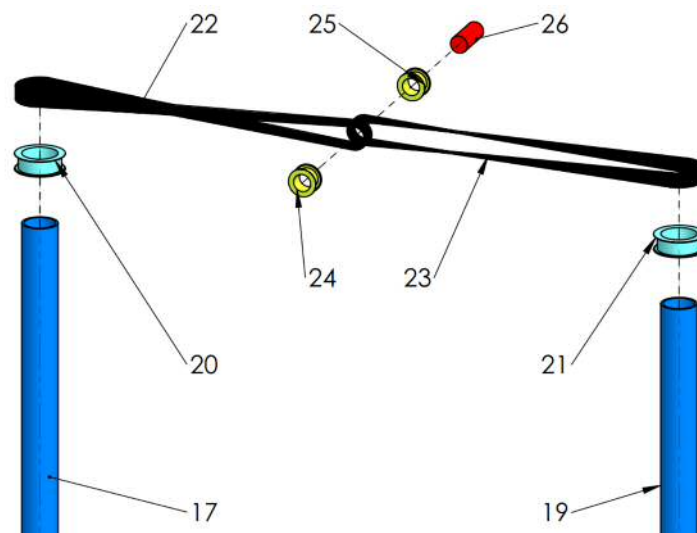


Figure 89. Exploded view of the drive train design

As rotor shafts, a 1" stainless steel pipe (ANSI B 36.19 Schedule XXS) was chosen in order to provide sufficient resistance against bending and buckling without the

heavy weight of a solid shaft. The main drive shaft is made of a 20mm solid stainless steel rod (grade 3031). The two timing belts (Contitech Synchronbelt HTD, 140 teeth, 1120mm length, 20mm width) transfer the rotors' counter-rotating motion onto the main shaft. The two timing belts are looped over each of the 44 teeth rotor pulleys and 28 teeth PTO pulleys in order to transmit the power between rotor and PTO. The assembly has a gear ratio of 11:7 and therefore reduces the torque and increases the speed of the main shaft.

### 6.3.9 Power take-off

The entire PTO is shown in Figure 90 in the form of dimensioned CAD drawings and a 3D visualisation. It is designed with the purpose of providing a flexible, structurally solid and cost-effective solution for both the initial mechanical testing phase and the long-term operation/power generation phase.

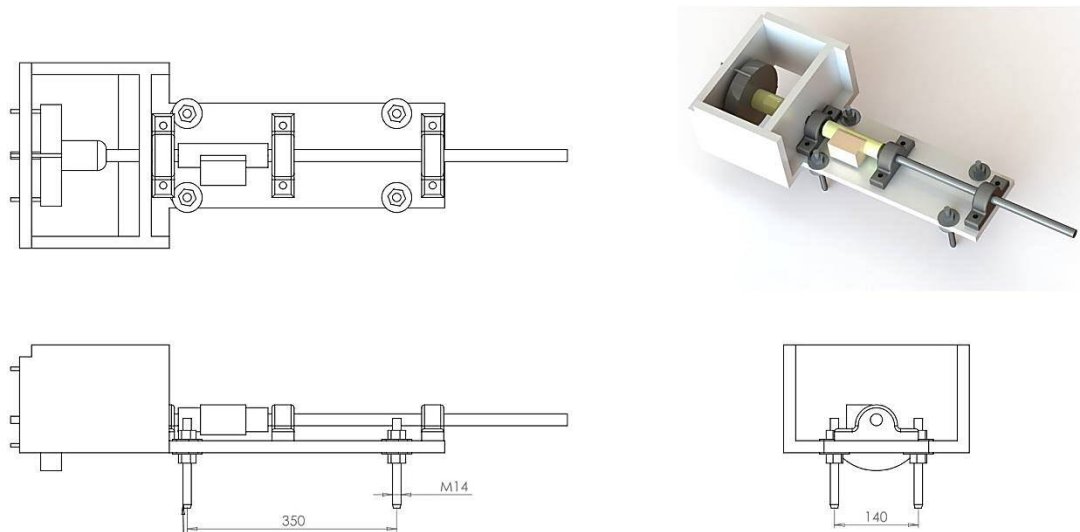


Figure 90. CAD design drawing of the PTO with major dimensions

The housing consists of 20mm thick aluminium plates which are bolted together. Attached to the front section are three pillow block bearings (RS Pro UCP204 cast iron pillow block bearing) which hold the main shaft. The outermost bearing is mounted adjacent to the two main shaft pulleys, the other two bearings host the torque transducer. Four M14 bolts are used to mount the PTO to the upper bridge of the turbine structure. The generator housing of the PTO is designed in order to accommodate the two different types of generators and a mechanical braking system for mechanical testing. The different generators, or alternatively the mechanical disc brake, are attached to a specific end plate which can be interchanged. Generator, disc brake and torque transducer are described in the following.

## 6.4 Turbine installation

The turbine is installed in one of the UV canals at RM Clayton, a waste water treatment plant (WWT) in Atlanta, Georgia, USA. The turbine is placed in the effluent channel of the final stage of the water treatment process (disinfection by ultraviolet light radiation, UV) Figure 91 depicts a typical plant design and an aerial view on RM Clayton). The installation took place on May 15<sup>th</sup> 2017 and was carried out by an engineering contractor (Abuck Ltd.). The site and the installation process is documented via photographs and described on the following pages.

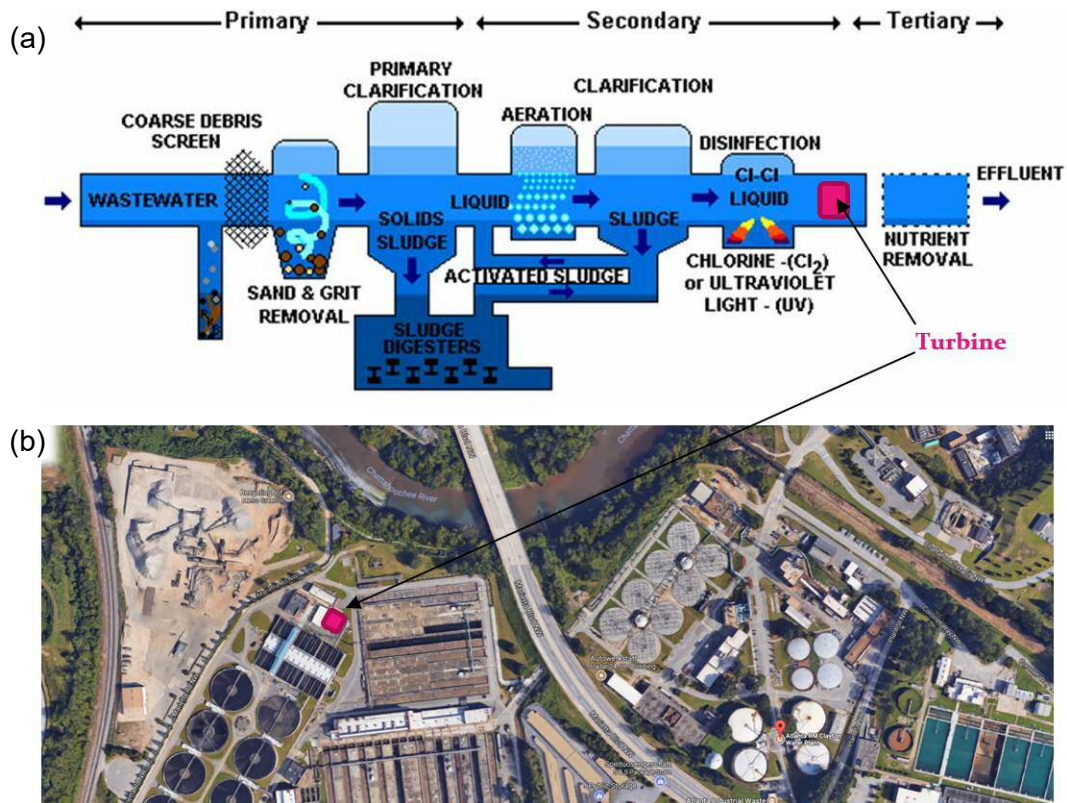


Figure 91. a) Schematic of a typical waste water treatment process with turbine position highlighted [155]; b) aerial picture of RM Clayton water treatment plant [156]

The 1:3 scale hydrokinetic twin VAT is placed in the second of five disinfection channels which host the final treatment stage (UV radiation) before the water is discharged into the Chattahoochee River (see Figure 90). The water enters the channels by spilling over weirs and the discharge in each channel depends on how many channels are in operation (usually two to three), time of the day and the weather. It is assumed that the total amount of water is distributed evenly amongst each channel in operation.



Figure 92. a) UV disinfection channels at RM Clayton. There are five UV canals in total of which three are in operation. Channel two is allocated for the turbine; b) non-immersed UV lamp housing of channel two (~2m above water level); c) downstream of UV lamp housing in channel two where the turbine is installed; d) UV channel effluent weir; e) installation of constriction

The width of the channel and the water depth are approximately 1.8m. The water surface is relatively constant and lies approximately 2m below the top of the canal due to the presence of the effluent weir downstream (see Figure 92 and drawings in the Appendix E). Therefore, the flow velocity varies proportional to the discharge.

The constriction or flow diverter is installed in order to increase the flow velocity. It is made of L-profiles bolted to the channel side walls and stainless steel sheets (see Figure 81 for construction drawing and Figure 92 as well as 93 for photographs taken during the installation). Two flanged stainless steel bearings are bolted onto the flat section of the constriction and their task is to support the lower end of each of the rotors' shafts axially and radially. Above the constriction, close to the water surface, the middle bridge is installed hosting two flanged cast iron bearings which provide radial support of the shafts and refrain the rotor shafts from vibrating, bending and buckling.

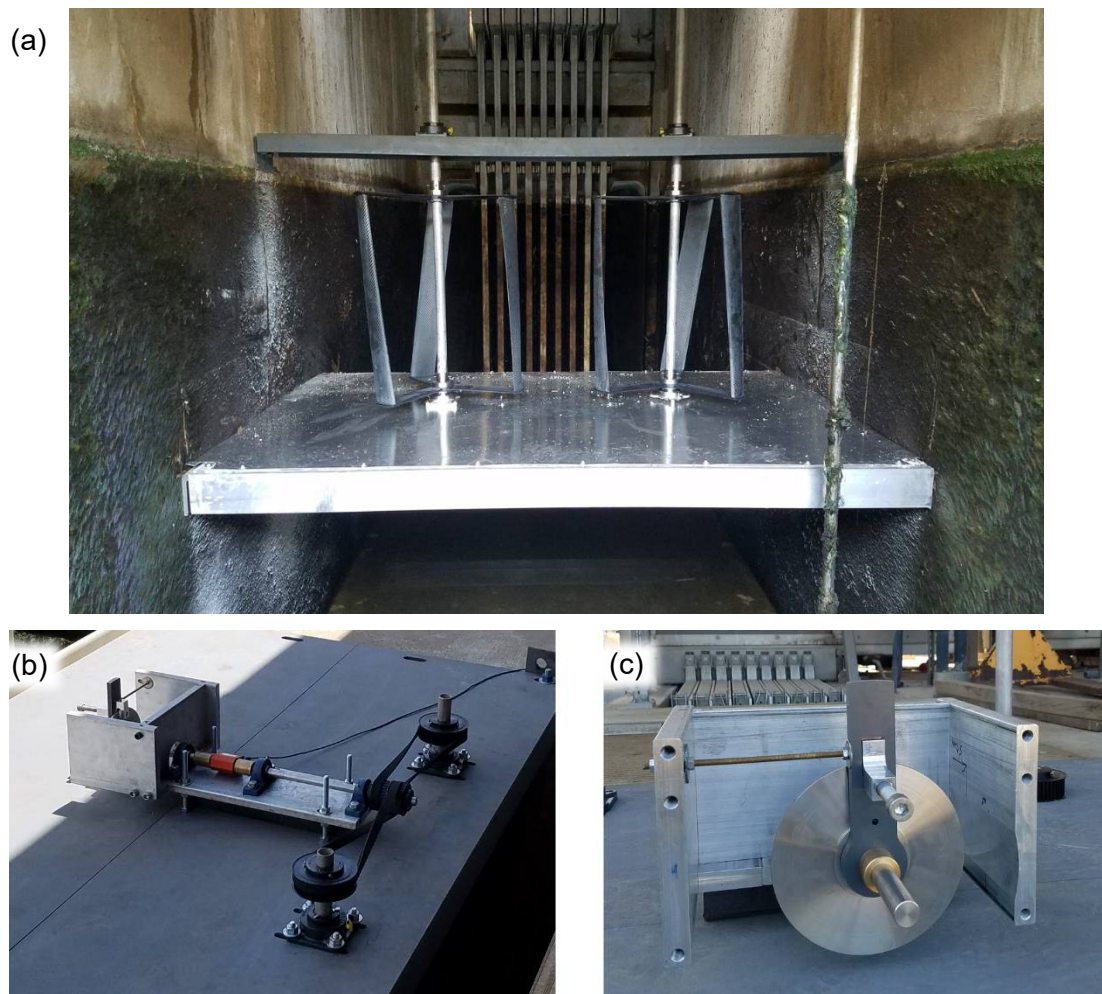


Figure 93. a) Installed constriction, rotors and middle bridge from downstream perspective; b) top bridge including belt drive and PTO with disc brake; c) Bottom left, close-up of disc brake

Further, a steel bridge is mounted across the top of the channel opening accommodating the upper flanged cast iron bearings and the PTO. The steel bridge also acts as cover of the channel.

Two 44 teeth timing belt pulleys are sleeved over the rotor shafts which are held in place via grub screws. Two 20mm wide, 1120mm long timing belts connect the large shaft pulleys with two 28 teeth timing belt pulleys which are sleeved over the main drive shaft and held in place via grub screws. Using the different sized pulleys leads to an increase in rotational speed and a decrease in the transferred torque at the common shaft with a ratio of 11:7.

The PTO's main drive shaft hosts a torque transducer (Futek TRS605) which allows quantification of  $\tau$  and  $\omega$ . Attached to the main shaft, three different devices are employed for testing:

- a) Disc brake, a mechanical braking mechanism similar to a bicycle brake
- b) Low RPM generator (DVE200)
- c) High RPM generator (LE450)

## 6.5 Procedure and Results

In order to quantify the efficiency of the turbine the flow velocity is needed. The measured mechanical power  $P_M$  and electrical power  $P_E$  is compared to the amount of kinetic power ( $P_a$ ) available to the turbine by employing Equation 1.2. The measurements of torque and rotational speed are collected at a frequency of 100Hz over a period of one minute by a Lab-Jack U6 and further analysed by a self-written code using DAQFactory®Express and MS-Excel. For the electrical tests, voltage and current are measured using a multimeter and recorded manually.

The flow velocity  $v$  is measured by a propeller meter (Global Water FP211, see Appendix H for specifications). The measurements are compared to the cross-sectional velocity as computed via the discharge data provided by the plant operator which are attached to the Appendix E.

The performance of the turbine during testing is quantified via a turbine performance curve in which the power coefficient  $C_P$  is plotted against the TSR consistent with the procedure adopted in previous chapters. The long-term and operational phase at RM Clayton aims at generating electricity for powering a display board and at gathering information about the VAT's durability, wear and tear and potential impacts on the plant operation.

For this operational phase, a PTO and PDA was designed and built at Cardiff University as presented in Chapter III and V. The PDA consists of a rectifier, a battery charging control, a dump load, a cooling fan and is connected to a 12V battery. It functions as a portable, off-grid device to use and divert the power generated by the turbine's generator. The generator charges the battery and supplies the power for monitoring purposes (e.g., by a laptop) and for operational purposes (e.g., the cooling fan of the PDA).

The field testing is divided into three phases (see also Table 15):

- Phase a                      Mechanical testing
- Phase b                      Electrical testing (low rpm (laboratory) generator).
- Phase c                      Electrical testing (high rpm generator) & hand-over.

### 6.5.1 Phase a

Figure 93 depicts the PTO setup for Phase a. The rotation and torque of the two rotors is combined to a common shaft via belts. The common shaft is held in place by three pillow block bearings with a torque transducer between bearing two and three and a disc brake at the end of the shaft.

The rotational speed and torque is recorded for one minute at a frequency of 100Hz and with a certain braking force applied. The first minute of the measurement period is conducted with free-wheeling of the rotors (i.e., no braking force applied) and the last minute measurement contains the immediate period before the turbine stalls (i.e., when the braking force is maximum and the turbine stops rotating). Three different measurement series are carried out and the results are summarized on the following pages. With the aim to calculate the efficiency of the turbine, the measured turbine power output is divided by the available kinetic energy from the flowing water. The results are shown in Figure 94 in form of turbine performance ( $C_P - \lambda$ ) graphs. In Appendices I, the variation of  $C_P$  is further investigated and compared with variations observed during laboratory experiments.

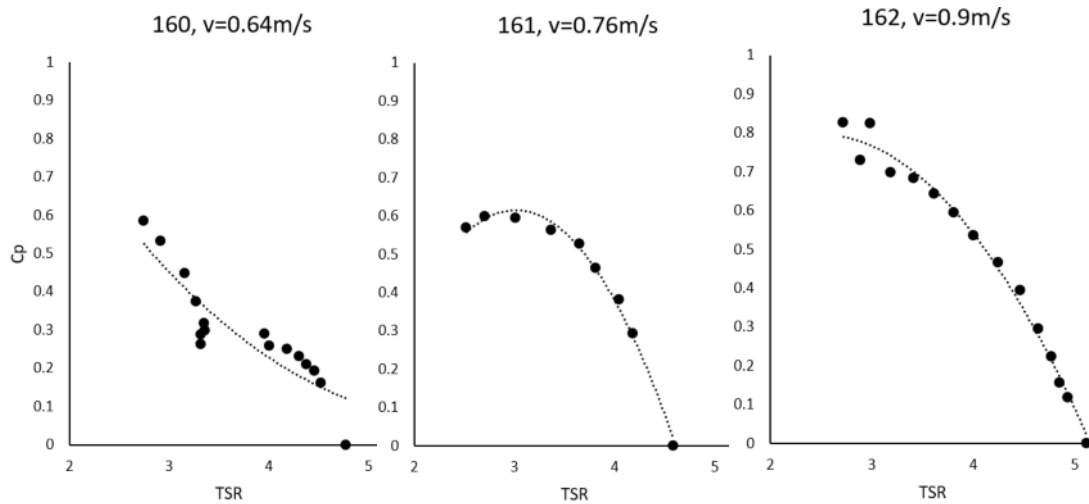


Figure 94. Turbine performance curves with  $C_p$  on the y-axis and  $\lambda$  on the x-axis, for the measured flow velocities ( $v$ ) for tests 160 - 162

The measurement of flow velocity with the propeller meter is not very accurate due to it being a point measurement at a few instants in time. Therefore, the measurements are validated with discharge data from the plant operator and are found to be within five per cent of the propeller meter measurement. Figure 95 presents turbine performance curves for the three tests and includes  $C_p - \lambda$  - curves that are obtained using the discharge data provided by the WWT plant operator. It can be seen that a minimal change in flow velocity can have a significant impact on the coefficient of performance (the smaller the velocity the higher  $C_p$ ) and on  $\lambda$  (the smaller the velocity the higher TSR) since both variables are functions of the flow velocity.

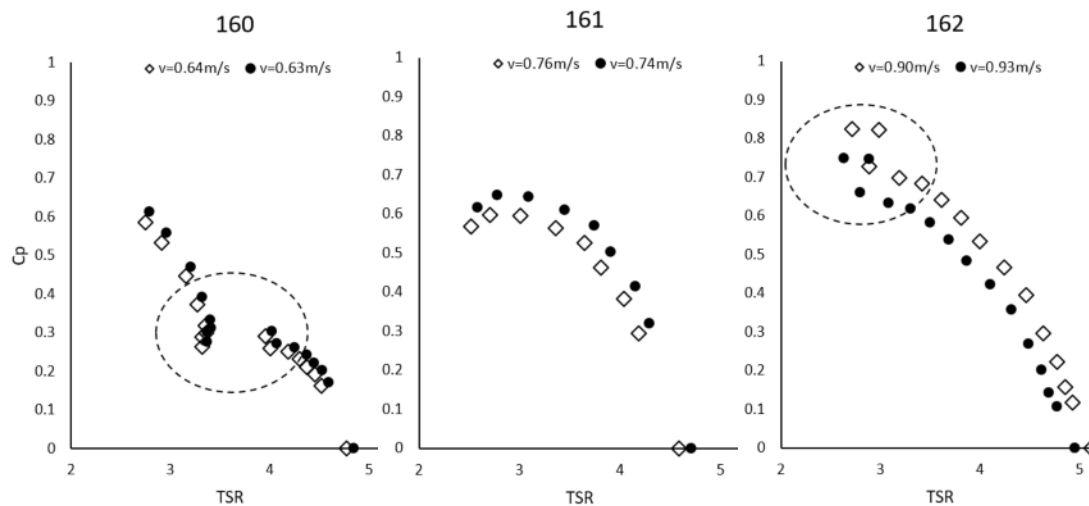


Figure 95. Test results with  $C_p$  on the y-axis and  $\lambda$  on the x-axis. Measured (rhombus) and calculated (dot) flow velocities ( $v$ )

It can further be seen that some measurement points do not follow the general trend of the curve. In the case of test 160, even a general trend is difficult to observe. The curve for test 161 has an almost ideal shape except for the last two points which are

somewhat lower than expected, however, they represent the area where the turbine is close to stalling. It is possible that the inertia of the rotors carry the turbine past the stall point. In the graph for test 162, the last two points are higher than expected. Here, it may be assumed that the discharge and, hence the velocity, has changed during testing which is not surprising given the fact that the discharge in the treatment plant always varies during the day. The time history of the discharge that is provided from the plant operator and a comparison of calculated velocities using the discharge provided by the plant and the cross-sectional area of the channel with the measured velocity are provided in the Appendix E.

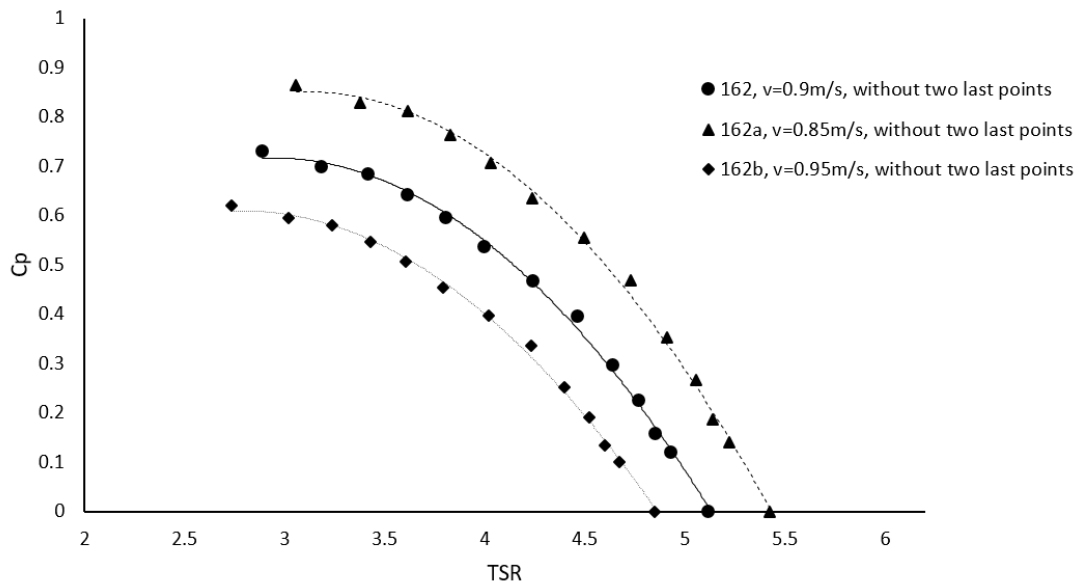


Figure 96. Results for Test 162 with  $C_p$  on the y-axis and  $\lambda$  on the x-axis considering various velocities ( $v$ )

Figure 96 presents two additional turbine performance curves, 162a and 162b together with the graph for test 162 presented in Figure 95, but with the last two uncertain measurement points removed. These curves highlight the effect of (chosen) flow velocity on the coefficient of performance. The  $C_p$  peak varies between 62% for an assumed velocity of  $v = 0.95\text{m/s}$  and 87% for  $v = 0.85\text{m/s}$ . The TSR at peak performance also varies between approximately  $\lambda = 2.7$  and  $\lambda = 3.1$ . This turbine design is expected to perform slightly worse than in the laboratory where the flow conditions are ideal and where maximum turbine efficiencies of around 80% have been achieved. In addition to the non-uniform flow conditions (due to the turbulence downstream of the UV lights and the flow acceleration from the diverter), the tested turbine employs three bearings due to the very long shaft and this introduces additional friction. Hence, the maximum  $C_p$  of test 162 is more likely to be around 70% instead of 88% as suggested by graph 162a. The TSR of slightly less than 3 is

expected, again due to the friction from bearings and belts and hence the curve 162 appears to best represent the turbine's performance for Phase a. The mechanical power output is just under 200W which is close to the rated power of the generator to be employed in Phase b.

### 6.5.2 Phase b

For Phase b testing, the disc brake is exchanged with a low rpm PMG (DVE200) as depicted in Figure 96. This PMG has been used for electrical testing at Cardiff University before. The electrical power output in terms of voltage and current is measured using two multimeters simultaneously. At the same time, rotational speed and torque is measured and recorded analogously to Phase a. Instead of applying a disk brake, the generator load is controlled using a resistor bank (see right hand side of Figure 97) and the resistance is varied manually.

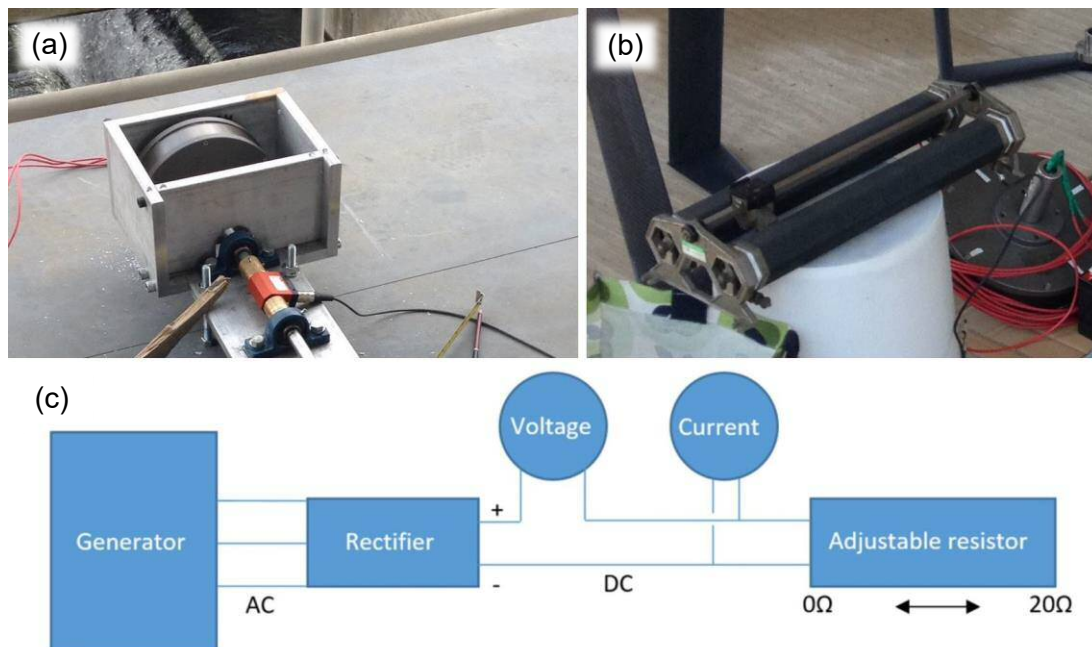


Figure 97. a) PTO of Phase b testing featuring a low rpm generator instead of disc brake; b) adjustable resistors for controlling electrical load; c) schematic of the electrical circuit for Phase b and c testing

Here, the three phases of the AC generator are attached via copper wires to an uncontrolled diode rectifier. The DC circuit consists of a resistor bank and two multimeters as depicted in Figure 97. The first reading is taken with an open circuit (resistor not attached, i.e., no load). Then, the resistance of the adjustable resistor is gradually increased until the turbine stalls. Over a period of one minute per resistor setting, the voltage and current average readings are recorded and, together with torque and rotational speed measurements from the torque transducer, the mechanical power as well as electrical power are computed.

Figure 98 shows the turbine performance curves from Phase b testing. The presented mechanical efficiency was calculated by considering a measured flow velocity of 0.9 m/s (blue, from the propeller meter) or a calculated velocity of 0.94 m/s (red, from the discharge data) and at a water level of 0.95m. There is some variation in the readings again because the discharge is not constant over the test period. The graph of Figure 98b represents a more realistic result of the performance using 1m/s flow velocity which was measured at the beginning of the test instead of the 0.9m/s measured near the end of the test. Measured data such as torque and rotational speed for mechanical power and voltage and current for electrical power are plotted versus TSR which is also presented in Figure 98. The difference between mechanical and electrical power output is much higher than previously observed in laboratory experiments where a peak efficiency of 85% was achieved. The difference from the gathered data to laboratory data is the higher torque and rotational speed from the bigger turbine. The generator is rated at 200W for 200rpm but the field testing turbine is producing ~230 Watt at 200rpm. Hence, the efficiency of the generator may be lower than 85%. Further, the resistor suffered from overheating towards the end of testing (when the electrical load becomes higher) which can be seen in the sudden drop of performance at about 150 Watt.

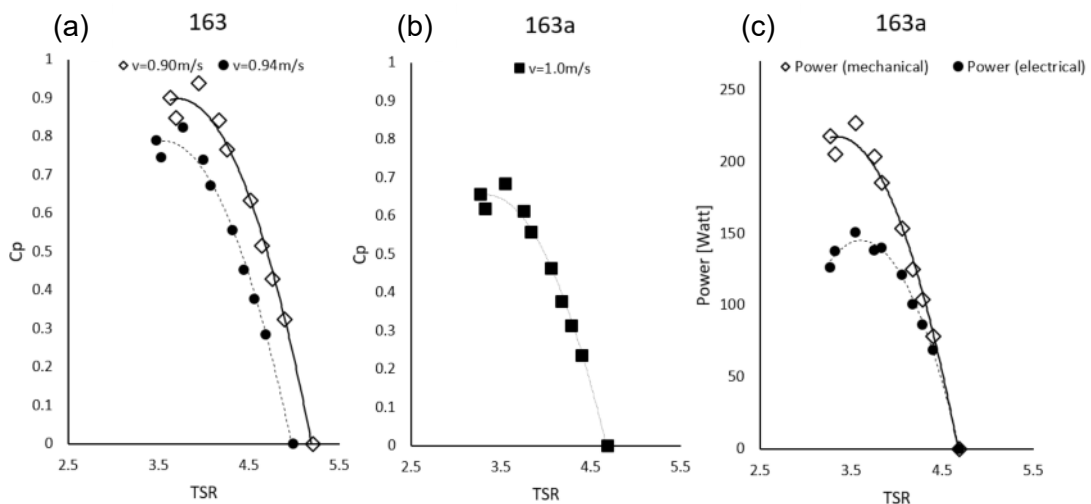


Figure 98. Performance curves with  $C_p$  on the y-axis and  $\lambda$  on the x-axis. a) Measured (rhombus) and calculated (dot) flow velocities ( $v$ ) of test 163; b) same curve as before with a velocity of 1m/s; c) power output in Watts from mechanical as well as electrical PTO as a function of  $\lambda$

### 6.5.3 Phase c and hand over

The testing in Phase c uses exactly the same setup as in the previous phase except that a high-rpm PMG is employed instead of the low-rpm PMG. Figure 99 depicts the modified generator housing including the high-rpm PMG. This generator (LE 450) has a rated speed of  $>1200$  rpm and is not designed for an efficient application with the

expected 150 – 250 rpm of the turbine at RM Clayton. Therefore, the efficiency is very low and the electro-magnetic resistance very limited which made it impossible to apply resistance big enough to stall the rotors. Nonetheless, measures were taken analogously to Phase b which are numerically presented in Table 16 instead of incomplete power curves.

The generator had been purchased initially to test the VAT in combination with a 30:1 gearbox which was not available during the tests at RM Clayton. It was planned to use the belt drive as reducer (i.e., to use belt-drive gear ratio to reduce rotational speed instead of increasing the rotation speed as previously). The main shaft would then have spun at approximately 80rpm when entering the gearbox. Consequently, with a geared rotational speed of ~2400rpm, the generator would have performed much better and provided more meaningful data. However, since the produced electrical power in the operational phase is only used to charge a battery which supplies power to LED lights of a display board, and hence very low power consumption was expected (approximately 6 Watt for 12 hours per day), the high-rpm generator was installed anyways and remained as a permanent installation at RM Clayton. It was further anticipated to learn more about the long term behaviour of all components such as bearings and belt-drive.

Table 16. Measured values (averaged) of electrical and mechanical quantities of Phase c

No.	163, measured flow velocity = 0.76m/s					
	Torque [τ]	Omega [ω]	Mechanical Power extracted [PM]	Voltage [V]	Current [A]	Electrical Power extracted [PE]
	Nm	rad/s	Watt	Volt	Ampere	Watt
1	0.0	23.9	0.0	16.2		0.0
2	0.62	23.5	14.7	10.2	0.6	6.1
3	0.77	23.4	18.0	8.6	0.82	7.1
4	0.91	23.5	21.4	7	1.04	7.3
5	1.05	23.6	24.8	5.6	1.24	6.9
6	1.22	23.7	28.9	3.9	1.49	5.8
7	1.35	23.8	32.2	2.5	1.73	4.3

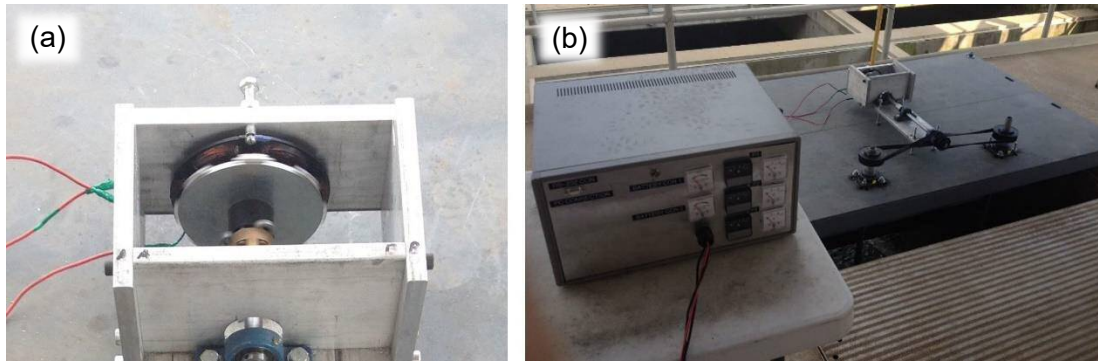


Figure 99. a) PTO of Phase c with high-rpm generator installed; b) PDA connected to generator

## 6.6 Summary

The hydrokinetic twin VAT in 1:3 scale was successfully built, installed and tested at RM Clayton. Conclusions and recommendations for future deployments from design to operation of the turbine can be summarised as follows:

**Design:** The turbine was designed based on successful laboratory tests carried out at Cardiff University. For the particular deployment site a flow diverter was designed to increase the flow velocity approaching the turbine in the otherwise very slowly flowing UV channel. The rotor design included a very long stainless steel thick-walled tube in order to save weight as compared to a solid shaft. However, the outer diameter varied slightly over the length and it was difficult to sleeve the bearings over the shaft. Hence a larger bearing diameter had to be used and the shaft did not fit well which led to unnecessary vibration and possibly performance losses. For future deployments, shaft and bearings should be chosen very carefully, ideally a solid shaft should be used.

**Manufacturing:** Except for the spokes, the rotor and PTO were manufactured at Cardiff University due to the availability of high-quality machining equipment and carbon fiber fabrication tools. Abuck Ltd., Atlanta, manufactured most of the material for the two bridges, delivered it to the site and installed them. The spokes, casted out of glass-reinforced nylon, were manufactured at Nylacast Ltd., Leicester, and came out fairly rough due the relatively crude post-processing. Also, manufacturing and shipment of the spokes was delayed. The manufacturing procedure should be reviewed.

**Installation:** The installation was successfully led by Abuck Ltd., Atlanta, with support from Emrgy Inc., Atlanta, and myself. The installation took longer than expected mainly due to missing or not matching components. The reasons for these delays vary but in general it was observed that a more careful design (see earlier notes on shafts) and preparation is necessary. In particular, it should be ensured that precision-

machined/manufactured components such as shaft and bearings match perfectly prior to installation/deployment.

Testing: The test procedure was identical to the one used for the laboratory tests at Cardiff University. The routine was successfully applied in more than 150 laboratory tests. The only uncertain quantity was the flow velocity due the varying effluent discharge. Initially, after installation, three channels were in operation and the discharge/flow velocities were very low (test 160,  $v=0.64\text{m/s}$  & 161,  $v=0.76\text{m/s}$ ). After the plant manager closed one of the three channels, the velocity increased to approximately  $v=0.9\text{ m/s}$ . Due to the fact that the tests took place in a fully operating treatment plant, the discharge varied and was never really constant over a typical total testing time of approximately half an hour (for a time history of the discharge see Appendix E). Hence, the quantification of the rotor's TSR and  $C_P$  include some uncertainty. In order to minimise the uncertainty, the measured approach flow velocity was cross-checked with discharge data from the plant operator and found to vary within 5%. Mechanically, a maximum  $C_P$  value of around 70% for an operation at TSR 3 was achieved. Two generator types were also tested and the water-to-wire turbine efficiency dropped dramatically, mainly due to the losses in the permanent magnet generator and the electrical circuit. In the future, it will be important to employ a high-efficiency generator and to match generator ratings and rotor outputs perfectly in terms of rotational speed and applied electrical load. For the latter, the electrical tests controlled the electrical load via a resistor bank manually. In the future, this aspect needs to be achieved automatically by a power controller.

Operation: The turbine is currently in operation and has been equipped with a PTO and PDA which divert the generated power either to a battery or a dump load (see Figure 100). The long-term operation of the turbine is important to gather information about wear and tear of individual components and to test the durability of the VAT. Regular site visits have been scheduled to observe the proper functioning of the system.

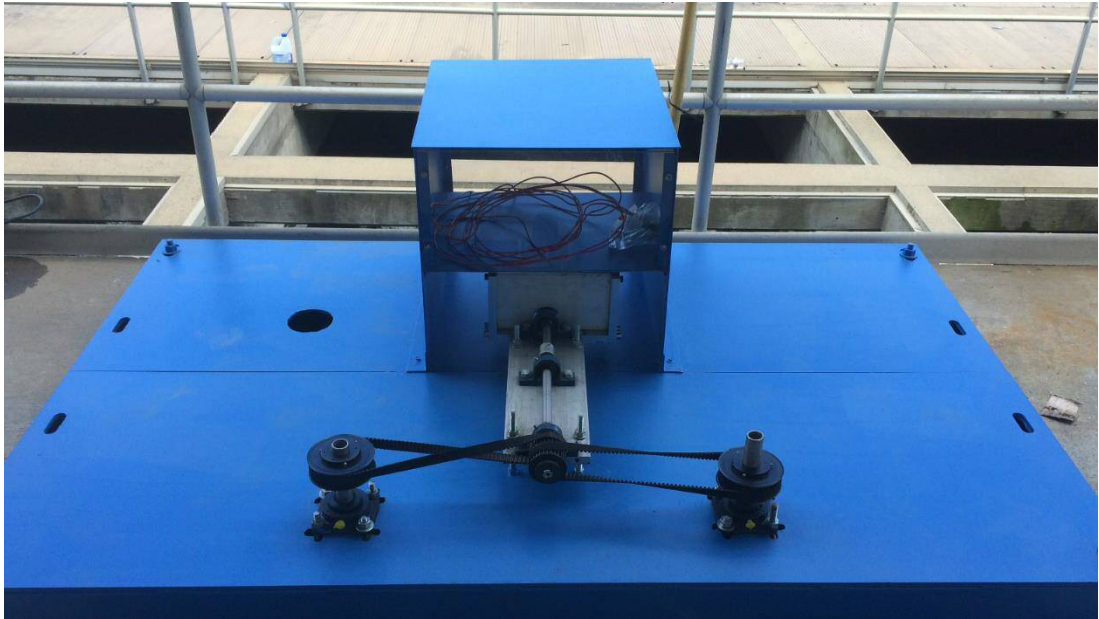


Figure 100. Top bridge of VAT system including PTO and PDA/battery case

In conclusion, the twin turbine showed very promising performance during field testing. Due to a reduced solidity ( $\sigma_{\text{field}} \approx 16.5\%$ ,  $\sigma_{\text{laboratory}} \approx 21\%$ ), the TSR increased without compromising on performance ( $\lambda \approx 3$ ,  $60\% < C_P < 75\%$ ) considering the increased resistance from an additional set of bearings and the more turbulent flow. In contrast to the laboratory turbine, the up-scaled turbine self-started at all times which is seen as a justification for the overall twin turbine design. For full scale testing, a further reduction in solidity is anticipated as presented in the following chapter.

## VII. Application in a fresh water canal

### 7.1 Introduction

The twin turbine system has been developed and refined through various stages, starting with a novel design that was tested as a 1:10 scaled model in the laboratory (Chapter III). The model turbine was successively refined and the system was up-scaled to 1:3 scale and in May 2017 deployed at RM Clayton Water Treatment Plant in Atlanta (Chapter VI). The twin turbine system was installed in a UV treatment channel where it underwent further successful testing and during which the turbine's laboratory performance was confirmed. The next step in the development stage of the turbine system was the deployment of a full scale turbine. For this stage, the South Boulder Canal (SBC) near Denver, US was chosen as deployment site. SBC is operated by Denver Water and diverts water from Gross Reservoir into Ralston Reservoir. The canal is divided into three sections (A, B and C) and, ultimately, ten turbines were installed. In June 2017, the first turbine was deployed and tested in section A, which is the last section of the SBC before the water enters the Ralston Reservoir via a dragon's teeth spillway structure (see Figure 101). The section is approximately 30m long and 5m wide, has a rectangular cross-sectional shape and the turbine was placed at the very end of section A. In the following, the turbine design, the testing procedure and the data analysis are documented.

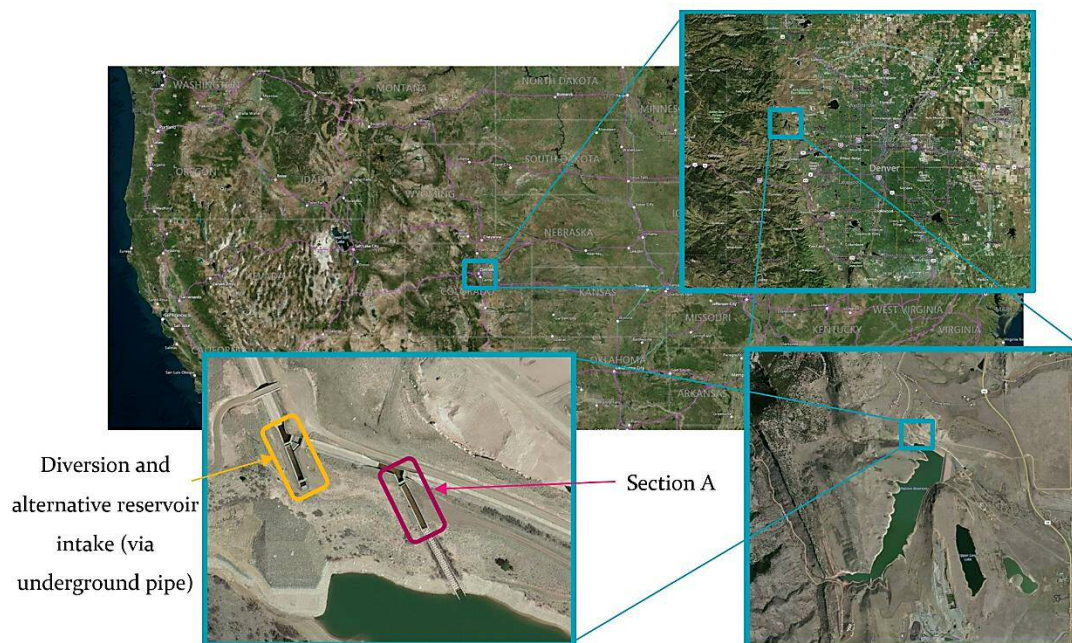


Figure 101. Aerial images of section A of the South Boulder Canal at Ralston, Colorado, US [157,158]

## 7.2 Turbine design and testing environment

The turbine assembly (see Figure 102) was designed and built by different parties funded by Emrgy Inc., Atlanta. The proposed hydrokinetic twin turbine design is based on the observations from Chapter III - V and was executed and supplemented by Egnuity Works Corporation, Atlanta. The installation of the turbines was performed by Vivid Engineering Group, Denver and Denver Water, Denver, the operator of Ralston Reservoir and SBC.



*Figure 102. Hydrokinetic twin VAT in full scale, installed in South Bolder Canal near Denver*

The turbine consists of a concrete/steel structure, two rotors (machined aluminium spokes and blades, stainless steel shaft), a chain-drive-train, a speed increaser gearbox and an asynchronous generator as depicted in Figure 103. The rotors have a height of 0.8 meters and a diameter of 1.36 meters. The twin-rotors are counter-rotating, i.e., the right rotor rotates clockwise and the left rotor rotates anticlockwise. Instead of a belt drive, each rotor shaft hosts a sprocket and the torque generated by the rotors is transmitted via a chain which drives the gearbox and eventually the generator. The gearbox has a ratio of 30:1 and increases the rotational speed and reduces the torque accordingly. The generator has a rated power output of 10 kW. The focus of the tests reported here is on the mechanical power generated by the turbine and hence the gearbox and generator were replaced by a mechanical PTO before deployment.

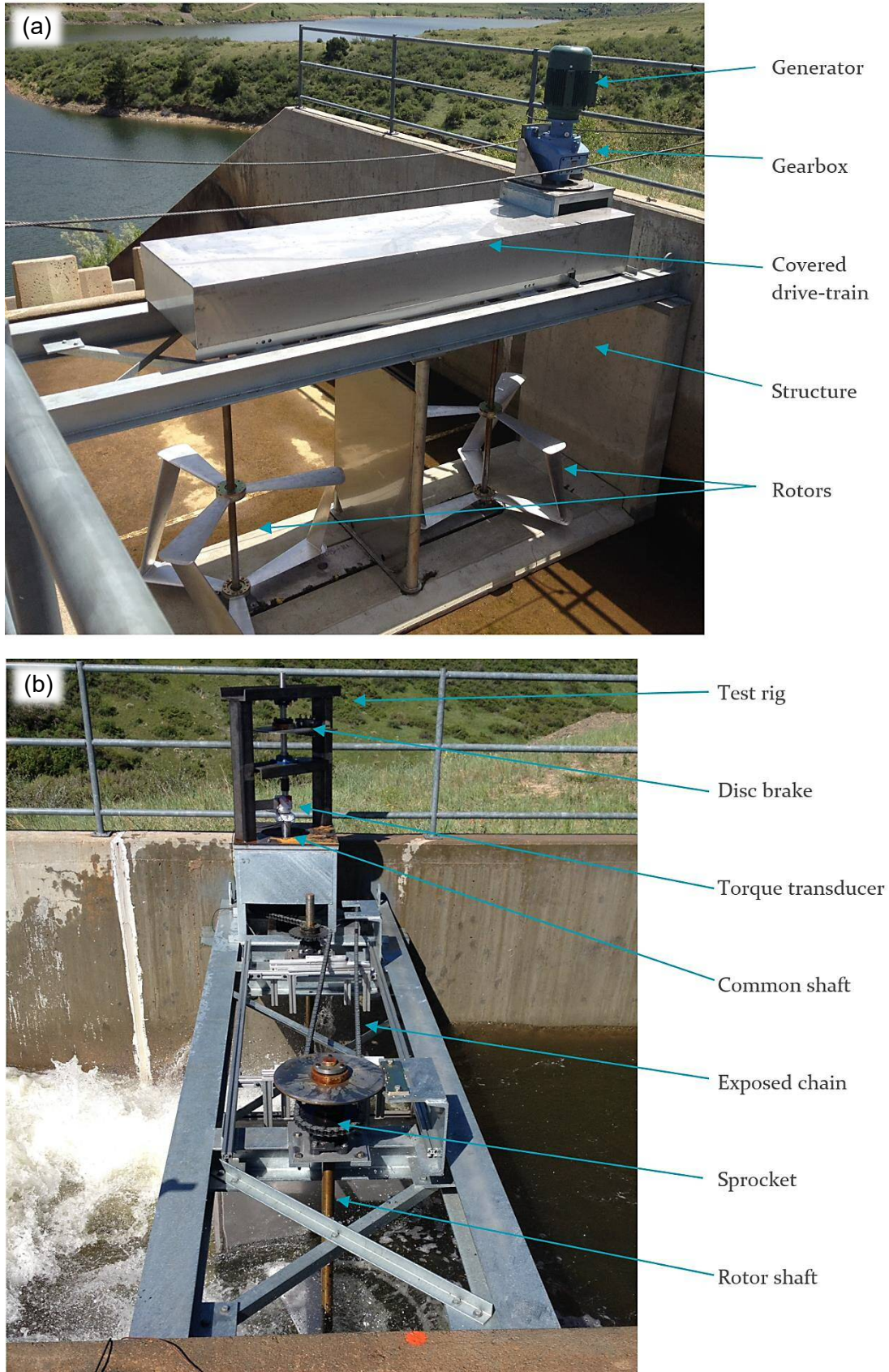


Figure 103. Hydrokinetic twin turbine and its main components installed at Ralston Reservoir. a) As in operation including gearbox, generator and chain cover; b) as tested including mechanical PTO

### 7.3 Procedure and results

As described in previous chapters, the turbine's performance was tested by comparing the mechanical power at the main PTO shaft with the hydrokinetic energy available in the flowing water. The gearbox/generator assembly was replaced with a mechanical PTO that consists of a hydraulic disc brake and a torque transducer as depicted on the left of Figure 104. A torque transducer similar to but with a higher capacity as that used previously in laboratory and field testing (see Appendix H for details) was placed immediately before the disc brake so that the measured torque and rotational speed included all losses of the rotor (mainly in the bearings) and the chain-drive.



Figure 104. a) Mechanical PTO featuring hydraulic disc brake and torque transducer; b) VAT rotor prior to installation

The flowrate  $Q$  in the SBC was provided by Denver Water and confirmed by measurements taken by the United States Bureau of Reclamation. The flow velocity was calculated by dividing the discharge  $Q$  by the submerged cross-sectional area  $A$  of the turbine housing at the position of the rotors. The estimation of  $A$  requires water level measurements just upstream and downstream of the housing and the average of the two readings is taken as the water depth.

The rotational speed and torque were recorded for one minute at a frequency of 200Hz with a certain braking force applied. The first one minute measurement period was conducted at free-wheeling of the rotors (i.e., no braking force applied) and during the last one minute measurement was just before the turbine stalled, i.e., when the braking force was maximum and the turbine stopped rotating. Five tests (Test 165 - 169) were carried out and the results are summarised on the following pages.

The time-averaged raw data from the torque transducer (torque and rotational speed) and the computed mechanical power (including drive-train losses) for tests 165 - 168 are presented in Figure 105 in the form of the previously established turbine performance curves. For each of the five tests the efficiency of the turbine, i.e., comparing the measured turbine power with the available kinetic energy from the flowing water at the turbine housing's cross-section, is computed using Equation 1.3 and the TSR is calculated using Equation 1.12. This is done for every 1 min measurement interval.

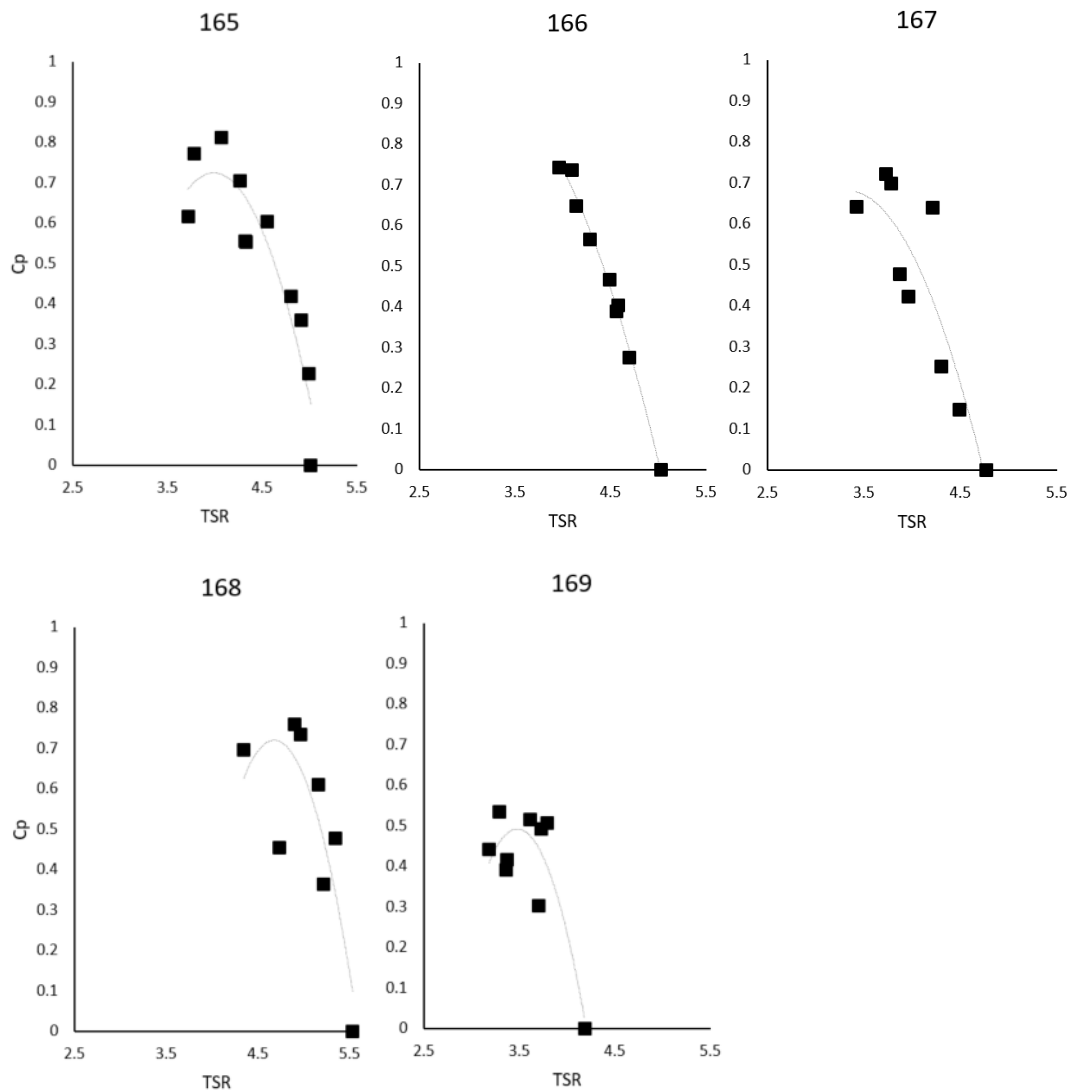


Figure 105. Turbine performance curves for five performance tests conducted, based on a flow velocity of  $v=1.56\text{m/s}$

The discharge was provided by the channel operator Denver Water and was supposedly constant during the tests at  $Q = 250\text{cfs}$  ( $7.08\text{m}^3/\text{s}$ ). Based on the average of measured upstream and downstream water depths (at the upstream and downstream side of the housing, see Appendix F), the submerged cross-sectional

area at the turbine shaft was calculated as  $A = 4.54\text{m}^2$ . With the given constant discharge, the flow velocity was computed as  $v = 1.56\text{m/s}$ . During tests 167 and 169 it was visually observed that the water level dropped slightly, suggesting that the discharge was not constant. It was observed that the rotors were sometimes fully submerged (during Tests 168), and sometimes not (during Tests 165, 166, 167 and 169) which has an impact on turbine performance. The turbine achieved peak efficiencies consistently above 70% during tests 165, 166, 167 and 168, whereas the peak efficiency of test 169 is lower with around 50%. As can be seen in the dashed trend lines of turbine performance curve, some data points lie clearly off the trend line, which underpins the variation in the flow conditions the turbine was operating under. The variation could be due to several factors, such as sudden discharge surges (increase, e.g., peaks around  $C_p = 80\%$  during test 165, or decrease, very low  $C_p$  values during test 169) or strong turbulence which would result in sudden and local velocity spikes and drops.

(a)



(b)



Figure 106. a) Rotors partially submerged and; b) fully submerged

The submergence of the rotor has a great effect on turbine performance as reported in Chapter III of this thesis. Obviously, if the rotor is fully submerged the entire blade surface area will be in contact with the water and therefore, more energy can be

extracted in comparison to a rotor that is not fully submerged and for which not the entire blade area is in contact with water. In addition, the blade hydrodynamics is disturbed if the blades are not fully submerged, e.g., by air-entrainment which reduces the density of the water that is in contact with the blade, and hence, this results in a reduction of lift forces generated in this area. On laboratory scale, the performance dropped by more than 50% for an emergent rotor. It was observed that during tests 165, 166, 167 and 169, the top part of the rotor, mainly the upper spokes, were slicing through the water surface during their upstroke movement (see Figure 106). This resulted in significant splashing and noise and most likely in additional drag torque on the rotor shaft which ultimately reduces the turbine's efficiency.

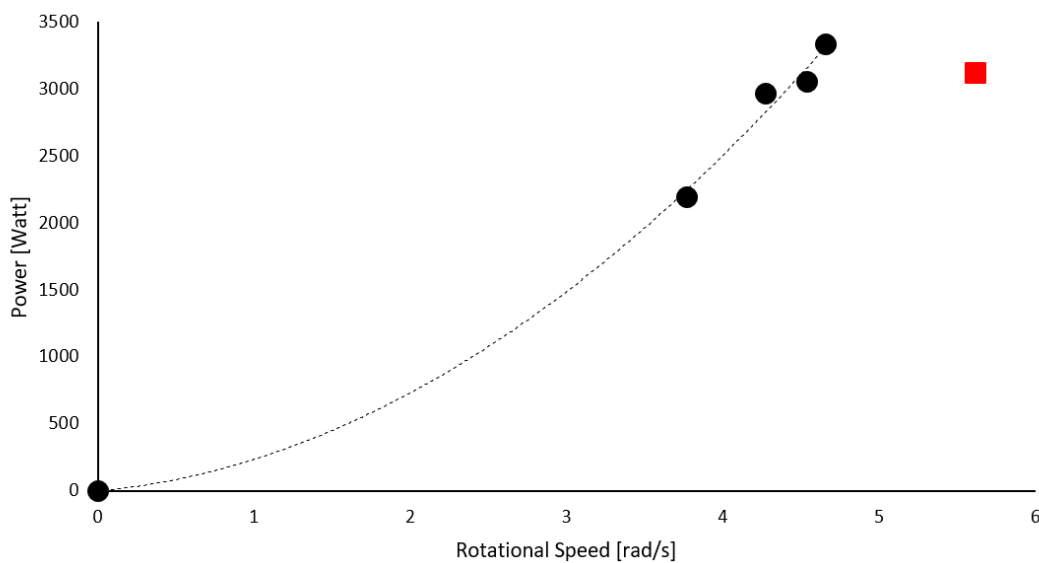


Figure 107. Turbine's mechanical power vs rotational speed curve for highest power reached all tests including a trend line through data points of tests 165, 166, 167, 169 (dots). Red square indicates peak power achieved during test 168

For tests 165-167, still relatively high efficiencies,  $C_P > 70\%$  were achieved. The peak of the performance curve in test 169 is only around 53%, and it seems that this is due to the discharge during this test being probably lower than 250cfs. This is supported by Figure 107, which plots the extracted power at peak performance on the y-axis as a function of measured rotational speed. The dots represent tests 165, 166, 167 and 169 fall very nicely on the dashed trend line. The lower data point is said test 169, and less discharge resulted in less rotational speed and less power produced. Test 168 was the only test where the rotor was fully submerged, but unfortunately, during this test, the discharge reduced and the test had to be aborted because at some point the rotor was not fully submerged anymore. The red data point clearly falls outside of the trend line. The rotational speed appears to be too high (point is too far to the right) and, as can be seen from Figure 107, with a TSR for the maximum power of

approximately 5, suggesting that the maximum power point was not yet reached. It re-mains to be seen whether a fully submerged rotor will be able to achieve even higher efficiencies than the ones achieved in tests 165, 166, 167, 169.

### 7.4 Scalability

The purpose of using dimensionless quantities for the turbine performance curve is to be able to demonstrate the scalability of the system, in other words, to be able to predict the turbine's performance irrespective of its size. Figure 108 presents three turbine performance curves obtained under different conditions for three turbines of different sizes, i.e., the laboratory turbine, the field testing turbine deployed at RM Clayton, Atlanta and the full scale turbine deployed at SBC, Denver. Due to the fact that each turbine has a slightly different rotor solidity the TSR was multiplied with the solidity to account for the fact that rotational speed is directly affected by TSR, i.e., the rotor spins faster at lower solidity and slower at higher solidity.

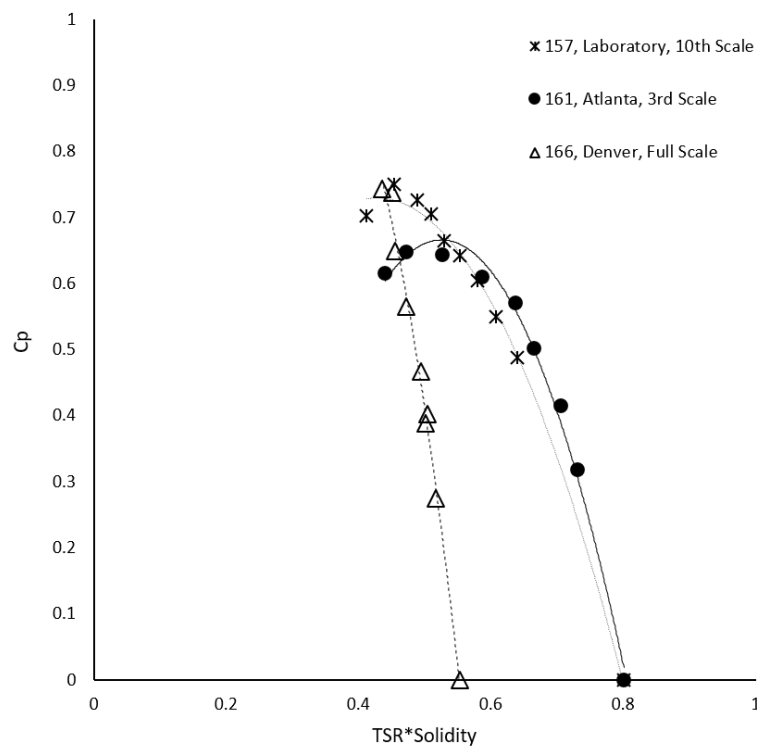


Figure 108. Performance curves of three selected tests for laboratory, field testing and application scale, operating in different environments and at different sizes

First of all, it seems that the three curves are very similar and peak efficiencies are around 70%. Secondly, the rotational speeds (times solidity) at free-wheeling are very similar for the Atlanta and laboratory turbines, whereas the Denver turbine appears to rotate slower than the other two. This is most likely the effect of non-submergence and aforementioned drag torque created when the arms slice through the water. In contrast, the Denver turbine appears to yet feature a greater peak efficiency and this

is most likely due to the fact that the Denver turbine operated in a housing whereas the other two turbines did not. Apparently, the Denver turbine benefitted from the additional flow acceleration caused near the housing side walls on the upstroke of the rotor. The effect of the housing on the turbine performance could not have been quantified in the laboratory and in Atlanta due to the limited width of the flume/canal.

### 7.5 Summary

The hydrokinetic twin turbine was successfully built and deployed in the South Boulder Canal near Denver Water's Ralston Reservoir, Denver, Colorado, US. During the tests, the turbine was subjected to a flowrate of  $Q \approx 250\text{cfs}$  and mechanical torque and rotational speed were measured at the main shaft of the turbine whilst different loads were applied using a hydraulic disc brake. The turbine achieved a coefficient of performance consistently above 70% and was operating at a TSR of up to 4 for most of the tests. During peak performance, up to 3.4kW of mechanical power (including drive-train losses) were generated.

However, significant variation in the outputs were observed. During one of the tests the turbine appeared to underperform, and the  $C_P$  was only about 50%. Detailed analysis of the measured torque and speed data suggested that the discharge must have decreased below the given 250cfs. The tests supported that rotor submergence is a critical factor in the operation of the turbine. An emergent rotor suffers from the additional drag torque when the rotor arms are slicing through the water surface and blade hydrodynamics are compromised when air is entrained. The turbine tests, however, highlighted that the turbine's efficiency remains high despite rotor non-submergence and it appears that the turbine housing, which provides local accelerations and thus high velocities that the rotor blades are exploiting during the rotor's upstroke, has a positive influence on turbine performance. The tests suggest that a fully submerged rotor operating in a turbine housing might be able to achieve efficiencies of above 80%.

Finally, the scalability of the turbine was confirmed, the full-scale turbine at Denver operated similarly, if not better, than its smaller-scale versions tested in the laboratory and in Atlanta. In the meantime, all ten units were installed and will be tested with the focus on turbine performance in an array, flow constrictions, backwater and electrical control.

In the following, the development stages of the VAT from a concept to a full-scale system are summarised and assessed with help of technology readiness levels.

## VIII. Technology readiness

This chapter is published in a similar form as a journal paper to the Journal of Power and Energy Engineering with the title “Technology Readiness of a Vertical-Axis Hydro-Kinetic Turbine”, co-authored with Prof. Thorsten Stoesser, Ms. Emily Morris and Ms. Madeleine White [159]. Some aspects of this chapter were already covered in previous chapters but it was decided to keep it close to its submitted form with the intention to present it as a self-contained chapter.

### 8.1 Introduction

Growing energy demand and climate change are the main drivers for the fast evolution of novel energy conversion systems. While energy production during the second half of the past century was focused on large-scale fossil or nuclear power plants, the 21<sup>st</sup> century might be the era of eco-sensitivity, sustainability and the decentralisation of power generation. In other words, many small, “green” generation units can replace a few large, environmentally questionable plants with the benefit of low capital costs, reduced transformational energy losses and potentially zero carbon emission [22].

Water current turbines, also called hydrokinetic or in-stream turbines, have received a growing interest in many parts of the world. Two main areas where hydrokinetic devices can be used for power generation purposes are tidal currents and river streams. These turbines generate power from the kinetic energy of a flowing stream of water without the use of a dam or a barrage and so that consequently do not need to interfere with the natural course of rivers. Water current turbines can be installed in any flow with a velocity greater than 0.5 m/s [160]. Because of low investment requirements and operational costs, hydrokinetic turbines promise to be cost-effective in comparison to other technologies. The continuous supply of electrical energy is a big advantage in comparison to solar or wind power.

On the following pages, the successful development of a hydrokinetic turbine for harvesting energy from flowing water in man-made channels (such as water-treatment plant effluents, irrigation channels, etc.) is described and assessed with help of technology readiness levels (TRL). As shown in Table 17, TRL is a scale ranging from 1 through 9, pioneered by the NASA and modified by the US Department of Energy (DOE) for identifying a technology development maturity. The purpose of the TRL characterisation is to help assessing a technology development process and iterating the design with respect to matching technical scope, schedule, costs and safety [161].

Table 17. Technology Readiness Levels from DOE guide, without detailed description [161].

Relative Level of Technology Development	Technology Readiness Level (TRL)	TRL-Definition
System Operations	TRL 9	Actual system operated over the full range of expected mission conditions.
	TRL 8	Actual system completed and qualified through test and demonstration.
System Commissioning	TRL 7	Full-scale, similar (prototypical) system demonstrated in relevant environment.
	TRL 6	Engineering/pilot-scale, similar (prototypical) system validation in relevant environment.
Technology Development	TRL 5	Laboratory scale, similar system validation in relevant environment.
	TRL 4	Component and/or system validation in laboratory environment.
Research to prove feasibility	TRL 3	Analytical experimental critical function and/or characteristic proof of concept.
	TRL 2	Technology concept and/or application formulated.
Basic technology research	TRL 1	Basic principles observed are reported.

## 8.2 Technology concept (TRL 1-3)

### 8.2.1 Overall design

The aim of the energy conversion system presented here is to convert the movement of flowing water in a channel into mechanical torque and further, into electricity in the most efficient and sustainable way. Each component of the turbine system has been designed to integrate as a unit and can be split into 5 subsystems (structure, rotor, drive train, gearbox, power take-off).

The concrete structure comprises four individual parts (a bottom plate, two columns and a bridge) and serves several purposes: as a structural member to hold the turbine components in place safely and as a gravity base (stays in place due to its weight) which makes additional foundation unnecessary. In operation, the bridge is not submerged and hosts the power take-off which consists of drive train, gear box and generator. The structure contains a co-rotating vertical axis twin rotor system which is placed between bridge and bottom plate. The rotors are held in place by four bearings. Each rotor consists of a stainless-steel shaft, three hubs, six spokes and three blades. As soon as water flows across the rotors at a certain minimum speed, the airfoil-shaped blades generates enough lift to start rotating.

The rotational movement of the rotor is transferred via the two rotor shafts to a belt drive which consists of two 90° twisted timing belts, two large pulleys, two small pulleys and a horizontally oriented main shaft. The belt drive enables transferring the torque from the two rotor shafts onto a main drive train shaft and allows a speed or torque adjustment to appreciate gearbox or generator specification. Attached to the main drive train shaft is a gearbox and subsequently an electrical generator (see Chapter III for further details). A patent was filed in October 2017 [98].

### 8.3 Technology development - Laboratory testing (TRL 3-5)

The laboratory tests were undertaken in the Hydro-Environmental Research Laboratory at Cardiff University. For testing the turbine, a 17m long, 1.2m wide and 1m deep flume was used. For most experiments, the water depth was set to 0.5m. The water is driven by an axial flow impeller which allows flow speeds of up to 1.5 m/s at the given water depth. The channel side walls are made out of glass which allows visual observations during testing.

The rotors were mounted to the bottom of the flume via lubricated stainless steel bearings which were screwed onto a PVC board that was glued to the flume bed. The PVC board has various threaded holes which allow for different rotor positions. The top of the rotors are held by pillow block bearings which are attached to a movable bridge across the top of the flume allowing a rotor displacement in any direction. Further, the bridge accommodates the PTO consisting of drive train, generator and measurement equipment.

In order to quantify the mechanical output of the twin-rotors, a torque transducer (Futek TRS605) was affixed at centre position of the main shaft. Either a disc brake or a generator was attached to the other end of the main shaft in order to apply a

resistance to the rotors. The measurements of the torque transducer were collimated by a Lab-Jack U6" and analysed by DAQFactory®Express and MS-Excel®.

More than 200 individual tests were conducted with the target to study and optimize the rotor, the housing structure and eventually the twin-rotor assembly. In the following, the researched aspects are individually introduced, theoretically explained and the results presented and discussed.

### 8.3.1 Experimental rotor optimisation

In contrast to a straightforward rotor design with very little moving parts, the hydrodynamics of VATs are complex due to a constantly changing angle of attack and the interaction of vortices [68]. Numerical research shed light on the detailed flow-turbine interaction. Large eddy simulations (LES) [72,162] and Reynolds averaged Navier-Stoke (RANS) methods [163,164] were successfully applied. Further, research outcomes from vertical axis wind turbine studies are considered even though a straight translation to the VAT application in water with its much higher density and lower flow velocities is not possible [165–167].

Considering outcomes from previous studies undertaken at Cardiff University [76, 99, 104], the most promising design parameter were chosen, experimentally tested, compared and analysed. In the following, only the final design is described. Each rotor has a diameter of 360mm and consists of: a 20mm stainless steel shaft; two hubs to host the six spokes and three twisted blades of 300mm height. The performance of the rotor was assessed by quantifying its  $C_p$  and plotted as a function of its TSR. At a flow velocity of 1.09m/s, the rotor achieved a  $C_p$  of up to 60% at a tip speed ratio of 1.9.

### 8.3.2 Twin turbine testing and optimisation

The aim of employing two rotors in a turbine system is to: generate more than twice the amount of energy than a single rotor with the equivalent swept area; improve the self-starting behavior; reduce torque fluctuations; and simplifying the PTO. [168] suggested that the optimally configured twin system may benefit from an increased power output of 25% and a reduction of torque fluctuations. However, it was also noted that the highest performance setting may not coincide with the least torque fluctuations [168,169].

In this study, the focus is on observing the best performing twin setup by optimising the: i) direction of rotation; ii) spacing between the rotors; and iii) rotor synchronisation. The blockage ratio  $\beta$  was constant at 36%. Several studies such as

[170,171] have investigated the impact of blockage on performance and how to appreciate this issue which comes from wind tunnel experiments where side wall effects from the testing environment had effects on the flow characteristics compared to an application in nature where no walls constrain the flow. However, the researched turbine is designed to operate in a blocked environment and a potential blockage correction was therefore not applied.

The torque a blade generates during a revolution is not constant and peaks between  $0^\circ$  and  $90^\circ$  [66]. It was therefore decided to assemble the rotors counter-rotating in such a way that their torque peak is towards the centre of the channel where the velocities are expected to be the highest. It was shown that the efficiency peaked at 78%.

Another parameter tested is the distance between the two rotors. Only symmetrical arrangements were tested with the centreline of the channel being the line of symmetry. Four different axis to axis spaces (1.4D, 1.5D, 1.6D and 1.75D) were tested in order to observe the best performing spacing between the rotors. For an axis to axis spacing of 1.5D, the  $C_P$  reached 79% at a flow velocity of 0.9m/s and 74% at a velocity of 1.09m/s which equates to an increase in efficiency of 23% compared to the previously described single rotor at 1.09m/s.

The twin rotor design includes the concept of having just one PTO for both rotors by occupying a timing-belt drive which combines both rotor motions to one common shaft instead of occupying two separate PTOs with much higher investment costs. Therefore, it was tested whether the combination of the motion and synchronisation of the rotors results in a disadvantageous performance compared to having both rotors spinning independently. It was confirmed that both, rotational speed and performance in the combined case ( $\lambda = 2.1$ ,  $C_P = 75\%$ ) lacked in comparison to individual rotor deployment ( $\lambda = 2.5$ ,  $C_P = 78\%$ ) which is due to the additional drag torque of the belt drive and PTO bearings. However, losses due to a second PTO were not considered.

### 8.3.3 Closure

The twin turbine design (scale 1:10) was successfully tested in the laboratory and efficiencies of more than 75% were achieved (detailed conclusions and recommendations are listed in the Summary section of Chapter III). It can be concluded that the system has reached TRL 5 and is ready for up scaled field testing in a real channel environment (TRL 6). Integrating the gearbox is planned for TRL 7, a functional power control and grid integration is planned for TRL 8.

## 8.4 Pilot scale testing (TRL 6)

The next step in the development of the turbine is to upscale the turbine (scale 1:3) and demonstrate its successful operation in a relevant environment with the goal to achieve TRL 6.

An upscaled version of the laboratory-scale twin-rotor vertical axis turbine system was designed and deployed in a UV radiation channel, the last stage of water treatment at the RM Clayton water treatment plant in Atlanta, Georgia. The deployed turbine consists of two low solidity, three-bladed, counter-rotating rotors, a belt drive to combine the rotational motion and torque to one shaft and a PTO system. In order to increase the flow velocity and achieve maximum performance, a flow diversion structure was installed in the channel. In the following, the steps from design to deployment are outlined and the test results in the form of power curves are reported (see Chapter VI for further details).

### 8.4.1 Testing environment and turbine design

The UV radiation channel is approximately 1.9m wide and 4m deep, and the inflowing water is controlled via a rectangular weir and a gate. The water flows at a depth of approximately 1.9m through the UV-radiation lamps upstream of the turbine rotors. The flow diverter's function is to force the water to flow through a smaller cross-sectional area thereby increasing its velocity so that reasonable amounts of hydrokinetic energy are available for extraction. The water then drives the two counter-rotating rotors and consequently the main drive shaft which is positioned on a PTO bridge above the channel. Downstream of the rotors, the water discharges over a weir into a channel which eventually releases the treated water into the Chattahoochee River.

The main aim of the flow diverter is to reduce the cross-sectional area of the channel with the aim to increase the flow velocity in the remaining cross-section. It is shaped to minimise hydrodynamic losses in the form of dead zones or recirculation zones and to smoothly accelerate the water before approaching the rotors by maintaining its slope just below 30°. The upstream extent of the constriction is limited by the UV lights clearance radius. The bottom shaft bearings of the rotors are attached to the constriction.

The water depth in the UV channel is approximately 1.9m, however the entire depth of the UV channel is approximately 4m. The PTO system is located on a bridge above the UV channel, hence, very long rotor shafts are required. In order to avoid extensive bending of the rotors' shafts, a middle bridge is introduced with two additional

bearings attached to it. The bridge was installed close to the water surface to minimise bending of the shaft close to the rotors.

The upper PTO bridge serves multiple purposes including supporting the top bearings of the rotor shafts, accommodating the PTO and covering the UV channel. It is designed in mild steel with a coating applied to prevent corrosion and is attached via bolts to the concrete channel.

The twin turbine rotors consist of three main components: three blades, six spokes and two hubs. The parameters of the rotor design and the general dimensions of the rotors utilised are determined by the geometry of the channel and the constriction design.

#### 8.4.2 Procedure and results

The hydrokinetic twin turbine is placed in the second of five disinfection channels which host the final treatment stage (UV radiation) before the water is discharged into the Chattahoochee River. It was assumed that the total amount of water is distributed evenly amongst each channel in operation. The water level was fairly constant and hence the flow velocity varies proportionally to the discharge.

The PTO shaft hosts a torque transducer (Futek TRS605) which allows quantification of  $\tau$  and  $\omega$ . The system was tested with a disc brake and a generator. In order to quantify the performance of the turbine and compare it to the laboratory results, the testing procedure was adopted from the laboratory tests as described before. In contrast to the laboratory flume, the discharge/velocity varies and cannot be set to a certain value. The flow velocity was therefore measured by a propeller meter (Global Water FP211) and the measurements compared with the cross-sectional velocity as computed via the discharge data provided by the plant operators.

It was observed that a minimal change in flow velocity can have a significant impact on the  $C_P$  (the smaller the velocity the higher  $C_P$ ) and also an impact on  $\lambda$  (the smaller the velocity the higher  $\lambda$ ) since both variables are functions of the flow velocity. It may be assumed that the discharge and, hence the velocity, has changed during testing which is not surprising given the fact that the discharge in the treatment plant always varies during the day.

The given turbine design is expected to perform slightly worse than in the laboratory where the flow conditions are ideal and where maximum turbine efficiencies of more than 75% have been achieved. In addition to the non-uniform flow conditions (due to the turbulence downstream of the UV lights and the flow acceleration from the

diverter), the tested turbine employs three bearings due to the very long shaft and this introduces additional friction. Hence the maximum  $C_P$  was found to be around 70% with a TSR of slightly less than 3.

A second set of performance data was gathered by employing a low rpm permanent magnet generator instead of the disc brake. The electrical power output in terms of voltage and current is measured using two multimeters simultaneously. At the same time, rotational speed and torque is measured and recorded analogously to previous tests. Instead of applying a disk brake the generator load is controlled using a resistor bank and the resistance is varied manually. Over a period of one minute per resistor setting, average readings of voltage and current are taken together with torque transducer values. From these measurements, mechanical power and electrical power are computed and compared. The difference between mechanical and electrical power output was observed to be very high (40% loss). There are significant electrical losses from the generator (peak efficiency of 85%), the rectifier and the resistor bank in particular as it got very hot towards the peak performance of the rotor, hence, the highest resistance. Further, the generator's rated speed was not matched and the efficiency of the generator may be lower than 85%.

#### 8.4.3 Closure

The upscaled twin turbine design (scale 1:3) was successfully built, installed and tested at a water treatment plant in Atlanta, and is ready for full scale application (TRL 7). The system is still in operation and it can be concluded that TRL 6 has been reached (detailed conclusions and recommendations are listed in the Summary section of Chapter VI).

### 8.5 System commissioning (TRL 7)

The next step in the development stage of the turbine system is the deployment of an array of full-size turbines into the South Boulder Canal (SBC) near Denver. In June 2017, the first turbine was deployed into the last section of the SBC before the water enters the Ralston Reservoir via a "dragon's teeth" spillway structure. The section is approximately 30m long and 5m wide, of rectangular cross-section. In the following, the rotor design, the testing procedure and the data analysis are summarised (see Chapter VII for further details).

#### 8.5.1 Testing environment and turbine design

The turbine design follows the overall design presented in Chapter III and consists of a concrete/steel structure, two rotors, a chain-drive-train (instead of belt-drive), a speed increaser gearbox and an induction generator.

The rotors have a height of 0.8 meters and a diameter of 1.36 meters. The twin-rotors are counter-rotating, i.e., the right-hand-side rotor rotates clockwise and the left-hand-side rotor rotates anticlockwise. Each rotor shaft hosts a sprocket and the torque generated by the rotors is transmitted via a chain which drives the gearbox and eventually the generator. The focus of the tests reported here is on the mechanical power generated by the turbine and, hence, the electrical PTO was replaced by a mechanical PTO before deployment.

### 8.5.2 Procedure and results

The turbine's performance was tested as described previously whereas the gearbox/generator assembly was replaced with a mechanical PTO that consists of a hydraulic disc brake and a torque transducer. The torque transducer was placed immediately before the disc brake so that the measured torque and rotational speed included all losses of the rotor (mainly in the bearings) and the chain drive. Five tests were undertaken and the results are summarised as follows.

The discharge was provided by the channel operator Denver Water and confirmed by flow velocity measurements taken by the United States Bureau of Reclamation ( $Q = 7.08\text{m}^3/\text{s}$ ). Based on the average of measured upstream and downstream water depths the submerged cross-sectional area at the turbine shaft was calculated as  $A = 4.54\text{m}^2$ . With the given constant discharge the flow velocity was computed as  $v = 1.56\text{m/s}$ . During some tests it was observed that the rotors were sometimes fully submerged and sometimes not which suggested that the discharge was not constant and, as described in Chapter III, has a negative impact on performance.

However, in four out of five cases, the turbine achieved peak efficiencies above 70%. Just 50% were achieved when the discharge further dropped and the rotors further emerged. The variation could be due to several factors, such as sudden discharge surges or strong turbulence which would result in sudden and local velocity spikes and drops. The exact decrease in performance of an emergent rotor has not been quantified, however, it was observed that during most tests the upper spokes were slicing through the water surface which resulted in significant splashing and most likely in an additional drag torque on the rotor shaft. For the testing results where the rotors were fully submerged, a higher rotational speed and performance was observed but unfortunately during this test the discharge reduced and the test had to be aborted because at some point the rotor was not fully submerged any more. Most noteworthy is the fact that in comparison the rotational speed appears to be too high, the TSR for the maximum power was at approximately 5 suggesting that the

maximum power point was not yet reached. It remains to be seen whether a fully submerged rotor will be able to achieve higher efficiencies than 75%.

### 8.5.3 Closure

The hydrokinetic twin turbine was successfully built and deployed in the South Boulder Canal near Denver, US. Considering the rotors were not always fully submerged, the turbine achieved a coefficient of performance above 70% and was operating at a TSR of up to 4 for most of the tests. During peak performance, up to 3.4kW of mechanical power (including drive-train losses) were generated. The tests suggest that a fully submerged rotor operating in a turbine housing might be able to achieve efficiencies above 80%. Moreover, the scalability of the turbine was confirmed since the full-scale turbine at Denver operated similarly, if not better, than its smaller-scale versions tested in the laboratory and in Atlanta and it can be concluded that the twin turbine has successfully reached TRL 7.

### 8.6 Summary

It is concluded that the previously described hydrokinetic twin turbine for harvesting energy from flowing water in man-made channels successfully reached TRL 7 (*Full-scale, similar (prototypical) system demonstrated in relevant environment*). The development started with a concept (TRL 1-3) of a counter-rotating, twin VAT embedded in a hydrodynamic beneficial housing to be deployed in engineered canals. Over a period of two years, a 10<sup>th</sup> scale model of the turbine was built and tested at Cardiff University. The laboratory tests concluded to turbine efficiencies of more than 75%. The turbine has reached TRL 5 (*laboratory scale, similar system validation in relevant environment*) and was ready for upscale testing in a real canal environment.

In May 2017, a 3<sup>rd</sup> scale turbine system was implemented into a UV radiation channel, the last stage of water treatment at the RM Clayton water treatment plant in Atlanta, US. The twin turbine was successfully built, installed and tested and is still in operation in order to supply an electronic display board which justifies TRL 6 (*engineering/pilot-scale, similar (prototypical) system validation in relevant environment*) and the readiness for full-scale application was achieved.

Later in 2017, the turbine system was deployed as an array of ten full-size turbines (Emrgy's Hydrokinetic Twin Turbine) into the South Boulder Canal (SBC) near Denver. The system was tested and compared to the previous development stages and the scalability of the design was confirmed as well as the functionality and the excellent performance. All design components such as housing, drive-train, gearbox and generator were tested and operational and TRL 7 was achieved.

## IX. Conclusions and recommendations

In this study, the design of a novel hydrokinetic vertical axis twin turbine for the application in a canal environment was proven successful and the results of performance tests at laboratory (1:10), field (1:3) and full scale were presented. The development stages were benchmarked using the Technology Readiness Level method. Further, the wake behind the turbine's rotor was investigated and the electrical components of the turbine system defined. In this chapter, it is evaluated how the objectives of the project were met before general recommendations for further research and practice are provided.

### 9.1 Conclusions

The first objective was to optimise rotor shape and twin rotor assembly. This was achieved by an increased performance and improved self-starting behaviour due to a novel spoke design and an optimised blade shape. Literature indicates that the design of VATs is not straightforward. Individual design aspects affect each other and no ideal design recipe is available. Several different rotor features such as blade- and spoke-shape were varied and tested with a focus on improving the VAT's efficiency. The latest design features a rotor with three NACA4421 airfoil shaped blades, a pitch angle of  $6^\circ$  and an angle of twist of  $20^\circ$  in combination with hydrodynamically optimised NACA0012/24 airfoil-shaped spokes. This VAT system performed best, self-started in many cases and led to a reduction in vibrations. It was further shown that the combination of two counter-rotating rotors improves the overall performance ( $C_{P\text{-single}} > 50\%$ ,  $C_{P\text{-twin}} > 70\%$ ) and the rotors self-starting behaviour.

The second objective was to investigate housing structure as well as flow augmentation and was achieved by an increased rotor performance due to optimised housing, foundation and flow augmentation design. The housing's key design purposes are to assemble the entire system in an effective way and to act as a gravity base and augmentation which was successfully demonstrated at application stage.

Closely related to the housing design is the third objective which was to examine blockage and rotor solidity. This was achieved by the successful investigation of the optimum blockage ratio and the justification of the proposed low solidity approach at laboratory, demonstrator and full scale. In laboratory experiments, the ideal position of the rotors within the structure was found at the centre of the opening, with an axis-to-axis spacing of 1.5 rotor diameters. The ideal channel width to rotor diameter ratio  $\beta'$  was found to be approximately 60% if the distance from rotor to bed and surface is kept constant and submergence granted. Due to the small scale, the laboratory rotor

solidity was chosen to be  $\sigma_{\text{laboratory}} = 21\%$  but was reduced for upscaling to  $\sigma_{\text{field}} = 16.5\%$  and  $\sigma_{\text{application}} = 11\%$  in order to increase the rotational speed and decrease material costs without compromising on performance ( $C_{P\text{-application}} > 70\%$ ).

Beyond achieving and exceeding the objectives, a journal article was published by the Journal of Power and Energy Engineering with the title “Technology Readiness of a Vertical-Axis Hydro-Kinetic Turbine” [159] where the overall turbine design was assessed using Technology Readiness Levels (TRL).

In addition, the wake recovery downstream of the turbine’s rotor was investigated yielding in a peer-reviewed publication in the Journal of Renewable Energy with the title “Three-dimensionality of the wake recovery behind a vertical axis turbine” [129]. In this study, three distinct regions were observed: (i) a near-wake region featuring a low-momentum area just downstream of the turbine rotor; (ii) a transitional-wake region, extending 2 to 5 rotor diameters (D) downstream of the turbine rotor that is characterised by a fast rate of momentum recovery and high intensity of turbulence; (iii) and a far-wake region with an almost full recovery of the momentum deficit as streamwise velocities reach values above 0.8 times the bulk velocity whilst high-order effects persist until a distance of 14D downstream of the turbine location.

The fourth objective was to acquire knowledge of component manufacturing which was successfully demonstrated by the manufacturing and testing of milled and laser-sintered components as well as unique carbon-fiber composite blades. Designed in a 3D-CAD environment (Solidworks®), the rotor components were machined in several ways. At laboratory stage, the highest quality was achieved by machining the rotor blades and spokes out of plastic sheet material using a milling machine. Further, blades and spokes were manufactured by rapid prototyping (SLS) and several composite approaches. The post-processing to achieve an acceptable level of surface-finish for the latter procedures was time-consuming but resulted in a similar surface as the milling machined blades. For field testing, the blades were manufactured as composites, with an SLS core, stainless steel inserts and a carbon-fiber shell whereas the spokes were milling-machined out of glass-reinforced nylon. For the full-scale application, spokes and blades were milling machined from a non-corrosive aluminium alloy.

The fifth objective was to investigate the power take-off of the twin rotor assembly which was achieved by identifying the advantages and disadvantages of a combined power take-off and demonstrating the workability of an innovative belt drive. The combined PTO of two rotors using a belt-drive was compared with two individual

PTOs. The aim of a combined PTO is to simplify the periphery (e.g., just one gearbox, generator, power-controller) by compromising on additional drive train friction losses which accounted for a 5% performance drop on laboratory level. The belt system was used successfully for the field tests on 3<sup>rd</sup> scale. Due to the uncertainty of service life, the full-scale turbine was equipped with a chain-drive instead of the belts but with the same mechanism. It appeared that the friction losses of the chain-drive was higher than the losses from the belt-drive.

The sixth objective was to understand the generation of electricity and the associated hurdles with respect to the given turbine at different scales. This objective was met by deriving the critical electrical design aspects for laboratory, demonstrator and full scale application. Further, in a collaboration with the electrical engineering department of the School of Engineering at Cardiff University, a MPPT controller was designed, built, tested which is reported in a peer-reviewed article entitled “Maximum Power Extraction from a Hydrokinetic Energy Conversion System” [146] published in the Journal of IET Renewable Power Generation. The ultimate goal of the VAT is to generate electricity. Therefore, the electrical components were defined and a differentiation between laboratory, field and full-scale application was presented by introducing a decision making process which highlights the important aspects of an integral hydrodynamic and electrical design. Three permanent magnet generators were tested with the laboratory and field testing turbine and it was observed that generator specifications must match the turbine’s rotational speed in order to achieve the highest performance. For field testing, a power diversion assembly was designed, built and successfully applied to charge batteries with the power generated from the turbine and used for operational purposes such as charging a laptop. At full-scale, the electrical design was not part of this study, however, a controller was designed which automatically operates the turbine at peak performance according to changes in rotational speed (e.g., flow speeds) and adjusts the produced electricity towards the load (e.g., battery voltage).

However, with so many tasks undertaken, many interesting questions and gaps in the literature were identified which are listed in the following in the order of chapters.

## 9.2 Recommendations

To the best of my knowledge, there is no global resource assessment available about the hydrokinetic potential in rivers and engineered canals. It would be helpful to have

such a data source in order to identify the most suitable sites for implementing hydrokinetic power schemes.

The data and observations gained in this study should be processed and extended in a wider scientific context in order to address concerns in the hydropower permission application procedure in natural waterways. The permitting process, at least in Wales, appears to be very comprehensive with a level of detail needed for a successful application which, at least financially, does not match the expected rate of return for a 10kW device since the costs for sophisticated pre-deployment studies are by far too high. It may be concluded that the permitting process is so comprehensive because of many uncertainties towards the impact on aquatic life, river-traffic, flooding, sedimentation and many more. A wider research base would help to identify issues related to the implementation of hydrokinetic extraction devices in rivers and provide the relevant authorities with more confidence in assessing and ultimately permitting a scheme.

Generally, the objectives of this study were met and exceeded. However, the design is not yet structurally assessed and the following procedure is recommended:

- Simulate hydrodynamics of rotor(s) and evaluate force distribution by employing computational fluid dynamics (CFD).
- Compare overall forces (CFD) with estimated forces (analytical procedure presented in Chapter I).
- Simulate force distribution on blades using finite element methods (FEM) and assess structural integrity (connection interfaces in particular).
- Confirm geometrical equality between design (CAD) and machined member (composite in particular, see Appendix G).
- Perform structural tests on machined/manufactured members (torsion, bending) and compare with FEM results.
- Revisit design.

A novel belt-drive was used to combine the rotational motion of both rotor shafts to a common shaft. In this case, the belts are twisted by 90 degrees which made sizing difficult since the manufacturers sizing tools [172] do not appreciate twisting. Some tests were undertaken in order to find the correct belt size and tension (see Appendix C) and the manufacturer supported to some extent. However, this uncertainty led to the deployment of a chain-drive for full-scale application which caused a higher investment compared to a belt-drive. Therefore, the belt-drive should be investigated in more depth.

Vibrations are inevitable for VATs [173]. However, with the latest rotor design, the performance and self-starting behaviour could be improved. From visual observations, the vibrations were also reduced in comparison to other rotor designs tested. It is suggested to analyse the torque ripple of the tests undertaken and simulate the impact of the changing forces on the structure, e.g., fatigue/durability and life-cycle analysis.

Design iterations are suggested for the overlapping part of the spoke. It is the outermost part of the rotor which means it rotates the fastest around the axis. Hence, any unwanted drag has the biggest impact on performance and a detailed CFD study of this part of the rotor may hint towards potential geometry and performance improvements. Further, cavitation has not been considered in this study as literature suggested that at low approach flow velocity  $< 2\text{m/s}$  and  $\text{TSR} < 4$  severe cavitation is unlikely [174]. Cavitation was never visually observed during turbine operation. However, a sophisticated cavitation study on a VAT would both, supplement existing literature and justify the previous statement.

It was decided to study the wake recovery of a single VAT rotor in order to fill a gap in literature and learn about flow structures behind VATs in general. It is recommended to extend the study to a twin rotor system as it is applied in the case of this thesis in the interest of research the interaction of two parallel wakes and observe possible impacts on the three distinct wake regions.

Ultimately, the turbine will be installed in an array of several turbines along a channel. It would be of highest interest to study the impact on the wake recovery in an array of VATs. Moreover, the turbine effect on backwater, hence, the flow conditions upstream the VAT should be researched. As mentioned in Chapter VII, the Bureau of Reclamation undertakes a detailed study about the impact on the channel flow in the SBC. This data should be compared to the results observed in this study and analysed in a similar fashion.

In Chapter V, a decision making process was derived by reviewing relevant literature. It is suggested to compare these recommendations with the commercial and technical experience gained on field testing and application level.

In a collaboration with the electrical engineering department of the School of Engineering at Cardiff University, a MPPT controller for laboratory and field testing purpose was designed, built and tested. It is recommended to extend the

development of the controller in spite of an induction generator (instead of PMG) and grid integration (instead of batteries).

Material choice is a critical element of product development. In this study, several materials and manufacturing procedures were applied such as milling/casting/sintering plastic and aluminium as well as composite manufacturing with the focus on receiving a cost effective part with a high surface-finish and durability. It is suggested to compare the different approaches from a material-science point of view.

Further, long term testing/observation on belt-drive durability, blade/rotor clogging, bearing lubrication, connection fastening, performance and the electrical circuit is suggested.

## List of references

- [1] P. Rochat, Five levels of self-awareness as they unfold early in life, *Conscious. Cogn.* 12 (2003) 717–731. doi:10.1016/S1053-8100(03)00081-3.
- [2] J.R. Hurford, M. Studdert-Kennedy, C. Knight, *Approaches to the evolution of language : social and cognitive bases*, Cambridge University Press, 1998. <http://www.forskningsdatabasen.dk/en/catalog/2398205914> (accessed September 10, 2018).
- [3] H.I. Dutton, *The patent system and inventive activity during the Industrial Revolution, 1750-1852*, Manchester University Press, 1984.
- [4] S. Strandh, *The History Of The Machine*, Bracken, 1989.
- [5] S.R. Weart, The Discovery of the Risk of Global Warming, *Phys. Today.* 50 (1997) 230. doi:10.1063/1.881664.
- [6] J.R. BROWN, J.L. THORNTON, Percivall Pott (1714-1788) and chimney sweepers' cancer of the scrotum., *Br. J. Ind. Med.* 14 (1957) 68–70. <http://www.ncbi.nlm.nih.gov/pubmed/13396156> (accessed February 2, 2018).
- [7] J. Zhang, R. Lindsay, M. Steele, A. Schweiger, What drove the dramatic retreat of arctic sea ice during summer 2007?, *Geophys. Res. Lett.* 35 (2008) L11505. doi:10.1029/2008GL034005.
- [8] N. Oreskes, Beyond the ivory tower. The scientific consensus on climate change., *Science.* 306 (2004) 1686. doi:10.1126/science.1103618.
- [9] B.K. Sovacool, M.A. Brown, Competing Dimensions of Energy Security: An International Perspective, *Annu. Rev. Environ. Resour.* 35 (2010) 77–108. doi:10.1146/annurev-environ-042509-143035.
- [10] W. Siemens, On the electro motive action of illuminated selenium, discovered by Mr. Fritts, of New York, *J. Franklin Inst.* 119 (1885) 453-IN6. doi:10.1016/0016-0032(85)90176-0.
- [11] J. Twidell, T. Weir, *Renewable energy resources*, n.d.
- [12] Facts about hydro power - Vattenfall, (n.d.). <https://corporate.vattenfall.com/about-energy/renewable-energy-sources/hydro-power/> (accessed March 14, 2018).
- [13] Nuclear Energy Institute, *World Nuclear Generation and Capacity, Statistic.* (2017) 1. <https://www.nei.org/Knowledge-Center/Nuclear-Statistics/World-Statistics/World-Nuclear-Generation-and-Capacity> (accessed February 2, 2018).
- [14] B. Wilmsen, Damming China's rivers to expand its cities: the urban livelihoods of rural people displaced by the Three Gorges Dam, *Urban Geogr.* (2017) 1–22. doi:10.1080/02723638.2017.1328578.
- [15] *hydro\_power\_plant3.jpg (1000×684)*, (n.d.). [https://corporate.vattenfall.com/globalassets/corporate/about\\_energy/illustrations/hydro\\_power\\_plant3.jpg](https://corporate.vattenfall.com/globalassets/corporate/about_energy/illustrations/hydro_power_plant3.jpg) (accessed March 14, 2018).
- [16] N.D. Laws, B.P. Epps, Hydrokinetic energy conversion: Technology, research, and outlook, *Renew. Sustain. Energy Rev.* 57 (2016) 1245–1259. doi:10.1016/J.RSER.2015.12.189.
- [17] H.R. Karbasian, J.A. Esfahani, E. Barati, Simulation of power extraction from

- tidal currents by flapping foil hydrokinetic turbines in tandem formation, *Renew. Energy*. 81 (2015) 816–824. doi:10.1016/J.RENENE.2015.04.007.
- [18] H.R. Karbasian, J.A. Esfahani, E. Barati, The power extraction by flapping foil hydrokinetic turbine in swing arm mode, *Renew. Energy*. 88 (2016) 130–142. doi:10.1016/J.RENENE.2015.11.038.
- [19] The Engineering Business Limited, RESEARCH AND DEVELOPMENT OF A 150KW TIDAL STREAM GENERATOR, (n.d.). <http://webarchive.nationalarchives.gov.uk/20060215222824/http://www.dti.gov.uk/renewables/publications/pdfs/T00211.pdf> (accessed February 2, 2018).
- [20] L.I. Lago, F.L. Ponta, L. Chen, Advances and trends in hydrokinetic turbine systems, *Energy Sustain. Dev.* 14 (2010) 287–296. doi:10.1016/J.ESD.2010.09.004.
- [21] M.J. Khan, G. Bhuyan, M.T. Iqbal, J.E. Quaiçoe, Hydrokinetic energy conversion systems and assessment of horizontal and vertical axis turbines for river and tidal applications: A technology status review, *Appl. Energy*. 86 (2009) 1823–1835. doi:10.1016/j.apenergy.2009.02.017.
- [22] M.S. Güney, K. Kaygusuz, Hydrokinetic energy conversion systems: A technology status review, *Renew. Sustain. Energy Rev.* 14 (2010) 2996–3004. doi:10.1016/j.rser.2010.06.016.
- [23] A. Harvey, *Micro-Hydro Design Manual*, Practical Action Publishing, Rugby, Warwickshire, United Kingdom, 1993. doi:10.3362/9781780445472.
- [24] A. Betz, Das Maximum der theoretisch möglichen Ausnützung des Windes durch Windmotoren, *Zeitschrift Für Das Gesamte Turbinenwes.* 26 (1920).
- [25] T. Burton, N. Jenkins, D. Sharpe, E. Bossanyi, *Wind energy handbook*, 2nd Editio, Wiley, 2011. <https://www.wiley.com/en-us/Wind+Energy+Handbook%2C+2nd+Edition-p-9780470699751> (accessed March 16, 2018).
- [26] R. Vennell, Exceeding the Betz limit with tidal turbines, *Renew. Energy*. 55 (2013) 277–285. doi:10.1016/J.RENENE.2012.12.016.
- [27] R. Vennell, S.W. Funke, S. Draper, C. Stevens, T. Divett, Designing large arrays of tidal turbines: A synthesis and review, *Renew. Sustain. Energy Rev.* 41 (2015) 454–472. doi:10.1016/J.RSER.2014.08.022.
- [28] T. Stoesser, *FroudeJump*, (2013).
- [29] R. Kumar, K. Raahemifar, A.S. Fung, A critical review of vertical axis wind turbines for urban applications, *Renew. Sustain. Energy Rev.* 89 (2018) 281–291. doi:10.1016/J.RSER.2018.03.033.
- [30] H.J. Vermaak, K. Kusakana, S.P. Koko, Status of micro-hydrokinetic river technology in rural applications: A review of literature, *Renew. Sustain. Energy Rev.* 29 (2014) 625–633. doi:10.1016/J.RSER.2013.08.066.
- [31] K. Sørnes, *Small-scale Water Current Turbines for River Applications*, (2010). <https://pdfs.semanticscholar.org/4b90/ab7c3e5edb5e5695e06a11ad84dca1b30a3b.pdf> (accessed March 15, 2018).
- [32] D. Kim, M. Gharib, Efficiency improvement of straight-bladed vertical-axis wind turbines with an upstream deflector, *J. Wind Eng. Ind. Aerodyn.* 115 (2013) 48–52. doi:10.1016/J.JWEIA.2013.01.009.

- [33] T. Bhatti, D. Kothari, Early development of modern vertical and horizontal axis wind turbines: A review, *Wind Eng.* 29 (2005) 287–299. <http://journals.sagepub.com/doi/pdf/10.1260/030952405774354859> (accessed January 8, 2018).
- [34] Plans for world’s “largest and most powerful” offshore wind turbine unveiled, (n.d.). <https://www.cnbc.com/2018/03/01/plans-for-worlds-largest-and-most-powerful-offshore-wind-turbine-unveiled.html> (accessed April 17, 2018).
- [35] V. Yaramasu, B. Wu, P.C. Sen, S. Kouro, M. Narimani, High-power wind energy conversion systems: State-of-the-art and emerging technologies, *Proc. IEEE.* 103 (2015) 740–788. doi:10.1109/JPROC.2014.2378692.
- [36] Z. Zhou, M. Benbouzid, J.-F. Charpentier, F. Scuiller, T. Tang, Developments in large marine current turbine technologies – A review, (2017). doi:10.1016/j.rser.2016.12.113.
- [37] 1280x720-\_gp.jpg (1280×720), (n.d.). [http://s2.dmcdn.net/lu8Q4/1280x720-\\_gp.jpg](http://s2.dmcdn.net/lu8Q4/1280x720-_gp.jpg) (accessed April 25, 2018).
- [38] tgl-tidal-1MW-turbine-lift.jpg (1100×742), (n.d.). <http://gcaptain.com/wp-content/uploads/2013/08/tgl-tidal-1MW-turbine-lift.jpg> (accessed April 25, 2018).
- [39] Meygen-Underwater-Turbine.jpg (1580×1593), (n.d.). <https://inhabitat.com/wp-content/blogs.dir/1/files/2016/09/Meygen-Underwater-Turbine.jpg> (accessed April 25, 2018).
- [40] Tidal Turbine Produces Electricity in Orkney (UK) | Subsea World News, (n.d.). <https://subseaworldnews.com/2012/05/17/tidal-turbine-produces-electricity-in-orkney-uk/> (accessed April 25, 2018).
- [41] RWE AG - Pressemitteilungen, (n.d.). <http://www.rwe.com/web/cms/de/37110/rwe/presse-news/pressemitteilungen/?pmid=4004991> (accessed April 25, 2018).
- [42] seagen-up.jpg (2654×1770), (n.d.). [http://www.siemens.co.uk/pool/news\\_press/news\\_archive/2012/seagen-up.jpg](http://www.siemens.co.uk/pool/news_press/news_archive/2012/seagen-up.jpg) (accessed April 25, 2018).
- [43] Alstoms tidal turbines have generated over 1GWh to the Scottish grid | Alstom, (n.d.). <https://www.alstom.com/press-releases-news/2014/11/alstoms-tidal-turbines-have-generated-over-1gwh-to-the-scottish-grid> (accessed September 10, 2018).
- [44] GE’s Tidal stream solutions, (n.d.). [https://www.ge.com/content/dam/gepower-renewables/global/en\\_US/documents/product-brochures/GEA32275\\_Tidal\\_Brochure\\_Final.pdf](https://www.ge.com/content/dam/gepower-renewables/global/en_US/documents/product-brochures/GEA32275_Tidal_Brochure_Final.pdf) (accessed April 25, 2018).
- [45] GE drops Oceade tidal turbine. Sinks NEPTHYD project | Marine Energy, (n.d.). <https://marineenergy.biz/2017/01/09/ge-drops-oceade-tidal-turbine-sinks-nepthyd-project/> (accessed April 25, 2018).
- [46] C.A. Douglas, G.P. Harrison, J.P. Chick, Life cycle assessment of the Seagen marine current turbine, *Proc. Inst. Mech. Eng. Part M J. Eng. Marit. Environ.* 222 (2008) 1–12. doi:10.1243/14750902JEME94.
- [47] Daniel Bernoulli | Swiss mathematician | Britannica.com, (n.d.). <https://www.britannica.com/biography/Daniel-Bernoulli#ref200813> (accessed

- September 10, 2018).
- [48] Fluid Dynamics -Study Material for IIT JEE | askITians, (n.d.). <https://www.askitians.com/iit-jee-physics/mechanics/fluid-dynamics.aspx> (accessed April 18, 2018).
- [49] M. Blanke, K.-P. Lindegaard, T.I. Fossen, Dynamic Model for Thrust Generation of Marine Propellers, *IFAC Proc. Vol. 33* (2000) 353–358. doi:10.1016/S1474-6670(17)37100-8.
- [50] P.J. Schubel, R.J. Crossley, Wind Turbine Blade Design, *Energies*. 5 (2012) 3425–3449. doi:10.3390/en5093425.
- [51] G. Pechlivanoglou, File:Blade with sections and vectors.svg - Wikimedia Commons, (n.d.). [https://commons.wikimedia.org/wiki/File:Blade\\_with\\_sections\\_and\\_vectors.svg](https://commons.wikimedia.org/wiki/File:Blade_with_sections_and_vectors.svg) (accessed April 26, 2018).
- [52] T. Thiringer, J. Linders, Control by variable rotor speed of a fixed-pitch wind turbine operating in a wide speed range, *IEEE Trans. Energy Convers.* 8 (1993) 520–526. doi:10.1109/60.257068.
- [53] Scheurich, Frank, T.M. Fletcher, R.E. Brown, The influence of blade curvature and helical blade twist on the performance of a vertical-axis wind turbine. In: 29th ASME Wind Energy Symposium, (2010). <https://strathprints.strath.ac.uk/27341/> (accessed February 15, 2018).
- [54] G.J.M. Darrieus, Turbine Having Its Rotating Shaft Transverse to the Flow of the Current, 1931. <https://patentimages.storage.googleapis.com/13/d6/3b/c8f2897a86ce96/US1835018.pdf> (accessed April 27, 2018).
- [55] A.M. Gorlov, UNIDIRECTIONAL HELICAL REACTION TURBINE OPERABLE UNDER REVERSIBLE FLUID FLOW FOR POWER SYSTEMS, 1994. <https://patentimages.storage.googleapis.com/f0/e1/df/7b00a68b3c003a/US5451137.pdf> (accessed April 27, 2018).
- [56] J.V. Akwa, H.A. Vielmo, A.P. Petry, A review on the performance of Savonius wind turbines, *Renew. Sustain. Energy Rev.* 16 (2012) 3054–3064. doi:10.1016/J.RSER.2012.02.056.
- [57] S.J. Savonius, ROTOR ADAPTED TO BE DRIVEN BY WIND OR FLOWING WATER, 1925. <https://patentimages.storage.googleapis.com/d8/1e/90/c4544094f98bbb/US1697574.pdf> (accessed April 27, 2018).
- [58] Scalable Grid Integrated Systems by Ocean Renewable Power Company (ORP, (n.d.). <http://www.orpc.co/our-solutions/scalable-grid-integrated-systems> (accessed May 30, 2018).
- [59] EnCurrent 125 Series - New Energy Corporation - A Leading Manufacturer and Developer of Hydrokinetic Turbines, (n.d.). <http://www.newenergycorp.ca/encurrent-125-series.html> (accessed May 31, 2018).
- [60] Instream Energy Systems | Vancouver | Hydrokinetic Power Generation | Technology, (n.d.). <https://www.instreamenergy.com/technology> (accessed May 31, 2018).

- [61] ch-TidGen-Power-System.jpg (880×271), (n.d.).  
<http://www.orpc.co/uploads/editoruploadimages/ch-TidGen-Power-System.jpg> (accessed May 31, 2018).
- [62] RivGen® Power System by Ocean Renewable Power Company (ORPC), (n.d.). <http://www.orpc.co/our-solutions/scalable-grid-integrated-systems/rivgen-power-system> (accessed May 31, 2018).
- [63] EnCurrent\_446726\_orig.jpg (822×616), (n.d.).  
[http://www.newenergycorp.ca/uploads/5/3/4/9/53492779/446726\\_orig.jpg](http://www.newenergycorp.ca/uploads/5/3/4/9/53492779/446726_orig.jpg) (accessed May 31, 2018).
- [64] EnCurrent\_2044670\_orig.jpg (1024×771), (n.d.).  
[http://www.newenergycorp.ca/uploads/5/3/4/9/53492779/2044670\\_orig.jpg](http://www.newenergycorp.ca/uploads/5/3/4/9/53492779/2044670_orig.jpg) (accessed May 31, 2018).
- [65] Instream Energy Systems - Installation - YouTube, (n.d.).  
<https://www.youtube.com/watch?v=RAbTLjdo34w> (accessed May 31, 2018).
- [66] M. Islam, D.S.K. Ting, A. Fartaj, Aerodynamic models for Darrieus-type straight-bladed vertical axis wind turbines, *Renew. Sustain. Energy Rev.* 12 (2008) 1087–1109. doi:10.1016/j.rser.2006.10.023.
- [67] G.L. Johnson, Wind Turbine Power , Energy , and Torque, *Wind Energy.* (2001) 1–54.
- [68] M. Shiono, K. Suzuki, S. Kiho, An Experimental Study of the Characteristics of a Darrieus Turbine for Tidal Power Generation, *Electr. Eng. Japan.* Vol. 132 (2000) 38–47. doi:10.1002/1520-6416(200008)132:3<38::AID-EEJ6>3.0.CO;2-E.
- [69] F. Scheurich, T. Fletcher, R. Brown, The Influence of Blade Curvature and Helical Blade Twist on the Performance of a Vertical-Axis Wind Turbine, in: 48th AIAA Aerosp. Sci. Meet. Incl. New Horizons Forum Aerosp. Expo., American Institute of Aeronautics and Astronautics, Reston, Virginia, 2010. doi:10.2514/6.2010-1579.
- [70] P. Ouro, T. Stoesser, An immersed boundary-based large-eddy simulation approach to predict the performance of vertical axis tidal turbines, *Comput. Fluids.* 152 (2017) 74–87. doi:10.1016/j.compfluid.2017.04.003.
- [71] P. Marsh, D. Ranmuthugala, I. Penesis, G. Thomas, Numerical investigation of the influence of blade helicity on the performance characteristics of vertical axis tidal turbines, *Renew. Energy.* 81 (2015) 926–935. doi:10.1016/J.RENENE.2015.03.083.
- [72] C. Li, S. Zhu, Y. Xu, Y. Xiao, 2.5D large eddy simulation of vertical axis wind turbine in consideration of high angle of attack flow, *Renew. Energy.* 51 (2013) 317–330. doi:10.1016/J.RENENE.2012.09.011.
- [73] M. Elkhoury, T. Kiwata, E. Aoun, Experimental and numerical investigation of a three-dimensional vertical-axis wind turbine with variable-pitch, *J. Wind Eng. Ind. Aerodyn.* 139 (2015) 111–123. doi:10.1016/J.JWEIA.2015.01.004.
- [74] A. Posa, C.M. Parker, M.C. Leftwich, E. Balaras, Wake structure of a single vertical axis wind turbine, *Int. J. Heat Fluid Flow.* 61 (2016) 75–84. doi:10.1016/J.IJHEATFLUIDFLOW.2016.02.002.
- [75] E. Segura, R. Morales, J.A. Somolinos, A. López, Techno-economic challenges of tidal energy conversion systems: Current status and trends,

- Renew. Sustain. Energy Rev. 77 (2017) 536–550.  
doi:10.1016/J.RSER.2017.04.054.
- [76] T. Harries, A. Kwan, J. Brammer, R. Falconer, Physical testing of performance characteristics of a novel drag-driven vertical axis tidal stream turbine; with comparisons to a conventional Savonius, *Int. J. Mar. Energy*. 14 (2016) 215–228. doi:10.1016/J.IJOME.2016.01.008.
- [77] NOAA Tides & Currents, (n.d.). <https://www.co-ops.nos.noaa.gov/faq2.html#26> (accessed May 21, 2018).
- [78] C. Peters, Severn Estuary Tidal Power, (2010). <http://www.assembly.wales/Research Documents/Severn Estuary Tidal Power - Research paper-10052010-180289/10-011-English.pdf> (accessed May 21, 2018).
- [79] GROWTH SCENARIOS FOR UK RENEWABLES GENERATION AND IMPLICATIONS FOR FUTURE DEVELOPMENTS AND OPERATION OF ELECTRICITY NETWORKS, (2008). [https://assets.publishing.service.gov.uk/government/uploads/system/uploads/attachment\\_data/file/42969/1\\_20090501131535\\_e\\_\\_\\_\\_SKMRESBERRFinal Report.pdf](https://assets.publishing.service.gov.uk/government/uploads/system/uploads/attachment_data/file/42969/1_20090501131535_e____SKMRESBERRFinal Report.pdf) (accessed May 21, 2018).
- [80] A.S. Iyer, S.J. Couch, G.P. Harrison, A.R. Wallace, Variability and phasing of tidal current energy around the United Kingdom, *Renew. Energy*. 51 (2013) 343–357. doi:10.1016/J.RENENE.2012.09.017.
- [81] Should we build the Severn Barrage? - Surely a no brainer! - TheGreenAge, (n.d.). <https://www.thegreenage.co.uk/should-we-build-the-severn-barrage-surely-a-no-brainer/> (accessed May 31, 2018).
- [82] M. Esteban, D. Leary, Current developments and future prospects of offshore wind and ocean energy, *Appl. Energy*. 90 (2012) 128–136. doi:10.1016/J.APENERGY.2011.06.011.
- [83] C. McGowin, R. Bedard, Ocean Tidal and Wave Energy, *Renewable Energy Technical Assessment Guide*, *Electr. Power Res. Inst.* . (2005). <https://www.epri.com/#/pages/product/%7B%7Bp.content.ShortProductId%7D%7D/> (accessed May 31, 2018).
- [84] Tidal Energy – Severn Estuary Coastal Group, (n.d.). <https://www.severnestuarycoastalgroup.org.uk/about/tidal-energy/> (accessed May 31, 2018).
- [85] A. Miles, 21 FERC ¶ 61,221 UNITED STATES OF AMERICA FEDERAL ENERGY REGULATORY COMMISSION (Docket No. PL08-1-000) Policy Statement on Conditioned Licenses for Hydrokinetic Projects, (n.d.). <https://www.ferc.gov/CalendarFiles/20071130153255-PL08-1-000.pdf> (accessed July 5, 2018).
- [86] A. Kumar, T. Schei, A. Ahenkorah, R. Caceres Rodriguez, J.-M. Devernay, M. Freitas, D. Hall, E. Branche, J. Burkhardt, S. Descloux, G. Heath, K. Seelos, C. Diaz Morejon, T. Krug, T. Schei, A. Ahenkorah, R. Caceres Rodriguez, J. Devernay, M. Freitas, D. Hall, Å. Killingtveit, 5 *Hydropower Coordinating Lead Authors: Lead Authors: Contributing Authors: Review Editors: This chapter should be cited as*, (n.d.). [https://www.ieahydro.org/media/8437dd01/IPCC\\_SRREN\\_Chapter5\\_Hydropower.pdf](https://www.ieahydro.org/media/8437dd01/IPCC_SRREN_Chapter5_Hydropower.pdf) (accessed July 5, 2018).

- [87] World Energy Assessment, 2000.  
[http://www.undp.org/content/dam/aplaws/publication/en/publications/environment-energy/www-ee-library/sustainable-energy/world-energy-assessment-energy-and-the-challenge-of-sustainability/World Energy Assessment-2000.pdf](http://www.undp.org/content/dam/aplaws/publication/en/publications/environment-energy/www-ee-library/sustainable-energy/world-energy-assessment-energy-and-the-challenge-of-sustainability/World%20Energy%20Assessment-2000.pdf) (accessed July 5, 2018).
- [88] Q. Lu, M.N. Futter, L. Nizzetto, G. Bussi, M.D. Jürgens, P.G. Whitehead, Fate and transport of polychlorinated biphenyls (PCBs) in the River Thames catchment – Insights from a coupled multimedia fate and hydrobiogeochemical transport model, *Sci. Total Environ.* 572 (2016) 1461–1470. doi:10.1016/J.SCITOTENV.2016.03.029.
- [89] P. Lucas Picher, V.K. Arora, D. Caya, R. Laprise, Implementation of a large scale variable velocity river flow routing algorithm in the Canadian Regional Climate Model (CRCM), *Atmosphere-Ocean.* 41 (2003) 139–153. doi:10.3137/ao.410203.
- [90] V.S. Neary, Reference Inflow Characterization for River Resource Reference Model: Reference Model 2 (RM2), (2011). <http://www.osti.gov/contact.html> (accessed July 6, 2018).
- [91] P. Duvoy, H. Toniolo, HYDROKAL: A module for in-stream hydrokinetic resource assessment, *Comput. Geosci.* 39 (2012) 171–181. doi:10.1016/J.CAGEO.2011.06.016.
- [92] D. Kumar, S. Sarkar, A review on the technology, performance, design optimization, reliability, techno-economics and environmental impacts of hydrokinetic energy conversion systems, *Renew. Sustain. Energy Rev.* 58 (2016) 796–813. doi:10.1016/J.RSER.2015.12.247.
- [93] J. Ahlgrimm, M.B. Bioengineering, T. Bigford, S.D. Stavrakas, D. Hall, Glenn Cada FeATURe: Michael Sale Potential Impacts of Hydrokinetic and Wave energy Conversion Technologies on Aquatic environments, (2005). [www.snopud.com](http://www.snopud.com) (accessed July 6, 2018).
- [94] L. Dubbs, A.G. Keeler, T. O’Meara, Permitting, Risk and Marine Hydrokinetic Energy Development, *Electr. J.* 26 (2013) 64–74. doi:10.1016/J.TEJ.2013.11.002.
- [95] R.D. Montoya Ramírez, F.I. Cuervo, C.A. Monsalve Rico, Technical and financial valuation of hydrokinetic power in the discharge channels of large hydropower plants in Colombia: A case study, *Renew. Energy.* 99 (2016) 136–147. doi:10.1016/J.RENENE.2016.06.047.
- [96] New Patagonia Film: Blue Heart | riverwatch.eu, (n.d.). <https://riverwatch.eu/en/balkanrivers/news/new-patagonia-film-blue-heart> (accessed July 15, 2018).
- [97] Natural Resources Wales / Before you apply, (n.d.). <https://naturalresources.wales/permits-and-permissions/water-abstraction-and-impoundment/hydropower/before-you-apply/?lang=en> (accessed July 6, 2018).
- [98] T. STOESSER, T. MORRIS, E. MORRIS, A. WALSH, J.S. VANSELOUS, C.L. PARYS, B.D. TUTAS, TURBINE HYDROKINETIC ENERGY SYSTEM UTILIZING CYCLOIDAL MAGNETIC GEARS, 2017. <https://patentscope.wipo.int/search/en/detail.jsf?docId=WO2017172747&recNum=1&maxRec=&office=&prevFilter=&sortOption=&queryString=&tab=PCT+Biblio> (accessed May 11, 2018).

- [99] L. Priegue, T. Stoesser, The influence of blade roughness on the performance of a vertical axis tidal turbine, *Int. J. Mar. Energy*. 17 (2017) 136–146. doi:10.1016/j.ijome.2017.01.009.
- [100] A.L. Niblick, Experimental and Analytical Study of Helical Cross-Flow Turbines for a Tidal Micropower Generation System, *Test*. (2012) 175.
- [101] L.P. Molinos, Philosophy Optimisation of a Vertical Axis Tidal Turbine and Testing of a Prototype in an Unblocked Environment, (2017).
- [102] J.R. Brammer, Physical and Numerical Modelling of Marine Renewable Energy Technologies , with Particular Focus on Tidal Stream and Tidal Range Devices, (2014).
- [103] T. Harries, Physical Testing and Numerical Modelling of a Novel Vertical - Axis Tidal Stream Turbine, (2014).
- [104] L. Priegue, T. Stoesser, S. Runge, priegue, in: *E-Proceedings 36th IAHR World Congr.*, The Hague, 2015: p. 11.
- [105] A.J. Fiedler, S. Tullis, Blade Offset and Pitch Effects on a High Solidity Vertical Axis Wind Turbine, 33 (2009) 237–246.  
<http://journals.sagepub.com/doi/pdf/10.1260/030952409789140955>  
(accessed April 18, 2018).
- [106] S.-C. Roh, S.-H. Kang, Effects of a blade profile, the Reynolds number, and the solidity on the performance of a straight bladed vertical axis wind turbine, *J. Mech. Sci. Technol.* 27 (2013) 3299–3307. doi:10.1007/s12206-013-0852-x.
- [107] B. Yang, X.W. Shu, Hydrofoil optimization and experimental validation in helical vertical axis turbine for power generation from marine current, *Ocean Eng.* 42 (2012) 35–46. doi:10.1016/J.OCEANENG.2012.01.004.
- [108] M. Islam, D.S.-K. Ting, A. Fartaj, Desirable Airfoil Features for Smaller-Capacity Straight-Bladed VAWT ABBREVIATIONS AND ACRONYMS, 31 (2007) 165–196.  
<http://journals.sagepub.com/doi/pdf/10.1260/030952407781998800>  
(accessed June 20, 2018).
- [109] C. Soraghan, W. Leithead, P.G. Jamieson Garrad Hassan, Influence of lift to drag ratio on optimal aerodynamic performance of straight blade vertical axis wind turbines. In: *EWEA Annual Wind Energy Influence of Lift to Drag Ratio on Optimal Aerodynamic Performance of Straight Blade Vertical Axis Wind Turbines*, (2013). <https://strathprints.strath.ac.uk/59292/> (accessed June 20, 2018).
- [110] M.R. Ahmed, Blade sections for wind turbine and tidal current turbine applications-current status and future challenges, *Int. J. Energy Res.* 36 (2012) 829–844. doi:10.1002/er.2912.
- [111] NACA 4 digit airfoil generator (NACA 2412 AIRFOIL), (n.d.).  
<http://airfoiltools.com/airfoil/naca4digit> (accessed June 20, 2018).
- [112] ME438 Aerodynamics (week 8), (n.d.).  
<https://www.slideshare.net/BilalSiddiqui33/me438-aerodynamics-week-8>  
(accessed June 20, 2018).
- [113] W. Li, H. Zhou, H. Liu, Y. Lin, Q. Xu, Review on the blade design technologies of tidal current turbine, (2016). doi:10.1016/j.rser.2016.05.017.

- [114] Y. TAKAMATSU, A. FURUKAWA, K. OKUMA, Y. SHIMOGAWA, Study on Hydrodynamic Performance of Darrieus-type Cross-flow Water Turbine, *Bull. JSME*. 28 (1985) 1119–1127. doi:10.1299/jsme1958.28.1119.
- [115] Z. Guang 裕, Y. Ran-sheng 冉, L. Yan 彦, Z. Peng-fei 彭, Hydrodynamic performance of a vertical-axis tidal-current turbine with different preset angles of attack \*, 25 (2013) 280–287. doi:10.1016/S1001-6058(13)60364-9.
- [116] Z. Cheng, H.A. Madsen, Z. Gao, T. Moan, Effect of the number of blades on the dynamics of floating straight-bladed vertical axis wind turbines, *Renew. Energy*. 101 (2017) 1285–1298. doi:10.1016/J.RENENE.2016.09.074.
- [117] B.K. Kirke, Tests on ducted and bare helical and straight blade Darrieus hydrokinetic turbines, *Renew. Energy*. 36 (2011) 3013–3022. doi:10.1016/J.RENENE.2011.03.036.
- [118] T. Maître, E. Amet, C. Pellone, Modeling of the flow in a Darrieus water turbine: Wall grid refinement analysis and comparison with experiments, *Renew. Energy*. 51 (2013) 497–512. doi:10.1016/J.RENENE.2012.09.030.
- [119] Y. Li, S.M. Calisal, Three-dimensional effects and arm effects on modeling a vertical axis tidal current turbine, *Renew. Energy*. 35 (2010) 2325–2334. doi:10.1016/J.RENENE.2010.03.002.
- [120] G. Wei, K. Hai-gui, C. Bing, X. Yu, W. Yin, Numerical and Experimental Study of the 3D Effect on Connecting Arm of Vertical Axis Tidal Current Turbine \*, *China Ocean Eng.* 30 (n.d.) 83–96. doi:10.1007/s13344-015-0080-5.
- [121] M. Gaunaa, J. Johansen, Determination of the Maximum Aerodynamic Efficiency of Wind Turbine Rotors with Winglets, *J. Phys. Conf. Ser.* 75 (2007) 012006. doi:10.1088/1742-6596/75/1/012006.
- [122] C. Jauch, A flywheel in a wind turbine rotor for inertia control, *Wind Energy*. 18 (2015) 1645–1656. doi:10.1002/we.1784.
- [123] M.M. Aslam Bhutta, N. Hayat, A.U. Farooq, Z. Ali, S.R. Jamil, Z. Hussain, Vertical axis wind turbine – A review of various configurations and design techniques, *Renew. Sustain. Energy Rev.* 16 (2012) 1926–1939. doi:10.1016/J.RSER.2011.12.004.
- [124] M. Somoano, F.J. Huera-Huarte, The dead band in the performance of cross-flow turbines: Effects of Reynolds number and blade pitch, *Energy Convers. Manag.* 172 (2018) 277–284. doi:10.1016/J.ENCONMAN.2018.06.087.
- [125] N.C. Batista, R. Melicio, V. Mendes, Darrieus vertical axis wind turbines: methodology to study the self-start capabilities considering symmetric and asymmetric airfoils, (2018). doi:10.17515/resm2017.39ds0108.
- [126] Q. Li, T. Maeda, Y. Kamada, J. Murata, K. Shimizu, T. Ogasawara, A. Nakai, T. Kasuya, Effect of solidity on aerodynamic forces around straight-bladed vertical axis wind turbine by wind tunnel experiments (depending on number of blades), *Renew. Energy*. 96 (2016) 928–939. doi:10.1016/J.RENENE.2016.05.054.
- [127] G.T.T. Houlsby, S. Draper, M.L.G.L.G. Oldfield, Application of Linear Momentum Actuator Disc Theory to Open Channel Flow by, (2008) 1–23.
- [128] C.R. Vogel, G.T. Houlsby, R.H.J. Willden, Effect of free surface deformation on the extractable power of a finite width turbine array, *Renew. Energy*. 88

- (2016) 317–324. doi:10.1016/J.RENENE.2015.11.050.
- [129] P. Ouro, S. Runge, Q. Luo, T. Stoesser, Three-dimensionality of the wake recovery behind a vertical axis turbine, *Renew. Energy*. 133 (2019) 1066–1077. doi:10.1016/J.RENENE.2018.10.111.
- [130] P. Bachant, M. Wosnik, Effects of Reynolds Number on the Energy Conversion and Near-Wake Dynamics of a High Solidity Vertical-Axis Cross-Flow Turbine, *Energies*. 9 (2016) 73. doi:10.3390/en9020073.
- [131] C. Simão Ferreira, G. van Kuik, G. van Bussel, F. Scarano, Visualization by PIV of dynamic stall on a vertical axis wind turbine, *Exp. Fluids*. 46 (2009) 97–108. doi:10.1007/s00348-008-0543-z.
- [132] P. FRAUNIE, C. BEGUIER, I. PARASCHIVOIU, G. BROCHIER, Water channel experiments of dynamic stall on Darrieus wind turbine blades, *J. Propuls. Power*. 2 (1986) 445–449. doi:10.2514/3.22927.
- [133] M. Somoano, F.J. Huera-Huarte, Flow dynamics inside the rotor of a three straight bladed cross-flow turbine, *Appl. Ocean Res.* 69 (2017) 138–147. doi:10.1016/J.APOR.2017.10.007.
- [134] G. Tescione, D. Ragni, C. He, C.J. Simão Ferreira, G.J.W. van Bussel, Near wake flow analysis of a vertical axis wind turbine by stereoscopic particle image velocimetry, *Renew. Energy*. 70 (2014) 47–61. doi:10.1016/J.RENENE.2014.02.042.
- [135] P. Bachant, M. Wosnik, Performance measurements of cylindrical- and spherical-helical cross-flow marine hydrokinetic turbines, with estimates of exergy efficiency, *Renew. Energy*. 74 (2015) 318–325. doi:10.1016/J.RENENE.2014.07.049.
- [136] M. Kinzel, Q. Mulligan, J.O. Dabiri, Energy exchange in an array of vertical-axis wind turbines, *J. Turbul.* 13 (2012) N38. doi:10.1080/14685248.2012.712698.
- [137] P. Ouro, T. Stoesser, Wake Generated Downstream of a Vertical Axis Tidal Turbine Large-Eddy Simulation in Hydraulics View project CFD simulation of a contact tank View project Wake Generated Downstream of a Vertical Axis Tidal Turbine, (n.d.). <https://www.researchgate.net/publication/319623714> (accessed July 4, 2018).
- [138] D.B. Araya, T. Colonius, J.O. Dabiri, Transition to bluff-body dynamics in the wake of vertical-axis wind turbines, *J. Fluid Mech.* 813 (2018) 346–381. doi:10.1017/jfm.2016.862.
- [139] V.F.-C. Rolin, F. Porté-Agel, Experimental investigation of vertical-axis wind-turbine wakes in boundary layer flow, *Renew. Energy*. 118 (2018) 1–13. doi:10.1016/J.RENENE.2017.10.105.
- [140] K.J. Ryan, F. Coletti, C.J. Elkins, J.O. Dabiri, J.K. Eaton, Three-dimensional flow field around and downstream of a subscale model rotating vertical axis wind turbine, *Exp. Fluids*. 57 (2016) 38. doi:10.1007/s00348-016-2122-z.
- [141] L. Cea, J. Puertas, L. Pena, Velocity measurements on highly turbulent free surface flow using ADV, *Exp. Fluids*. 42 (2007) 333–348. doi:10.1007/s00348-006-0237-3.
- [142] I. Nezu, H. Nakagawa, International Association for Hydraulic Research., *Turbulence in open-channel flows*, Balkema, 1993.

- [143] D.B. Araya, J.O. Dabiri, A comparison of wake measurements in motor-driven and flow-driven turbine experiments, *Exp. Fluids*. 56 (2015) 150. doi:10.1007/s00348-015-2022-7.
- [144] L.P. Chamorro, M. Guala, R.E.A. Arndt, F. Sotiropoulos, On the evolution of turbulent scales in the wake of a wind turbine model, *J. Turbul.* 13 (2012) 1–13. doi:10.1080/14685248.2012.697169.
- [145] L.P. Chamorro, F. Porté-Agel, L.P. Chamorro, F. Porté-Agel, A Wind-Tunnel Investigation of Wind-Turbine Wakes: Boundary-Layer Turbulence Effects, *Boundary-Layer Meteorol.* 132 (2009) 129–149. doi:10.1007/s10546-009-9380-8.
- [146] M. Michas, C.E. Ugalde-Loo, W. Ming, N. Jenkins, S. Runge, Maximum power extraction from a hydrokinetic energy conversion system, *IET Renew. Power Gener.* (2019). doi:10.1049/iet-rpg.2018.5642.
- [147] J. Twidell, T. Weir, A.D. Weir, *Renewable Energy Resources*, Taylor & Francis, 2006.
- [148] J. Ekanayake, P. Cartwright, O. Anaya-Lara, N. Jenkins, M. Hughes, *Wind energy generation : modelling and control*, Wiley, 2013. <https://www.wiley.com/en-gb/Wind+Energy+Generation%3A+Modelling+and+Control-p-9781119964209> (accessed June 29, 2018).
- [149] B.K. Hodge, *Alternative energy systems and applications*, n.d. <https://www.wiley.com/en-gb/Alternative+Energy+Systems+and+Applications,+2nd+Edition-p-9781119109211> (accessed June 29, 2018).
- [150] S. Peake, Open University, *Renewable energy : power for a sustainable future*, n.d. <https://global.oup.com/ukhe/product/renewable-energy-9780198759751?cc=gb&lang=en> (accessed June 29, 2018).
- [151] UIS RENEWABLE POWER: Hydro, (n.d.). <http://rp.uiscorp.com/our-services/hydro> (accessed June 29, 2018).
- [152] VENSYS Energy AG – Generator / PM technology, (n.d.). <http://www.vensys.de/energy-en/technologie/generator-pm-technologie.php> (accessed June 29, 2018).
- [153] Three-Phase Induction Motors, (n.d.). [http://www.etcs.ipfw.edu/~lin/ECET211/spring2014/1-Lectures/ECET211\\_Lect\\_3pIM.htm](http://www.etcs.ipfw.edu/~lin/ECET211/spring2014/1-Lectures/ECET211_Lect_3pIM.htm) (accessed June 29, 2018).
- [154] Aeroform Composites- Standard Autoclaves, (n.d.). <https://www.aeroform-composites.com/en/products/process-solutions/standard-autoclaves/> (accessed July 13, 2018).
- [155] [sewagetreatment-waste-watertreatment-process.jpg](http://watertreatmentprocess.net/wp-content/uploads/2010/12/sewagetreatment-waste-watertreatment-process.jpg) (964×436), (n.d.). <http://watertreatmentprocess.net/wp-content/uploads/2010/12/sewagetreatment-waste-watertreatment-process.jpg> (accessed July 1, 2018).
- [156] Atlanta RM Clayton Water Reclamation Plant - Google Maps, (n.d.). <https://www.google.co.uk/maps/place/Atlanta+RM+Clayton+Water+Reclamation+Plant/@33.8239939,-84.4604182,703m/data=!3m1!1e3!4m5!3m4!1s0x0:0x84cb7ece70cc756b!8m>

- 2!3d33.822398!4d-84.4547572 (accessed July 1, 2018).
- [157] Google Maps Ralston Reservoir, (n.d.).  
<https://www.google.co.uk/maps/@39.8350988,-105.2452924,626m/data=!3m1!1e3> (accessed July 2, 2018).
- [158] Bing Maps - Ralston Reservoir, (n.d.).  
<https://www.bing.com/maps?osid=2db84ca3-e50f-4a68-b03b-73ddfc25b13f&cp=39.836517~-105.245266&lvl=19&style=h&v=2&sV=2&form=S00027> (accessed July 2, 2018).
- [159] S. Runge, T. Stoesser, E. Morris, M. White, Technology Readiness of a Vertical-Axis Hydro-Kinetic Turbine, *J. Power Energy Eng.* 06 (2018) 63–85. doi:10.4236/jpee.2018.68004.
- [160] M.S. Guney, Evaluation and measures to increase performance coefficient of hydrokinetic turbines, *Renew. Sustain. Energy Rev.* 15 (2011) 3669–3675. doi:10.1016/J.RSER.2011.07.009.
- [161] U.S. Department of Energy, Technology Readiness Assessment Guide, 2015. <https://www.directives.doe.gov/directives-documents/400-series/0413.3-EGuide-04-admchg1/@@images/file> (accessed January 23, 2018).
- [162] P.O. Barba, T. Stoesser, R. McSherry, Large-Eddy Simulation of a Vertical Axis Tidal Turbine Using an Immersed Boundary Method, in: 2015: pp. 49–58. doi:10.1007/978-3-319-16202-7\_5.
- [163] G. Martinat, M. Braza, Y. Hoarau, G. Harran, Turbulence modelling of the flow past a pitching NACA0012 airfoil at 105 and 106 Reynolds numbers, *J. Fluids Struct.* 24 (2008) 1294–1303. doi:10.1016/j.jfluidstructs.2008.08.002.
- [164] J. McNaughton, F. Billard, A. Revell, Turbulence modelling of low Reynolds number flow effects around a vertical axis turbine at a range of tip-speed ratios, *J. Fluids Struct.* 47 (2014) 124–138. doi:10.1016/J.JFLUIDSTRUCTS.2013.12.014.
- [165] N.C. Batista, R. Melicio, J. Matias, R. Melício, J.C.O. Matias, J.P.S. Catalão, New blade profile for Darrieus wind turbines capable to self-start Enhancing Smart GRIDS for Sustainability View project Call for chapter: New Trends for the Biomass Energy Development: From Wood to Circular Economy View project NEW BLADE PROFILE FOR DARRIEUS WIND TURBINES CAPABLE TO SELF-START, (2011). doi:10.1049/cp.2011.0219.
- [166] I.S. Hwang, S.Y. Min, I.O. Jeong, Y.H. Lee, S.J. Kim, Efficiency improvement of a new vertical axis wind turbine by individual active control of blade motion, in: Y. Matsuzaki (Ed.), *International Society for Optics and Photonics*, 2006: p. 617311. doi:10.1117/12.658935.
- [167] I. Paraschivoiu, O. Trifu, F. Saeed, H-Darrieus Wind Turbine with Blade Pitch Control, *Int. J. Rotating Mach.* 2009 (2009) 1–7. doi:10.1155/2009/505343.
- [168] Y. Li, S.M. Calisal, Modeling of twin-turbine systems with vertical axis tidal current turbine: Part II—torque fluctuation, *Ocean Eng.* 38 (2011) 550–558. doi:10.1016/j.oceaneng.2010.11.025.
- [169] Y. Li, S.M. Calis-AI, Modeling of twin-turbine systems with vertical axis tidal current turbines: Part I—Power output, *Ocean Eng.* 37 (2010) 627–637.

- doi:10.1016/j.oceaneng.2010.01.006.
- [170] T. Kinsey, G. Dumas, Impact of channel blockage on the performance of axial and cross-flow hydrokinetic turbines, *Renew. Energy*. 103 (2017) 239–254. doi:10.1016/J.RENENE.2016.11.021.
- [171] J. Schluntz, R.H.J. Willden, The effect of blockage on tidal turbine rotor design and performance, *Renew. Energy*. 81 (2015) 432–441. doi:10.1016/J.RENENE.2015.02.050.
- [172] ContiTech - Design software CONTI® Professional, (n.d.). <https://www.contitech.de/en-GL/Solutions/Power-Transmission/Mechanical-engineering/Drive-Belts/CONTI-Professional> (accessed July 10, 2018).
- [173] J.D. Winchester, S.D. Quayle, Torque ripple and variable blade force: A comparison of Darrieus and Gorlov-type turbines for tidal stream energy conversion, (n.d.). [http://www.homepages.ed.ac.uk/shs/WaveEnergy/EWTEC2009/EWTEC2009\(D\)/papers/257.pdf](http://www.homepages.ed.ac.uk/shs/WaveEnergy/EWTEC2009/EWTEC2009(D)/papers/257.pdf) (accessed July 10, 2018).
- [174] W. Shi, M. Atlar, R. Rosli, B. Aktas, R. Norman, Cavitation observations and noise measurements of horizontal axis tidal turbines with biomimetic blade leading-edge designs, *Ocean Eng.* 121 (2016) 143–155. doi:10.1016/J.OCEANENG.2016.05.030.
- [175] Contitech Synchrobelt HTD, Timing Belt, 133 Teeth, 665mm Length X 9mm Width | 665 5M 9 | RS Components, (n.d.). <https://uk.rs-online.com/web/p/timing-belts/4746457/> (accessed July 12, 2018).
- [176] Contitech Synchrobelt HTD, Timing Belt, 150 Teeth, 1.2m Length X 20mm Width | 1200 8M 20 | RS Components, (n.d.). <https://uk.rs-online.com/web/p/timing-belts/4750670/> (accessed July 12, 2018).
- [177] Three phase bridge (rectifier), (n.d.). <https://eu.mouser.com/datasheet/2/427/vs-36mtseries-71716.pdf> (accessed July 12, 2018).
- [178] 500W Dump Load for Leading Edge wind turbines, (n.d.). [https://www.leadingedgepower.com/shop/store/wind-turbines/wind-turbine-controllers-accessories/500w-wind-turbine-dump-load-1013002.html?pid=1013002&gclid=Cj0KCQjw-JvaBRDGARIsAFjqkPvVFXRoQ2TmsqNfL7c1BfeVSnPK9r56-soD2iD33J\\_PzC1upgRikaAIMGEALw\\_wcB](https://www.leadingedgepower.com/shop/store/wind-turbines/wind-turbine-controllers-accessories/500w-wind-turbine-dump-load-1013002.html?pid=1013002&gclid=Cj0KCQjw-JvaBRDGARIsAFjqkPvVFXRoQ2TmsqNfL7c1BfeVSnPK9r56-soD2iD33J_PzC1upgRikaAIMGEALw_wcB) (accessed July 12, 2018).
- [179] TriStar - Morningstar Corporation, (n.d.). <https://www.morningstarcorp.com/products/tristar/> (accessed July 10, 2018).
- [180] Bureau of Reclamation : Research and Development | Research and Development Office, (n.d.). <https://www.usbr.gov/research/projects/detail.cfm?id=1707> (accessed July 13, 2018).
- [181] Plastic Material (polyamide) for 3D Printing: 3D printing plastic, (n.d.). <https://www.sculpteo.com/en/materials/plastic-material/> (accessed July 12, 2018).
- [182] TRS605 Non-Contact Shaft to Shaft Rotary Torque Sensor with Encoder, (n.d.). <http://www.futek.com/product.aspx?t=torque&m=trs605> (accessed July 10, 2018).

- [183] TRD305 Square Drive Rotary Torque Sensor with Encoder, (n.d.).  
<http://www.futek.com/product.aspx?t=torque&m=trd305> (accessed July 10, 2018).
- [184] Acoustic velocimeter for 3D water velocity fluctuations | Nortek, (n.d.).  
<https://www.nortekgroup.com/products/vectrino> (accessed July 10, 2018).
- [185] LE-300 most reliable 300W small wind turbine, (n.d.).  
<https://www.leadingedgepower.com/shop/index/le-300-wind-turbine-standard-1013010.html> (accessed July 11, 2018).
- [186] Flow Probe, Digital Water Velocity Meter. Flow monitor,water,global,flow probe,velocity,probe,water flow meter,propeller,velocity,meters,environmental,flow,water,velocity,monitor,sensor,rate,water,flow,sewer,measurements,propeller,flow,meter,velocity,sensors,water,flow,meters,water,turbo,prop., (n.d.).  
<http://www.globalw.com/products/flowprobe.html> (accessed July 11, 2018).
- [187] S.E. Ben Elghali, M.E.H. Benbouzid, J.F. Charpentier, Marine Tidal Current Electric Power Generation Technology: State of the Art and Current Status, in: 2007 IEEE Int. Electr. Mach. Drives Conf., IEEE, 2007: pp. 1407–1412. doi:10.1109/IEMDC.2007.383635.

# Appendices

## A. Test result overview

Test #	Description	SS			V <sub>approach</sub>	Blockage	Solidity	C <sub>p</sub> max (electr)	TSR@C <sub>p</sub> max (geared)	Comments
		yes	no	maybe (if it self starts from most positions)						
001	Disc_3xNACA0018_2_5deg				0.92	50%	24%	44%	1.7	-
002	"				1.16	"	"	49%	1.8	-
003	Disc_3xEppler80_2_5deg				0.92	"	19%	-	-	aborted
004	Disc_3xEppler80_7_5deg				0.92	"	"	-	-	aborted
005	Disc_3xEppler80_5deg				0.92	"	"	27%	2.1	-
006	"				1.16	"	"	31%	2.2	-
007	Disc_3xEppler120_5deg				0.92	"	29%	38%	1.5	-
008	"				1.16	"	"	42%	1.6	-
009	Disc_3xEppler120_5deg_Cylinder180				0.92	"	"	34%	1.7	Cylinders over shaft
010	"				1.16	"	"	37%	1.7	-
011	Disc_3xEppler120_5deg_Cylinder140				0.92	"	"	36%	1.6	-
012	"				1.16	"	"	40%	1.7	-
013	Disc_3xEppler120_5deg_Cylinder100				0.92	"	"	38%	1.6	-
014	"				1.16	"	"	42%	1.7	-
015	Disc_3xEppler120_5deg_Cylinder060				0.92	"	"	39%	1.6	-
016	"				1.16	"	"	42%	1.6	-
017	Disc_3xEppler80_5deg_Cylinder060				0.92	"	19%	27%	2.1	early stall
018	"				1.16	"	"	31%	2.1	early stall
019	Disc_3xEppler80_5deg_Cylinder100				0.92	"	"	24%	2.1	-
020	"				1.16	"	"	27%	2.2	-
021	Disc_3xEppler80_5deg_Cylinder140				0.92	"	"	22%	2.1	-
022	"				1.16	"	"	26%	2.3	-
023	Disc_3xEppler80_5deg_Cylinder180				0.92	"	"	17%	2	-
024	"				1.16	"	"	20%	2	-
025	Disc_3xNACA0018_2_5deg				0.92	"	24%	36%	1.5	Turbine displaced 23cm downstream
026	"				1.16	"	"	40%	1.5	-
027	Disc_3xNACAsmall_2_5deg				0.92	"	11%	-	-	aborted
028	Disc_2xEppler80_5deg				1.16	"	13%	25%	2.5	-
029	"				0.92	"	"	21%	2.6	-
030	Disc_2xEppler100_5deg				0.92	"	16%	32%	2.3	-
031	"				1.16	"	"	35%	2.3	-
032	Disc_2xEppler120_5deg				0.92	"	19%	39%	2.2	-
033	"				1.16	"	"	42%	2.1	-
034	Disc_2xNACA0018_100_2_5deg				0.92	"	16%	41%	2.1	-
035	"				1.16	"	"	44%	2.1	-
036	Disc_4xEppler80_5deg				0.92	"	25%	26%	1.9	-
037	"				1.16	"	"	30%	2	-
038	Disc_4xEppler100_5deg				0.92	"	32%	32%	1.6	-
039	"				1.16	"	"	36%	1.6	-
040	Disc_4xEppler120_5deg				0.92	"	38%	35%	1.4	-
041	"				1.16	"	"	38%	1.5	-
042	Disc_4xEppler100Twist30_5deg				0.92	"	32%	31%	1.6	Not sure with solidity since twisted...
043	"				1.16	"	"	35%	1.7	-
044	Disc_3xEppler100Twist30_5deg				0.92	"	24%	34%	2	-
045	"				1.16	"	"	39%	2	-
046	Disc_2xEppler100Twist30_5deg				0.92	"	16%	30%	2.4	-
047	"				1.16	"	"	35%	2.4	-
048	Disc_3xEppler100_5deg				0.92	"	24%	35%	1.8	-
049	"				1.16	"	"	39%	1.9	-
050	Disc_3xNACA4421_2_5deg				0.85	33%	14%	-	-	aborted
051	"				0.98	"	"	-	-	aborted
052	Spokes60cm_3xNACA4421_CL59_machined				0.85	50%	9%	50%	3.2	-
053	"				0.98	"	"	52%	3.1	-
054	"				1.09	"	"	56%	3.2	-
055	Spokes60cm_3xNACA4421_CL59_machined_6kgFlywheel				0.85	"	"	51%	3.2	worse in starting
056	"				0.98	"	"	51%	3.1	-
057	"				1.09	"	"	54%	3.2	-
058	Spokes60cm_3xNACA4421_CL59_machined_12kgFlywheel				0.85	"	"	50%	3	-
059	"				0.98	"	"	52%	3.1	-
060	"				1.09	"	"	54%	3.2	-
061	Disc_3xNACA4421_CL59_machined				0.85	33%	14%	21%	2.2	-
062	"				0.98	"	"	20%	2.2	-
063	"				1.09	"	"	33%	2.3	-
064	"				1.15	"	"	29%	2.2	-
065	Spokes60cm_3xNACA4421_CL59_composite3xMC				0.85	50%	9%	25%	3.1	-
066	"				0.98	"	"	29%	3.1	-
067	"				1.09	"	"	31%	3	-
068	Spokes60cm_3xNACA4421_CL59_composite3xMC_ChangedScrews				0.85	"	"	41%	3.4	-
069	"				0.98	"	"	44%	3.2	-
070	"				1.09	"	"	45%	3.3	-
071	Spokes60cm_3xEppler_CL100_straight				0.85	"	16%	47%	2.8	-
072	"				0.98	"	"	67%	3.2	aborted, high torque
073	"				1.09	"	"	60%	3.4	-
074	Spokes60cm_3xNACA0018_CL100				0.85	"	"	69%	2.6	-
075	"				0.98	"	"	66%	3.1	aborted, high torque
076	Spokes60cm_3xNACA4421_CL59_machined				0.92	75%	9%	41%	3	-
077	"				1.16	"	"	45%	3.1	-
078	Twin_60degOffset_Disc20cm_3xNACA4421_CL59_machined_composite_15mmBelt				0.92	50%	28%	35%	1.6(2.1)	gear ratio 3:4, high vibrations in the belt
079	"				1.16	"	"	40%	1.7(2.2)	-
080	Twin_NoOffset_Disc20cm_3xNACA4421_CL59_machined_composite_15mmBelt				0.92	"	"	36%	1.5(2)	-
081	"				1.16	"	"	42%	1.7(2.2)	-
082	Twin_NoOffset_Disc20mm_3xNACA4421_CL59_machined_composite_6mmBelt				0.92	"	"	42%	1.7	-
083	"				1.16	"	"	44%	1.7	belt slipped -> test aborted
084	"				1.16	"	"	47%	1.5	increased belt tension -> belt snapped
085	Twin_OneRotor_Disc20mm_3xNACA4421_CL59_machined_9mmx600Belt				1.16	25%	"	36%	1.4(1.9)	5/16lb belt tension, just one rotor
086	"				1.42	"	"	39%	1.5(2)	-
087	"				1.16	"	"	35%	1.4(1.9)	as 085 but counter rotating
088	"				1.42	"	"	40%	1.4(1.9)	as 086 but counter rotating
089	Twin_OneRotor_Disc20mm_3xNACA4421_CL59_composite_9mmx600Belt				1.16	"	"	26%	1.5(2)	-
090	"				1.42	"	"	30%	1.4(1.9)	-
091	Disc20mm_3xNACA4421_CL59_machined				0.92	"	"	34%	1.3	At centre position, without belts
092	"				1.16	"	"	44%	1.5	-
093	"				1.42	"	"	45%	1.5	-
094	Twin_NoOffset_Disc20cm_3xNACA4421_CL59_machined_composite_9mmBelt				0.92	50%	"	-	-	aborted, too high belt tension (2lb)
095	"				0.92	"	"	38%	1.7(2.2)	belt tension 3/4lb
096	"				1.16	"	"	44%	1.6(2.1)	-
097	"				1.42	"	"	40%	1.5(2)	-
098	Twin_NoOffset_Disc40mm_3xNACA4421_CL59_machined_composite_15x670mmBelt				0.98	67%	14%	28%	2.7(3.6)	very poor selfstarting
099	"				1.09	"	"	31%	2.6(3.4)	-
100	same as before but opposite rotation				1.09	"	"	29%	2.6(3.4)	-

Test #	Description	SS			Vapproach	Blockage	Solidity	Cp max (electr.)	TSR@Cp max (geared)	Comments
		SS	Blockage	Solidity						
101	Twin_60degOffset_Disc40mm_3xNACA4421_CL59_machined_composite_15x670mmBelt	SS	yes	no	1.09	"	"	26%	2.6(3.4)	"
102	Twin_NoOffset_Disc40mm_3xEppler_CL100_Twist15&30_15x670mmBelt	SS	yes	no	0.59	"	24%	29%	2.3(3.1)	No selfstarting, but much better
103	"	SS	yes	no	0.72	"	"	38%	2.3(3.1)	"
104	"	SS	yes	no	0.85	"	"	44%	2.4(3)	"
105	"	SS	yes	no	0.98	"	"	46%	2.3(3.1)	"
106	"	SS	yes	no	1.09	"	"	46%	2.3(3.1)	"
107	Twin_SchererMini_unsanded_Spoke36mm_15x670mmBelt	SS	yes	no	1.09	60%	21%	38%	1.8(2.4)	Untreated sintered material
108	Twin_SchererMini_Spoke36mm_15x670mmBelt	SS	yes	no	1.09	"	"	72%	2.4(3.2)	Sanded and painted, aborbed high torque
109	"	SS	yes	no	0.98	"	"	72%	2.3(3.1)	"
110	"	SS	yes	no	0.85	"	"	72%	2.3(3.1)	"
111	Twin_SchererMini_Spoke36mm_9x600mmBelt	SS	yes	no	1.09	"	"	76%	2.2(4.4)	New gear ratio 1:2
112	Twin_SchererMini_Spoke36mm_15x800mmBelt	SS	yes	no	0.85	"	"	75%	2.3(4.5)	"
113	"	SS	yes	no	0.98	"	"	70%	2.4(4.8)	Video, belt too loose, aborbed
114	"	SS	yes	no	0.98	"	"	70%	2.4(4.8)	"
115	"	SS	yes	no	1.09	"	"	68%	2.2(4.5)	"
116	Twin_SchererMini_Spoke36mm_15x750mmBelt	SS	yes	no	0.85	"	"	79%	2.4(4.8)	"
117	"	SS	yes	no	0.98	"	"	74%	2.3(4.6)	"
118	"	SS	yes	no	1.09	"	"	74%	2.2(4.4)	"
119	Twin_SchererMini_Spoke36mm_15x700mmBelt	SS	yes	no	0.85	"	"	79%	2.4(4.8)	"
120	"	SS	yes	no	0.98	"	"	76%	2.4(4.8)	"
121	"	SS	yes	no	1.09	"	"	-	-	System too hot, aborbed
122	"	SS	yes	no	1.09	"	"	74%	2.2(4.3)	"
123	Twin_SchererMini_Spoke36mm_15x700mmBelt_GeneratorLE300	SS	yes	no	1.09	"	"	-	-	Generator did not perform, aborbed
124	Twin_SchererMini_Spoke36mm_15x700mmBelt_GeneratorLuis	SS	yes	no	0.85	"	"	71% (58)	2.4	"
125	"	SS	yes	no	0.98	"	"	71% (58)	2.3	"
126	"	SS	yes	no	1.09	"	"	68% (57)	2.2	"
127	Single_SchererMini_Spoke36mm	SS	yes	no	0.72	30%	"	32%	2.2	"
128	"	SS	yes	no	0.85	"	"	42%	2.1	"
129	"	SS	yes	no	0.98	"	"	50%	2.1	"
130	"	SS	yes	no	1.09	"	"	60%	1.9	"
131	"	SS	yes	no	1.15	"	"	52%	2.1	performance drop maybe due to wave
132	Single_SchererMini_Spoke36mm_2bladed_clocked	SS	yes	no	0.85	"	14%	36%	2.3	& not fully submerged
133	"	SS	yes	no	0.98	"	"	41%	2.5	offset, not clocked
134	"	SS	yes	no	1.09	"	"	47%	2.7	"
135	"	SS	yes	no	1.15	"	"	46%	2.4	"
136	Single_SchererMini_Spoke36mm_3bladed_clocked	SS	yes	no	0.72	"	21%	36%	2.1	"
137	"	SS	yes	no	0.85	"	"	32%	2.1	"
138	"	SS	yes	no	0.98	"	"	41%	2.1	"
139	"	SS	yes	no	1.09	"	"	48%	2	"
140	"	SS	yes	no	1.15	"	"	59%	2	"
141	Twin_SchererMini_Spoke36mm_Individual	SS	yes	no	0.98	60%	"	44%	3.2	Overall results from 2 Individual data sets
142	"	SS	yes	no	0.98	"	"	52%	3.1	"
143	"	SS	yes	no	0.98	"	"	60%	2.9	"
144	"	SS	yes	no	0.98	"	"	69%	2.8	"
145	"	SS	yes	no	0.98	"	"	69%	2.8	"
146	"	SS	yes	no	0.98	"	"	72%	2.7	"
147	"	SS	yes	no	0.98	"	"	77%	2.5	"
148	"	SS	yes	no	0.98	"	"	75%	2.4	"
149	"	SS	yes	no	0.98	"	"	78%	2.4	"
150	Twin_SchererMini_Spoke36mm_BothClockwise	SS	yes	no	0.98	"	"	42%	3	"
151	"	SS	yes	no	0.98	"	"	69%	2.5	"
152	"	SS	yes	no	0.98	"	"	72%	2.5	"
153	"	SS	yes	no	0.98	"	"	75%	2.3	"
154	"	SS	yes	no	0.98	"	"	76%	2.2	"
155	Twin_SchererMini_Spoke36mm_15x700mmBelt_GeneratorLuis_ForMarios	SS	yes	no	0.72	"	"	75%	2.4(3.2)	TD combined with electrical load
156	"	SS	yes	no	0.85	"	"	77%	2.4(3.2)	"
157	"	SS	yes	no	0.98	"	"	75%	2.2(3.1)	Limit TD
158	"	SS	yes	no	1.09	"	"	69%	2.4(3.2)	Limit TD
159	"	SS	yes	no	1.15	"	"	70%	2.6(3.5)	Limit TD
160	Atlanta	SS	yes	no	0.64	58%	17%	58%	2.8	Uncertainty with discharge/velocity
161	"	SS	yes	no	0.76	"	"	60%	2.7	"
162	"	SS	yes	no	0.9	"	"	82%	3	"
163	"	SS	yes	no	0.9	"	"	94%	3.9	"
164	"	SS	yes	no	0.76	"	"	22%	4.8	High RPM generator
165	Denver	SS	yes	no	1.56	65%	11%	81%	4.1	"
166	"	SS	yes	no	"	"	"	74%	4	"
167	"	SS	yes	no	"	"	"	72%	3.7	"
168	"	SS	yes	no	"	"	"	76%	4.9	"
169	"	SS	yes	no	"	"	"	53%	3.3	"
170	Rep. of Test 156 RightToLeft(negativePumpPower)InwardsRotating	SS	yes	no	0.85	60%	21%	72%	2.4	"
171	" LeftToRight(PositivePumpPower)OutwardsRotating	SS	yes	no	"	"	"	71%	2.4	"
172	" LeftToRight(PositivePumpPower)InwardsRotating	SS	yes	no	"	"	"	76%	2.4	High initial torque, adjusted by 0.15Nm
173	" LeftToRight(PositivePumpPower30%)InwardsRotating@0.45m	SS	yes	no	0.95	"	"	11%	1.53	"
174	" LeftToRight(PositivePumpPower27%)InwardsRotating@0.45m	SS	yes	no	0.85	"	"	16%	1.9	"
175	" LeftToRight(PositivePumpPower30%)InwardsRotating@0.40m	SS	yes	no	1.06	"	"	20%	1.9	"
176	" LeftToRight(PositivePumpPower24%)InwardsRotating@0.40m	SS	yes	no	0.85	"	"	31%	2.4	"
177	" LeftToRight(PositivePumpPower30%)InwardsRotating@0.35m	SS	yes	no	1.22	"	"	13%	1.5	"
178	" LeftToRight(PositivePumpPower21%)InwardsRotating@0.35m	SS	yes	no	0.85	"	"	11%	1.6	"
179	" LeftToRight(PositivePumpPower40%)InwardsRotating@0.65m	SS	yes	no	0.84	"	"	70%	2.2	"
180	" LeftToRight(PositivePumpPower50%)InwardsRotating@0.65m	SS	yes	no	1.05	"	"	74%	2.1	"
181	Twin_2BladedClocked_15x700Belt_GeneratorLuis_NotOffset	SS	yes	no	0.72	"	14%	35%	2.6	Less belt tension
182	"	SS	yes	no	0.72	"	"	39%	2.6	"
183	"	SS	yes	no	0.85	"	"	43%	2.5	"
184	"	SS	yes	no	0.98	"	"	44%	2.4	"
185	"	SS	yes	no	1.09	"	"	50%	2.4	"
186	"	SS	yes	no	1.15	"	"	50%	2.4	"
187	Twin_2BladedClocked_15x700Belt_GeneratorLuis_Offset	SS	yes	no	0.72	"	"	36%	2.7	"
188	"	SS	yes	no	0.85	"	"	45%	2.5	"
189	"	SS	yes	no	0.98	"	"	45%	2.6	"
190	"	SS	yes	no	1.09	"	"	52%	2.4	"
191	"	SS	yes	no	1.15	"	"	49%	2.2	"
192	Twin_2BladedClockedWithDiscs_15x700Belt_GeneratorLuis_NotOffset	SS	yes	no	0.72	"	"	42%	2.7	"
193	"	SS	yes	no	0.85	"	"	49%	2.6	"
194	"	SS	yes	no	0.98	"	"	46%	2.5	"
195	"	SS	yes	no	1.09	"	"	51%	2.6	"
196	"	SS	yes	no	1.15	"	"	50%	2.2	"
197	Twin_NoOffset_Disc20mm_3xNACA4421_CL59_machined_composite_15x670mmBelt	SS	yes	no	1.15	33%	28%	32%	1.6	"
198	"	SS	yes	no	1.09	"	"	-	-	Immediate stall
199	"	SS	yes	no	0.98	"	"	-	-	"
200	2BladedClockedSingle	SS	yes	no	1.09	30%	14%	44%	2.2	Vibration test, 5Min

## B. Technical drawings of VAT

### Turbine concept

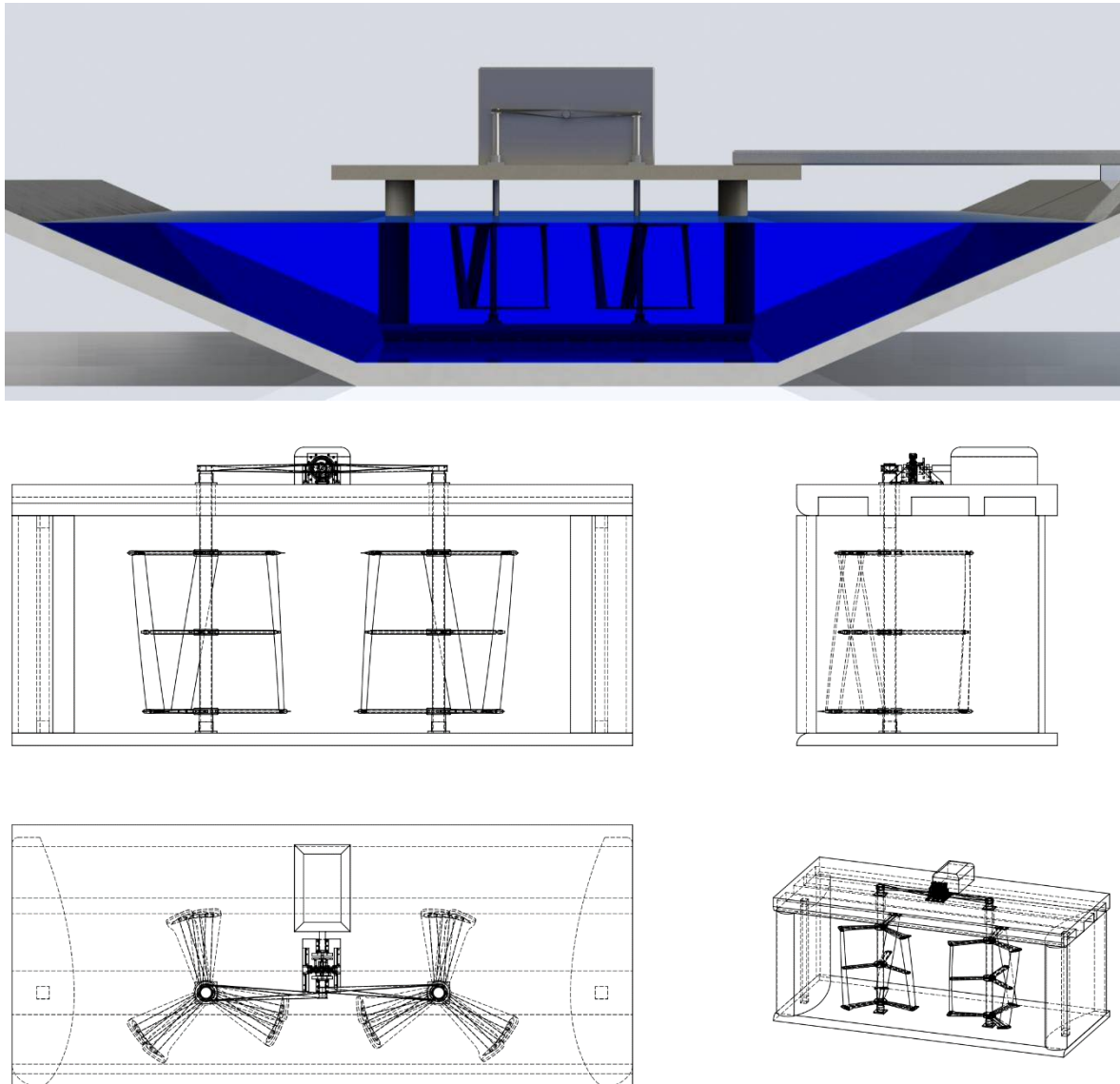


Figure B1. Technical drawing of turbine concept (not to scale)

## Laboratory components

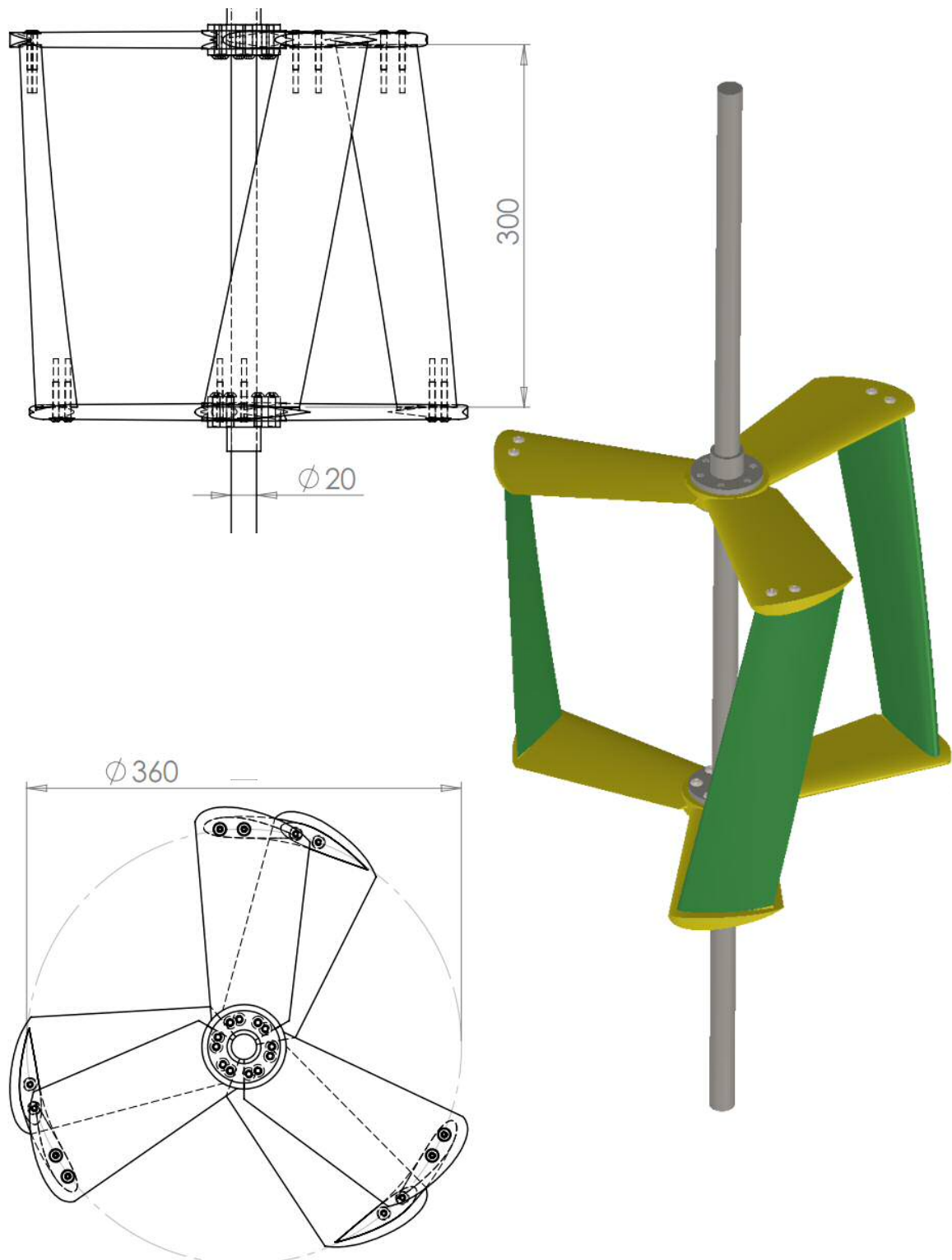


Figure B2. Technical drawing of laboratory rotor (not to scale)

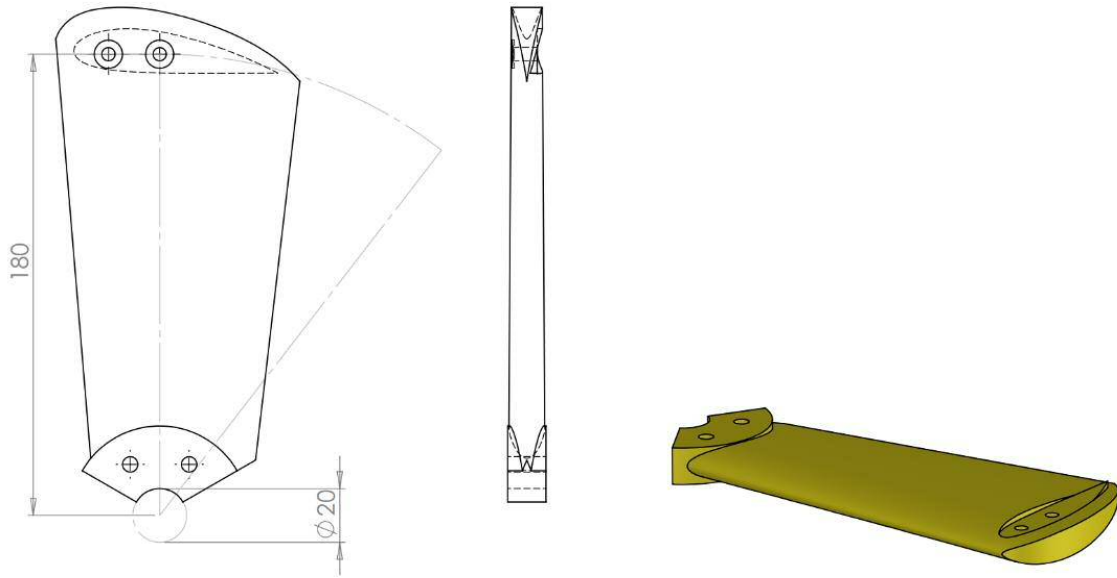


Figure B3. Technical drawing of the spoke of the laboratory rotor (not to scale)

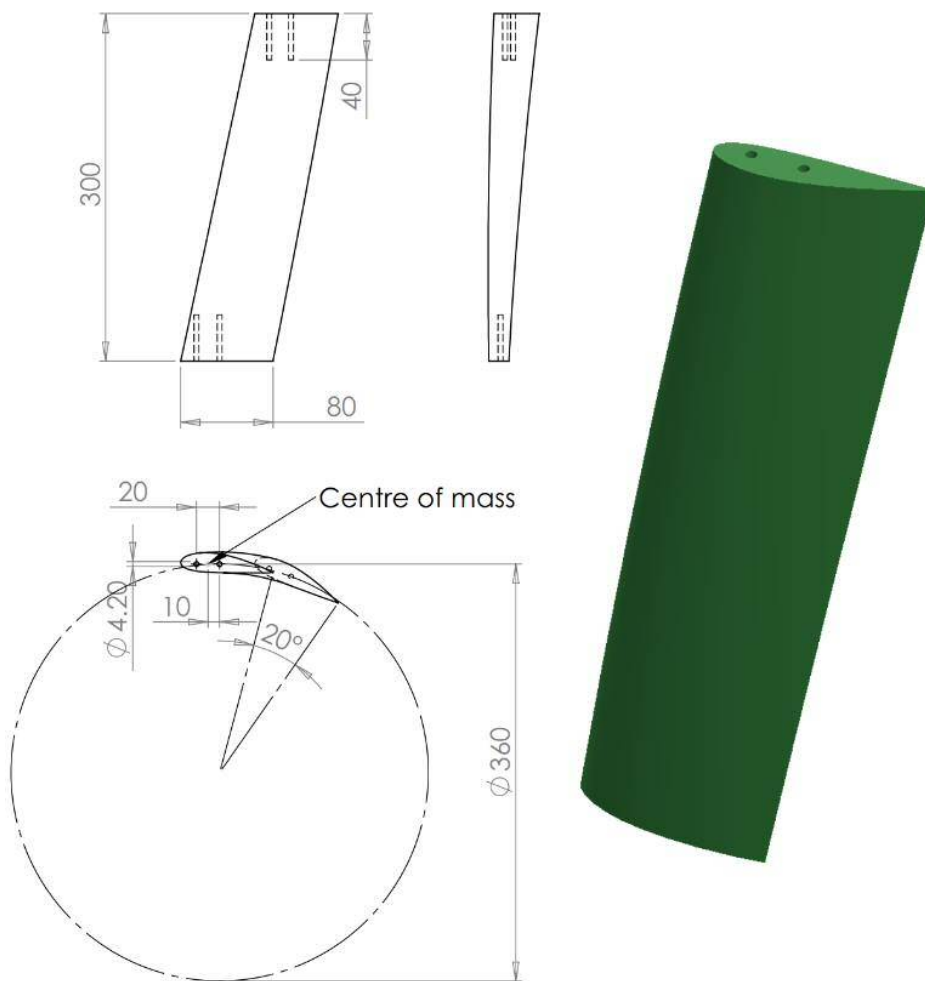


Figure B4. Technical drawing of the blade of the laboratory rotor (not to scale)

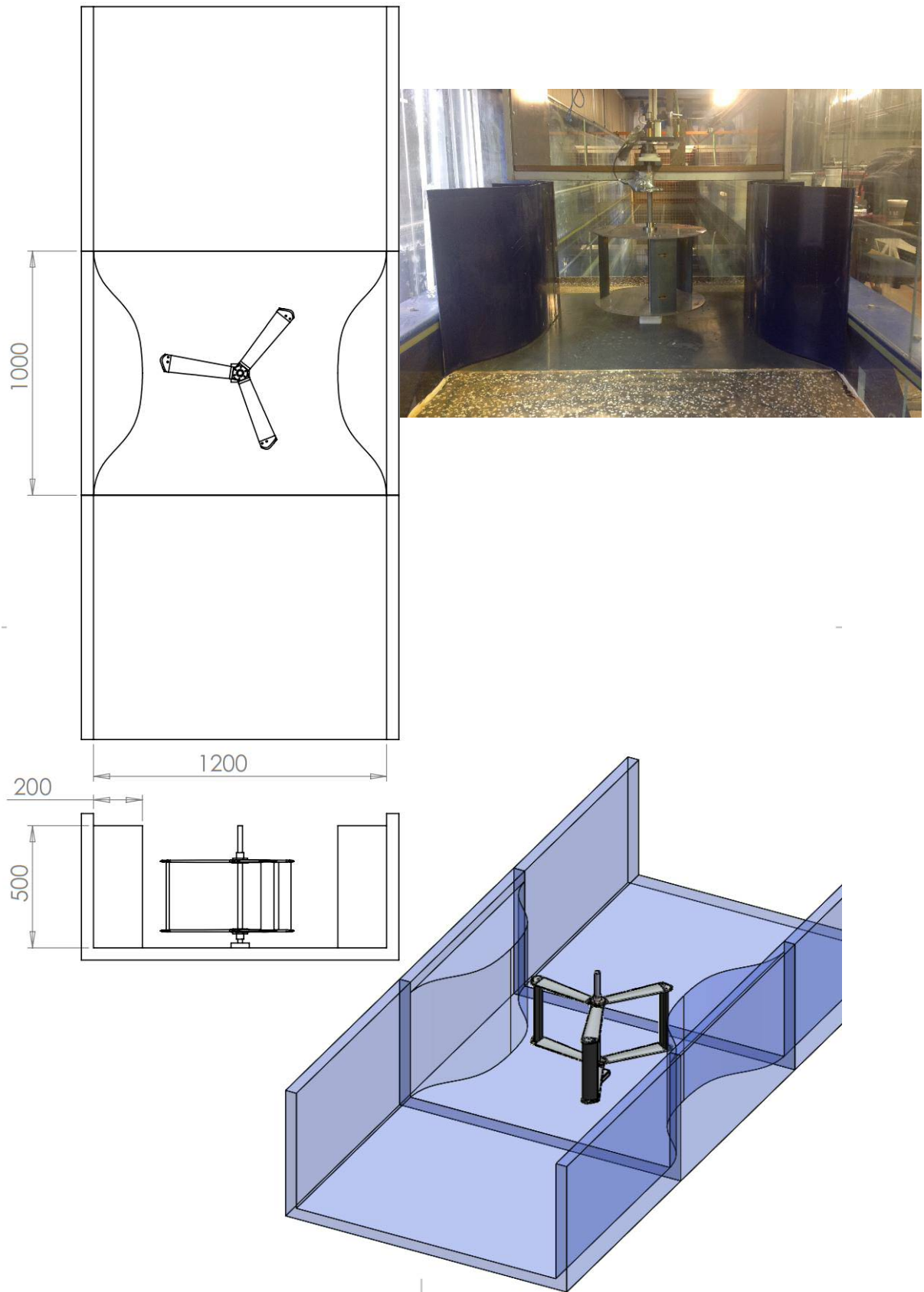


Figure B5. Technical drawing of the initial blockage structure (not to scale) and photograph of the structure as installed in the laboratory flume. The structure was used for calibrating but not for testing

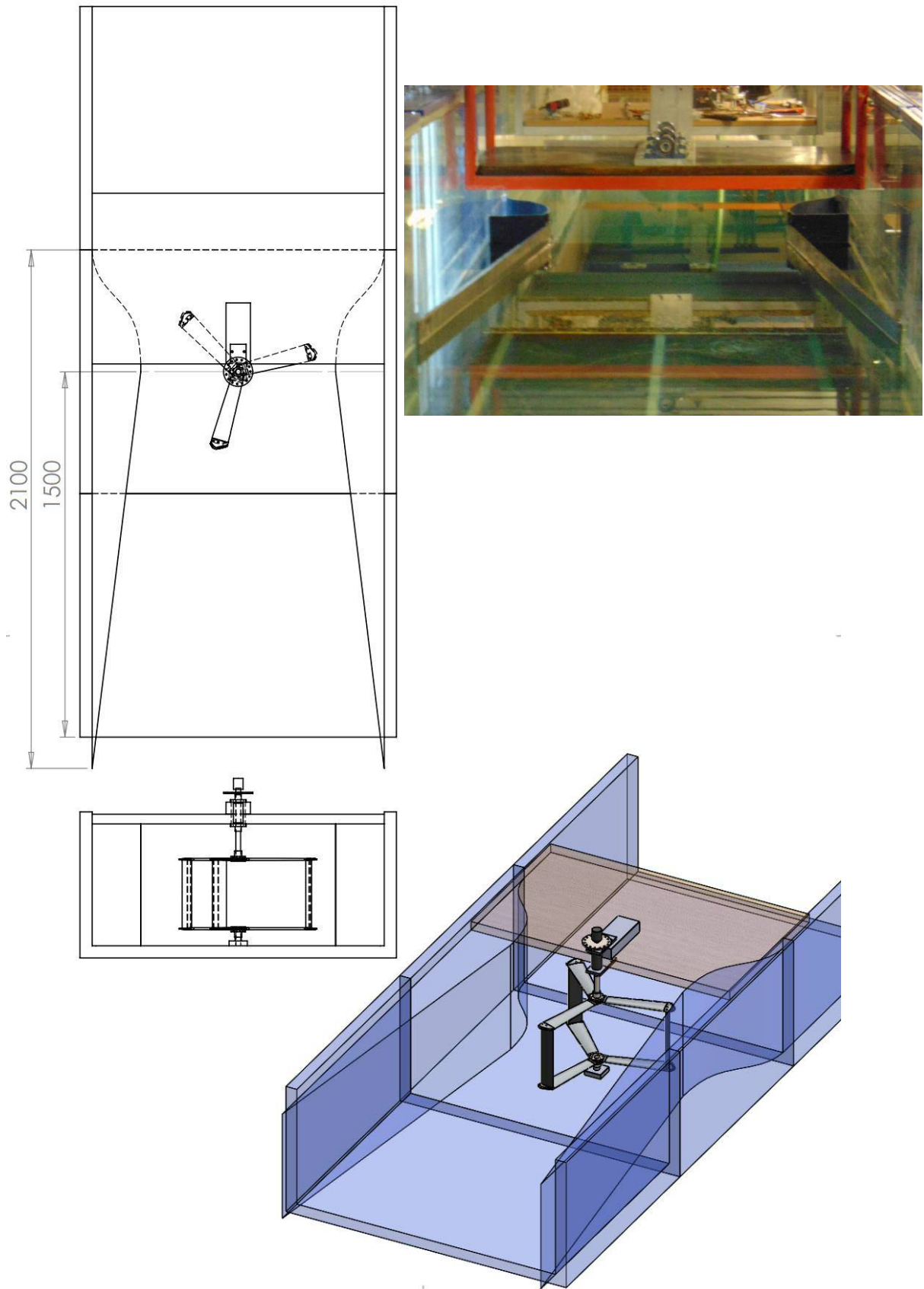


Figure B6. Technical drawing of the blockage structure with increased downstream length including top bridge as well as PTO (not to scale) and photograph of the structure as installed in the laboratory flume for testing

### C. Belt drive sizing and tension

Both rotors of the twin-turbine assembly are rotate vertically and in opposite direction. The main shaft, however, rotates clockwise and horizontally. In order to change direction and combine the rotors torque, a belt system was introduced. In a series of tests, it was investigated what the ideal belt size and the corresponding belt tension is for the laboratory turbine.

Three different sized belts (6, 9, and 15mm wide) were tested. The smallest belt (6mm) stands out by its low friction losses but snapped if the load was too high. Both, 9 and 15mm belts performed well by compromising on higher friction losses proportionally to the width. Therefore, for laboratory testing, the 9mm belt was used [175], for field testing in Atlanta, a 20mm belt was chosen [176].

In order to translate the torque and rotational speed, the belt needs a certain tension to engage with the pulley properly. Since the twisted application of the timing belts is not specified with the manufacture, the ideal tension was evaluated experimentally. Here, a tension gauge (see Figure C1, RHS) was used in such a way that the force needed for a displacement of 10mm at mid-span of the belt was measured. The tension of the belts was varied by moving the rotor shafts relative to the main shaft.

It was observed that the turbine stalled much earlier if the belt tension was too high (see Figure C1, LHS). 3/4lb was found to be the ideal belt tension for this particular set-up.

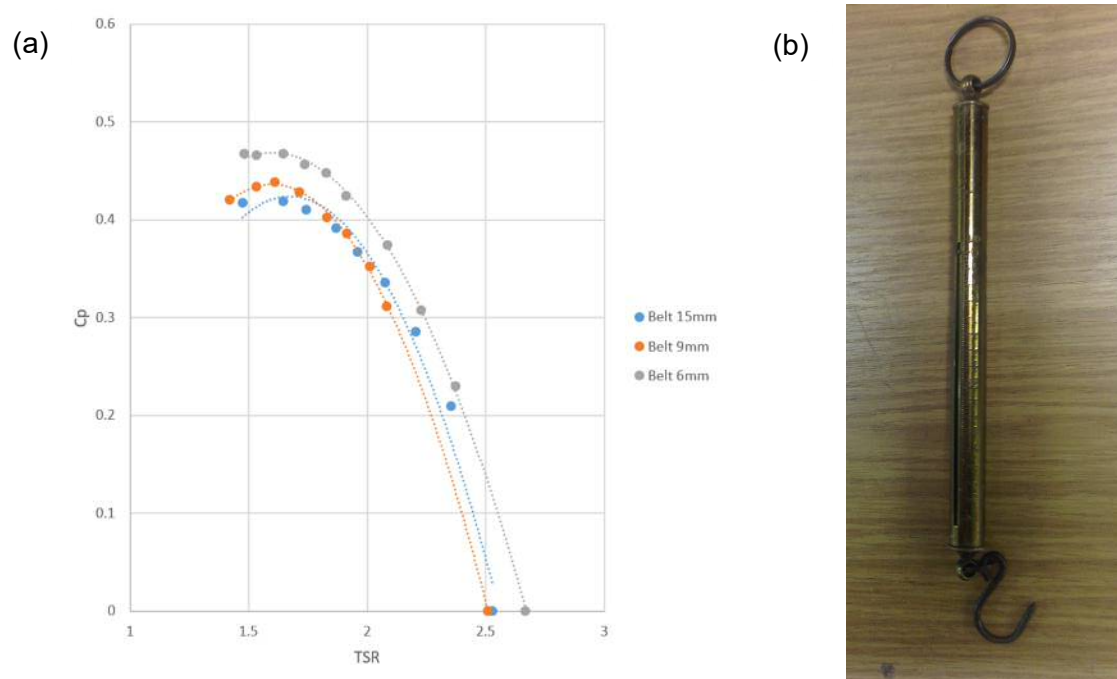


Figure C1. a) Belt size comparison in terms of performance drop. Highest resistance from 15mm wide belt ( $C_P = 42\%$ ), 9mm belt  $C_P = 44\%$ , 6mm belt  $C_P = 47\%$ . Test 081, 084, 096; b) tension gauge used to measure the belt's tension

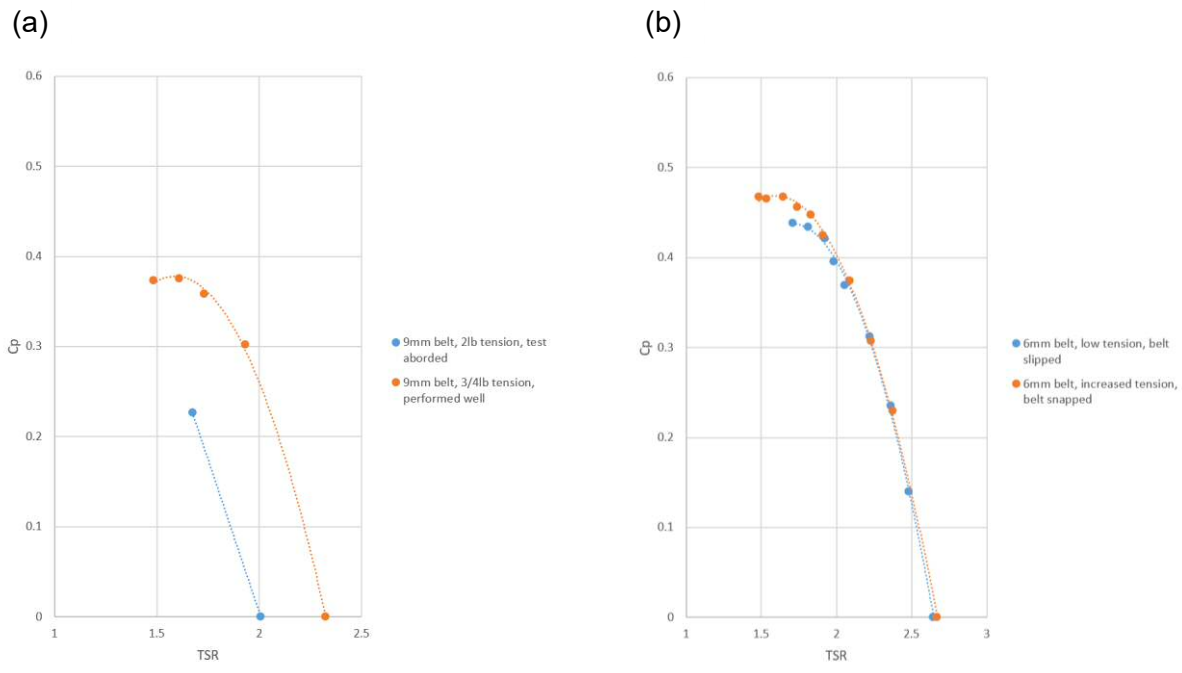


Figure C2. Belt tension comparison. a) Tension (2lb) too high, reduced tension (3/4lb) performed well; b) 6mm belt was found to be too small. At low tension it slipped through the pulleys, at higher tension it snapped when loaded. Test 083, 084, 094, 095.

#### D. Power diversion assembly

Main component of the PDA is the diversion controller (Tristar 45A) including a computer interface (RS-232 CON). The housing is a standard aluminium and steel instrument case (350x430x222.5mm). Further, an uncontrolled diode rectifier (36MT100, [177]) and a 500 Watt dump load [178] were used.

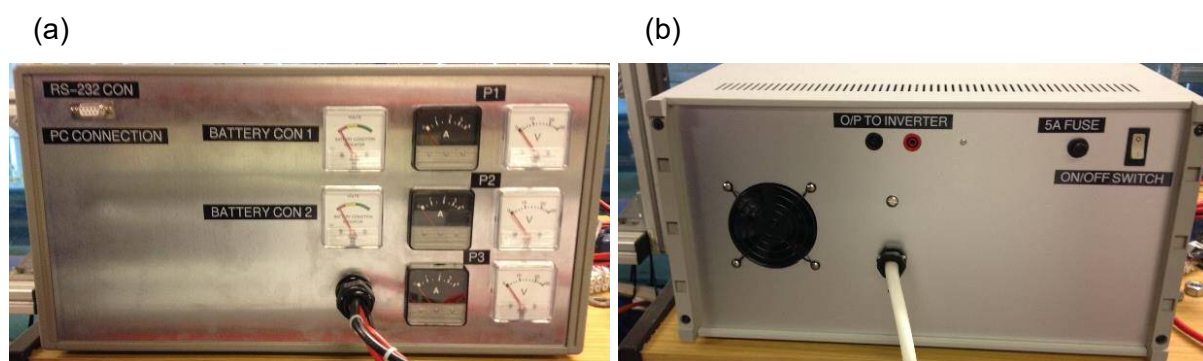


Figure D1. LHS, PDA front view incl. meters, cables to/from batteries and RS-232 interface  
 RHS, PDA back view incl. fan, power supply connector, cable to/from generator, fuse and main switch

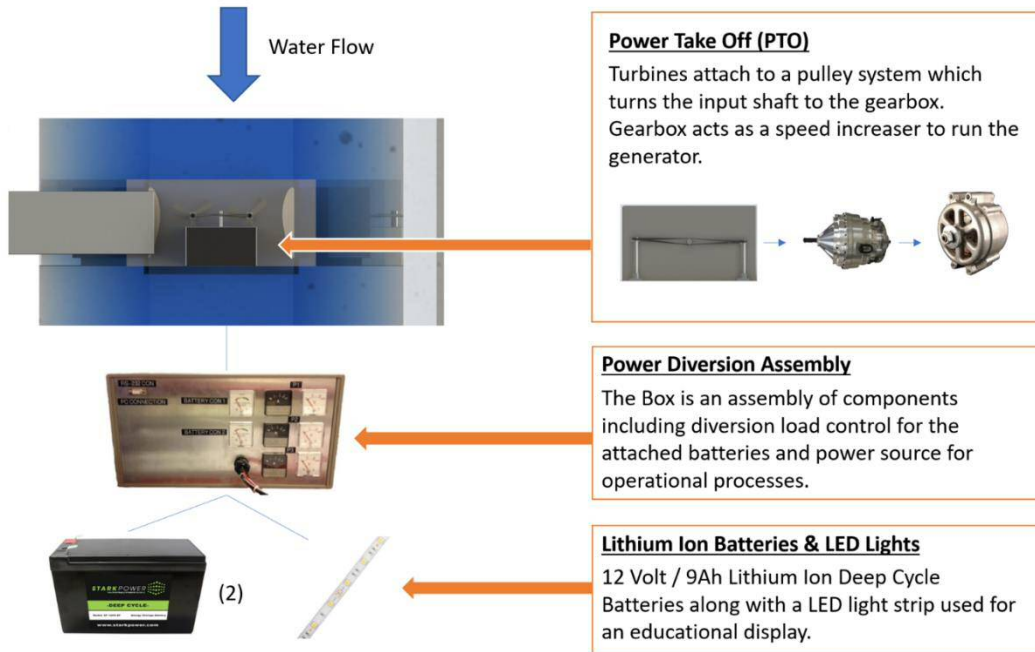


Figure D2. System description of turbine, PTO, PDA and batteries/load



**MORNINGSTAR**  
World's Leading Solar Controllers & Inverters

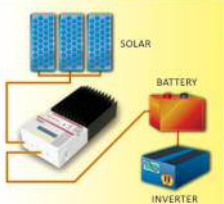
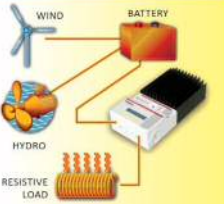
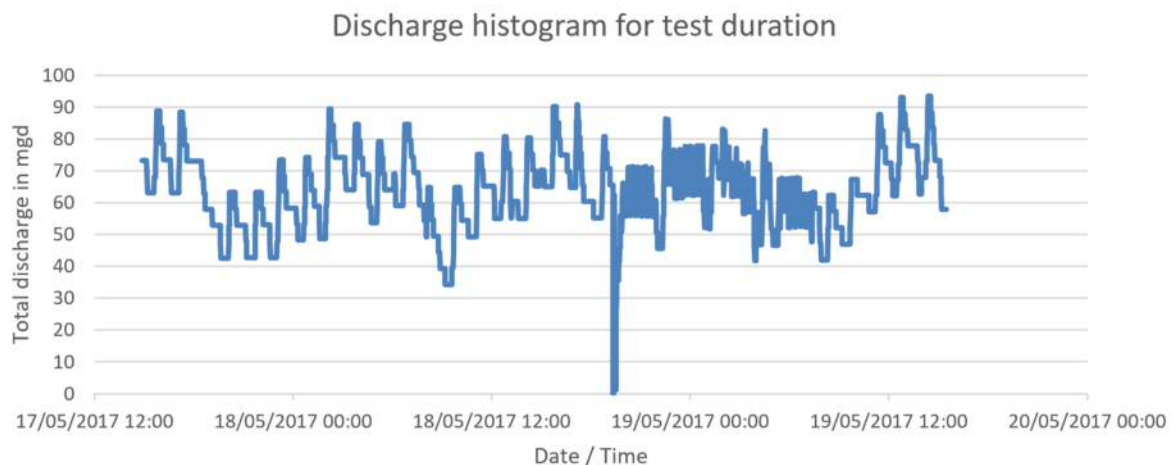
CHARGE CONTROL	LOAD CONTROL	DIVERSION CONTROL
		
<ul style="list-style-type: none"> <li>Constant voltage series PWM design to provide highly efficient battery charging</li> <li>4-stage charging to increase battery capacity and life: bulk charge, PWM regulation, float and equalize</li> <li>Parallel for larger solar arrays up to 300 amps or more</li> </ul>	<ul style="list-style-type: none"> <li>Starts large loads including motors and pumps with no damage to controller</li> <li>Allows inrush current to 300 amps</li> <li>Electronic short-circuit and overload protection with automatic reconnect</li> <li>LVD is current compensated and has a delay to avoid false disconnects</li> </ul>	<ul style="list-style-type: none"> <li>May be used for solar, wind or hydroelectric</li> <li>To protect against battery overcharge, excess energy is diverted from the battery to an alternate DC resistive load</li> <li>PWM reduces power into diversion load during overcurrent conditions</li> </ul>
TECHNICAL SPECIFICATIONS		
<p><b>Electrical</b></p> <ul style="list-style-type: none"> <li>Rated solar, load or diversion current                             <ul style="list-style-type: none"> <li>TriStar-45 45A</li> <li>TriStar-60 60A</li> </ul> </li> <li>System Voltage 12-48V</li> <li>Accuracy 12/24V <math>\leq 0.1\% \pm 50mV</math> 48V <math>\leq 0.1\% \pm 100mV</math></li> <li>Minimum voltage to operate 9V</li> <li>Maximum solar voltage (Voc) 125V</li> <li>Self-consumption                             <ul style="list-style-type: none"> <li>Controller &lt;20mA</li> <li>Meter 7.5mA</li> </ul> </li> </ul> <p><b>Mechanical</b></p> <ul style="list-style-type: none"> <li>Dimensions                             <ul style="list-style-type: none"> <li>Height: 26.0cm/10.3 in</li> <li>Width: 12.7cm/5.0 in</li> <li>Depth: 7.1cm/2.8 in</li> </ul> </li> <li>Weight 1.6 kg/3.5 lb</li> <li>Largest Wire 35mm<sup>2</sup>/2 AWG</li> <li>Conduit knockouts Eccentric 2.5/3.2 cm (1.0/1.25 in)</li> <li>Enclosure Type 1, indoor rated</li> </ul>	<p><b>Environmental</b></p> <ul style="list-style-type: none"> <li>Operating ambient temperature                             <ul style="list-style-type: none"> <li>Controller -40°C to +60°C</li> <li>Meter -40°C to +60°C</li> </ul> </li> <li>Storage temperature -55°C to +85°C</li> <li>Humidity 100% (non-condensing)</li> <li>Tropicalization Conformal coating on both sides of all printed circuit boards</li> </ul> <p><b>Electronic Protections</b></p> <ul style="list-style-type: none"> <li>Reverse polarity protection (any combination)</li> <li>Short-circuit protection</li> <li>Overcurrent protection</li> <li>Lightning and transient surge protection using 4500W transient voltage suppressors</li> <li>High temperature protection via automatic current reduction or complete shut down</li> <li>Prevents reverse current from battery at night</li> </ul>	<p><b>Options</b></p> <ul style="list-style-type: none"> <li><b>TriStar Meter</b> — 2 x 16 display mounts to controller and provides system and controller information, data logging, bar graphs and choice of 5 languages</li> <li><b>TriStar Remote Meter</b> — Includes 30 meters of cable for mounting meter away from the controller</li> <li><b>Remote Temperature Sensor</b> — Provides temperature compensated charging by measuring temperature at the battery (10 meter cable)</li> </ul> <p><b>Certifications</b></p> <ul style="list-style-type: none"> <li>CE Compliant</li> <li>ETL Listed (UL 1741)</li> <li>cETL (CSA-C22.2 No.107.1-95)</li> <li>TUV (IEC 62109-1)</li> <li>Complies with U.S. National Electric Code</li> <li>Manufactured in a certified ISO 9001 facility</li> <li>MET Labs (EN 60335-1, EN 60335-2-29)</li> </ul>
		
WARRANTY: Five year warranty period. Contact Morningstar or your authorized distributor for complete terms.		
Revision: 4/2016 EN Control no. MS-001798 Copyright 2016 www.morningstarcorp.com		

Figure D3. Tristar 45A Diversion Controller specifications [179]



Discharge data field testing Atlanta



Flow data from plant operator (highlighted) including derived values for flow velocity

Test No 160 (measured flow velocity = <b>0.64m/s</b> , water level = 0.85m)					
Date / Time of testing 3 UV channels in operation	Total discharge	Total discharge	Individual discharge	Flow area	Flow velocity
	mgd	m <sup>3</sup> /s	m <sup>3</sup> /s	m <sup>2</sup>	m/s
17/05/2017 14:53	73.24	3.21	1.07	1.60	0.67
17/05/2017 15:08	73.24	3.21	1.07	1.60	0.67
17/05/2017 15:09	68.23	2.99	1.00	1.60	0.62
17/05/2017 15:11	68.23	2.99	1.00	1.60	0.62
17/05/2017 15:12	63.12	2.76	0.92	1.60	0.58
17/05/2017 15:22	63.12	2.76	0.92	1.60	0.58
<b>Average</b>					<b>0.63</b>

Test No 161 (measured flow velocity = <b>0.76m/s</b> , water level = 0.90m)					
Date / Time of testing 3 UV channels in operation	Total discharge	Total discharge	Individual discharge	Flow area	Flow velocity
	mgd	m <sup>3</sup> /s	m <sup>3</sup> /s	m <sup>2</sup>	m/s
17/05/2017 15:48	88.72	3.89	1.30	1.69	0.77
17/05/2017 15:56	88.72	3.89	1.30	1.69	0.77
17/05/2017 15:57	83.65	3.66	1.22	1.69	0.72
17/05/2017 16:03	83.65	3.66	1.22	1.69	0.72
17/05/2017 16:04	78.46	3.44	1.15	1.69	0.68
17/05/2017 16:06	78.46	3.44	1.15	1.69	0.68
<b>Average</b>					<b>0.74</b>

Flow data continue

Test No 162 (measured flow velocity = <b>0.90m/s</b> , water level = 0.95m)					
Date / Time of testing 2 UV channels in operation	Total discharge	Total discharge	Individual discharge	Flow area	Flow velocity
	mgd	m <sup>3</sup> /s	m <sup>3</sup> /s	m <sup>2</sup>	m/s
18/05/2017 12:45	80.72	3.54	1.77	1.79	0.99
18/05/2017 12:53	80.72	3.54	1.77	1.79	0.99
18/05/2017 12:54	75.61	3.31	1.66	1.79	0.93
18/05/2017 13:03	75.61	3.31	1.66	1.79	0.93
18/05/2017 13:04	70.60	3.09	1.55	1.79	0.87
18/05/2017 13:08	70.60	3.09	1.55	1.79	0.87
18/05/2017 13:09	60.29	2.64	1.32	1.79	0.74
<b>Average</b>					<b>0.93</b>

Test No 163 (measured flow velocity = <b>0.90m/s</b> , water level = 0.95m)					
Date / Time of testing 2 UV channels in operation	Total discharge	Total discharge	Individual discharge	Flow area	Flow velocity
	mgd	m <sup>3</sup> /s	m <sup>3</sup> /s	m <sup>2</sup>	m/s
19/05/2017 13:23	77.89	3.41	1.71	1.79	0.96
19/05/2017 13:44	77.89	3.41	1.71	1.79	0.96
19/05/2017 13:45	72.77	3.19	1.59	1.79	0.89
19/05/2017 13:47	72.77	3.19	1.59	1.79	0.89
19/05/2017 13:47	Interrupted, Low flow				
19/05/2017 14:09					
19/05/2017 14:10	67.77	2.97	1.48	1.79	0.83
19/05/2017 14:11	67.77	2.97	1.48	1.79	0.83
<b>Average</b>					<b>0.94</b>

Test No 164 (measured flow velocity = <b>0.76m/s</b> , water level = 0.90m)					
Date / Time of testing 2 UV channels in operation	Total discharge	Total discharge	Individual discharge	Flow area	Flow velocity
	mgd	m <sup>3</sup> /s	m <sup>3</sup> /s	m <sup>2</sup>	m/s
19/05/2017 15:20	57.89	2.54	1.27	1.69	0.75
19/05/2017 15:29	57.89	2.54	1.27	1.69	0.75
<b>Average</b>					<b>0.75</b>

## F. SBC Denver, CO

### Water levels up and downstream VAT application testing Denver

The measures were taken during test 165 with a ranging rod, immediately up and downstream of the turbine housing. No significant change in elevation difference was observed between test 165/1, free-wheeling and test 165/10, fully loaded rotor.

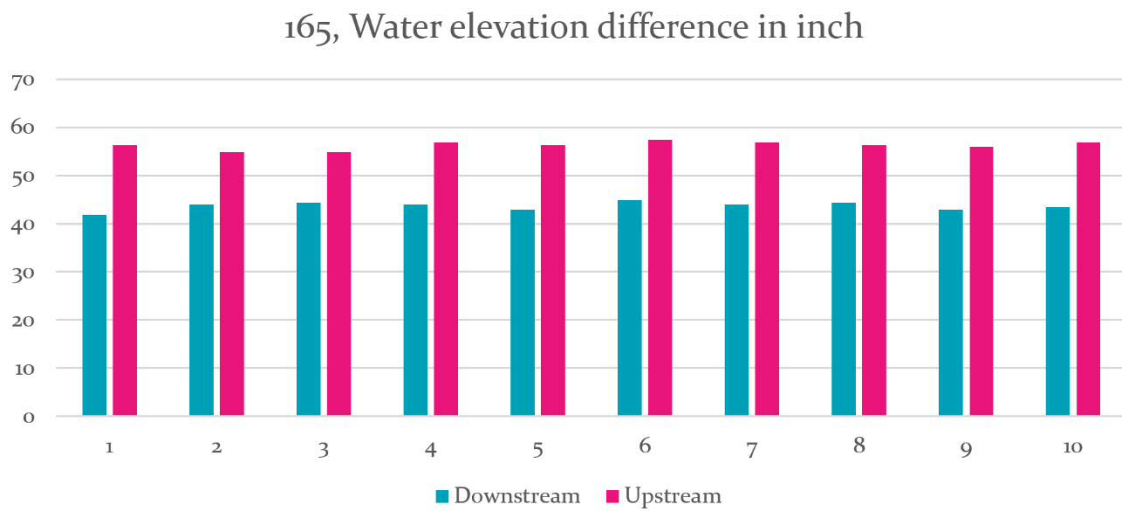


Figure F1. Water elevation measured up- and downstream the turbine during test 165



Figure F2. Velocity measurements taken by the US Bureau of Reclamation during testing [180]

## G. Component manufacturing

### Sintering/rapid prototyping

The sinter procedure as performed at the MEC laboratories at Cardiff University contained the following steps [181].

- *CAD-model transfer to 3D printer*
  - *A 3D CAD model (i.e., a Solidworks part) is converted into a printer-specific file.*
- *Object is 3D printed*
  - *SLS (selective laser sintering) uses a laser that sinters thin layers of polyamide powder together one layer at a time. After each round of lasering, the printing bed is lowered and another layer of powder is evenly swept across the top for another round of sintering. This process is repeated until the object is completed.*
- *Removal from batch*
  - *After the printer cools, the block of sintered powder is removed from the printer manually. The leftover powder is recycled for use in a future print.*
- *Brushing and sandblasting*
  - *The object is then brushed, which removes a large portion of the powder, and sandblasted, which removes the fine powder that the brush may have missed, see Figure G1.*

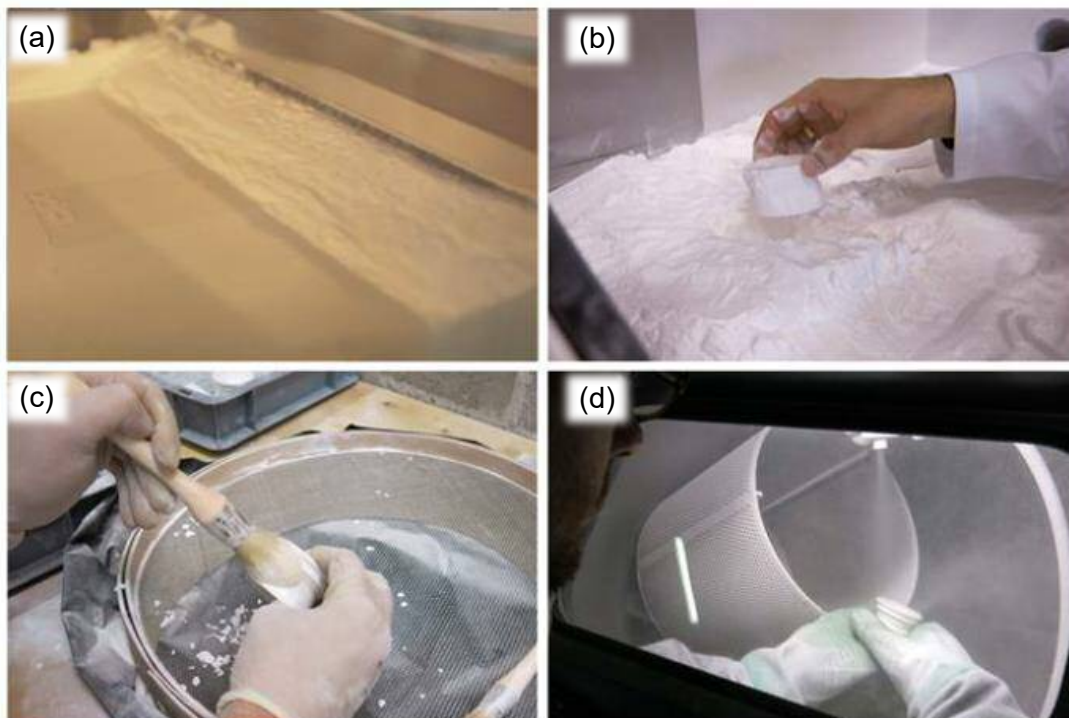


Figure G1. SLS procedure. a) Sinter process; b) object removal; c) brushing and; d) sandblasting.

## Composite blade manufacturing

In this summary, the procedure of three different composite blade manufacturing approaches (e.g., mould, core and mould & core) is assessed in terms of a cost/time/quality benchmark. The blades were manufactured at Cardiff University by myself with help from technicians and academics with experience in composite materials. It is hoped that the research can be continued and completed with a geometrical, structural and hydrodynamical assessment.

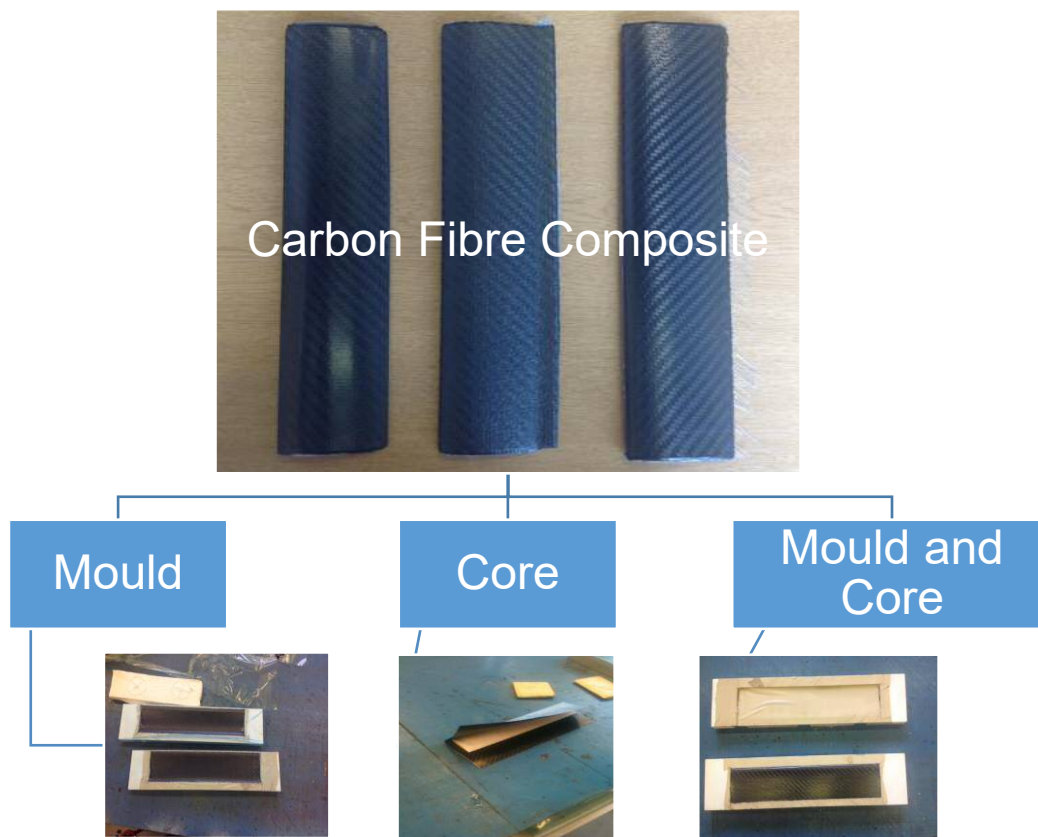


Figure G2. Three different composite blade manufacturing approaches

Three blades were produced using carbon fibre composite by applying three different techniques.

- Mould: Using sintered moulds, the upper and lower half of the blade was produced separately and glued together afterwards.
- Core: A sintered core was covered with carbon fibre plies.
- Mould and Core: A sintered core was covered with carbon fibre plies and placed in-between two moulds.

The mould and Core technique scored best in the cost/time/quality benchmark as listed in Table G1.

Table G1. Initial scoring for different approaches (Scoring: 1=poor, 2=ok, 3=good. Result out of nine, the higher the better).

Criterion	Mould	Core	Mould and Core
Costs (SLSr)	(2)	(3)	(1)
Time/Labour	(1)	(2)	(3)
Quality/Post-processing	(2)	(1)	(3)
Total	5	6	7

In the following, the different approaches are explained, the ten procedural steps described and assessed as well as concluded where applicable.

**Mould**

The upper and lower half of a blade was produced by laying four plies of carbon fibre prepreps (pre-impregnated composite materials) onto a mould and put into the autoclave (machine that applies heat and pressure). The two halves were then glued together using a two component adhesive (Permabond). Even though no core exists, small inserts were included in order to have sufficient material for attaching the blade to the spokes via screws and to increase the bonding surface. In this case, six inserts were evenly distributed throughout the length of the blade. Finally, the surface was ground off.

1. CAD drawing

Description: A blade (NACA4421, chord length 59mm) was drawn by using a CAD Software package (Solidworks) followed by both halves of the mould and six inserts (see Figure G3).

Costs: N.A.

Time: 5 hrs

Quality: N.A.

Conclusion: The objective was achieved and no major obstacle were met.

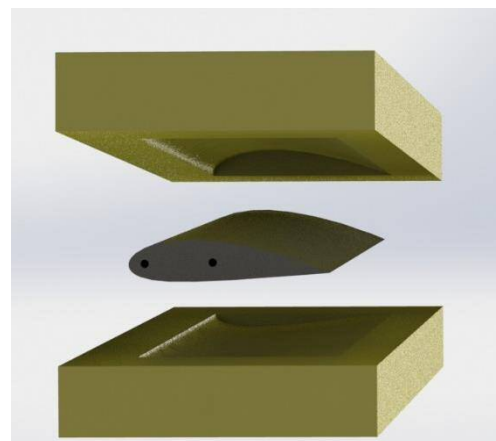


Figure G3. Screenshot of CAD drawing

## 2. Sintering (rapid prototyping)

Description: The drawings were forwarded to the Cardiff University Mechanical Workshop and the parts pictured in Figure G4 were sintered (SLS).

Costs: £144

Time: 2 days

Quality: Fair

Conclusion: Very fast process (about one day machining time, one day cooling and post-processing) when compared to using a CNC milling machine (about two weeks). Low costs since no material beside the sinter powder is necessary. Due to the process itself, the surface is not even and slender parts are slightly bended. Further, limitation in strength and sinter material is prone to absorption of water when compared to machined plastic or stainless steel.

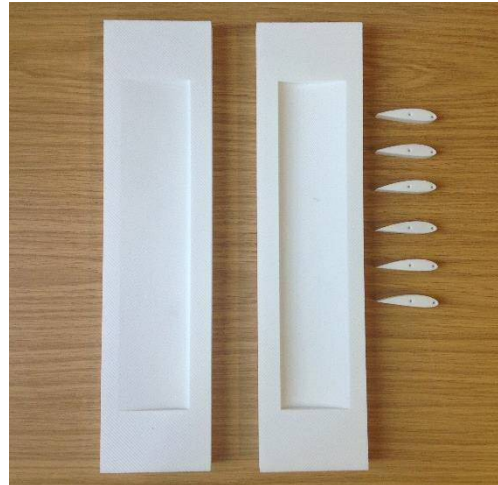


Figure G4. Moulds and inserts

## 3. Preparing the mould

Description: Sintering is a process which melts powder layer by layer to a solid body. On a curved surface, corrugations appear which would be copied to the surface of the carbon fibres (see Figure G5). Therefore, the inner surface of the mould must be sanded. Further, in order to avoid bonding between mould and composite, the mould needs to be coated with a non-adhesive film (see Figure G6).

Costs: N.A.

Time: 3 hrs

Quality: N.A.

Conclusion: The inner surface of the mould was equally copied to the surface of the composite.



Figure G5. Corrugation on sintered surface



Figure G6. Mould preparation

Therefore, extensive surface improvement (sanding with differentially coarse sandpapers) was undertaken in order to smoothen the corrugated surface of the sintered parts.

#### 4. Setting in carbon fibre stripes

Description: MTM 28 prepregs by Cytec were used which are made of an epoxy matrix resin. The prepregs were firmly set onto the mould in four plies and a ninety degree offset (see Figure G7 and G8).

Costs: N.A.

Time: 1.5 hrs

Quality: N.A.

Conclusion: Due to the tiny curvature of the imprint of the blade and the stickiness of the prepregs, it was difficult to place four layers on the mould. However, this obstacle was overcome and the objective achieved.

#### 5. Bagging the assembly

Description: In order to receive a perfect imprint of the mould and to avoid leaking epoxide, the assembly was placed in a sealed vacuum bag and covered by soft fabric. Here, the different components were compressed very firmly by extracting most of the vacuum bag's air via two valves (see Figure G9 and G10).

Costs: N.A.

Time: 1.5 hrs

Quality: N.A.

Conclusion: The vacuum bag was sealed with a soft rubber sealant. Several attempts were needed



Figure G7. Cutting stripes of carbon fibre

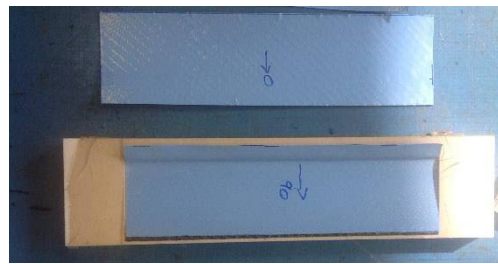


Figure G8. Setting in stripes on the mould



Figure G9. Preparation of the moulds



Figure G10. Vacuuming the bag

until a sufficient sealing (i.e., stable pressure) was achieved which was time consuming.

#### 6. Heat and pressure

Description: The autoclave includes a chamber which controls temperature and pressure with respect to time. A standard, pressure-free, heat cycle was applied (details see autoclave test cycle attached to this summary) and the vacuum of the bag was controlled. The processes was successfully finished after six hours (see Figures G11 and G12).

Costs: N.A.

Time: 6.5 hrs

Quality: N.A.

Conclusion: In order to operate the equipment and machinery, special knowledge/training is needed and was provided by Cardiff University staff.



Figure G11. Cardiff University autoclave

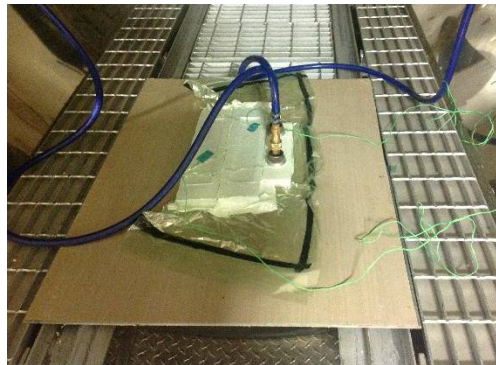


Figure G12. Vacuum bag in the autoclave

#### 7. Surface improvement

Description: As a result, two imprints of the two halves of the blade were generated. The overlapping material (red circles in Figure G13) was cut off and abraded.

The ends of the blade halves were squashed inwardly (red circle in Figure G14) and were cut-off and abraded as well.

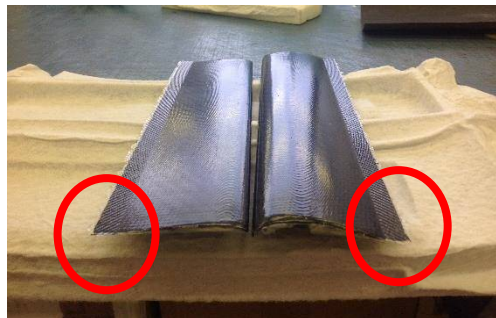


Figure G13. Released blade-halves after curing

Costs: N.A.

Time: 6 hrs

Quality: N.A.

Conclusion: This additional machining step became necessary since the prepreg could not be placed onto the mould perfectly and, therefore, deformation of the edges took place. In the future, the mould should be approximately 5% longer than the aimed blade length to allow for trimming of the deformed edge.

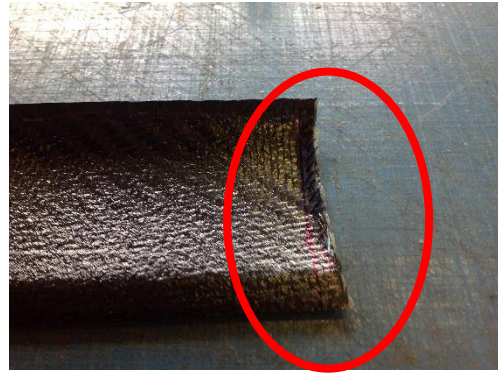


Figure G14. Deviated edges

## 8. Inserts

Description: The two halves of the blade have a wall thickness of approximately 1mm. Assembled together, they form a hollow blade. In order to connect the blade to the rotor arms, small inserts with outer dimensions of the inner surface of the hollow blade were sintered. At certain positions, two M3 threads were cut vertically into the insert (see Figure G15).



Figure G15. Blade insert with two M3 threads

Further, the low wall thickness of the halves led to concerns whether the area of contact is big enough to glue them together (without inserts). It was therefore decided to distribute six inserts equally over the length of the blade in order to increase the contact surface (see Figure G16).



Figure G16. Distribution of the inserts across the blade

Costs: N.A.

Time: 2 hrs

Quality: N.A.

Conclusion: The objective was achieved and no major obstacle were met.

9. Gluing together

Description: The composite parts were ground off (see Figure G17) in order to have straight and smooth edges and the best possible conditions for applying the two component adhesive (Permabond, see Appendix H).

Then, the Permabond was mixed and applied on the edges and the insert spaces (see Figure G18). The parts were then assembled and weighted. Curing time was 72h at room temperature.

Costs: N.A.

Time: 3 hrs + 72 hrs curing

Quality: N.A.

Conclusion: This was a labour intensive stage with potential error sources such as too much sanding, misalignment and poor bonding due to dirty/greasy surface.



Figure G17. Sanding the edges



Figure G18. Assembling blade and inserts

10. Final surface improvement

Description: Some of the Permabond adhesive was squashed out and little misalignments were ground off (see Figure G19 and G20).

Costs: N.A.

Time: 1 hrs

Quality: N.A.

Conclusion: The objective was achieved and no major obstacle were met.



Figure G19. Assembled blade after gluing together



Figure G20. Blade after surface finishing

**Summary Mould:**

- Fair costs
- Very labour intensive
- Many manufacturing steps
- Potential for misalignments/errors
- Good surface
- Poor edges
- Minimum material input (total weight 90g)
- Gluing (Permabond) necessary

**Core**

Four plies of MTM 28 preregs were wrapped around a sintered core and put into the autoclave. The surface was then coated and smoothed.

**1. CAD drawing**

Description: The initially drawn blade (NACA4421, chord length 59mm) was adapted (see Figure G21).

Costs: N.A.

Time: 1 hrs

Quality: N.A.

Conclusion: The objective was achieved and no major obstacle were met.

**2. Sintering (rapid prototyping)**

Description: The drawing was forwarded to the Cardiff University workshop and the core was sintered (see Figure 20 and 21)

Costs: £30

Time: 2 days

Quality: fair

Conclusion: Very fast process (about one day machining time, one day cooling and post-processing) when compared to using a CNC milling machine (about two weeks). Low costs since no material beside the sinter powder is necessary. Due to the process itself, the surface

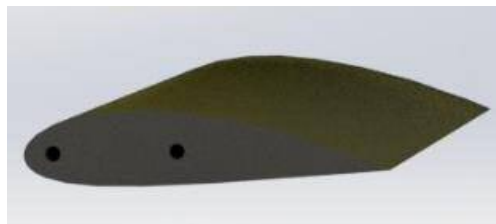


Figure G21. 3D sketch of the core

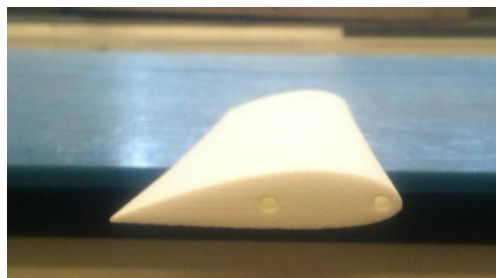


Figure G22. Core with two M3 threads

is not even and slender parts are slightly bended. Further, limitation in strength and sinter material is prone to absorption of water when compared to machined plastic or stainless steel.



Figure G23. Axial bending of the core

### 3. Preparing the core

Description: No further preparation was necessary. The core was used without further alterations.

Costs: N.A.

Time: N.A.

Quality: N.A.

Conclusion: N.A.

### 4. Setting in carbon fibre stripes

Description: The MTM 28 prepregs were firmly set onto the core in four plies at a ninety degree offset (see Figure G24).

Costs: N.A.

Time: 1 hrs

Quality: N.A.

Conclusion: The objective was achieved and no major obstacle were met.



Figure G24. Cutting stripes of carbon fibre

### 5. Bagging the assembly

Description: In order to avoid displacement of the wrapped core and to avoid leaking of the epoxide, the assembly was placed in a vacuum bag, covered by a soft fabric (see Figure G25). In contrast to the previous approach, the core-prepreg-assembly was placed on a ridged metal sheet in order to compensate for the axial bending of the sintered core and force it into

a straight position. This was achieved by the thermal treatment in the autoclave and the associated molecular relaxation of the sintered core under temperature.

Costs: N.A.

Time: 1.5 hrs

Quality: N.A.

Conclusion: The vacuum bag was sealed with a soft rubber sealant. Several attempts were needed until a sufficient sealing (i.e., stable pressure) was achieved which was time consuming.



Figure G25. Vacuum bag attached to a metal sheet

## 6. Heat and pressure

Description: The same procedure as described for the mould approach before was adopted with the exception of an application of pressure (6 bar).

Costs: N.A.

Time: 6.5 hrs

Quality: N.A.

Conclusion: In order to operate the equipment and machinery, special knowledge/training is needed and was provided by Cardiff University staff.

## 7. Surface improvement

Description: Since the surface of the composite is an imprint of the surface of the surrounding material, the blade surface is very rough (see Figure G26) as a result of the breather fabric it was wrapped-in. The overlapping edge was trimmed and abraded.

Costs: N.A.

Time: 6 hrs

Quality: N.A.

Conclusion: Without further processing, surface conditions were unacceptable.



Figure G26. Left hand side (smooth), mould was used, right hand side (rough), no mould was used

## 8. Inserts

Description: No inserts were needed since a solid core was used.

## 9. Gluing together

Description: The blade is one part and no gluing was needed.

## 10. Final surface improvement

Description: At the position where the sintered core ended (see Figure G27 red circle), it was decided to grout the buckled surface with Permabond (see Figure G28). Due to the rough surface, a layer of epoxide was applied and the whole blade was sanded (see Figure G29). The bottom surface of the blade lost its shape since it was lying on a flat surface during production in the autoclave. This could not be corrected.

Costs: N.A.

Time: 6 hrs & 24 hrs curing twice

Quality: N.A.

Conclusion: This was a labour and skill intensive step which included many different steps.



Figure G27. Buckled section of blade surface



Figure G28. Grouted edge of the blade



Figure G29. Final surface finishing

**Summary Core:**

- Low costs
- Except final surface improvement not very labour-intensive
- Less manufacturing steps
- Simple and straight forward
- Poor surface
- Poor edges/shape
- Fair material input (total weight of 150g)
- Buckling and roughness could probably be avoided with an improved vacuum technique.

**Mould and Core**

Here, a combination of both previously described approaches was used. The sintered core was wrapped by four plies of prepregs, placed into the two moulds, locked and put into the autoclave. With a minimum of surface improvement, the blade was smoothed.

**1. CAD drawing**

Description: As before, moulds and blade (NACA4421, chord length 59mm) were drawn using Solidworks (see Figure G30).

Costs: N.A.

Time: 5 hrs

Quality: N.A.

Conclusion: The objective was achieved and no major obstacle were met.

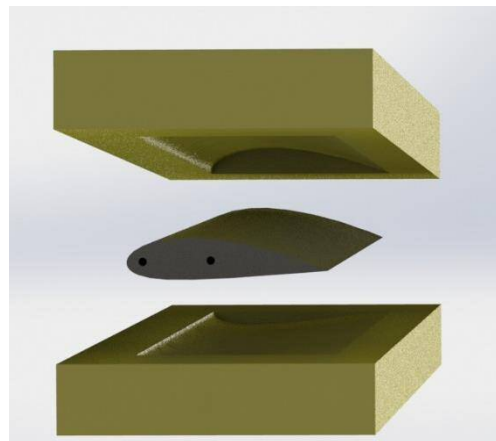


Figure G30. Screenshot of CAD drawing

**2. Sintering (rapid prototyping)**

Description: The drawings were forwarded to the Cardiff University workshop and the parts described before were sintered (see Figure 29).

Costs: £174

Time: 2 days

Quality: fair

Conclusion: Very fast process (about one day machining time, one day cooling and post-processing) when compared to using a CNC milling machine (about two weeks). Low costs since no material beside the sinter powder is necessary. Due to the process itself, the surface is not even and slender parts are slightly bended. Further, limitation in strength and sinter material is prone to absorption of water when compared to machined plastic or stainless steel.

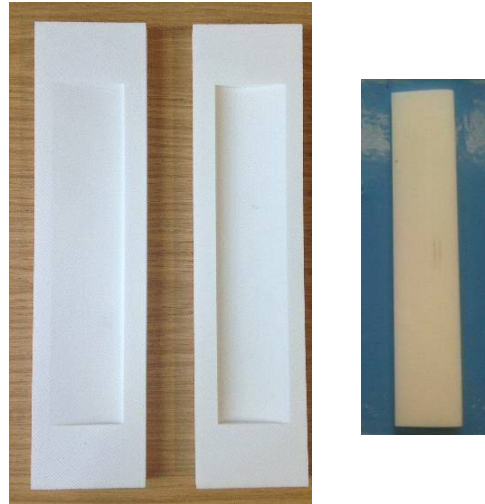


Figure G31. Moulds and core

### 3. Preparing the mould

Description: Sintering is a process which melts powder layer by layer to a solid body. On a curved surface, small corrugation appears which would be copied to the surface of the carbon fibres (see Figure G32). Therefore, the inner surface of the mould must be sanded. Further, in order to avoid bonding between mould and composite, the mould needs to be coated with a non-adhesive film (see Figure G33).



Figure G32. Corrugation on sintered surface

Costs: N.A.

Time: 3 hrs

Quality: N.A.



Figure G33. Mould preparation

Conclusion: The inner surface of the mould was equally copied to the surface finish of the composite. Therefore, extensive surface improvement (sanding with differentially coarse sandpapers) was undertaken in order to smoothen the corrugated surface of the sintered parts.

#### 4. Setting in carbon fibre stripes

Description: The MTM 28 prepregs were firmly set onto the core in four plies and a ninety degree offset. Then, the blade assembly was placed in the mould (see Figure G34) and the mould locked together with soft fabric and adhesive tape (see Figure G35).

Costs: N.A.

Time: 2 hrs

Quality: N.A.

Conclusion: The objective was achieved and no major obstacle were met.



Figure G34. Wrapped core placed in the mould



Figure G35. Setting-in stripes on the mould

#### 5. Bagging the assembly

Description: In order to apply the vacuum and press the components together, the assembly was placed in a vacuum bag, covered by another layer of soft breather fabric (see Figure G36).

Costs: N.A.

Time: 1.5 hrs

Quality: N.A.

Conclusion: As before, several attempts were needed until a sufficient sealing was achieved which took most of the time.



Figure G36. Vacuum bag

## 6. Heat and pressure

Description: The same procedure as described for the core approach was applied.

Costs: N.A.

Time: 6.5 hrs

Quality: N.A.

Conclusion: In order to operate the equipment and machinery, special knowledge/training is needed and was provided by Cardiff University staff.

## 7. Surface improvement

Description: No intermediate surface improvement necessary.

## 8. Inserts

Description: No inserts were needed since a solid core was used.

## 9. Gluing together

Description: The blade is one part and no gluing was needed.

## 10. Final surface improvement

Description: An almost perfect finish was achieved after releasing the composite from the mould. The resin strings were ground off easily (see Figure G37 and G38). The wave shaped texture is an imprint from the SLS core. The surface, however, was smooth as the inside of the mould.

No further work was necessary at the ends of the blade.

Costs: N.A.

Time: 1 hrs

Quality: N.A.

Conclusion: Just a minimum of surface improvement was necessary.



Figure G37. Released blade after curing



Figure G38. Very smooth surface with some hardened resin strings attached to it.

**Summary Mould and Core:**

- Costly since moulds and core are needed
- Least labour intensive
- Least manufacturing steps
- Simple and straight forward since least manual surface improvement
- Very good surface
- Very good edges
- Highest material input (total weight 150g & two moulds are necessary)

**Summary**

Three different composite manufacturing approaches were undertaken (see Figure G39 and G40). All prices reported refer to the purchased SLS material. Other materials such as prepregs, fabrics, sealants, etc., were provided by Cardiff University and are assumed to be similar for all three approaches. Time includes manufacturing, machining and curing.

**Mould:**

By using two moulds, two blade halves were manufactured and glued together. Here, labour requirements were quite high (about 150 hrs in total).

The costs were relatively high (£144) due to the fact that the mould was just used once. If more blades were to be manufactured, the costs for the mould would reduce. It was not quantified how often the mould could be used.

Several different working steps are involved and the likelihood of making alignment mistakes is high. The achieved quality (surface finish and shape) is fair.



Figure G39. Finished blades in comparison

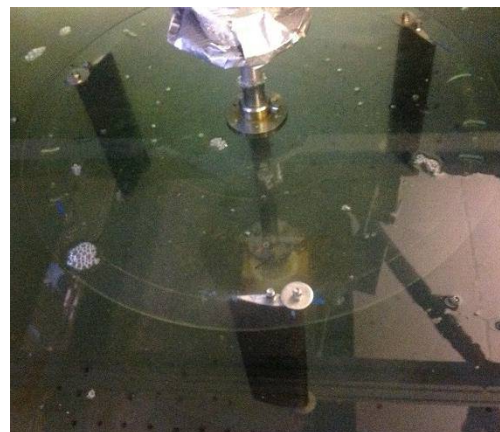


Figure G40. Blades mounted on the laboratory turbine.

Core:

Here, the prepregs were wrapped around a sintered core, bagged, vacuumed and put into the autoclave. Beside the extensive surface improvement which was needed to smooth the blade, labour requirements were low (about 118 hrs in total).

The costs were low (£30), just the core was needed. However, the quality achieved was poor due to the rough surface and the flat bottom half of the blade.

Mould and core:

Finally, a combination of both processes was undertaken. The prepregs were wrapped around a sintered core and placed between both moulds. With a total of 67 hours, this was by far the quickest and simplest approach.

In comparison, the costs were the highest (£174) but, as described before, the moulds (£144) could be reused. The resultant blade was of the highest quality and very little surface improvement was necessary.

In conclusion, the combined mould and core approach is most promising due to the high quality output and a minimum of labour needed. In future, a simplified form of this approach could be considered by only using the lower mould as support and pattern.

Please note: Workshop labour, material and the machines were kindly provided by Cardiff University and a friendly research group. The costs for the sintered parts were covered by my student account.

### Autoclave test cycle

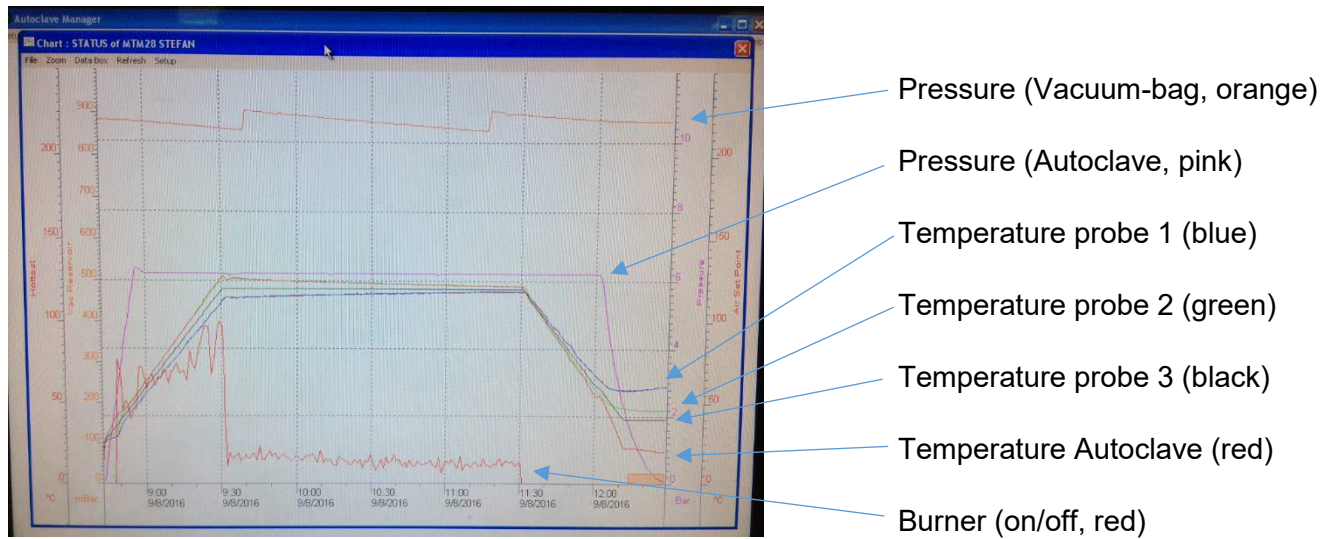


Figure G41. Screenshot of the autoclave cycle with time on the x-axis and temperature/pressure on the y-axis (A screenshot is used since the computer interface of the autoclave was not working and the data could not be extracted)

### Torsion test results for laboratory composite blades

Three composite blades (mould & core (1), core (2) and mould (3)) were tested in a torsion testing apparatus which twisted the blade up to 1.5 degrees and measured the torsional resistance. It was aimed at not deforming the blades plastically as they were used for turbine testing. The results are compared to data from a similarly shaped milling machined blade.

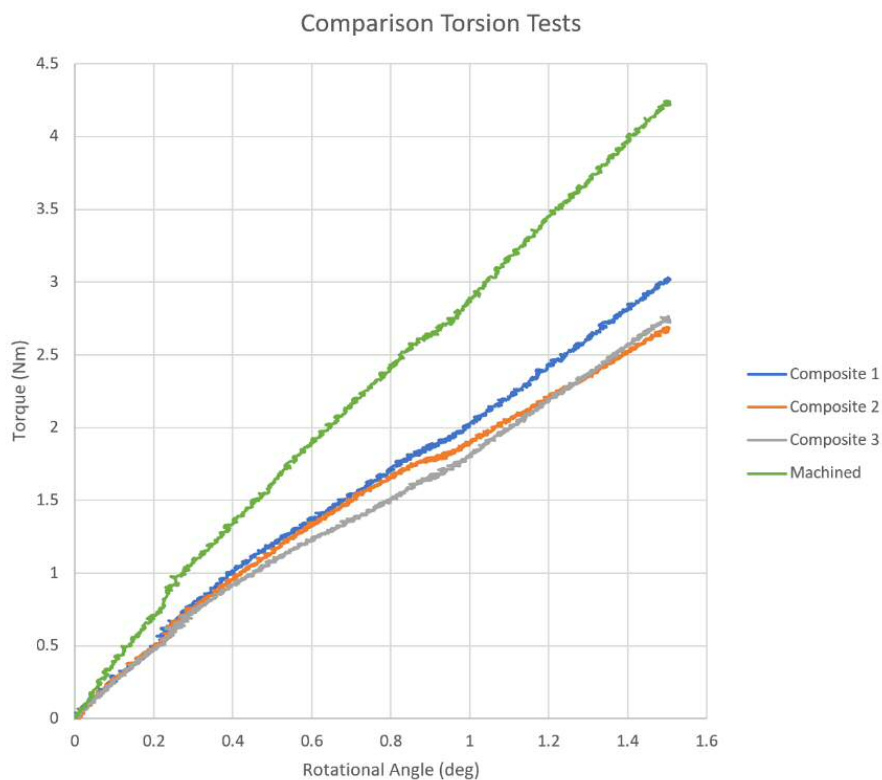


Figure G42. Comparison between three composite blades (1, 2, 3) and a milling machined plastic blade

### Blades for potential structural/hydrodynamical assessment

As recommended, the blades shown in Figure G43 could be used for performing structural tests on machined/manufactured members (torsion, bending) and for comparisons to FEM results.

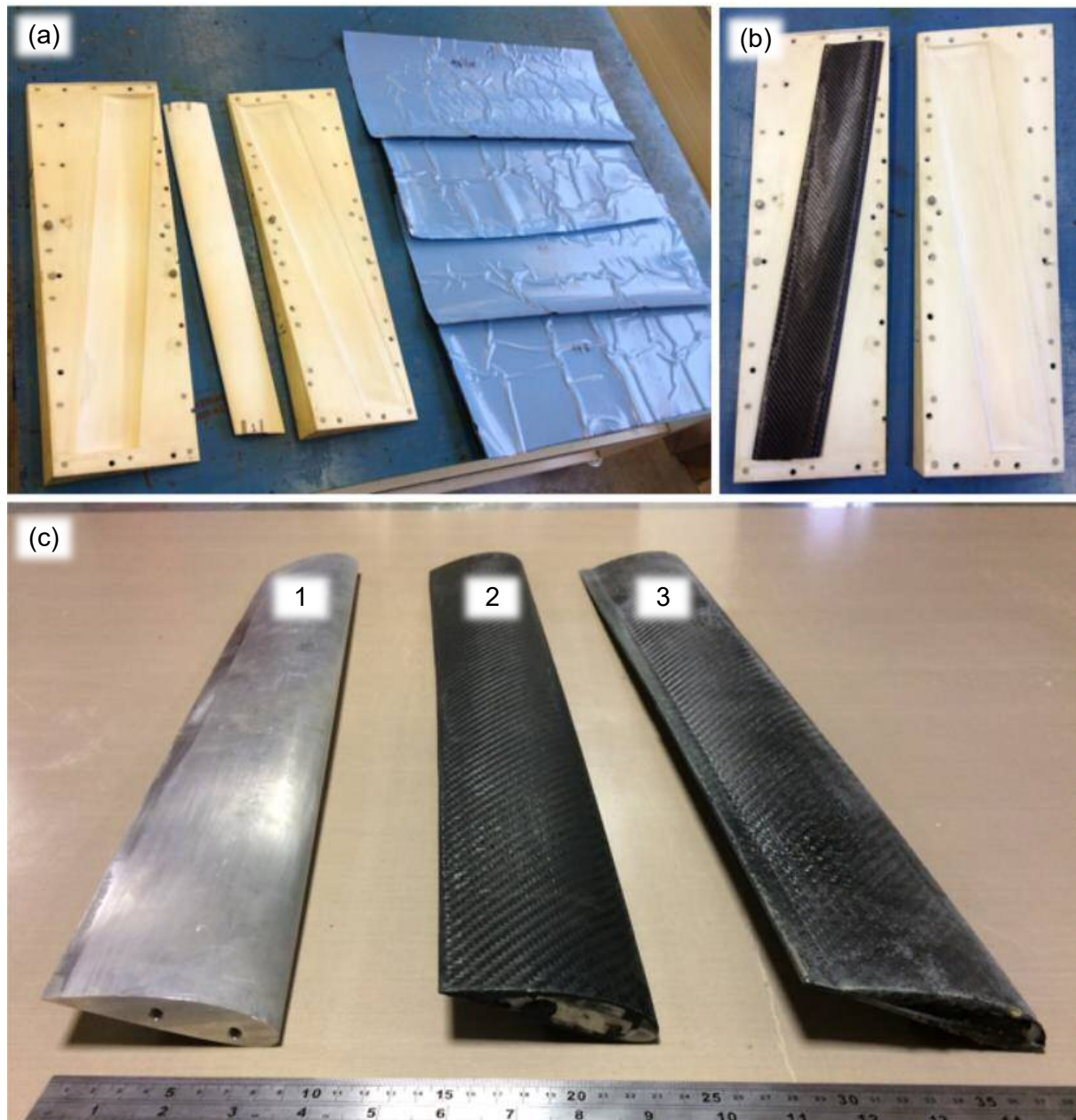


Figure G43. a) Sintered mould halves, blade core and composite prepregs; b) blade core with composite prepregs applied put into the mould; c) blades for potential structural/hydrodynamical assessment: 1) aluminium; 2) sanded composite; 3) untreated composite

## H. Data sheets

### Torque transducer



MODEL TRS605

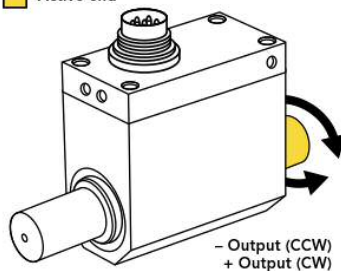
**Non-Contact Shaft-to-Shaft Rotary Torque Sensor  
with Encoder**



#### FEATURES

- Utilizes strain gauge technology
- Angle speed feedback
- Compact size
- Can operate up to 7000 RPM

  Active end



SPECIFICATIONS	
PERFORMANCE	
Nonlinearity	±0.2% of RO
Hysteresis	±0.1% of RO
Nonrepeatability	±0.2% of RO
Rotational Speed	7000 Max
ELECTRICAL	
Rated Output (RO)	±5 VDC
Excitation	11–26 VDC, 1 Watt
Connector	12 pin Binder Series #581 (09-0331-90-12)
MECHANICAL	
Safe Overload	150% of RO
Zero Balance	±1% of RO
Material	Aluminum (Housing), Steel Alloy (Shaft)
IP Rating	IP40
TEMPERATURE	
Operating Temperature	–13 to 176°F (–25 to 80°C)
Compensated Temperature	41 to 122°F (5 to 50°C)
Temperature Shift Zero	±0.01% of RO/°F (±0.02% of RO/°C)
Temperature Shift Span	±0.01% of RO/°F (±0.02% of RO/°C)
CALIBRATION	
Calibration Test Excitation	12 VDC
Calibration (standard)	Certificate of Conformance
Calibration (available)	5-pt CW & CCW
Shunt Calibration Value	With sensor fully connected apply 11–26 VDC to Pins A & K to generate 5 VDC nom output
ENCODER	
Output	Impulse (TTL)
Pulses per Revolution	2 × 360
Excitation	5 VDC, 40 mA max
Angle 1	Leading Pulse
Angle 2	Trailing Pulse (90°)
CONFORMITY	
RoHS	2014/30/EU
CE	<a href="#">Declaration of Conformity</a>

**Sensor Solution Source**  
Load · Torque · Pressure · Multi-Axis · Calibration · Instruments · Software  
[www.futek.com](http://www.futek.com)



ROHS



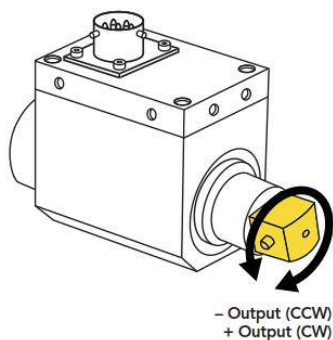
Figure H1. Torque transducer used for laboratory and field testing (capacity up to 20Nm) [182].



**FEATURES**

- Utilizes strain gauge technology
- Compact size
- Can operate up to 3000 RPM
- Slip ring assembly

 Active end



SPECIFICATIONS	
PERFORMANCE	
Nonlinearity	±0.2% of RO
Hysteresis	±0.1% of RO
Nonrepeatability	±0.2% of RO
Rotational Speed	3000 RPM Max
ELECTRICAL	
Rated Output (RO)	2 mV/V nom
Excitation (VDC or VAC)	11 max
Bridge Resistance	350 Ohm nom
Connection	10 Pin Bendix PT02A-12-10P
MECHANICAL	
Safe Overload	150% of RO
Material	Aluminum (Housing) Steel Alloy (Shaft)
IP Rating	IP40
TEMPERATURE	
Operating Temperature	14 to 194°F (-10 to 90°C)
Compensated Temperature	41 to 122°F (5 to 50°C)
Temperature Shift Zero	±0.01% of RO/°F (±0.02% of RO/°C)
Temperature Shift Span	±0.01% of Load/°F (±0.02% of Load/°C)
CALIBRATION	
Calibration Test Excitation	10 VDC
Calibration (standard)	Certificate of Conformance
Calibration (available)	5-pt CW & CCW
Shunt Calibration Value	43 kOhm
ENCODER	
Output	Impulse (TTL)
Pulses per Revolution	2 × 360
Excitation	5 VDC, 40 mA max
Angle 1	Leading Pulse
Angle 2	Trailing Pulse (90°)
CONFORMITY	
RoHS	2014/30/EU
CE	<a href="#">Declaration of Conformity</a>

Sensor Solution Source  
Load · Torque · Pressure · Multi-Axis · Calibration · Instruments · Software  
[www.futek.com](http://www.futek.com)



RoHS



Figure H2. Torque transducer used for application testing (capacity up to 1000Nm) [183].

Acoustic Doppler Velocimeter (ADV)

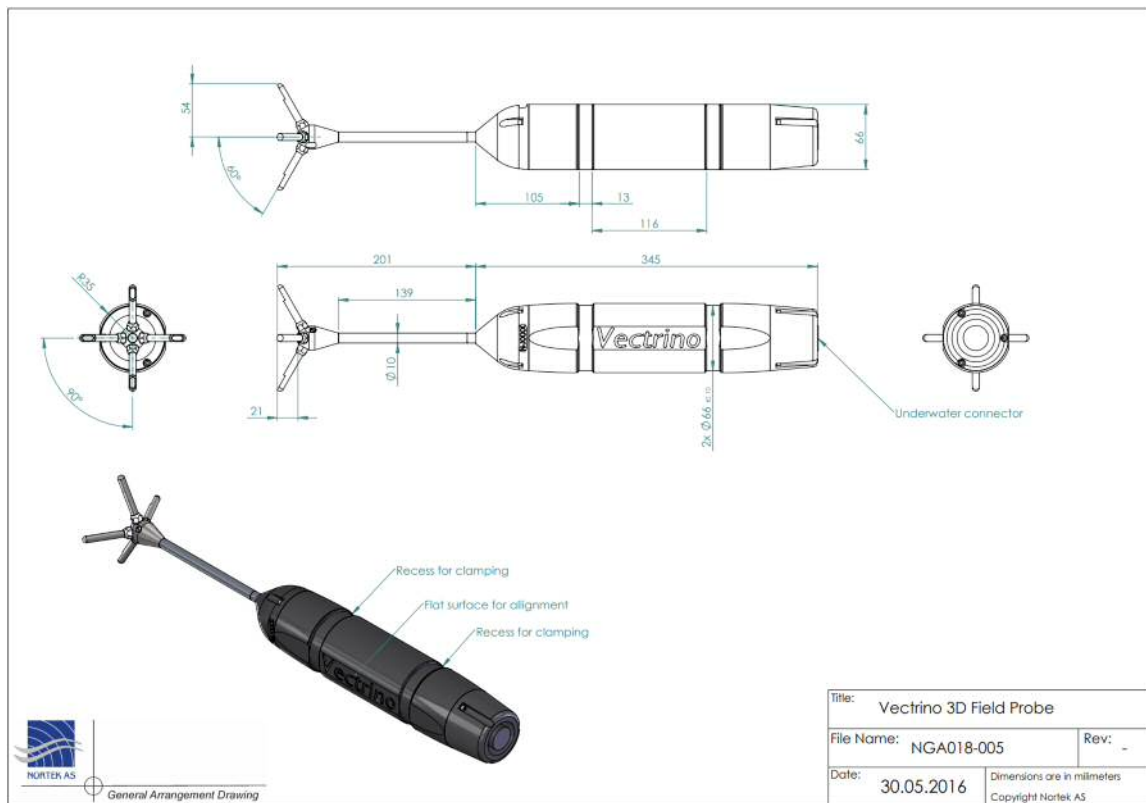


Figure H3. Technical drawing Vectrino 3D field probe [184]

Generators

DVE200

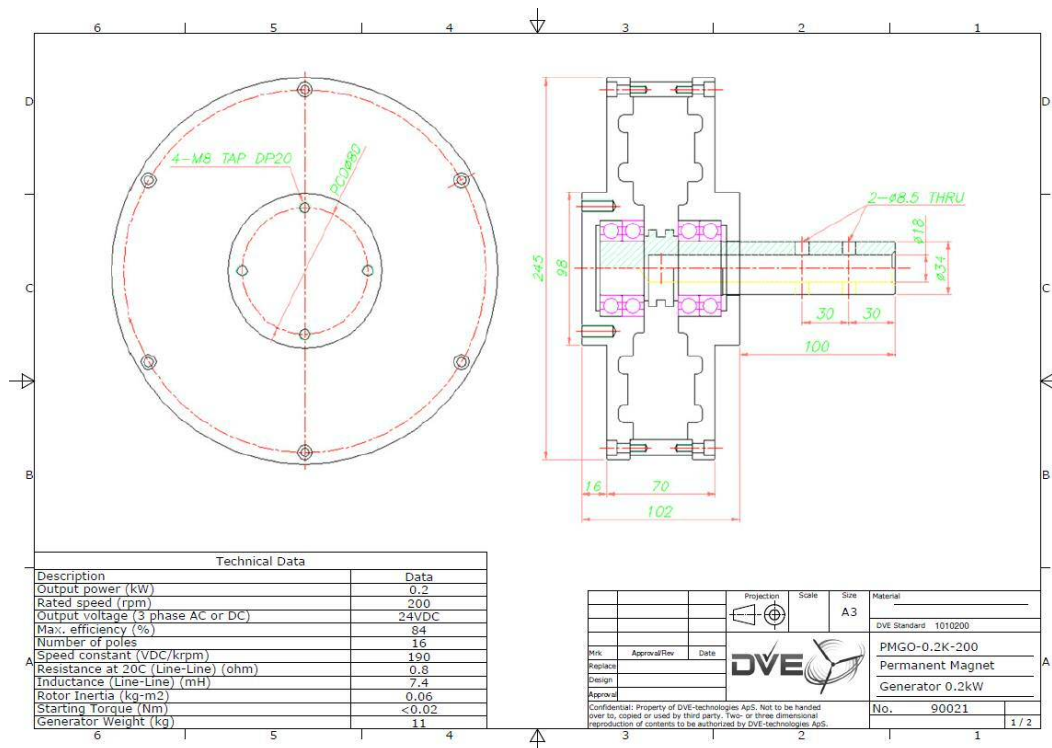


Figure H4. Technical drawing generator DVE200

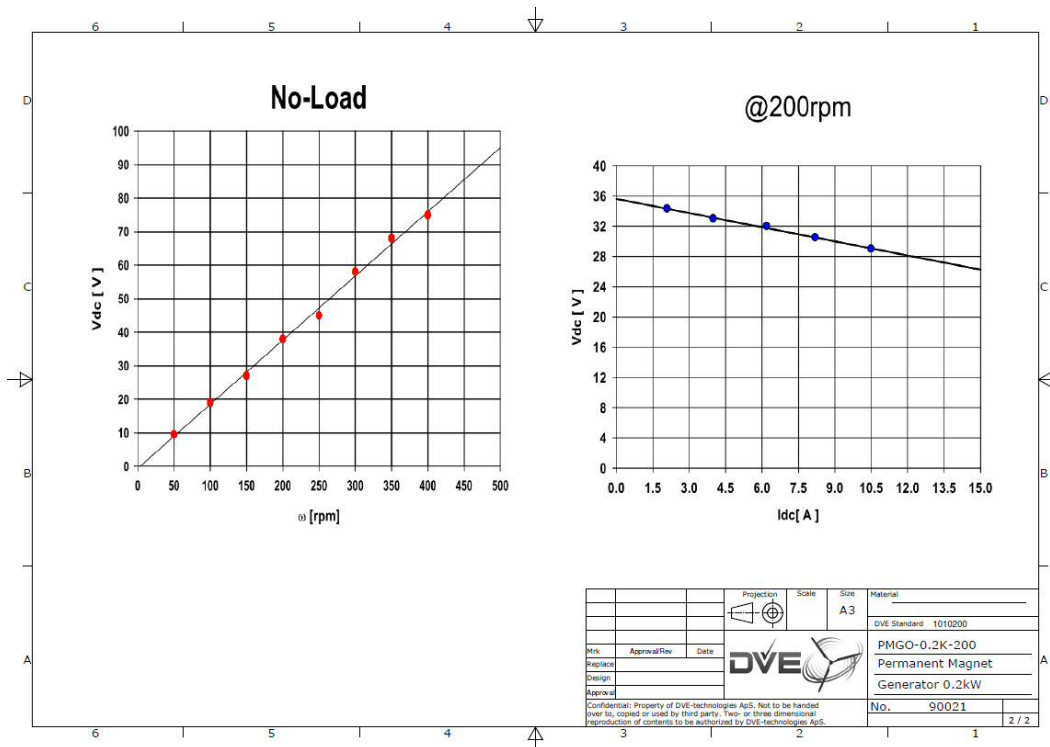


Figure H5. Generator DVE200 manufacturer performance graph

LE300/450

The two generators are identical except for more windings and thicker magnets in the LE450. The generators were designed for mini wind turbines (see Figure H8) and were manufactured in Herefordshire, UK by Leading Edge Turbines Ltd.. The following drawing depicts the backing plate to which the copper windings are attached to.

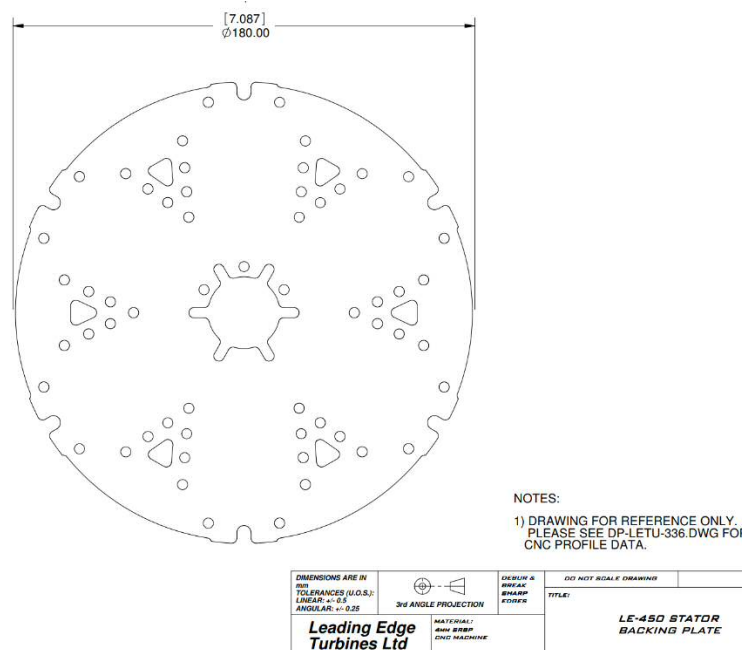


Figure H6. Technical drawing of generator LE300/450 backing plate

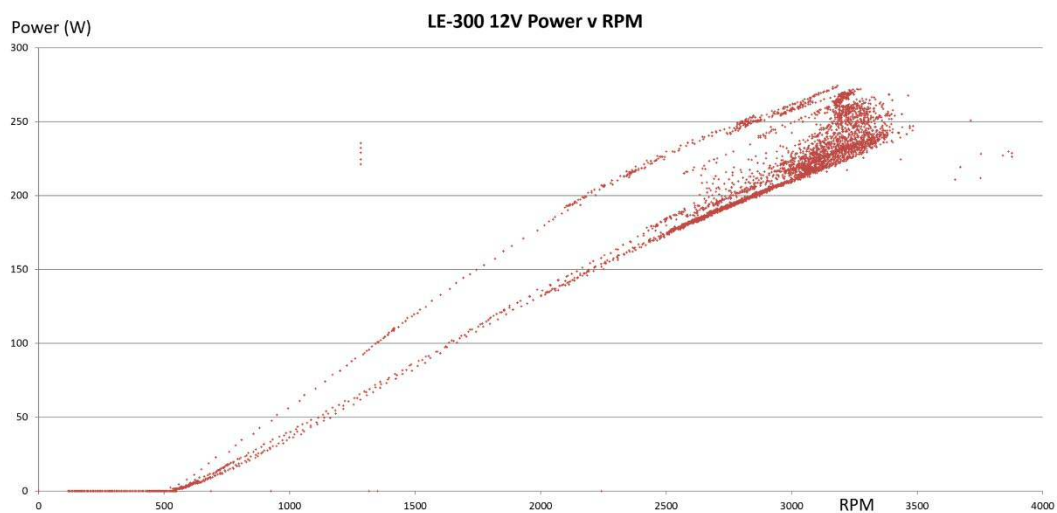


Figure H7. Generator LE300 manufacturer performance graph



Figure H8. LHS, Generator built in VAT-PTO, RHS, generator built into a wind turbine housing [185]

## Water flow probe



## Specifications

<b>Velocity Meter</b>	
<b>Range</b>	0.3-19.9 FPS (0.1-6.1 MPS)
<b>Accuracy</b>	0.1 FPS
<b>Averaging</b>	True digital running average. Updated once per second.
<b>Display</b>	LCD, Glare, and UV Protected
<b>Control</b>	4 button
<b>Datalogger</b>	30 sets, MIN, MAX, and AVG
<b>Features</b>	Timer, Low battery warning
<b>Sensor Type</b>	Protected Turbo-Prop propeller with magnetic pickup.
<b>Weight</b>	Instrument: 2 lbs (0.9 kg) (FP111); 3 lbs (1.4 kg) (FP211); 2.8 lbs (1.3 kg) (FP311) Shipping: 13 lbs (5.9 kg) (FP111); 23 lbs (10.4 kg) (FP211); 19 lbs (8.6 kg) (FP311)
<b>Expendable Length</b>	3.7 to 6 ft (1.1 to 1.8 m) (FP111); 5.5 to 14 ft (1.7 to 4.3 m) (FP211); 2.5 to 5.5 ft (0.76 to 1.7 m) (FP311)
<b>Materials</b>	Probe: PVC and anodized aluminum with stainless steel water bearing Computer: ABS/Polycarbonate housing with polyester overlay
<b>Power</b>	Internal Lithium Battery, Approx 5 years life with typical use, Non-Replaceable
<b>Auto Shutoff</b>	After 5 minutes of inactivity
<b>Operating Temperature</b>	-4 °F to 158 °F (-20 °C to 70 °C)
<b>Storage Temperature</b>	-22 °F to 176 °F (-30 °C to 80 °C)
<b>Carrying Case</b>	The Flow Probe is shipped in a padded carrying case.
<b>Certificates</b>	CE

For ordering information and options, please visit [www.globalw.com](http://www.globalw.com)

Figure H9. Global Water FP111 [186]

## SLS polyamide




---

 Material data sheet
 

---

**PA 2200****1 General**

Typical applications of the material are fully functional parts with high end finish right from the process, which easily withstand high mechanical and thermal load.

PA 2200 is suitable for processing on the following systems:

- EOSINT P 730, P 700
- EOSINT P 390, P 385, P 380i, P 380, with or without powder conveying system  
EOSINT P 360 with upgrade S&P, P 350/2 with upgrade 99 and upgrade S&P
- FORMIGA P 100

**2 Technical data****General material properties**

Average grain size	ISO 13320-11	56	µm
	Laser diffraction	2.20	mil
Bulk density	EN ISO 60	0.45	g/cm <sup>3</sup>
Density of laser-sintered part	EOS method	0.93	g/cm <sup>3</sup>
		58	lb/ft <sup>3</sup>

**Mechanical properties**

Tensile modulus	EN ISO 527	1700	MPa
	ASTM D638	247	ksi
Tensile strength	EN ISO 527	48	MPa
	ASTM D638	6962	psi

PA 2200  
AHO / 12.08

1 / 2

**EOS GmbH - Electro Optical Systems**

Robert-Stirling-Ring 1  
D-82152 Krailling / München

Telephone: +49 (0)89 / 893 36-0  
Telefax: +49 (0)89 / 893 36-285  
Internet: [www.eos.info](http://www.eos.info)



## Material data sheet

Elongation at break	EN ISO 527	24	%
Elongation at break	ASTM D638	24	%
Flexural modulus	EN ISO 178	1500	MPa
	ASTM D790	217	ksi
Flexural strength	EN ISO 178	58	MPa
	ASTM D790	8412	psi
Charpy - Impact strength	EN ISO 179	53	kJ/m <sup>2</sup>
Charpy - Notched impact strength	EN ISO 179	4.8	kJ/m <sup>2</sup>
Izod - Impact strength	EN ISO 180	32.8	kJ/m <sup>2</sup>
Izod - Notched impact strength	EN ISO 180	4.4	kJ/m <sup>2</sup>
Ball indentation hardness	EN ISO 2039	78	N/mm <sup>2</sup>
Shore D - hardness	ISO 868	75	-
	ASTM D2240	75	-

The mechanical properties depend on the x-, y-, z-position and on the exposure parameters used.

### Thermal properties

Melting point	EN ISO 11357-1	172 - 180	°C
Vicat softening temperature B/50	EN ISO 306	163	°C
	ASTM D1525	325	°F
Vicat softening temperature A/50	EN ISO 306	181	°C
	ASTM D1525	358	°F

The data are based on our latest knowledge and are subject to changes without notice. They do not guarantee properties for a particular part and in a particular application.

© 2008 EOS GmbH – Electro Optical Systems. All rights reserved.

## Composite epoxy matrix resin prepregs

Cyttec  
Industrial Materials

1 of 4

MTM<sup>®</sup> 28 series  
PDS1033\_05.13\_Issue14MTM<sup>®</sup> 28 series

MTM28 series prepregs are based on 120°C (248°F) curing toughened, epoxy matrix resins that have been specifically developed for the manufacture of components requiring high damage tolerance.

## Features

- Versatile processing: autoclave, oven vacuum bag and press moulding
- 30 days out life at 21°C (70°F)
- 12 months storage at -18°C (0°F)
- 85 to 160°C (185 to 320°F) cure
- Good tack and drape
- Excellent impact resistance
- Excellent adhesion to core materials
- 80°C (176°F) end use temperature

## Product variants

- MTM28: Good adhesive properties and bonds to honeycomb material without an additional adhesive film
- MTM28B: Black pigmented version of MTM28
- MTM28-1: Formatted for unidirectional fibre reinforcement
- MTM28-1B: Black pigmented version of MTM28-1
- MTM28-2: Lower tack level
- MTM28-2B: Black pigmented version of MTM28-2
- MTM28-3: Higher grab characteristics for tube rolling
- MTM28-3B: Black pigmented version of MTM28-3
- MTM28-4: Higher viscosity
- MTM28-4B: Black pigmented version of MTM28-4
- MTM28-5: Very low tack level
- MTM28-5B: Black pigmented version of MTM28-5

## Related documents

- De-bulking guidelines (TDS1036)
- Oven vacuum bag processing – lay-up and bagging guidelines (TDS1041)
- Autoclave processing lay-up and bagging guidelines (TDS1037)

## Related products

- MTA240 adhesive film (PDS1166)
- VTF266 surface improvement film (PDS1255)

## Cure cycle

## Oven vacuum bag cure

Vacuum bag pressure	Minimum of 980mbar (29" Hg)* <sup>†</sup>
Ramp rate	1 to 3°C (1.8 to 5.4°F)/minute
Recommended cure cycle	1 hour at 120°C, +5/-0°C (248°F, +9/-0°F)
Cool down	Maximum of 3°C (5.4°F)/minute to 60°C (140°F)

\*This is the ideal vacuum level, however, it is recognised that it is not always possible to attain. If in doubt, please contact our technical support staff for advice.

DELIVERING TECHNOLOGY BEYOND OUR CUSTOMERS' IMAGINATION  
Aerospace Materials | Industrial Materials | Process Materials

Autoclave cure

Vacuum bag pressure	Minimum of 980mbar (29" Hg)*†
Autoclave pressure	6.2 bar (90 psi)**
Ramp rate	1 to 3°C (1.8 to 5.4°F)/minute
Recommended cure cycle	1 hours at 120°C, +5/-0°C (248°F, +9/-0°F)
Cool down	Maximum of 3°C (5.4°F)/minute to 60°C (140°F)

\*This is the ideal vacuum level, however, it is recognised that it is not always possible to attain. If in doubt, please contact our technical support staff for advice.

†If manufacturing complex shapes, the vacuum can be vented when the pressure reaches 2 bar (30psi) if there is a perceived risk of a bag burst and hence the need to avoid pressurised air going down the vacuum line.

\*\*If producing sandwich panels, apply the maximum pressure allowable for the honeycomb type.

Press cure

Mould tools should restrain the flow sufficiently under moulding conditions to avoid fabric or fibre distortion.

Press pressure	Minimum of 2.8 bar (40 psi)
Ramp rate	A suitable rate (dependant on mould tooling)
Recommended cure cycle	1 hour at 120°C, +5/-0°C (248°F, +9/-0°F)
Cool down	A suitable rate (dependant on mould tooling) to 60°C (140°F)

Note:

- Demoulding at the cure temperature may be possible if the tooling is suitably designed. A specific trial is recommended.

Alternative cure cycles

Temperature	Duration
85°C (185°F)	13 hours
140°C (284°F)	25 minutes
150°C (302°F)	15 minutes
160°C (320°F)	7 minutes

Physical properties

Test	Sample conditions		Results
Cured resin density	1 hour at 120°C (248°F)	All variants	1.21 g/cm <sup>3</sup>
DMA E' onset Tg			100°C (212°F)

### Mechanical properties

Material: MTM28-1/T700-36% RW  
Cure cycle: 1 hour at 120°C (248°F), 6.2 bar (90 psi)  
Test conditions: Room tempertaure, dry

Test	Test method	Units	Results
0° Tensile strength	ASTM D3039	MPa (ksi)	2735 (397.0)
0° Tensile modulus		GPa (msi)	127.0 (18.4)
90° Tensile strength		MPa (ksi)	55.4 (8.04)
90° Tensile modulus		GPa (msi)	8.40 (1.22)
0° Compressive strength	ASTM D695 (MOD)	MPa (ksi)	1309 (190.0)
0° Compressive modulus		GPa (msi)	116.0 (16.8)
±45 In-plane shear strength (IPSS)	ASTM D3518	MPa (ksi)	127.0 (18.4)
±45 In-plane shear modulus (IPSM)		GPa (msi)	3.69 (0.54)
0° Flexural strength	CRAG 200	MPa (ksi)	1782 (258.0)
0° Flexural modulus		GPa (msi)	117.0 (17.0)
0° Interlaminar shear strength (ILSS)	ASTM D2344	MPa (ksi)	87.0 (12.6)

Data normalised to 60%Vf except for ILSS and IPSS & IPSM.

### Availability

MTM28 series prepregs are available in a wide range of reinforcing fabrics and unidirectional tapes, including glass, carbon, aramid and hybrids.

### Storage

Out life* at 21°C (70°F)	All variants	30 days
Storage at -18°C (0°F)	All variants	12 months from date of manufacture

\*Out life refers to accumulated time out of the freezer before the part is cured.

**Note:**

The actual freezer storage life and out life are dependent on a number of factors, including; fibre type, format and application. For certain formats, it may be possible for the storage life and out life to be longer than stated. Please contact our technical support staff for advice.

### Exotherm

MTM28 series prepregs are reactive formulations which can undergo severe exothermic heat up during the initial curing process if incorrect curing procedures are followed.

Great care must be taken to ensure that safe heating rates, dwell temperatures and lay-up/bagging procedures are adhered to, especially when moulding solid laminates in excess of 10mm (0.4in) thickness. The risk of exotherm increases with lay-up thickness and increasing cure temperature. It is strongly recommended that trials, representative of all the relevant circumstances, are carried out by the user to allow a safe cure cycle to be specified. It is also important to recognise that the model or tool material and its thermal mass, combined with the insulating effect of breather/bagging materials can affect the risk of exotherm in particular cases.

Please contact our technical department for further information on exotherm behaviour of these systems.

### Health & safety

MTM28 series resins contain epoxy resins which can cause allergic reaction on prolonged or repeated skin contact. Avoid contact with the skin. Gloves and protective clothing must be worn.

Wash skin thoroughly with soap and water or resin removing cream after handling. Do not use solvents for cleaning the skin.

Use mechanical exhaust ventilation when heat curing the resin system. Exhaust from vacuum pumps should be vented to external atmosphere and not into the work place.

For further information, consult Cyttec Safety Data Sheet numbers:

MTM28/MTM28B:	SDS 051
MTM28-1/MTM28-1B:	SDS 416
MTM28-2/MTM28-2B:	SDS 417
MTM28-3/MTM28-3B:	SDS 418
MTM28-4/MTM28-4B:	SDS 360
MTM28-5/MTM28-5B:	SDS 361

All statements, technical information and recommendations contained in this data sheet are given in good faith and are based on tests believed to be reliable, but their accuracy and completeness are not guaranteed. They do not constitute an offer to any person and shall not be deemed to form the basis of any subsequent contract. All products are sold subject to the Cyttec's Standard Terms and conditions of Sale. Accordingly, the user shall determine the suitability of the products for their intended use prior to purchase and shall assume all risk and liability in connection therewith. It is the responsibility of those wishing to sell items made from or embodying the products to inform the user of the properties of the products and the purposes for which they may be suitable, together with all precautionary measures required in handling those products. The information contained herein is under constant review and liable to be modified from time to time.  
© Copyright 2012 – Cyttec Industrial Materials (Derby) Ltd. All rights reserved worldwide. All trademarks or registered trademarks are the property of their respective owners.

**DELIVERING TECHNOLOGY BEYOND OUR CUSTOMERS' IMAGINATION**  
Aerospace Materials | Industrial Materials | Process Materials



Permabond



**PERMABOND® ET5429**

*Two-Part Epoxy*

Technical Datasheet

**Features & Benefits**

- 💧 Ideal for bonding composite materials
- 💧 Easy to apply
- 💧 High shear and peel strength
- 💧 Good impact strength
- 💧 High temperature resistance

**Description**

PERMABOND® ET5429 is a thixotropic two part adhesive with excellent resistance to impact and vibration. The controlled flow properties as well as its ease of mixing and application, enables the adhesive to be used where gap filling or vertical application is required. Permabond® ET5429 has been found to provide exceptional performance even at elevated temperatures. It is ideal for use in construction of composite assemblies.

**Typical Performance of Cured Adhesive**

Shear strength* (ISO4587)	Mild Steel: 18-22 N/mm <sup>2</sup> (2600-3200psi) FRP Glass/Polyester: 7-10 MPa (1000-1450psi) FRP Glass/Epoxy: 14-18 MPa (2000-2600psi) Carbon Fibre: 20-37 MPa (2900-5400psi)
Peel strength (aluminium) (ISO4578)	150-230 N/25mm (33-51 PIW)
Hardness (ISO868)	65-75 Shore D
Elongation at break (ISO37)	<5%
Glass transition temperature Tg	50-60°C (122-140°F)
Dielectric strength	15-25 kV/ mm

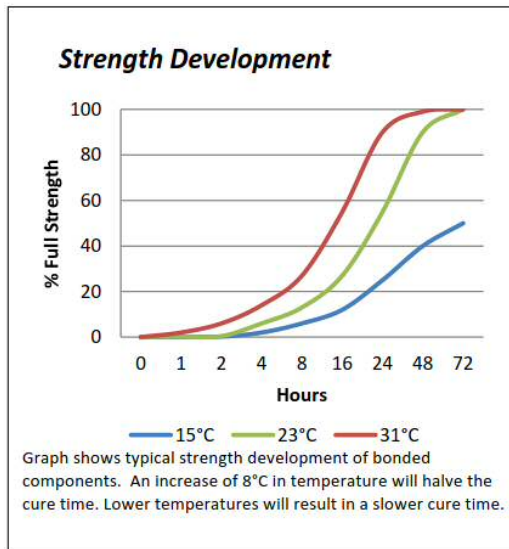
\*Strength results will vary depending on the level of surface preparation and gap.

**Physical Properties of Uncured Adhesive**

	ET5429A	ET5429B
Chemical composition	Epoxy Resin	Polyamine Hardener
Appearance	White	Black
Mixed appearance	Charcoal black	
Viscosity @ 25°C	20rpm: 150,000-250,000 mPa.s (cP) 2rpm: 200,000-400,000 mPa.s (cP)	20rpm: 40,000-80,000 mPa.s (cP) 2rpm: 100,000-200,000 mPa.s (cP)
Specific gravity	1.0	1.0

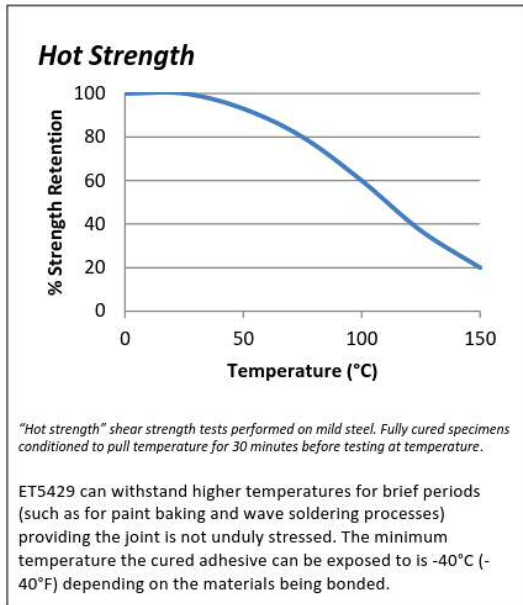
**Typical Curing Properties**

Mix ratio	2:1 by volume 2:1 by weight
Maximum gap fill	5 mm 0.2 in
Usable / pot life @23°C 10g mixed	2-4 hours
Handling time	23°C: 6-10 hours
Working strength	23°C: 24 hours 60°C: 1 hour
Full cure	23°C: 72 hours 60°C: 2 hours



The information given and the recommendations made herein are based on our research and are believed to be accurate but no guarantee of their accuracy is made. In every case we urge and recommend that purchasers before using any product in full-scale production make their own tests to determine to their own satisfaction whether the product is of acceptable quality and is suitable for their particular purpose under their own operating conditions. THE PRODUCTS DISCLOSED HEREIN ARE SOLD WITHOUT ANY WARRANTY AS TO MERCHANTABILITY OR FITNESS FOR A PARTICULAR PURPOSE OR ANY OTHER WARRANTY, EXPRESS OR IMPLIED.

No representative of ours has any authority to waive or change the foregoing provisions but, subject to such provisions, our engineers are available to assist purchasers in adapting our products to their needs and to the circumstances prevailing in their business. Nothing contained herein shall be construed to imply the non-existence of any relevant patents or to constitute a permission, inducement or recommendation to practice any invention covered by any patent, without authority from the owner of this patent. We also expect purchasers to use our products in accordance with the guiding principles of the Chemical Manufacturers Association's Responsible Care® program.



**Directions for Use**

1. Dual cartridges:
  - a) Insert the cartridge into the application gun and guide the plunger into the cartridge.
  - b) Remove the cartridge cap and dispense material until both sides are flowing.
  - c) Attach the static mixer to the end of the cartridge and begin dispensing the material.
2. Apply material to one of the substrates.
3. Join the parts. Parts must be joined within 2-4 hours of mixing the two epoxy components.
4. Large quantities and/or higher temperature will decrease the usable life or pot life.
5. Apply pressure to the assembly by clamping for 6-10 hours or until handling strength is obtained.
6. Full cure will be obtained after 72 hours at 25°C (77°F). Heat can be used to accelerate the curing process.

**Storage & Handling**

Storage Temperature	5 to 25°C (41 to 77°F)
---------------------	------------------------

**Additional Information**

This product is not recommended for use in contact with strong oxidizing materials.

Information regarding the safe handling of this material may be obtained from the safety data sheet.

Users are reminded that all materials, whether innocuous or not, should be handled in accordance with the principles of good industrial hygiene.

**Surface Preparation**

Surfaces should be clean, dry and grease-free before applying the adhesive. Use a suitable solvent (such as acetone or isopropanol) for the degreasing of surfaces. Some metals such as aluminium, copper and its alloys will benefit from light abrasion with emery cloth (or similar), to remove the oxide layer.

**Contact Permabond:**

- Americas +1 732 868 1372
- US 800-640-7599
- Asia + 86 21 5773 4913
- Europe +44 (0) 1962 711661
- UK 0800 975 9800
- Deutschland 0800 111 388
- France 0805 111 388

[info.americas@permabond.com](mailto:info.americas@permabond.com)  
[info.europe@permabond.com](mailto:info.europe@permabond.com)  
[info.asia@permabond.com](mailto:info.asia@permabond.com)

The information given and the recommendations made herein are based on our research and are believed to be accurate but no guarantee of their accuracy is made. In every case we urge and recommend that purchasers before using any product in full-scale production make their own tests to determine to their own satisfaction whether the product is of acceptable quality and is suitable for their particular purpose under their own operating conditions. THE PRODUCTS DISCLOSED HEREIN ARE SOLD WITHOUT ANY WARRANTY AS TO MERCHANTABILITY OR FITNESS FOR A PARTICULAR PURPOSE OR ANY OTHER WARRANTY, EXPRESS OR IMPLIED.

No representative of ours has any authority to waive or change the foregoing provisions but, subject to such provisions, our engineers are available to assist purchasers in adapting our products to their needs and to the circumstances prevailing in their business. Nothing contained herein shall be construed to imply the non-existence of any relevant patents or to constitute a permission, inducement or recommendation to practice any invention covered by any patent, without authority from the owner of this patent. We also expect purchasers to use our products in accordance with the guiding principles of the Chemical Manufacturers Association's Responsible Care® program.

## Aluminium

### 6061 Aluminium

#### Technical Datasheet



#### Commercial Aluminium Alloy

Service. Quality. Value.

#### Applications

- Shipbuilding
- Motorboats
- Aircraft structures
- Truck bodies
- Pylons & towers
- Rail coaches

#### Key features:

- Medium to high strength heat-treatable alloy
- Medium fatigue strength
- Very good corrosion resistance
- Typically used in heavy duty structures

#### Product Description

6061 aluminium is an American alloy and one of most versatile of the heat-treatable alloys. The alloy is typically used in heavy duty structures. It is a medium to high strength heat-treatable material with very good corrosion resistance and medium fatigue strength. 6061 in the annealed condition offers excellent weldability and formability and is readily disposed to furnace brazing.

#### Corrosion Resistance

Very good

#### Availability

Sheet, plate and extrusions

#### Chemical Composition (weight %)

	Mn	Fe	Mg	Si	Cu	Zn	Ti	Cr	Al			
min.			0.80	0.40	0.15			0.04	Bal			
max.	0.15	0.70	1.20	0.80	0.40	0.25	0.15	0.35	Bal			

#### Mechanical Properties

Tensile Strength	310 MPa
Proof Stress	270 MPa
Shear Strength	190 MPa
Elongation A50 mm	12%
Brinell Vickers	100 HV

#### Physical Properties

Density	2.70 g/cm <sup>3</sup>
Melting Point	650 °C
Thermal Expansion	23.4 x10 <sup>-6</sup> /K
Modulus of Elasticity	70 GPa
Thermal Conductivity	166 W/m.K

#### Technical Assistance

Our knowledgeable staff backed up by our resident team of qualified metallurgists and engineers, will be pleased to assist further on any technical topic.

[www.smithmetal.com](http://www.smithmetal.com)

[sales@smithmetal.com](mailto:sales@smithmetal.com)

Biggleswade 01767 604 604	Birmingham 01889 576 117	Bristol 0117 971 2800	Chelmsford 01245 466 664	Gateshead 0191 469 5428	Horsham 01403 261 981	Leeds 0113 307 5167
London 020 7241 2430	Manchester 0161 794 8650	Nottingham 0115 925 4801	Norwich 01603 789 878	Redruth 01209 217 628	Verwood 01202 824 347	General 0845 527 3331

All information in our data sheet is based on approximate testing and is stated to the best of our knowledge and belief. It is presented apart from contractual obligations and does not constitute any guarantee of properties or of processing or application possibilities in individual cases. Our warranties and liabilities are stated exclusively in our terms of trading. © Smiths Metal Centres 2015



## Nylon

**Product Details****Glass Filled Nylon 66**

Environmental: Glass filled Nylon 66 is unaffected by ultra-violet light. Strong acids (pH<3) will cause dimensional change due to absorption. Strong alkalis (pH>11) have no affect. Hot water and chlorinated hydrocarbons produce signs of mild attack by absorption.

High temperature static applications

30% glass filling reinforces stiffness

Excellent dimensional stability

Increased strength and performance in comparison to standard nylon 66

Black in colour

Max. Service Temp.	+110°C
Elongation	3.5 - 5%
Density	1.35 g/cm
Hardness (Rockwell-Shore D)	M90 (Rockwell)
Flammability Rating	UL 94 HB
Water Absorption	5.5% at saturation

**Specifications:**

Colour	Black
Length	500mm
Width	300mm
Thickness	16mm
Material	Glass Reinforced Plastic
Density	1.35g/cm <sup>3</sup>
Tensile Strength	140 (Wet) MPa, 160 (Dry) MPa
Hardness	M 90 Rockwell
Flammability Rating	UL 94 HB
Water Absorption	5.5%
Thermal Conductivity	0.27W/mK
Maximum Operating Temperature	+100°C

## I. Data variation

### Variation of torque

The continuous variation of angle of attack due to the rotational movement of the rotors' blades relative to the flow direction as well as local approach flow velocity differences or turbulences cause variations in torque (e.g., torque ripple or vibrations). For that reason, the average value of generated torque over a certain period of time is used to quantify the extracted energy and performance of the turbine. In Chapter 1.3.3, an analytical approach was presented to estimate the forces generated at a given position of the blade relative to the flow direction and the variation of the amount of torque relative to the rotational speed was highlighted. In Figure I1, the standard deviation of  $C_P$  in three exemplary tests with different turbine scales is presented as measure of variation. The standard deviation (SD) is calculated as shown in Equation I.1:

$$SD = \sqrt{\frac{\sum_{i=1}^N (x_i - \bar{x})^2}{N - 1}} \quad (I.1)$$

where  $x_i$  represents the measured value of the test point increment,  $\bar{x}$  the mean of all measured test increments and  $N$  the total number of increments (6000 in most cases). It can be seen that the SD for the laboratory test is much higher in magnitude as compared to the 3<sup>rd</sup> and full scale test which might be due to the much lower inertia of the smaller and lighter blades at smaller scale and higher response to flow turbulences, which is indicated by a decreased SD at bigger scale, especially with an increased TSR.

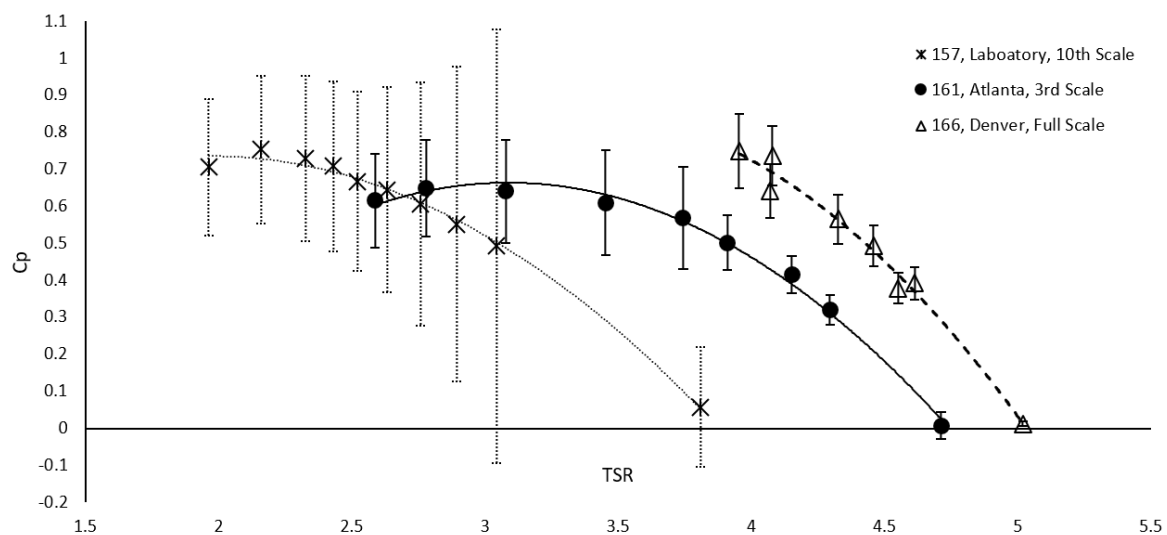


Figure I1. Performance curves of three exemplary tests for laboratory, field testing and application scale, operating in different environments and at different sizes. Whiskers indicate plus/minus one SD from the mean.

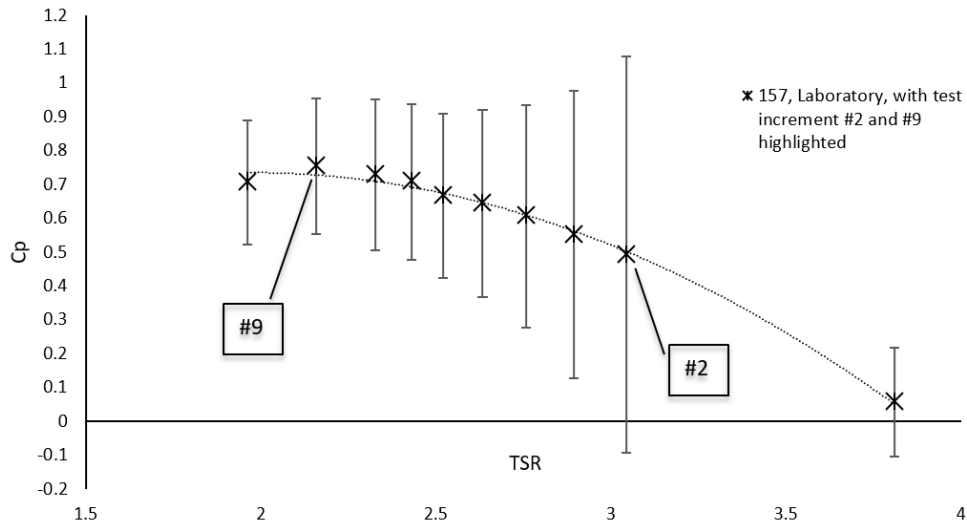


Figure 12. Performance curve of laboratory test 157 with test points #2 and #9 highlighted. Whiskers indicate plus/minus one SD from the mean.

The two measures captured during the tests are torque and rotational speed which, in conjunction with flow speed and rotor geometry, are used to quantify the coefficient of performance. Test point #2 ( $SD_{157\#2}=2.64$ ) and #9 ( $SD_{157\#9}=1.19$ ) of laboratory test 157 (see Figure 12) are further decomposed in order to show the variation of torque and rotational speed over a random period of time of the 60 second lasting test (see Figure I3-4).

In Figure 12, it can be seen that for test point #2 the SD is the largest. Figure I3 shows period of 0.6 seconds of the 60 second lasting test which were chosen using a random number generator. As predicted in Chapter 1.3.3, a significant variation of torque can be observed with values oscillating around the mean (dotted line) reaching even negative values occasionally. A variation of rotational speed is also observed but much less severe as the changes in torque.

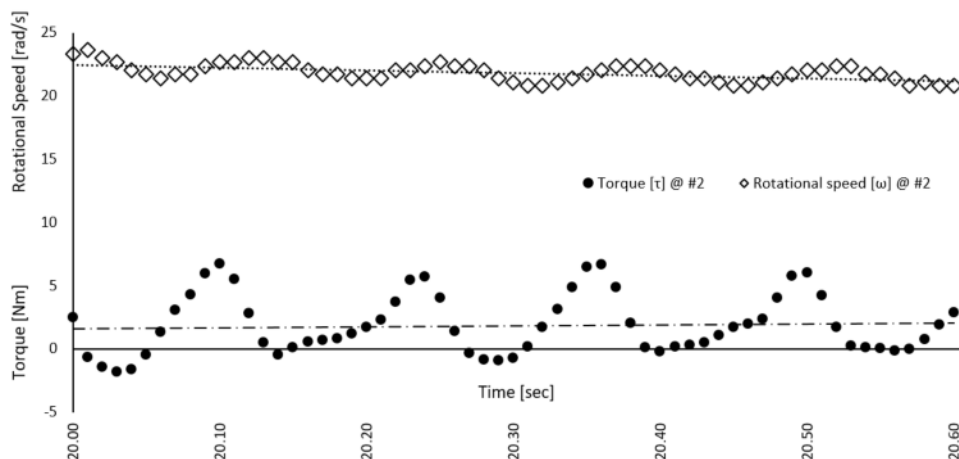


Figure 13. Variation of rotational speed and torque over a period of 0.6 seconds at test point #2

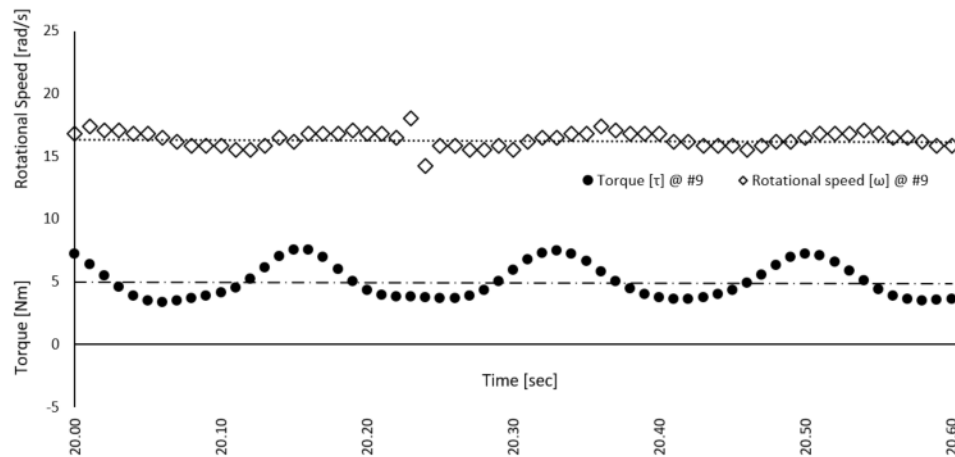


Figure 14. Variation of rotational speed and torque over a period of 0.6 seconds at test point #9

At test point #9 however, the torque variation is reduced as presented in Figure 14. One could expect that, due to the reduced rotational speed / TSR, the impact of torque variations is amplified as the results suggest shown in Figure 11 where the larger scale turbines show a reduced SD at higher TSR's.

It is not fully understood why this atypical behaviour happens at laboratory scale and it is suggested to further investigate torque ripple and variations across all scales. However, it may be that approach flow turbulences, as observed in Chapter IV, may have a much higher impact on laboratory scale. Rotor components are mainly made out of plastic and therefore are lighter than their bigger scale counterparts which are made out of composite materials or aluminium. In conjunction with small overall dimensions at laboratory scale, the rotor inertia is smaller compared to larger scales and the rotor could be more vulnerable to turbulent flow conditions (see also Chapter IX for further recommendations).

In the following, the variation of torque for two particular examples from Chapter III (blade twist, Chapter 3.3.2.4 and rotor offset, Chapter 3.3.4.5) are shown in more detail.

### Torque ripple and blade twist

In Chapter 3.3.2.4, it was stated that, counterintuitively, torque ripple was not reduced if the rotor's blades are twisted. The graphs depicted in Figure 15 and 16 show the variation in torque from the mean (dotted line) over several increments of test 045 (30° twisted blade) and 049 (non-twisted blade) at test points #2 and #9. As shown in Figure 17, test point #2 is close to free-wheeling, test point #9 is close to peak performance. Two different periods are shown (20–20.6 seconds and 41.0–41.6 seconds) which were chosen using a random number generator.

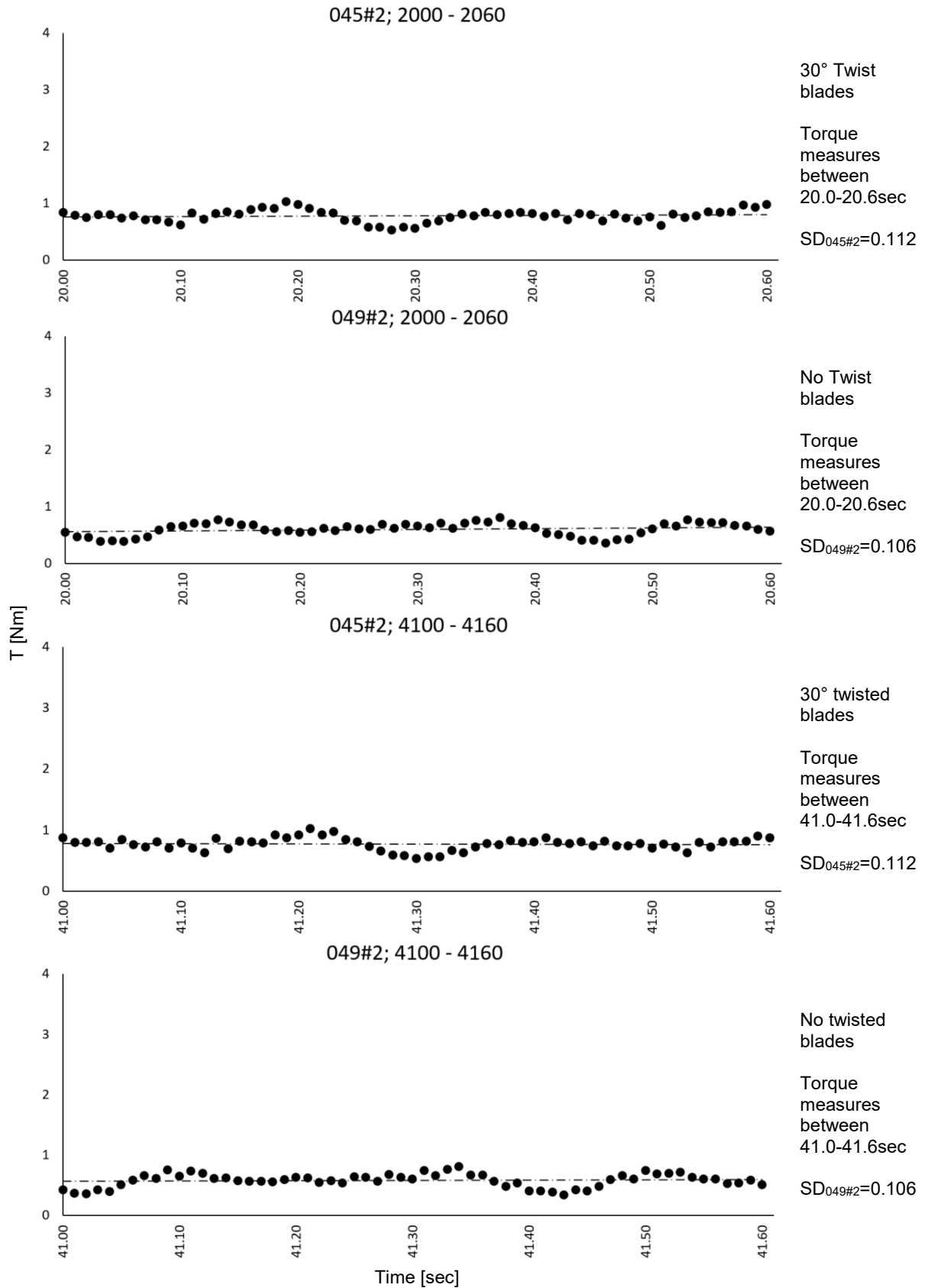


Figure 15. Variation of torque over a period of 0.6 seconds of twisted (045#2) and non-twisted (049#2) blades at two different periods of time during test point #2.

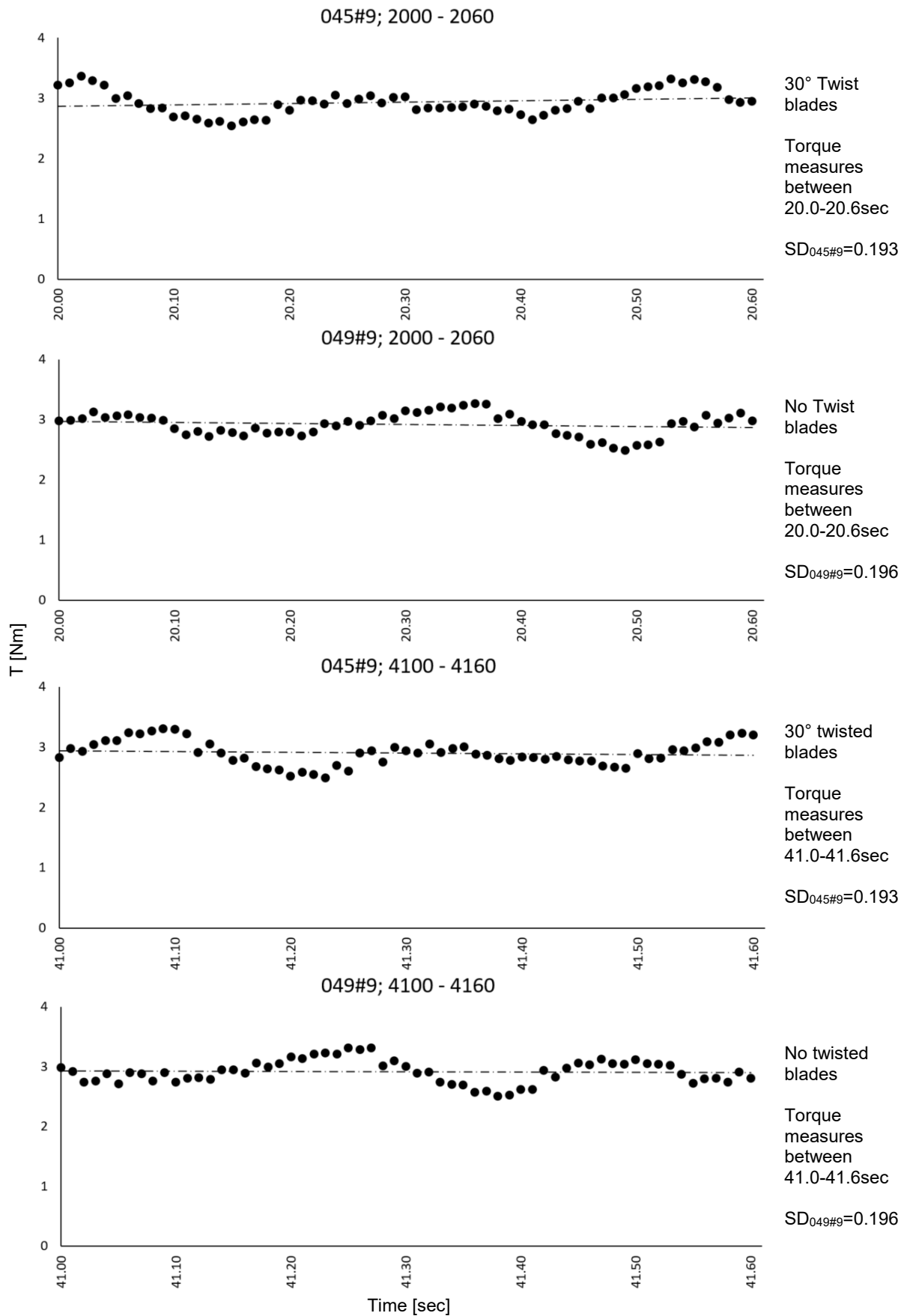


Figure 16. Variation of torque over a period of 0.6 seconds of twisted (045#9) and non-twisted (049#9) blades at two different periods of time during test point #9.

The SD at test point #2 for the twisted blades ( $SD_{045\#2}=0.112$ ) is slightly higher than for the non-twisted blades ( $SD_{049\#2}=0.106$ ), whereas the SD closer towards peak performance at test point #9 for the twisted blades ( $SD_{045\#9}=0.193$ ) is slightly lower than for the non-twisted blades ( $SD_{049\#9}=0.196$ ) which concludes not to be a meaningful result in either way and further investigation is needed (see also Chapter IX).

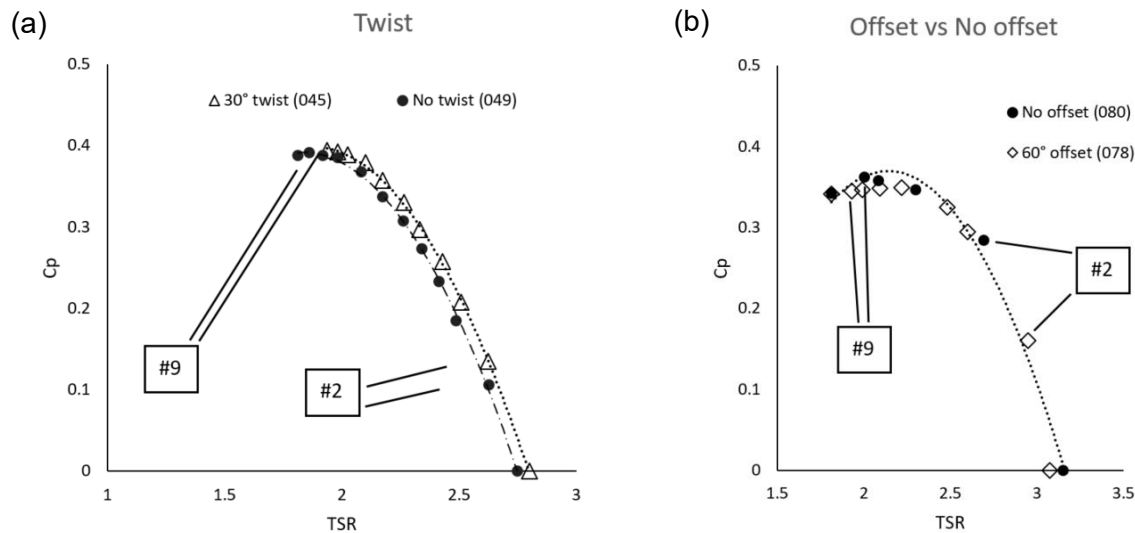


Figure 17. Performance curve of a) laboratory test 045 (30° twisted blade) and 049 (non-twisted blade) as well as b) laboratory test 078 (60° rotor offset) and 080 (no rotor offset) with test points #2 and #9 highlighted.

### Torque ripple and rotor offset

In Chapter 3.3.4.5, it was suggested that if the rotors are offset in a twin assembly, the torque ripple of both rotors will not occur at the same time and it was predicted that an offset of the rotors may reduce the torque ripple. However, with the rotors tested, the vibrations became much worse if offset by 60° which was visually observed during the experiment. The related data is presented in a similar manner as before.

The graphs depicted in Figure 18 and 19 show the variation in torque from the mean (dotted line) at several increments of time of test 078 (60° rotor offset) and 080 (no rotor offset) at test point #2 and #9. Two different time increments are shown (20 – 20.6 seconds and 41.0 – 41.6 seconds). The SD at test point #2, close to free-wheeling for the offset rotors ( $SD_{078\#2}=0.573$ ), is much higher than the SD for the non-offset rotors ( $SD_{080\#2}=0.222$ ). The SD closer towards peak performance at test point #9 for the offset rotors ( $SD_{078\#9}=0.283$ ) is still higher than for the non-offset rotors ( $SD_{080\#9}=0.195$ ). The increase in torque variation is not fully understood and further investigation is needed (see also Chapter IX).

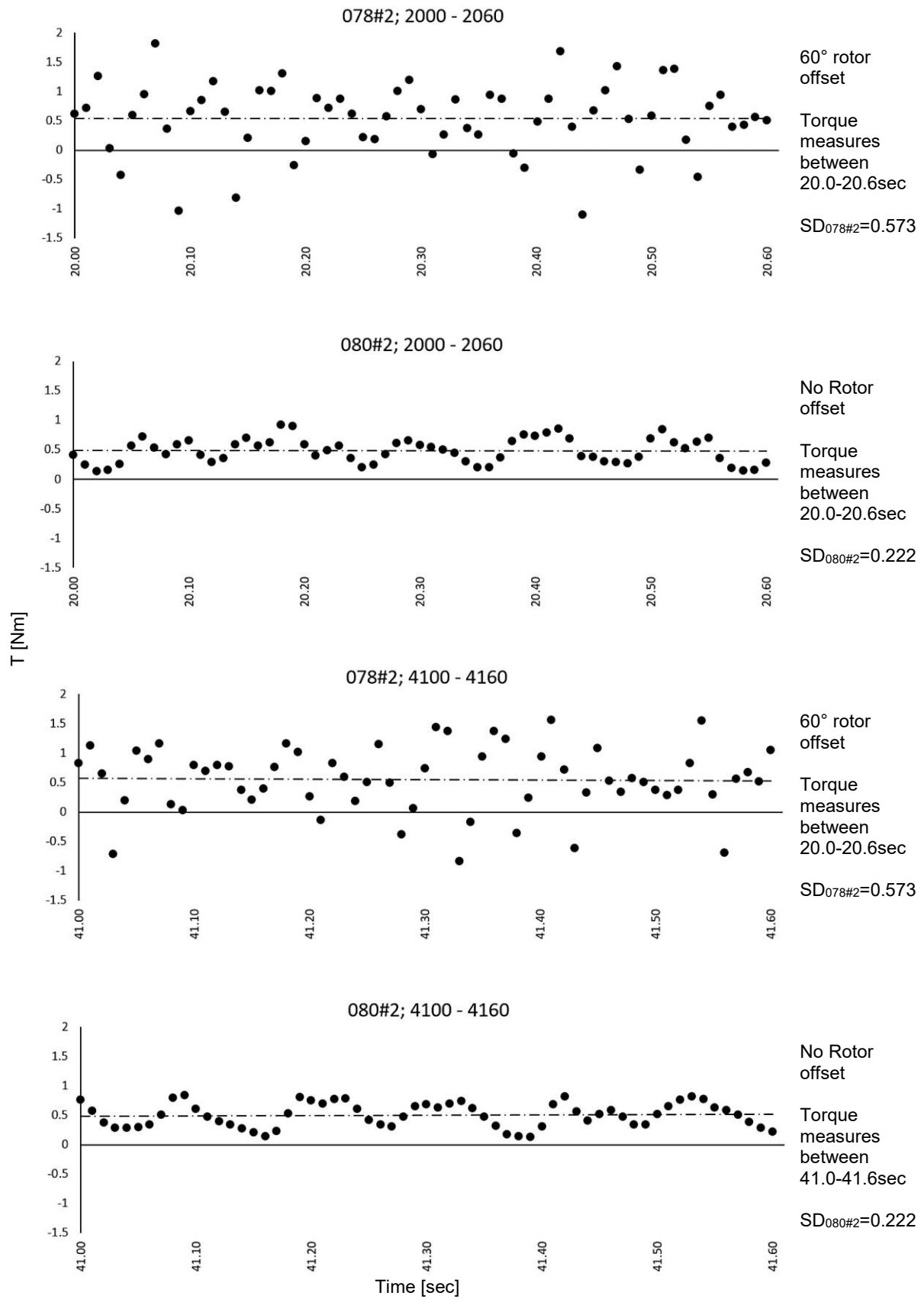


Figure 18. Variation of torque over a period of 0.6 seconds of offset (078#2) and non-offset (080#2) rotors at two different periods of time during test point #2.

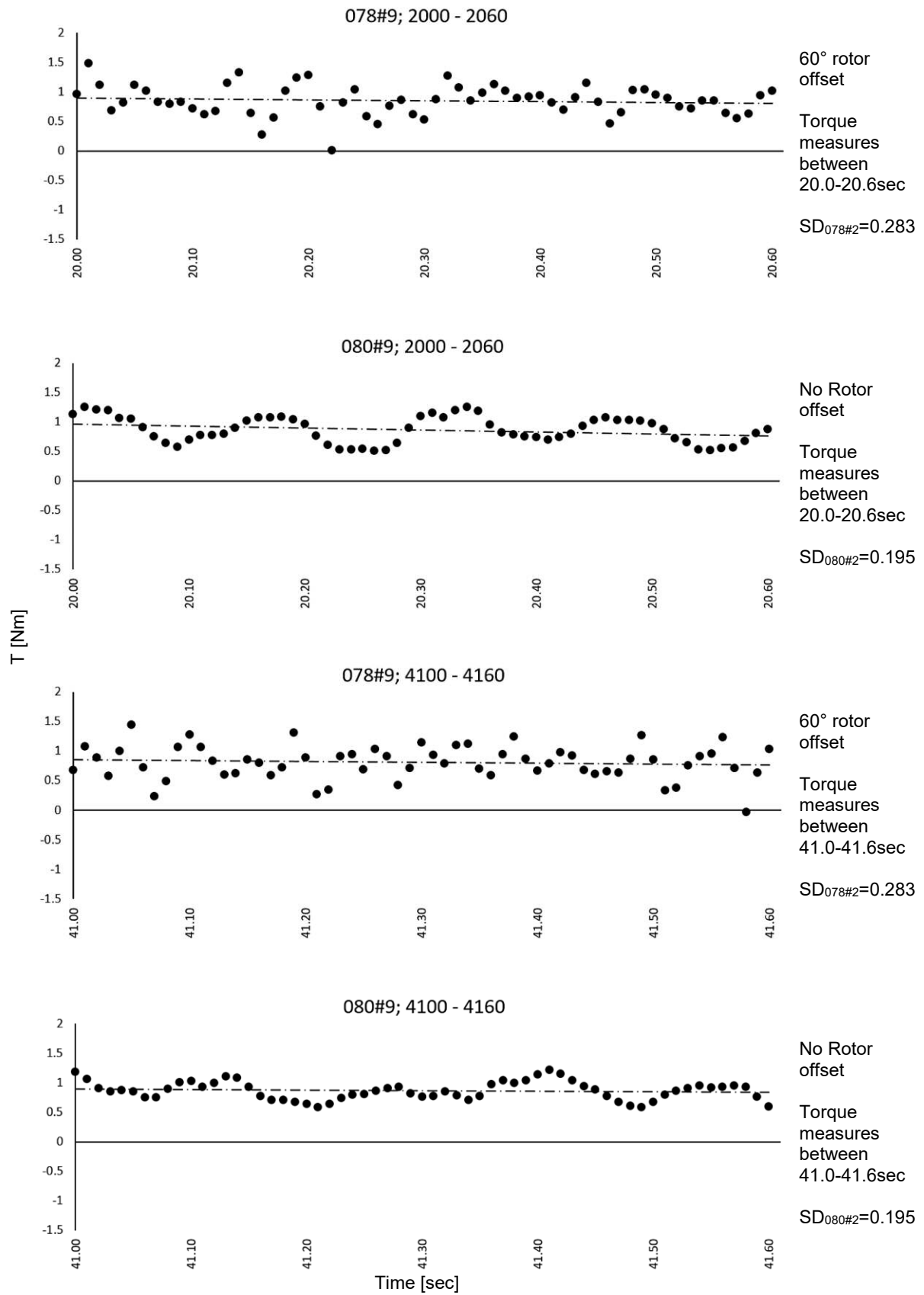


Figure 19. Variation of torque over a period of 0.6 seconds of offset (078#9) and non-offset (080#9) rotors at two different periods of time during test point #9.



Stefan Runge  
School of Engineering  
Cardiff University, UK  
2018

